PREPARATION, STRUCTURE, MAGNETIC AND ELECTROCHEMICAL PROPERTIES OF CeO_2-BASED NANOSTRUCTURES

Somchai Sonsupap

Thesis Submitted in Partial Fulfillment of the Requirements for the
Degree of Doctor of Philosophy in Physics
Suranaree University of Technology
Academic Year 2018

การเตรียมโครงสร้าง สมบัติแม่เหล็กและไฟฟ้าเคมีของโครงสร้างนาโนกลุ่มซีเรียมออกไซด์

นายสมชาย สอนสุภาพ

วิทยานิพนธ์นี้เป็นส่วนหนึ่งของการศึกษาตามหลักสูตรปริญญาวิทยาศาสตรดุษฎีบัณฑิต
สาขาวิชาฟิสิกส์
มหาวิทยาลัยเทคโนโลยีสุรนารี
ปีการศึกษา 2561

PREPARATION, STRUCTURE, MAGNETIC AND ELECTROCHEMICAL PROPERTIES OF CeO_2-BASED NANOSTRUCTURES

Suranaree University of Technology has approved this thesis submitted in partial fulfillment of the requirements for the Degree of Doctor of Philosophy.

Thesis Examining Committee

(Assoc. Prof. Dr. Sirichok Jungthawan)
Chairperson

(Prof. Dr. Santi Maensiri)
Member (Thesis Advisor)

Narong Chanlek
(Dr. Narong Chanlek)
Member (Thesis Co-Advisor)

Pinit K.
(Dr. Pinit Kidkhunthod)
Member (Thesis Co-Advisor)

(Assoc. Prof. Dr. Supree Pinitsoontorn)
Member

(Prof. Dr. Santi Maensiri)
Vice Rector for Academic Affairs
and Internationalization

(Assoc. Prof. Dr. Worawat Meevasana)
Dean of Institute of Science

สมชาย สอนสุภาพ : การเตรียมโครงสร้าง สมบัติแม่เหล็กและไฟฟ้าเคมีของโครงสร้างนาโนกลุ่มซีเรียมออกไซด์ (STRUCTURE, MAGNETIC AND ELECTROCHEMICAL PROPERTIES OF CeO_2-BASED NANOSTRUCTURES). อาจารย์ที่ปรึกษา : ศาสตราจารย์ ดร.สันติ แม้นศิริ, 212 หน้า

ซีเรียมออกไซด์/ โครงสร้างนาโน/ ออกไซด์เจือแม่เหล็ก/ ช่องว่างออกซิเจน/ ตัวเก็บประจุยิ่งยวด

การศึกษานี้รายงานการเตรียมโครงสร้างนาโนของกลุ่มซีเรียมออกไซด์ (CeO_2 และ $Ce_{1-x}M_xO_2$ เมื่อ M = Fe Co Cu หรือ La; $0 \le x \le 0.10$) ด้วยวิธีสารละลายอย่างง่าย (simple solution method) และวิธีอิเล็กโทรสปินนิง (electrospinning technique) เพื่อเป็นออกไซด์เจือแม่เหล็ก (dilute magnetic oxide) โครงสร้างนาโนที่เตรียมขึ้นถูกวิเคราะห์ด้วยตรวจสอบคุณลักษณะทางกายภาพด้วยเทคนิคเลี้ยวเบนรังสีเอกซ์ (XRD) เทคนิคอินฟราเรดสเปกโทรสโคปี (FTIR) กล้องจุลทรรศน์อิเล็กตรอนแบบส่องกราด (FE-SEM) กล้องจุลทรรศน์แบบส่องผ่าน (TEM) เทคนิคอัลตราไวโอเลตและวิสิเบิลสเปกโทรสโกปี (UV-VIS Spectroscopy) เทคนิค Brunauer-Emmett-Teller (BET) เทคนิคสเปกโทรสโกปีโดยรังสีเอ็กซ์ (XPS) และเทคนิคการดูดกลืนรังสีเอ็กซ์ (XANES) คุณสมบัติทางแม่เหล็กของสารที่เตรียมได้ถูกศึกษาด้วยเทคนิค vibrating sample magnetometry (VSM) และสมบัติทางไฟฟ้าเคมีถูกศึกษาด้วยเทคนิค CV GCD และ EIS

การศึกษาแสดงให้เห็นว่าวิธีการสารละลายอย่างง่าย และอิเล็กโทรสปินนิงให้โครงสร้างแบบอนุภาคนาโน (nanoparticle) และ เส้นใยนาโน (nanofiber) ตามลำดับ ซึ่งโครงสร้างทั้งสองแบบแสดงคุณลักษณะคล้าย ๆ กัน เส้นใยนาโนมีขนาดเส้นผ่านศูนย์กลาง 31.4±2 ถึง 59.2±2 นาโนเมตร และอนุภาคนาโนมีขนาดประมาณ 11.1±1.9 ถึง 50.1±0.9 นาโนเมตร ที่อุณหภูมิเผาและปริมาณการเจือเพิ่มขึ้นทำให้ขนาดอนุภาคใหญ่ขึ้น ทำให้เทคนิค XRD พบโครงสร้างผลึกแบบลูกบาศก์ฟลูออไรด์ของซีเรียมออไซด์ ผล UV-vis แสดงการดูดกลืนแบบ redshift ซึ่งเป็นผลมาจากการเจือโลหะทรานซิชัน เทคนิคสเปกโทรสโกปีโดยรังสีเอ็กซ์และเทคนิคดูดกลืนรังสีเอ็กซ์แสดงสถานะเลขออกซิเดชันของแต่ละธาตุคือ Ce^{4+} Ce^{3+} $Fe^{3+/2+}$ $Co^{2+/3+}$ Cu^{2+} และ La^{3+} แสดงถึงการมีอยู่ของช่องว่างออกซิเจน (V_o) ในโครงสร้าง ที่อุณหภูมิห้องโครงสร้างนาโน CeO_2 แสดงพฤติกรรมแม่เหล็กแบบเฟอโรและไดอา แต่ในตัวอย่างโครงสร้างนาโน $Ce_{1-x}Fe_xO_2$ แสดงพฤติกรรม RTFM ที่ให้ค่าแมกนีไตเซชันอิ่มตัวที่ 0.305 emu ต่อกรัม ที่เงื่อนไขเส้นใยนาโน

$Ce_{0.90}Fe_{0.10}O_2$ ความเป็นแม่เหล็กเฟอโรนั้นอธิบายจาก F-center exchange ที่เชื่อมโยงกับช่องว่างออกซิเจนรวมทั้งเป็นผลมาจาก Fe Co และ La อยู่ในโครงสร้าง

นอกจากนี้เส้นใยนาโนสารประกอบคาร์บอนและซีเรียมออกไซด์ (Carbon-CeO_2 (C/CeO_2) composite nanofibers) ยังได้ถูกเตรียมขึ้นโดยวิธีอิเล็กโทรสปินนิงในงานนี้ โดยเส้นใยนาโนที่เตรียมขึ้นจะถูกศึกษาคุณสมบัติทางกายภาพและขึ้นรูปเพื่อเป็นขั้วไฟฟ้าจากนั้นศึกษาสมบัติไฟฟ้าเคมี โดย CeO_2 นั้นให้ค่าการกักเก็บประมาณ 30 ฟารัดต่อกรัม ส่วนเส้นใยนาโนสารประกอบคาร์บอนและซีเรียมออกไซด์ แสดงพฤติกรรมแบบ EDLC ยืนยันจาก CV และได้ค่าความจุ 232 ฟารัดต่อกรัม ที่เงื่อนไข C/CeO_2 20 wt.% ทำให้เกิดรูพรุนและพื้นที่ผิวจำเพาะสูงที่ 754 ตารางเมตรต่อกรัม สามารถนำไปประยุกต์ใช้ในตัวเก็บประจุยิ่งยวดได้เนื่องจากมีคุณสมบัติที่ชาจเร็วและมีความหนาแน่นพลังงาน (power density) ที่สูง พร้อมกับมีการรักษาความสามารถของการคายประจุได้สูงกว่าร้อยละ 90 หลังจากผ่านการทดสอบอย่างน้อย 1000 รอบ

สาขาวิชาฟิสิกส์ ลายมือชื่อนักศึกษา______________

ปีการศึกษา 2561 ลายมือชื่ออาจารย์ที่ปรึกษา______________

ลายมือชื่ออาจารย์ที่ปรึกษาร่วม______________

ลายมือชื่ออาจารย์ที่ปรึกษาร่วม______________

SOMCHAI SONSUPAP : PREPARATION, STRUCTURE, MAGNETIC
AND ELECTROCHEMICAL PROPERTIES OF CeO_2-BASED
NANOSTRUCURE. THESIS ADVISOR : PROF. SANTI MAENSIRI,
D.Phil. 212 PP.

CERIUM OXIDE/ NANOSTRUCTURES/ DILUTE MAGNETIC OXIDE/
OXYGEN VACANCIES/ SUPERCAPACITOR

This study reports the synthesis of nanostructures of CeO_2 and $Ce_{1-x}M_xO_2$ where M is Fe, Co, Cu, or La ($0 \leq x \leq 0.10$) as a dilute magnetic oxides (DMOs) material by simple solution method and electrospinning technique. The prepared nanostructures were characterized by XRD, FTIR, Raman, FE-SEM, TEM, BET techniques, XPS and XANES. The magnetic and optical properties of the prepared nanostructures were studied by VSM and UV-Vis. Moreover, the electrochemical properties of the prepared CeO_2 based nanostructures were investigated by CV, GCD, and EIS.

The study indicates that the simple solution method and electrospinning technique give the structures of nanoparticles and nanofibers, respectively. Both nanostructures exhibit similar characteristics. The prepared nanoparticles and nanofibers have particle sizes of between ~11.1±1.9 to 50.1±0.9 nm and diameters of between 31.4±2 to 59.2±2 nm, respectively. The particle size increases with calcination temperature and doping concentration. The XRD result suggests the formation of CeO_2 cubic fluorite structure. UV-Vis spectra show a redshift of the band gap energy due to transition metal substitution. The XAS and XPS spectra indicate the presence of Ce^{4+}, Ce^{3+}, $Fe^{3+/2+}$, $Co^{2+/3+}$, Cu^{2+}, and La^{3+} states which suggests the formation of oxygen vacancies (V_o) in structures. At 10 kOe and room temperature, the CeO_2 nanostructures exhibit both weak ferro and diamagnetic behavior, while the $Ce_{1-x}Fe_xO_2$ nanostructures exhibit the RTFM behavior. The highest saturation magnetization (M_s) value of 0.305 emu/g was reached for the $Ce_{0.90}Fe_{0.10}O_2$ NFs sample. The ferromagnetic behavior of this system can be explained by F-center exchange, which is associated with the presence of V_o. The magnetic cationic (Fe, Co) and nonmagnetic cationic (La) valence states also play an important role in the FM of the samples.

In addition, the Carbon-CeO_2 (C/CeO_2) composite nanofibers were fabricated by electrospinning technique in this work. Their physical properties were studied. The nanofibers were prepared as an electrode and their electrochemical performance was investigated. The CeO_2 nanofibers show the specific capacitance of ~30 F g^{-1}, while C/CeO_2 composite nanofibers exhibit a likely rectangular CV of electric double layer capacitance (EDLC) behavior with the capacitances of 232 F g^{-1} (for C/CeO_2 20 wt.%). C/CeO_2 20 wt.% electrodes stored the charge by a combination of both EDLC forming on high surface area of carbon matrix (~754 m^2 g^{-1}) and the pseudocapacitive process of metal and/or metal oxides composited in each electrode. Furthermore, most the electrodes showed the imposing cycling capacity retention more than 90% after 1000 cycles.

School of physics
Academic Year 2018

Student's Signature Somchai Sonsupap
Advisor's Signature____________________
Co-advisor's Signature____________________
Co-advisor's Signature____________________

ACKNOWLEDGEMENTS

There are many people who I would like to express my sincere word of acknowledgment:

I would like to express my deepest and my mine to my supervisor, Prof. Santi Maensiri. Without his scientific supervision, instructive guidance and support this work would not be possible and successful. He has encouraged me both knowledge and understanding of nanotechnology, Physics and Materials Science.

Thank you, my co-advisor and my thesis examination committee members, Dr. Narong Chanlek, Dr. Pinit Kidkunthod, Assoc. Prof. Dr. Supree Pinitsoontorn and Assoc. Prof. Dr. Sirichok Jungthawan for their support many comments.

I would like to thank the School of Physics Institute of Science Suranaree University of Technology, Suranaree University of Technology, Advanced Materials Physics (AMP) Laboratory, Science Khon Kaen University, for providing many research facilities, Synchrotron Light Research Institute (Public Organization), Nakhon Ratchasima, Thailand for XAS and XPS facilities. I am grateful to Science Achievement Scholarship Programmed of Thailand (SAST) from Thai Government for financial support.

Finally, I would like to thank my parent: my father, Prajim Sonsupap; my mother, Pisamai Sonsupap and my older brother, Akadet Sonsupap and Surasak Sonsupap their very love for always standing by me, to give me brave heart, to bring me up and give the great live.

Somchai Sonsupap

CONTENTS

Page

CHAPTER

CONTENTS (Continued)

Page

CONTENTS (Continued)

Page

CONTENTS (Continued)

CONTENTS (Continued)

LIST OF TABLES

LIST OF TABLES (Continued)

LIST OF TABLES (Continued)

Table **Page**

LIST OF TABLES (Continued)

Table **Page**

LIST OF FIGURES

Figure **Page**

LIST OF FIGURES (Continued)

Figure **Page**

LIST OF FIGURES (Continued)

Figure **Page**

LIST OF FIGURES (Continued)

Figure **Page**

LIST OF FIGURES (Continued)

Figure **Page**

LIST OF FIGURES (Continued)

Figure **Page**

LIST OF FIGURES (Continued)

Figure **Page**

LIST OF FIGURES (Continued)

Figure **Page**

LIST OF FIGURES (Continued)

Figure **Page**

LIST OF FIGURES (Continued)

LIST OF FIGURES (Continued)

LIST OF FIGURES (Continued)

Figure **Page**

CHAPTER I

INTRODUCTION

1.1 Background and significance of the study

Dilute magnetic oxides (DMOs) are nonmagnetic oxides such as ZnO, TiO_2, SnO_2, In_2O_3 and CeO_2 which are doped with 3d-transition metals (3d-TM), such as Mn, Fe, Co, and Ni, to improve their properties, such as magnetic and optical properties. Typically, DMOs are optically transparent and exhibit ferromagnetic (FM) property at room temperature (RT) with a Curie temperature above RT (Pearton, Heo, Ivill, Norton and Steiner, 2004). In recent years, DMOs have attracted much attention due to their potential usages in spintronic and magneto-optoelectronic applications (Bryan, Heald, Chambers and Gamelin, 2004, Fitzgerald et al., 2004, Venkatesan et al., 2007, Wongsaprom, Sonsupap, Maensiri and Kidkhunthod, 2015).

Cerium (IV) oxide is an oxide from the rare earth metal cerium. Cerium can form cerium (III) oxide, Ce_2O_3, which is unstable and will be oxidized to cerium (IV) oxide with cubic (fluorite) structures. CeO_2 is enable by duality of cerium ions which easily toggles between Ce^{4+} and Ce^{3+} without changing the structure. CeO_2 has been widely studied as DMO materials. The magnetic and optical properties of CeO_2 doped with many 3d-TM ions such as Mn, Fe, Co and Ni have been intensively investigated (El-Hagary, Shaaban, Moustafa and Gad, 2019, Mousavi-Kamazani and Azizi, 2019, Yang et al., 2019). However, to the best of our knowledge, the electrochemical properties of CeO_2 doped with 3d-TM ions have been rarely studied. CeO_2 can be synthesized in different nanostructure forms such as nanoparticle (Bednarski, 2014, Phokha, Prabhakaran, Boothroyd, Pinitsoontorn and Maensiri, 2014), nanospheres (MingYan et al., 2014)), one-dimensional, nanorods (Qu et al., 2015), nanowires(Li et al., 2016), nanofibers (Yang, Shao, Liu, Mu and Guan, 2005)) or two-dimension (usually realized as thin films or stacks of thin films (Wang, Chang, Lv and Long, 2015)). These nanostructures can be applied to many novel applications such as spintronic devices (Gupta, Ghosh and Kahol, 2010), gas sensor (Yan et al., 2016), magneto-optoelectronic applications, magnetic recording etc. Several synthesis techniques can be applied to prepare CeO_2 nanostructures, such as a template-free hydrothermal method (Shan, Guo, Liu and Wang, 2012), solvothermal method (Yang et al., 2018), facile sol–gel spin coating method (Wang et al., 2015) etc.

In this work, two nanostructures: nanoparticles and nanofibers, of CeO_2 and transition metal-doped CeO_2, $Ce_{1-x}M_xO_2$, where M is either $Fe^{3+/2+}$, $Co^{3+/2+}$, Cu^{2+}or La^{3+} were synthesized in order to develop a new shape of nanostructure of DMO materials. The CeO_2 based DMOs nanoparticles were prepared by simple solution method. This synthesis method is cost effective, less synthesis time, processing and the large amount of final product compared with other methods. The CeO_2 based DMOs nanofibers were fabricated by electrospinning technique. The electrospinning technique is simple, convenient, environmentally-friendly, and efficient(Choi et al., 2010, Yan et al., 2015). This technique has been developed to fabricate materials with nanofibrous structures. It is suitable method for preparing polymer fibers and ceramic fibers with both solid and hollow interiors that are exceptionally long in length, uniform in diameters ranging from tens of nanometers to several micrometers, and diversified in compositions (Tang, Fu, Zhao, Xie and Teng, 2015).

The prepared CeO_2-based nanostructures were characterized by several characterization techniques including X-ray diffraction (XRD), Fourier transform infrared spectroscopy (FTIR), Raman spectroscopy (Raman), field emission scanning electron microscopy (FE-SEM), transmission electron microscopy (TEM), Brunauer-Emmett-Teller (BET) techniques, X-ray photoelectron spectroscopy (XPS) and X-ray absorption near edge structure spectroscopy (XANES). The magnetic and optical properties of the prepared nanostructures were studied by vibrating sample magnetometry (VSM) and UV-Visible spectroscopy (UV-Vis). The origin of magnetism of the prepared CeO_2 based nanostructures is also discussed. Moreover, the electrochemical properties of the prepared CeO_2 based nanostructures were investigated by using cyclic voltammetry (CV), galvanostatic charge discharge (GCD), and electrochemical impedance spectroscopy (EIS). Their potential uses in energy storage applications are discussed.

In addition to the CeO_2 based nanostructures, we have extended our study to other CeO_2 based nanostructures. Carbon-CeO_2 (C/CeO_2) composite nanofibers were also fabricated by electrospinning technique in this work. Their physical properties were studied, and their electrochemical performance was investigated.

1.2 Research objectives

1.2.1 To fabricate CeO_2 and $Ce_{1-x}M_xO_2$ nanostructures (M = Fe, Co, Cu or La) where $0 \leq x \leq 10$ (% mole) by simple solution method and electrospinning technique.

1.2.2 To characterize the prepared CeO_2 and $Ce_{1-x}M_xO_2$ nanostructures by X-ray Diffraction (XRD), Scanning electron microscope (SEM), Transmission electron microscope (TEM), Raman spectroscopy (RS), Fourier Transform Infrared Spectroscopy (FT-IR), X-ray absorption near edge structure (XANES) and X-ray photoelectron spectroscopy (XPS)

1.2.3 To study optical, magnetic and electrochemical properties of the prepared CeO_2 and $Ce_{1-x}M_xO_2$ nanostructures materials by using UV–visible spectroscopy (UV-vis), vibrating sample magnetometry (VSM), cyclic voltammetry (CV), galvanostatic charge discharge (GCD), and electrochemical impedance spectroscopy (EIS).

1.2.4 To study the effect of the M concentration on the structure and properties of the $Ce_{1-x}M_xO_2$ nanostructures.

1.3 Limitation of the study

1.3.1 Synthesis of CeO_2 and $Ce_{1-x}M_xO_2$ (M = Fe, Co or La) nanostructures where $0 \leq x \leq 10$ (% by mole).

1.3.2 Characterization of the prepared CeO_2 and $Ce_{1-x}M_xO_2$ nanostructures by TG/DSC, XRD, SEM, TEM, HRTEM, SAED, EDX, RAMAN, FTIR, XPS and XAS.

1.3.3 Study of physical adsorption of gas molecules on a solid surface of the fabricated CeO_2 and $Ce_{1-x}M_xO_2$ nanostructures by Brunauer–Emmett–Teller (BET).

1.3.4 Study of magnetic properties of the synthesized CeO_2 and $Ce_{1-x}M_xO_2$ nanostructures by VSM.

1.3.5 Study of electrochemical properties of CeO_2 and $Ce_{1-x}M_xO_2$ nanostructures for energy storage applications.

1.4 Location of research

1.4.1 Advanced Materials Physics Laboratory (AMP), School of Physics, Institute of Science, Suranaree University of Technology (SUT), Nakhon Ratchasima, 30000 Thailand.

1.4.2 The Center for Scientific and Technological Equipment (SUT), Suranaree University of Technology (SUT), Nakhon Ratchasima, 30000 Thailand.

1.4.3 Department of Physics, Faculty of Science, KhonKaen University, KhonKaen, 40002 Thailand.

1.4.4 Department of Chemistry, Faculty of Science, KhonKaen University, KhonKaen, 40002 Thailand.

1.4.5 Synchrotron Light Research Institute (SLRI), 111 Surapat 3, Suranaree University of Technology, University Avenue, Muang District, Nakhon Ratchasima, 30000 Thailand.

1.5 Anticipated outcomes

1.5.1 Understanding of synthesis of CeO_2 and $Ce_{1-x}M_xO_2$ nanostructures with excellent optical, electrochemical and magnetic properties.

1.5.2 Explain possible mechanism of magnetic properties in CeO_2 and $Ce_{1-x}M_xO_2$ nanostructures.

1.5.3 International publication (ISI).

1.6 Dissertation structure

This dissertation is organized into five chapters. The introduction of thesis is given in Chapter I. Review of the literatures which are relevant to this research, including DMOs, origin of magnetism in DMO and CeO_2 are presented in Chapter II. The research methodology including the sample preparations and characterizations are described in Chapter III. The characterization results, optical, magnetic and electrochemical properties of CeO_2 and $Ce_{1-x}M_xO_2$ (M = Fe, Co or La) nanostructures are presented and discussed in Chapter IV. The synthesis and electrochemical properties study of of Carbon-CeO_2 composite are presented in Chapter V. Finally, conclusions and suggestions are given in Chapter VI.

CHAPTER II

LITERATURE REVIEW

This chapter presents the background knowledge of dilute magnetic oxides, cerium oxide and basic theories which describe the optical, electrochemical and magnetic properties of CeO_2 and doped-CeO_2 nanostructures.

2.1 Dilute magnetic oxides and their magnetism

2.1.1 General knowledge of dilute magnetic oxides

Metal elements are able to form a large diversity of oxide compounds (Kung, 1989, Noguera, 1996). These can adopt a vast number of structural geometries with an electronic structure that can exhibit metallic, semiconductor or insulator character. Metal oxides play a very important role in many research areas, such as chemistry, physics and material science. In technological applications, the metal oxides are used in the fabrications of microelectronic circuits, sensors, piezoelectric devices, fuel cells, coatings for the passivation of surfaces against corrosion, and as catalysts (Bäumer and Freund, 1999, Rodriguez et al., 2002). The structure of metal oxides is composed of metal cations bonding with oxygen anions (oxygen has an ionic radius of = 0.140 nm). Metal cations can be surrounded by oxygens forming octahedral interstices (6 oxygen), tetrahedral interstices (4 oxygen) or linear as shown in Figure 2.1.

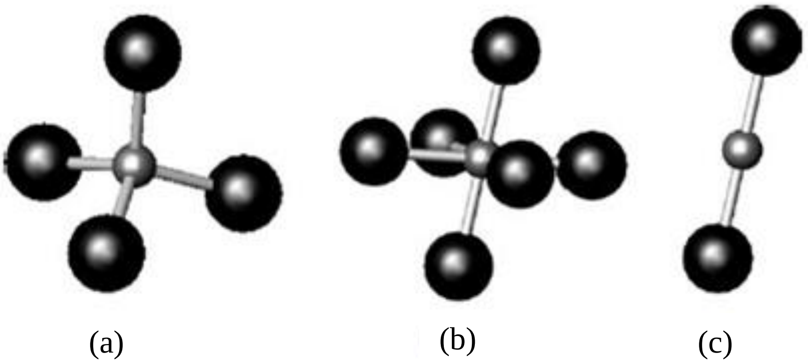

Figure 2.1 Structure of general metal oxides (a) tetrahedral interstices (b) octahedral interstices and (c) linear (Ingram, Gonzalez, Kammler, Bertoni and Mason, 2004).

Normally, the oxide material is an insulator or semiconductor with wide energy band gap. The number of electrons or holes can be changed by adding additives or creating nonstoichiometric in the material. These electrons and holes will be in the trap level and do not affect the conductivity of the oxide. It is widely known that the properties of metal oxides such as optical and magnetic properties can be enhanced by adding few percent of 3d-transition metal (3d-TM) ions such as Mn, Fe, Co, and Ni into metal oxide structure. This is the so-called dilute magnetic oxide (DMO) (Fitzgerald et al., 2004, Bednarski, 2014, Abbas, Jan, Iqbal and Naqvi, 2015). The general formula of dilute magnetic oxide can be written as

$$(M_{1-x}T_x)_nO \tag{2.1}$$

where T is cation of metal with magnetic properties.

M is cation of metal with nonmagnetic properties.

n is numeral or fraction.

x is doping value of cation $0 \leq x \leq 1$. It may also be shown in percent.

(Coey, Venkatesan and Fitzgerald, 2005).

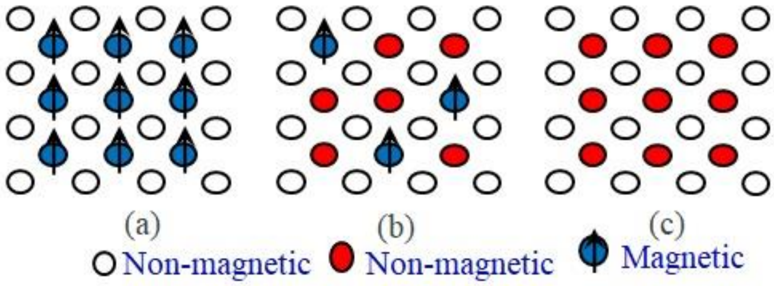

Figure 2.2 The schematic diagram of the formations of (a) a magnetic oxide (b) a diluted magnetic oxide and (c) a nonmagnetic oxide (Ohno, 1998).

The formation of DMO can be simply shown as a Figure 2.2. Typically, 3d orbital or 4f orbitals metal ions are substituted into metal host in oxide. For the solid solution, atoms or ions in the structure can be replaced by other atoms or ions, so-called ionic substitution. This can happen for both whole substitution and part substitution. The factors that determine the substitution of the ions in such structures include.

- The number of charged ions -should not be more than ± 1 for examples, Mg^{2+}/ Fe^{2+} or Al^{3+}/Si^{4+} ions, if their charges are not equal, additional ions are required to balance the charge.
- The size of the ion - should not be different more than 15% for whole substitution and 15-30% for part substitution. It is rarely found when the size difference is higher than 30%.
- Temperature - at high temperature, the bond between ions are vibrating more than usual. The structure will expand and can easily accommodate replacing ions. Therefore, large ions can be easily replaced at high temperature.

For DMOs, candidate dopants manganese (Mn^{25}), iron (Fe^{26}), cobalt (Co^{27}) and nickel (Ni^{28}). Their charges, electron configurations, ions certain radius arrangement of electrons in the 3d transition metal are shown in Table 2.2 and Table 2.3.

The spin of electrons from individual atoms are coupled together as a net magnetic moment of unit cell. Assuming the moment of the unit cell perpendicular to the page, the unit cell of the crystal is composed of iron many domains. Within each domain, which is arrangement of orderly now of the adjacent cell. However, the pack will contain both crystalline arrangement of the disorder of moment these scattered in all directions. The process of the magnetic moment of these will be make available in an orderly and cause permanent moment (Novák, 2016).

Table 2.1 An example of transition metals with their charges, electron configurations and ions certain radius (Adapted from Coey (2006)).

Ions	**charge**	**configuration**	**radius (nm)**
Ti	3^+ / 4^+	$3d^1$ / $3d^0$	0.069/0.061
Cr	3^+	$3d^3$	0.064
Mn	2^+ / 3^+ / 4^+	$3d^5$ / $3d^4$ / $3d^3$	0.083/0.065/0.053
Fe	2^+ / 3^+	$3d^6$ / $3d^5$	0.082/0.065
Co	2^+ / 3^+	$3d^7$ / $3d^6$	0.082/0.061
Ni	2^+ / 3^+	$3d^8$ / $3d^7$	0.078/0.069
Cu	2^+	$3d^9$	0.072

Table 2.2 The arrangement of electrons in the 3d transition metal (Adapted from (Galperin, 1975)).

Ions	**Electron in 3d orbital**	**electron configuration in 3d orbital**	**Net spin S**
Sc^{3+} Ti^{4+}	$3d^0$	[ ][ ][ ][ ][ ]	0
Ti^{3+}	$3d^1$	[↑][ ][ ][ ][ ]	1/2
Ti^{2+} V^{3+}	$3d^2$	[↑][↑][ ][ ][ ]	1
V^{2+} Cr^{3+}	$3d^3$	[↑][↑][↑][ ][ ]	3/2
Cr^{2+} Mn^{3+}	$3d^4$	[↑][↑][↑][↑][ ]	2
Mn^{2+} Fe^{3+}	$3d^5$	[↑][↑][↑][↑][↑]	5/2
Fe^{2+} Co^{3+}	$3d^6$	[↑↓][↑][↑][↑][↑]	2
Co^{2+} Ni^{3+}	$3d^7$	[↑↓][↑↓][↑][↑][↑]	3/2
$Ni^{2+}Cu^{3+}$	$3d^8$	[↑↓][↑↓][↑↓][↑][↑]	1
Cu^{2+}	$3d^9$	[↑↓][↑↓][↑↓][↑↓][↑]	1/2

Table 2.3 Study of oxide magnetic materials in some groups with the Curie temperature (Tc) and the magnetic moment of the cation dopant (Adapted from Coey (2006)).

Materials	Energy band gap E_g (eV)	Dopant	Magnetic moments (μ_B)	Curie temperature (K)
TiO_2	3.2	V – 5%	4.2	>400
		Co – 1-2%	0.3	>300
		Co – 7%	1.4	>650
		Fe – 2%	2.4	300
SnO_2	3.5	Fe – 5%	1.8	610
		Co – 5%	7.5	650
ZnO	3.3	V – 15%	0.5	>350
		Mn – 2.2%	0.16	>300
		Fe – 5%	0.75	550
		Co – 10%	2.0	280-300
		Ni – 0.9%	0.06	>300
Cu_2O	2.0	Co – 5%	0.2	>300
		Mn – 0.3%	0.6	>300
In_2O_3	3.7	Fe – 5%	1.4	>600
		Cr – 2%	1.5	900
CeO_2	3.4	Co – 3%	6.0	~800

2.1.2 Magnetic properties in dilute magnetic oxides

Magnetism of oxide material has been a subject of intense study for long time. In 2000, Dietl et al., theoretically predicted that the ferromagnetism (FM) at high temperature could be obtained in many semiconductors such as ZnO, GaAs, GaN by doping with Mn (Dietl, Ohno, Matsukura, Cibert and Ferrand, 2000). Later on, the room temperature ferromagnetism (RTFM) were observed on TiO_2 (Matsumoto et al., 2001) and ZnO (Ueda, Tabata and Kawai, 2001) doped with a few percent of a transition metal such as, Co, Mn, Cr and Ni. Much attention has been paid to study the ferromagnetism in thin films including TiO_2 with V, Cr, Fe, Co or Ni, SnO_2 with V, Cr, Mn, Fe or Co and ZnO with Ti, V, Cr, Mn, Fe, Co, Ni or Cu (Coey, 2006). The 3d dopant concentrations are generally below 10% (Coey et al., 2005). Nanoparticles of some of these systems are also reported to be ferromagnetic, but well-crystallized, bulk material does not order magnetically. Previous studies on the dilute magnetic oxides, dopants and their Curie temperatures (T_c) and magnetic moment are reported in Table 2.1.

Despite the many studies, the basic principles and mechanisms of the magnetism of DMOs are still unclear. There is no clear understanding whether the magnetic oxide is originated from the electron in the 3d orbital or 4f orbitals of transition metal, and the rare earth metal cation which is the source of the magnetic moment will exhibit room temperature ferromagnetism (RTFM) or higher than room temperature ferromagnetism. Many models of FM have been proposed, including an exchange mechanism related to donor electrons in an impurity (Coey et al., 2005), a superexchange or double exchange interaction (Zener, 1951, Spaldin, 2003), and a defect mediated mechanism like Bound Magnetic Polaron model (BMP) (Coey, Venkatesan and Fitzgerald, 2005).

2.2 Mechanism of magnetism in dilute magnetic oxide

2.2.1 The Zener model

In the Zener model, the *direct superexchange* interaction (Anderson, 1950) between half-filled d-shell electrons of transition metal (TM) cations nearest neighbor via filled p-orbitals of anion (for e.g O^{2-} in case of oxides) is antiferromagnetic (AFM) configuration (see in Figure 2.3). The electrons are from the same valence (number of electrons) and are coupled with the spins of ions. The d-shell electrons from both adjacent TM atoms occupy the same p-level. Their spins must be opposite according to Pauli Exclusion Principle. This leads to an AFM coupling of nearest-neighbor TM cations through a shared anion.

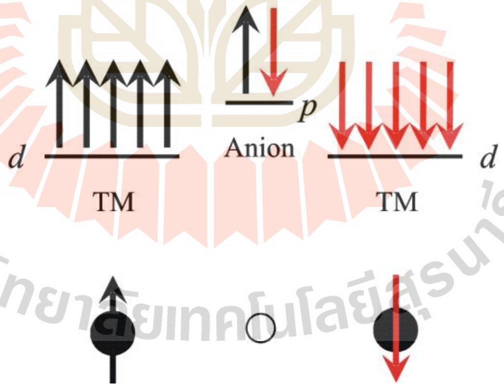

Figure 2.3 Direct super-exchange interaction: Anti-ferromagnetic coupling of adjacent d orbital of TM cations through a shared p orbital of anion (Zener, 1951).

On the contrary, the *indirect superexchange* interaction between localized d-shell electrons of TM cations is connected at 90 degrees to anion, then the interaction can be a ferromagnetic interaction (see Figure 2.4). In the Zener model, ferromagnetism is only possible when the indirect exchange interaction dominates over the direct superexchange interaction.

Since the superexchange is predominantly AFM and short ranged, it cannot account for long range ferromagnetic ordering seen in transition metal doped DMSs. But as the dopant concentration approaches the χ_p associated with nearest neighbor cation coupling, AFM coupling between nearest neighbor cations does start occurring and this reduces the average magnetic moment per dopant ion.

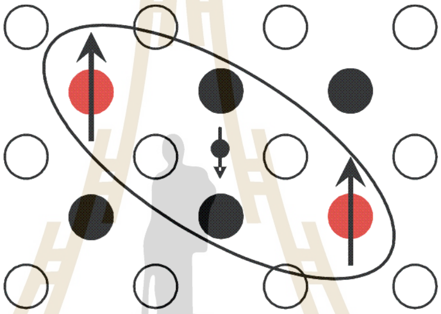

Figure 2.4 Indirect super-exchange interaction: Ferromagnetic coupling of localized spins through the conduction electrons (Zener, 1951).

2.2.2 Superexchange and Double exchange

The magnetic properties of oxides can be explained by electron exchange mechanism. Two magnetic metal ions are bonded with oxygen as shown in Figure 2.5. The charge of two metal ions may be equal or unequal. The metal ions interact to each other though oxygen and result in magnetism of the oxides. This is the so-called magnetic interaction. Consider the case of Mn-O bond, electrons are filled in d orbitals of Mn^{3+} as shown in Figure 2.6. When Mn bonds with oxygen, the relationship between Mn-O-Mn occurs.

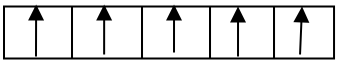

Figure 2.5 Electron configuration in d orbitals of the Mn^{3+}.

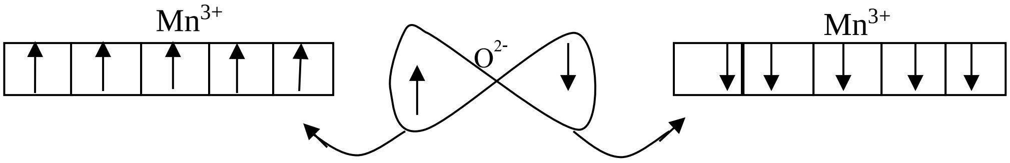

Figure 2.6 Electron configuration in d orbitals of the Mn^{3+} and mechanism superexchange (Adapted from Spaldin (2003)).

The spin up electrons in d orbitals of Mn^{3+} (on the left) pair with spin up single electron in p orbitals of O^{2-}. The electron left in p orbitals of O^{2-} is spin down according to the Hund's rule and the Pauli Exclusion Principle. This electron will pair with electrons in d orbitals of Mn^{3+} (on the left) and cause them spin down as shown in Figure 2.8. General mechanisms related to orbital of oxygen as intermediaries in the coupling between the electrons of the metal is known as superexchange and cause the antiferromagnetic properties.

Consider the case of Fe-O bond when ions are not equal as in figure 2.7. The electrons in d orbitals of Fe^{3+} (on the left) will pair with an electron in p orbitals of O^{2-} as the above condition. However, the d orbitals of Fe^{2+} (on the right) do not overlap with the p orbitals of the O^{2-} ion. Single electron in the orbital arrangement will be regulated by a single electron spin in parallel with the rest. This arrangement is more stable. The electrons in d orbitals of Fe^{3+} (on the left) and Fe^{2+} (on the right) spin in the same direction. This is called double exchange interaction and cause ferromagnetic properties (Spaldin, 2003).

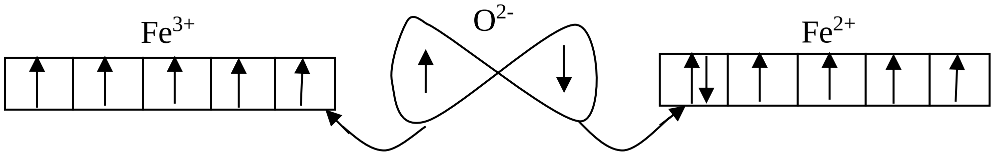

Figure 2.7 Arrangement of electrons in d orbitals of the Fe^{3+} and mechanism double exchange interaction (Adapted from Spaldin (2003)).

2.2.3 Face center exchange

Coey *et al.* (2006) has proposed that RT-FM in the DMO is associated with orbital and space of oxygen (oxygen vacancies) or defect (defect) occurred in the structure of the oxides. This interaction model is known as Face center exchange (FCE). The magnetic interaction together by oxygen vacancy as intermediaries result in ferromagnetism as shown in Figure 2.8. The F-center leads to the formation of bound magnetic polarons (BMP) (Berciu & Bhat, 2001; Bhat, Berciu, Kennett & Wan, 2002; Dietl et al., 2002; Sharma, Hwang, & Kaminiski, 2003)

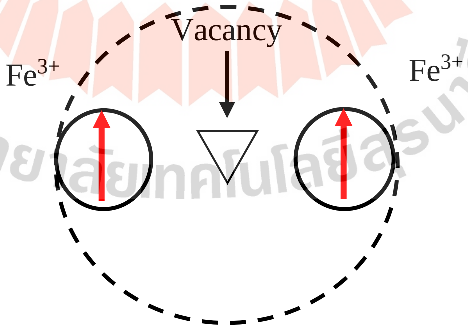

Figure 2.8 Indirect super-exchange interaction: Ferromagnetic coupling of localized spins through the conduction electrons (Coey, Douvalis, Fitzgerald and Venkatesan, 2004).

2.2.4 Bound magnetic polaron (BMP)

Defects in the structure and oxygen vacancies which are present in the structure can interact with electrons forming the so-called bound magnetic polaron (BMP) resulting in a large magnetic moment (Coey et al., 2005). The magnetism in DMO can be divided into three cases as shown in Figure 2.9. In the first case, the separation between the metal ions is larger than Bohr's radius. The spin of anions is independent and result in paramagnetism. In the second case, the separation between the metal ions is of the order of a few Bohr radii. Neighboring BMPs can overlap. If neighboring BMPs do not interact strongly with each other, the BMPs couple in paramagnetic fashion. However, the BMPs may couple in a ferromagnetic fashion at certain BMP-BMP distances, typically in the order of a few Bohr radii (E. Angelescu and N. Bhatt, 2001, Durst, Bhatt and Wolff, 2002). In the third case, the transition metal ions are as close as possible. The exchange of electrons between a pair of ions through ion of oxygen is superexchange resulting antiferromagnetism.

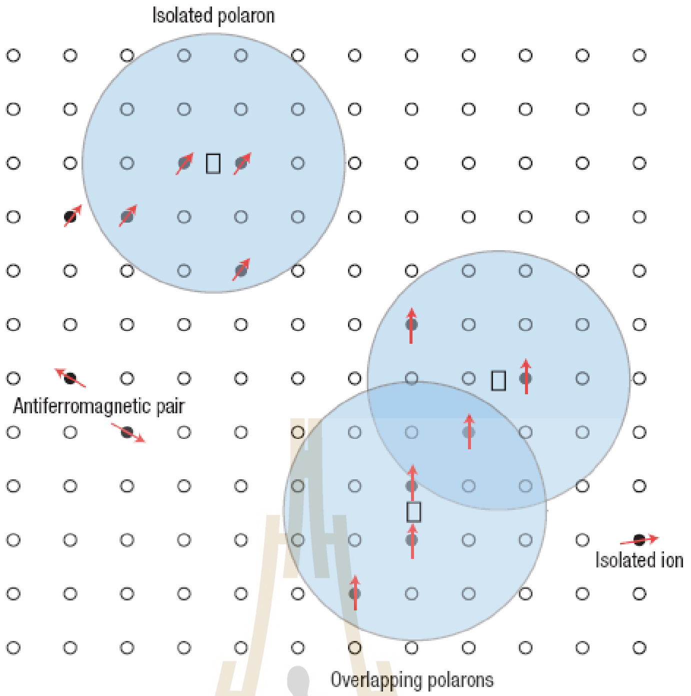

Figure 2.9 Representation of interaction bound magnetic polarons (BMP). By ↑ is spin of transition metal, ○ is position of transition ions, and □ is oxygen vacancies (Coey, 2006).

2.3 Cerium oxide nanostructure (CeO_2)

2.3.1 Structure and properties of cerium oxide nanostructure

Cerium (IV) oxide, CeO_2, is an oxide from of the rare earth metal cerium. Cerium also forms cerium (III) oxide, Ce_2O_3, which is unstable and will be oxidized to cerium (IV) oxide with cubic (fluorite) structures (shown in figure 2.10). The basic physical properties for CeO_2 are listed in Table 2.4.

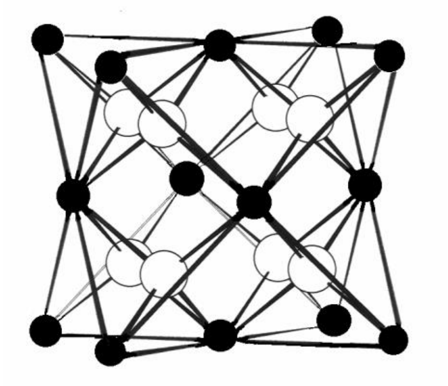

Figure 2.10 FCC structure for CeO_2 (circle represents oxygen, solid ball represents cerium) (Kilbourn, 1992).

Table 2.4 Physicochemical properties of pure stoichiometric CeO_2 (Bamwenda and Arakawa, 2000, Mogensen, Sammes and Tompsett, 2000).

Properties	**Value (unit)**
Color	Yellow White
Density	7.22 g cm^{-1}
Surface area	~9.5 m^2 g^{-1}
Melting point	Ca. 2750 K
Acidity	Weak base
Conductivity	1.2 ~ $2x10^{-8}$ $\Omega^{-1}cm^{-1}$
Thermal Conductivity	Ca. 12 W $m^{-1}K^{-1}$
Refractive index	Ca. 2.1 visible
	Ca. 2.2 infrared
Absorption Edge	~420 nm

Table 2.4 Physicochemical properties of pure stoichiometric CeO_2 (Bamwenda and Arakawa, 2000, Mogensen et al., 2000) (Continued).

Band gap	~2.95 eV (UV) 5.5 eV (electronic cal.)
Curie temperature	>300 K

In recent years, the nanometer-sized particles and nanostructures of CeO_2 based materials have attracted much attention because of their unique physical and chemical properties significantly different from their bulk counterparts as well as their potential applications in industry. Various types of CeO_2 based nanomaterials have been synthesized by many methods such as hydrothermal, sol-gel method, co-precipitation method, etc. Diverse applications have been reported as shown in Table 2.5.

He et al. reported the synthesis of CeO_2 nanoparticles (NPs)via a sol–gel process in the range of room temperature to 65 °C with the nonionic surfactant PVP (polyvinylpyrrolidone).

The synthesized CeO_2 NPs have the particle size of about 10 nm (He et al., 2012).Hou et al. investigated the removal of biological nitrogen in a sequencing batch biofilm reactor (SBBR) by CeO_2NPs (Hou et al., 2015). Malleshappa et al. reported the synthesis CeO_2 nanoparticles by hydrothermal method. The synthesized CeO_2 nanoparticles exhibited CeO_2cubic fluorite structure confirmed by selected area electron diffraction (SAED) and their photo catalytic and antibacterial properties were studied (Malleshappa et al., 2015). Miri and Sarani synthesized CeO_2nanoparticles by aqueous extract of aerial parts of *Prosopis farcta*. The synthetized nanoparticles had cytotoxic activity against the HT-29 cancer cell line. The synthesized CeO_2 nanoparticles exhibited the fluorite structure of CeO_2, with particles size of 30 nm. (Miri and Sarani, 2018).

Oxygen vacancy (V_o) is a common native point defects that plays crucial roles in determining the physical and chemical properties of metal oxides such as ZnO, TiO_2 (Nakamura et al., 2000, Li, Song, Liu and Zeng, 2014). However, fundamental understanding of V_o is still very sparse. The oxygen vacancy formation in ceria results in partial reduction of the material where two electrons are left when removing a neutral O atom. In the cubic fluorite structure of CeO_2, the oxygen ions are not closely packed for which ceria form many oxygen vacancies while maintaining the basic fluorite structure. The photoexcitation process in ceria is represented by Kroger-Vink notation given by

$$4Ce_{Ce} + O_O \rightarrow 2Ce_{Ce} + 2CeCe + VO\bullet\bullet + (1/2)\,O_2\,(g) \qquad (2.2)$$

Cerium oxides with oxygen vacancies or defect (by Ce^{3+} ions) (see in Figure 2.12) in lattice structure play a crucial role in magnetic and optical properties. V_o or defect in CeO_2 structure can be experimentally observed by many methods. Meng et al. reported the synthesis hexagonal nanosheet of CeO_2 with thickness of 300-400 nm by facile hydrothermal technique. The prepared CeO_2 nanosheet showed excellent optical properties and M-H curve exhibited room temperature ferromagnetism (RTFM) with saturation magnetization (M_s) of 3.02 x 10^{-2} emu/g and coercivity (H_c) of 210 Oe. The formation of V_o was investigated by Raman spectra as shown in Figure 2.13 (a).The samples showed the F_{2g} mode of CeO_2 at about 450 cm^{-1} and peaks of intrinsic at about 577 cm^{-1}.The intensity of intrinsic Raman active mode in structure of hexagonal CeO_2

sheets samples showed the presence of V_o in structure which leads to RTFM in the CeO_2 samples.

XPS technique can be also used to study V_o on surface of CeO_2. Grover et al. reported the radiation stability of ceria with microstructure under the electronic excitation regime. The XPS studies provided concrete evidence for the presence of Ce^{3+} and oxygen ion vacancies in the samples (see in Figure 2.15) (Grover et al., 2014).

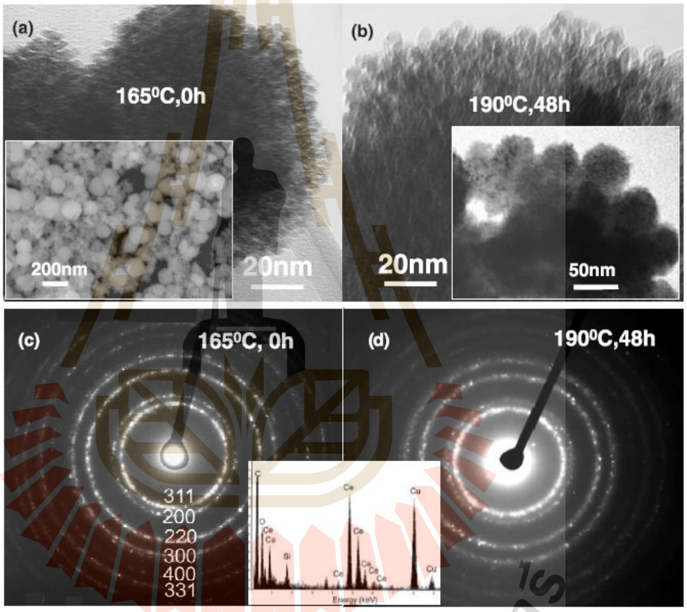

Figure 2.11 SEM and TEM images of CeO_2 nanoparticles. (a) TEM and SEM images of ceria synthesized at 165 °C for 0 h. (b) TEM and SEM images of ceria synthesized at 190 °C for 48 h. The electron diffraction of ceria at (c) 165 °C and (d) 190 °C (Malleshappa et al., 2015).

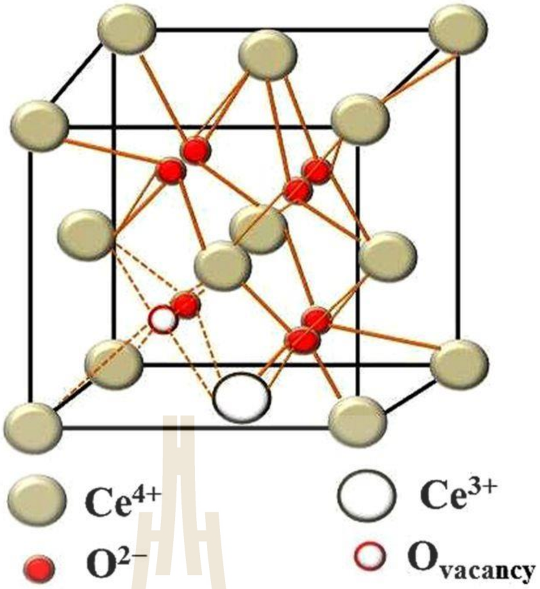

Figure 2.12 Schematic model of the CeO$_2$ structure showing Ce^{3+}-ions and oxygen vacancy. The whitish color ball is Ce^{4+}; the red color ball is O^{2-} on the lattice site; the red color circled ball is oxygen vacancy; the unfilled white ball represents Ce^{3+} on the lattice site formed after removing oxygen either from surface or from the interior of CeO$_2$ (Khan, Khan and Cho, 2017).

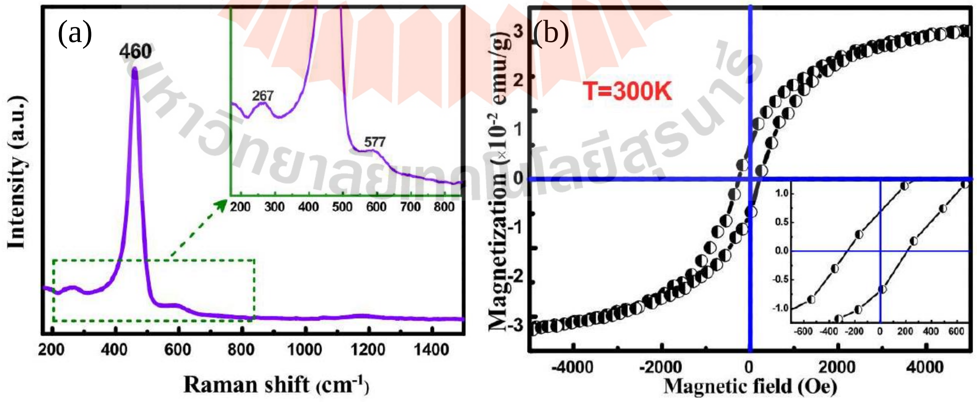

Figure 2.13 (a) RAMAN spectra and (b) *M*-H curve of hexagonal CeO$_2$ sheets (Meng et al., 2015)..

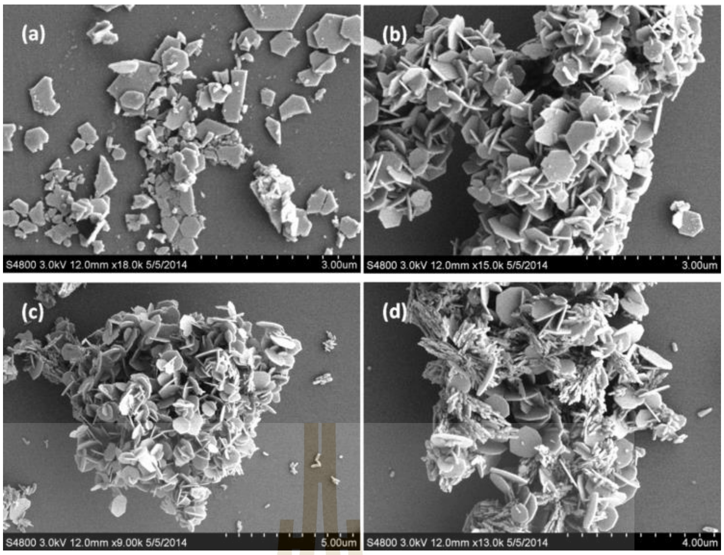

Figure 2.14 SEM images of CeO_2 nanosheets synthesized at 180 °C for 48 h doped with $CeCl_3.7H_2O$ of (a) 1 m mol, (b) 2 m mol, (c) 6 m mol, and (d) 8 m mol (Meng et al., 2015).

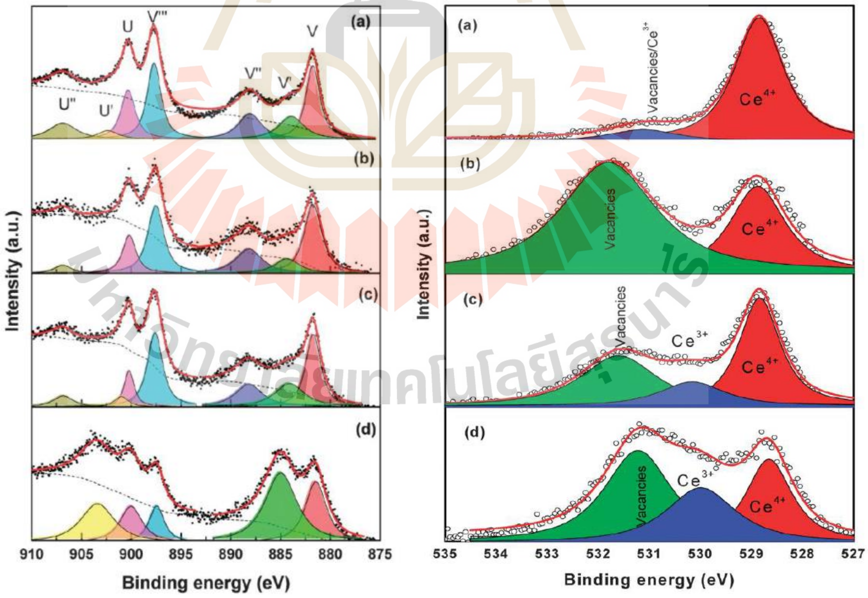

Figure 2.15 XPS Ce 3d and O 1s spectra for (a) S800 before irradiation, (b) S800 after irradiation, (c) S1300 before irradiation, and (d) S1300 after irradiation (Grover et al., 2014).

Table 2.5 List of previous studies of CeO_2 nanostructures.

Materials	Remark studies /applications	Reference
CeO_2 nanoparticles	Structure and biological nitrogen removal property	(Hou et al., 2015)
CeO_2 nanocrystal	Structure and optical property	(Wang, Quan and Lin, 2007)
CeO_2 nanoparticles	Structure and catalytic and optical property	(Wang et al., 2010)
CeO_2 nanoparticles	Structure and biological and optical property	(Malleshappa et al., 2015)
CeO_2 nanoparticles	Structure and optical property	(Chenguo, Zuwei, Hong, Puxian and Zhong Lin, 2006)
Nanocrystalline CeO_2 film	Structure and magnetic property	(Wang et al., 2015)
CeO_2 nanocolumns	Structure and magnetic property	(Meng et al., 2015)

2.3.2 Transition metal-doped CeO_2

CeO_2 nanostructures doped with metals such as Fe, Co, Ni, Cu or Zn. have been intensively studied as shown in Table 2.6. Sharma et al. and Phokha et al. reported the study of Fe-doped CeO_2 nanoparticles which exhibited RT-FM with high Curie temperature (Sharma et al., 2010, Phokha, Pinitsoontorn and Maensiri, 2013). Murugan et al. and Qi-Ye et al. reported the investigation of Co-doped CeO_2 nanostructures which exhibited RT-FM. The oxygen vacancy or defect in the structure played an important role on magnetism of the samples (Qi-Ye et al., 2007, Murugan, Vijayaprasath, Mahalingam and Ravi, 2016).

The addition of metal to CeO_2 nanostructure have been observed to improve the magnetic property and electronic conductivity. Enhancement of the magnetic properties and conductivity can improve the rate capability and the power density of the CeO_2 nanostructure coaxial cable electrode.

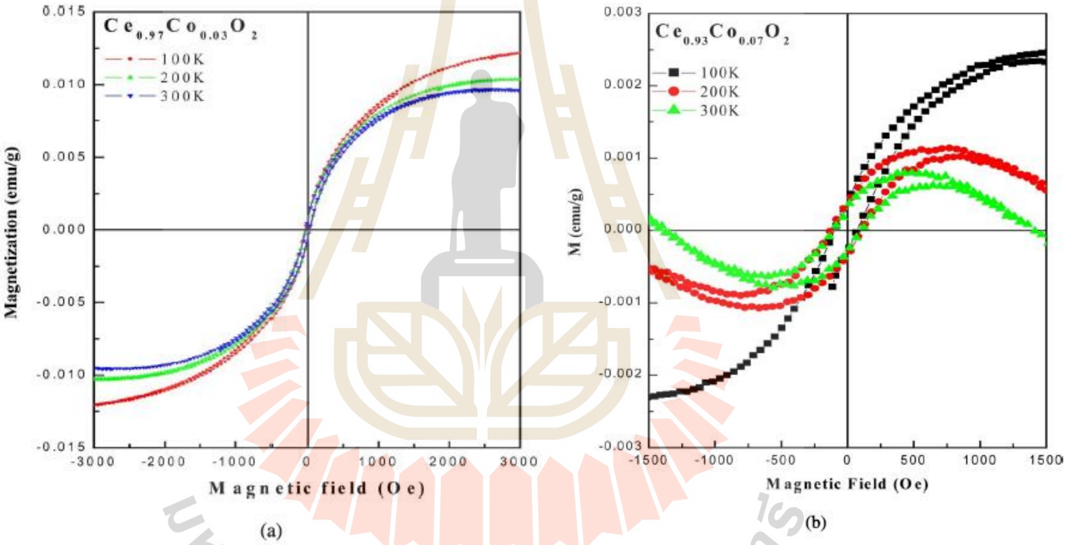

Figure 2.16 (a) Magnetization hysteresis loop for $Ce_{0.97}Co_{0.03}O_2$ nanoparticles at different temperatures. (b) Magnetization hysteresis loop for $Ce_{0.93}Co_{0.07}O_2$ nanoparticles at different temperatures (Kumar, Kim, Koo, Choi and Lee, 2009).

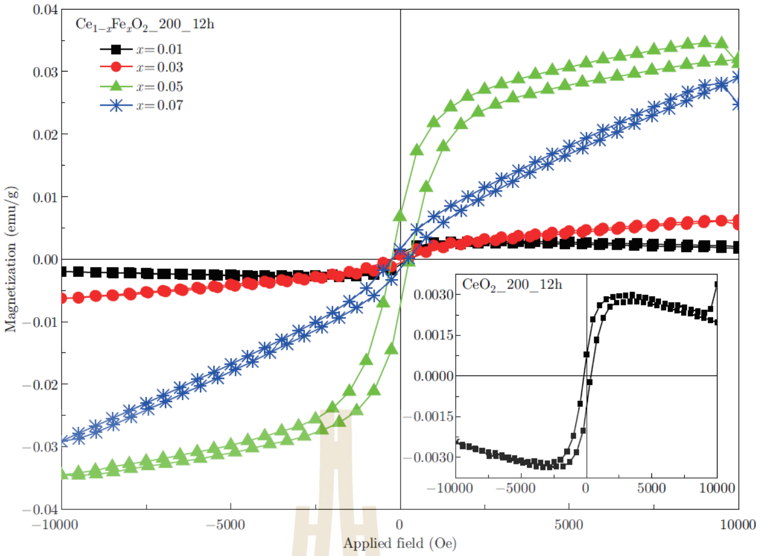

Figure 2.17 Magnetic properties of Fe-doped CeO_2 nanospheres prepared at 200 °C for 12 h (inset shows magnetic loop of undoped CeO_2) (Phokha et al., 2013).

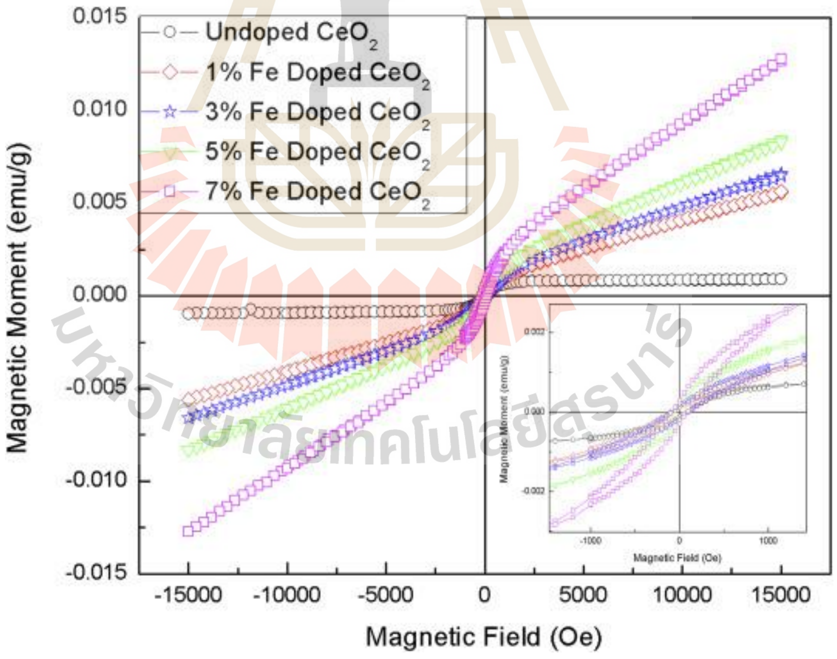

Figure 2.18 M-H loops of undoped and Fe doped CeO_2 nanoparticles (Inset of the figure shows opened loops) (Abbas et al., 2015).

Table 2.6 List of previous studies of the $Ce_{1-x}M_xO_2$ nanostructures.

Materials	**Dopant**	**Remark studies / magnetic properties**	**Magnetic moments (μ_B)**	**Reference**
CeO_2 thin film	Co 5-15%	Structure and defect/ RT-FM	~$10x10^{-5}$ emu/cm^3	(Murugan et al., 2016)
CeO_2 nanoparticles	Co 3-7%	Structure and defect/ RT-FM	~$0.9x10^{-3}$ emu/g	(Kumar et al., 2009)
CeO_2 powders	Co 3%	Structure and defect/ RT-FM	0.486 emu/g	(Song et al., 2010)
CeO_2 nanospheres	Fe 1-7%	Structure and defect/ RT-FM	0.027 emu/g	(Phokha et al., 2013)
CeO_2 thin film	Fe 1-3%	Structure and defect/ RT-FM	0.15 emu/g	(Sharma et al., 2010)
CeO_2 nanoparticles	Fe 1-7%	Structure, defect, optical property/ RT-FM	$12.6x10^{-3}$ emu/g	(Abbas et al., 2015)
CeO_2 nanoparticles	Mn 3-10%	Structure and defect/ RT-FM	0.009 emu/g	(Kumar et al., 2012)
CeO_2 nanoparticles	Zn 20-100%	Structure and optical property	-	(Ramasamy and Vijayalakshmi, 2015)
CeO_2 nanoparticles	Ni 1-7%	Structure, defect, optical property/ RT-FM	0.0357 emu/g	(Abbas et al., 2015)

2.4 Electrochemical properties of CeO_2 nanostructure

Electrochemical property of CeO_2 nanostructures were first reported by LavrenčičŠtangar et al. (LavrenčičŠtangar, Orel, Grabec, Ogorevc and Kalcher, 1993). It was found that CeO_2-TiO_2 films were able to insert greater quantity of Li^+ ions (10 mC/cm^2) as compared to pure CeO_2 films. Therefore, the enhanced electrochemical stability and large intercalated effective charge can be enhanced (see in Figure 2.19). Wen et al. (2011) fabricated (CeO_2) modified titanium dioxide (TiO_2) nanotube array film by electrode position. The cyclic voltammetry and chronoamperometric charge/discharge measurement results indicated that the CeO_2 modification increased the charge storage capacity of the TiO_2 nanotubes (in Figure 2.20). The charge transfer process at the surface, that is, the pseudocapacitance, was the dominate mechanism of the charge storage in CeO_2-modified TiO_2 nanotubes. The greater number of surface-active sites resulting from uniform application of the CeO_2 NPs to the well-aligned TiO_2 nanotubes contributed to the enhancement of the charge storage density(Wen, Liu, Yang, Li and Yu, 2011). Mujtaba et al. (2016) synthesized the catalytic compositions of CuO@CeO_2 hybrid oxides (xCuO@CeO_2, x = 5-25 wt.%) by precipitation/impregnation method. The prepared samples 10CuO@CeO_2 was found to exhibit highly improved available surface area, lowest charge transfer resistance, but when x was more than 10 wt.% performance reduced because of CuO in structure (see in Figure 2.21) (Mujtaba and Janjua, 2016).

It is seen from the above reports that CeO_2 exhibits reasonable electrochemical properties. CeO_2 is also a feasible charge storage material. Specific capacitance of CeO_2 between obtain to 57 F g^{-1} (Wang et al., 2011) to 73.70 F g^{-1} (Deng et al., 2017) have been reported. There has been interest in synthesis of CeO_2 NPs composite with carbon structure to enhance energy storage applications. Aravinda et al. reported the Cerium oxide (CeO_2)/activated carbon (AC) based composite electrode prepared by a simple mechanical mixing method exhibiting the specific capacitance of 162 Fg^{-1} (Aravinda, Udaya Bhat and Ramachandra Bhat, 2013) (see in Figure 2.22). Luo et al. reported the CeO_2/CNTs hybrid electrode prepared by a hydrothermal method exhibiting a specific capacitance of 818 F g^{-1} at scan rate of 1 mV s^{-1} (Luo, Yang, Zhao and Zhang, 2017).

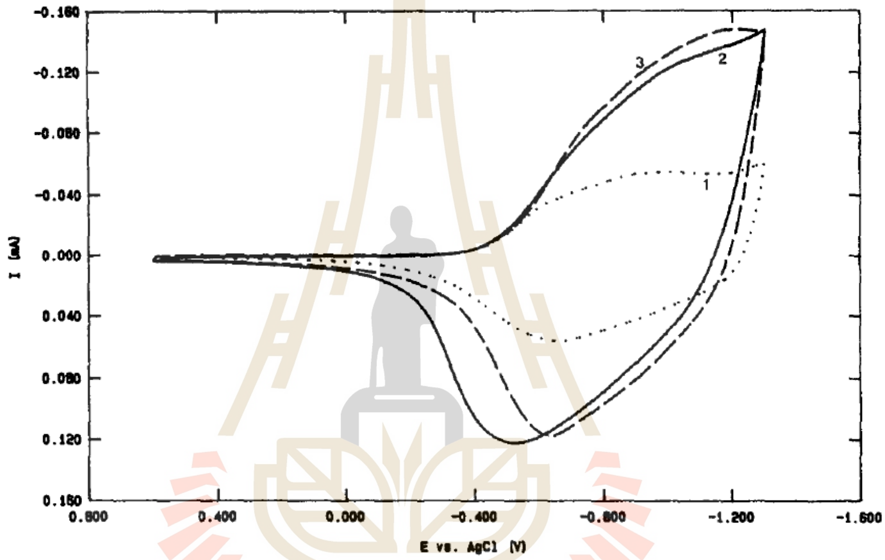

Figure 2.19 Cyclic voltammogram of CeO_2 film (single layer) in 0.1 M LiOH at difference sol concentration: (1) 4.8 x 10^{-3} mol (20 nm); (2) 7.2 x 10^{-3} mol (60 nm); 9.6 x 10^{-3} mol (70 nm) (at 500 °C) (LavrenčičŠtangar et al., 1993).

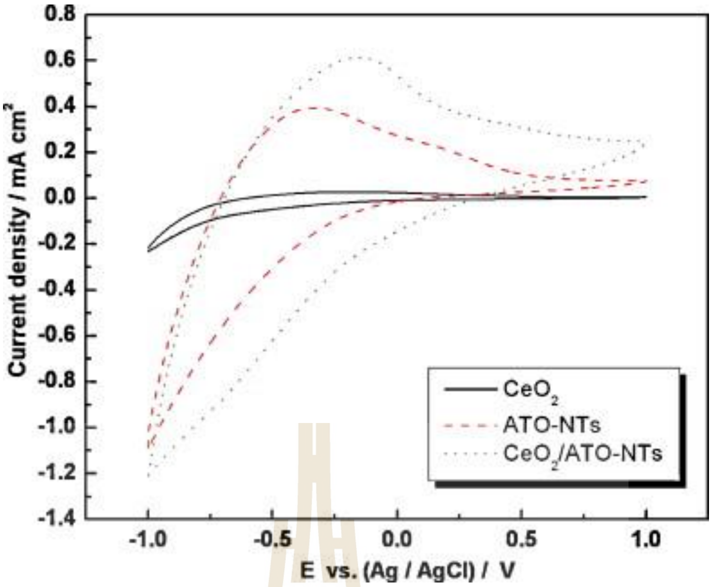

Figure 2.20 Cycle voltammograms of ATO-NTs, CeO_2/ATO-NTs, and CeO_2 films on ITO glass. The scanning speed was ν = 50 mV/s (Wen et al., 2011).

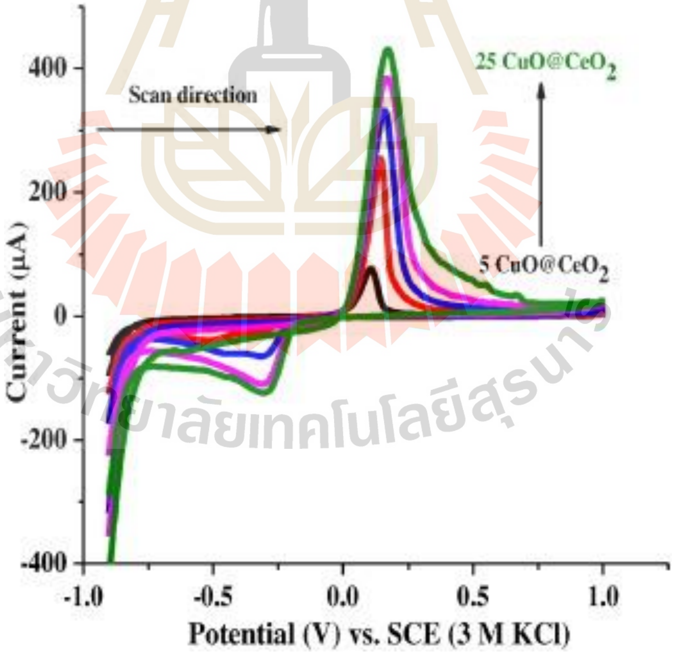

Figure 2.21 Cyclic voltammograms of CuO@CeO_2 catalysts series in 0.5 M H_2SO_4 (Mujtaba and Janjua, 2016).

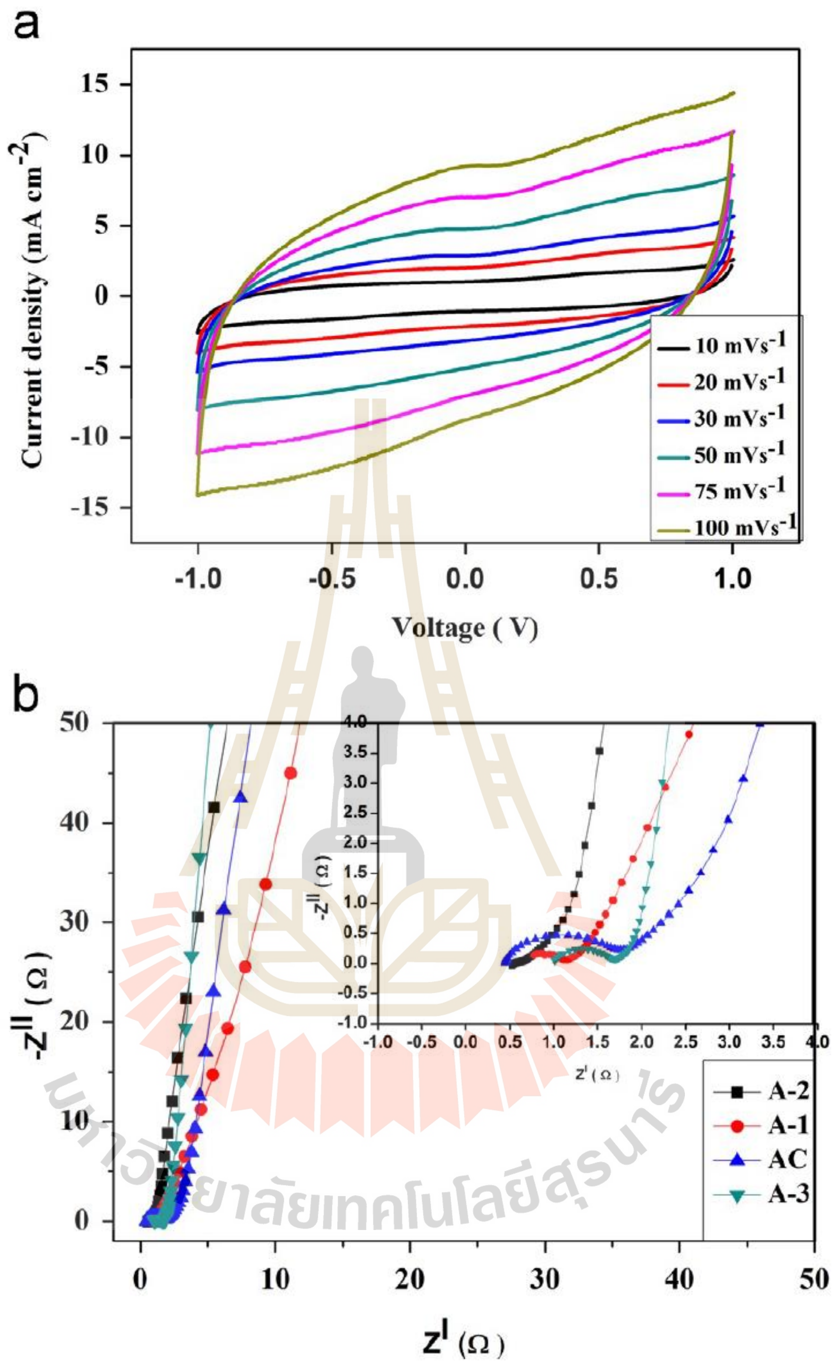

Figure 2.22 (a) CV curves of A-2 electrode at a scan rate of 10 mV s^{-1} -100 mV s^{-1} and (b) Nyquist plot of AC, A-1, A-2, A-3 and inset represents the enlarged version at low frequency region (Aravinda et al., 2013).

CHAPTER III

RESEARCH METHODOLOGY

Chapter III describes the experimental methods of the research. The CeO_2-based nanostructures were synthesized by two different methods: a simple solution method and an electrospinning method. The C/CeO_2 composite nanofibers were prepared by electrospinning technique. The phase, crystal structure, microstructure and morphology of the prepared nanostructures were characterized by TGA/DSC, XRD, Raman, TEM, HRTEM and SEM. The specific surface area and pore size distribution were explained by BET and BJH technique. Optical properties of samples measured by FTIR and UV-Vis. The chemical compositions and electronic state were characterized by XPS and XAS. Magnetic properties were evaluated by VSM. Electrochemical performance was investigated by CV, GCD, and EIS methods.

3.1 Materials

The materials used in this research are listed in Table 3.1.

Table 3.1 Materials used in this research.

Material	Source	Purity
Cerium (III) nitrate ($Ce(NO_3)_3 .6H_2O$)	Kanto	99.99%
Iron (III) nitrate ($Fe(NO_3)_3.9H_2O$)	Kanto	99.9%
Cobalt (II) nitrate ($Co(NO_3)_2.6H_2O$)	Kanto	99.95%
Copper (II) nitrate ($Cu(N_2O_6).5H_2O$)	Sigma-Aldrich	99.99%
Lanthanum (ll) nitrate $LaN_3O_9.6H_2O$	Sigma-Aldrich	99.99%
Polyvinyl pyrrolidone (PVP, M_n = 1300000)	Sigma-Aldrich	-
Polyacrylonitrile (PAN, Mw 150,000)	Sigma-Aldrich	-

3.2 Nanoparticles preparation

3.2.1 Preparation of CeO_2-based nanoparticles by simple solution method

In this work, nanoparticles of undoped CeO_2 and 3*d*-cation (Fe, Co and Cu)-doped CeO_2 and 4*f*-cation (La)-doped CeO_2 (i.e. $Ce_{1-x}M_xO_2$, x = 0.04, 0.06, 0.08, and 0.10 for Fe, Co, Cu and La ions) were synthesized by a simple solution method. This synthesis method has several advantages such as low cost, less synthesis time, large amount of final product.

The undoped CeO_2 and metal doped-CeO_2 nanoparticles were prepared in the same procedure. Metal sources including $Ce(NO_3)_2$, $Fe(NO_3)_3$, $Co(NO_3)_2$, $Cu(N_2O_6)$ and LaN_3O_9 were added into a bare PVP/ethanol solution with the weight content as listed in Table 3.2. 2.3 g of Polyvinyl pyrrolidone (PVP, Mn = 1300000, Aldrich) was mixed with 20 mL of ethanol by magnetic stirrer at room temperature (27 °C) for 1 h. Subsequently, 4 mmol of $Ce(NO_3)_3.6H_2O$ (99.99%, Kento) for undoped CeO_2, $Fe(NO_3)_3.9H_2O$ (99.9%, Kanto), $Co(NO_3)_2.6H_2O$ (99.95%, Kanto), $Cu(N_2O_6).5H_2O$ (99.99%, Aldrich), and $La(N_3O_9)_2.6H_2O$ (99.99%, Aldrich) were dissolved in 20 mL of DMF at room temperature for 1 h as metal solution. The metal solution was slowly added to the PVP solution to obtain a well-dissolved solution for Fe-, Co-, Cu-, and La-doped CeO_2, respectively. After being strongly stirred at room temperature for 2 h, (Figure 3.3). The homogeneous solution was then transferred into an alumina crucible and calcined at 500, 600, 700 and 800 °C for 2 h. Then, the alumina crucible was cooled naturally to room temperature. The sample preparation and characterization are schematically shown in Figures 3.1 and 3.4, respectively.

3.3 Nanofibers preparation

In this study, CeO_2-based nanofibers were fabricated by electrospinning technique in order to develop new shape of dilute magnetic oxides material. The electrospinning is simple, convenient, environment-friendly, and can be prepared oxide nanofibers (Sonsupap, Kidkhunthod, Chanlek, Pinitsoontorn and Maensiri, 2016).

3.3.1 Electrospinning system of nanofibers

The electrospinning process was setup as shown in Figure 3.2. The prepared homogenous precursor solution (described in section 3.3.2 and 3.3.3) was loaded into a 10-ml syringe and delivered to a stainless-steel needle (No.22). The parameters for electrospinning were as follows: the applied voltage was 7.5-12 kV, the tip-collector distance (TCD) was fixed at 12 cm (15 cm for carbon nanofiber), and the solution flowing rate was 0.5-0.6 ml h^{-1} depending on the concentration of the metal source added in the precursor solution. The electrospun fibers were collected as a random woven sheet on a rotating aluminum foil drum which was connected to the ground electrode. The sheet of as-spun nanofibers was stored in an incubator at 70 °C at least 24 h before calcination.

3.3.2 Fabrication of CeO_2-based nanofibers by electrospinning technique

The undoped CeO_2 and metal doped-CeO_2 nanofibers were prepared in the same precursor, PVP solution. The metal sources including $Ce(NO_3)_2$, $Fe(NO_3)_3$, $Co(NO_3)_2$, $Cu(N_2O_6)$ and LaN_3O_9 were added into a bare PVP/ethanol solution with the weight content as listed in Table 3.1. After electrospinning process the electrospun nanofibers were calcined at 500, 600, 700 and 800 °C for 2 h. The sample preparation and characterization are schematically shown in Figures 3.2 and 3.4, respectively.

3.3.3 Fabrication of Carbon-CeO_2 composites nanofibers by electrospinning technique

$Ce(NO_3)_2$ was added into a PAN/DMF solution with the weight content as listed in Table 3.3. The solution was magnetically stirred for 2 h and then the solution was ultrasonicated for 1 h to obtain a homogeneous solution. After electrospinning process, heat treatment was performed to produce a carbon sheet. This step was carried out at 100 °C for 4 h in air mixed argon atmosphere with a heating rate of 2 °C/min to remove water or moisturizer in electrospun sheet. The stabilized samples were carbonized at 500 °C for 2 h under flow of argon atmosphere to obtain CNF. After that, CO_2 was flow at 160 ml/min as an activation process to increase the porosity in CNFs. A schematic illustration of the preparation of the C/CeO_2 composite nanofibers and their characterization are schematically shown in Figures 3.3 and 3.5, respectively.

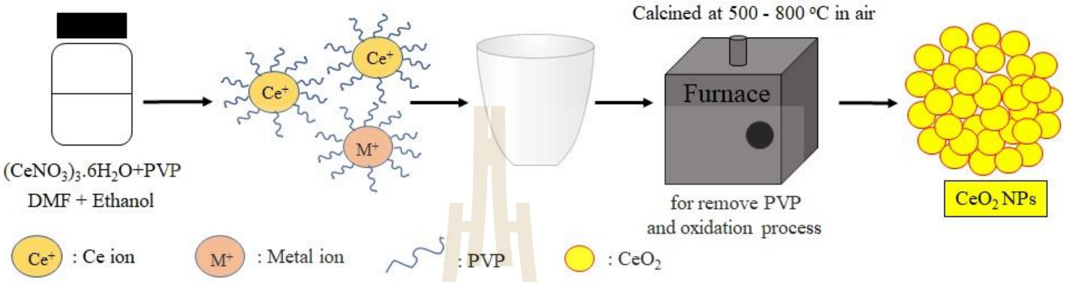

Figure 3.1 Schematic representation of CeO_2 nanoparticles preparation and experimental apparatus.

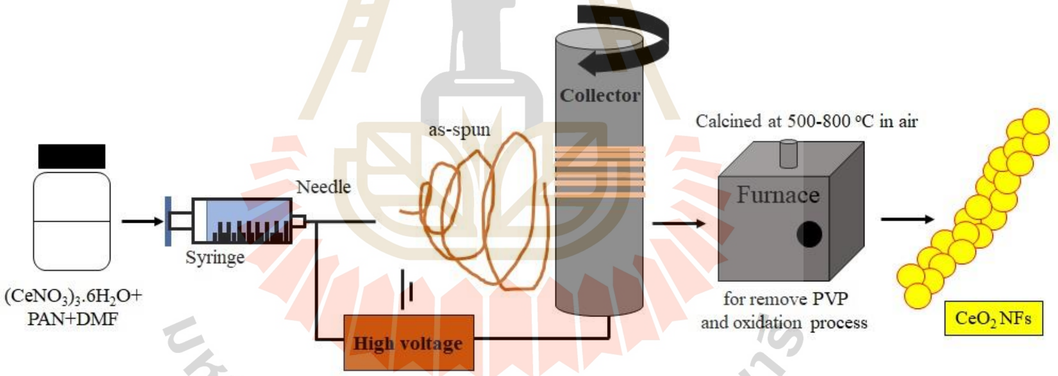

Figure 3.2 Schematic representation of CeO_2 nanofibers preparation and experimental apparatus.

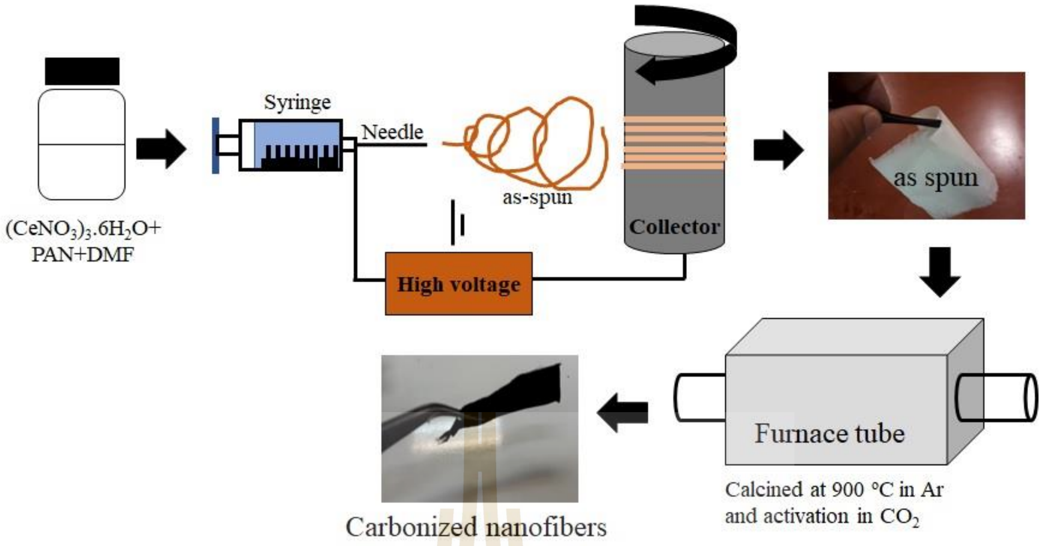

Figure 3.3 Schematic representation of C/CeO$_2$ composite nanofibers fabrication and experimental apparatus.

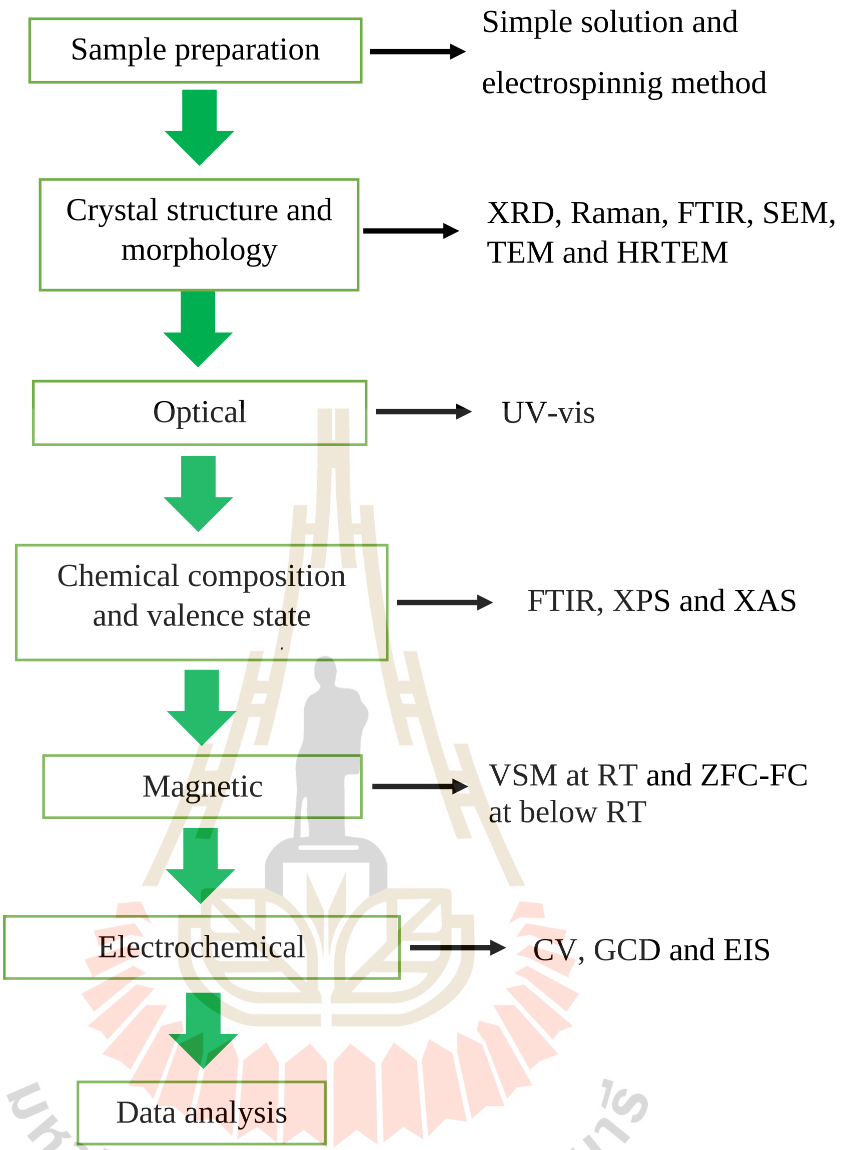

Figure 3.4 Diagram showing preparation and characterization of CeO$_2$ and Ce$_{1-x}$M$_x$O$_2$ nanostructures, M is Fe, Co, Cu and La in which x varies as 0.04, 0.06, 0.08 and 0.10, synthesized by simple solution and electrospinning method.

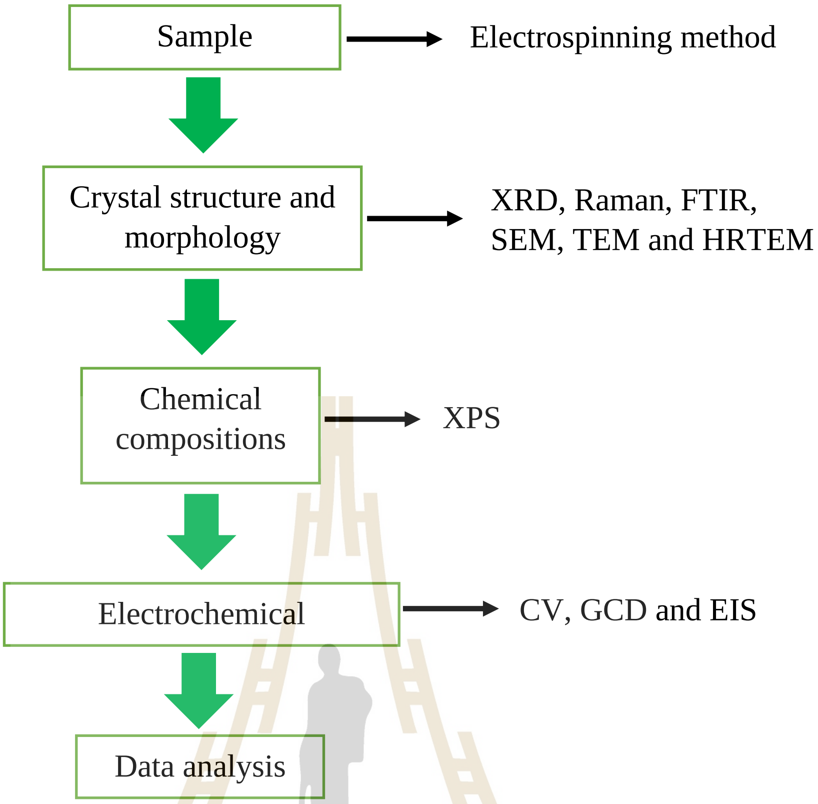

Figure 3.5 Diagram showing preparation and characterization of C/CeO_2 composite nanofibers, in which CeO_2 varies as 0, 10, 20 and 40 wt.%, synthesized by electrospinning method.

Table 3.2 List of weight content of raw materials for the preparation of CeO_2 and $Ce_{1-x}M_xO_2$ in PVP solution with different chemical compositions.

$Ce_{1-x}Fe_xO_2$				
Doping level	$Ce(NO_3)_3 .6H_2O$ (g)	$Fe(NO_3)_3.9H_2O$ (g)	PVP (g)	Chemical compositions
x = 0	1	-	2.30	CeO_2
x = 0.04	1.042	0.040	2.30	$Ce_{0.96}Fe_{0.04}O_2$
x = 0.06	1.020	0.061	2.30	$Ce_{0.94}Fe_{0.06}O_2$
x = 0.08	0.999	0.081	2.30	$Ce_{0.92}Fe_{0.08}O_2$
x = 0.10	0.977	0.101	2.30	$Ce_{0.90}Fe_{0.10}O_2$

$Ce_{1-x}Co_xO_2$				
Doping level	$Ce(NO_3)_3 .6H_2O$ (g)	$Co(NO_3)_2.6H_2O$ (g)	PVP (g)	Chemical compositions
x = 0	1	-	2.30	CeO_2
x = 0.04	1.064	0.022	2.30	$Ce_{0.96}Co_{0.04}O_2$
x = 0.06	1.042	0.029	2.30	$Ce_{0.94}Co_{0.06}O_2$
x = 0.08	1.02	0.044	2.30	$Ce_{0.92}Co_{0.08}O_2$
x = 0.10	0.999	0.058	2.30	$Ce_{0.90}Co_{0.10}O_2$

Table 3.2 List of weight content of raw materials for the preparation of CeO_2 and $Ce_{1-x}M_xO_2$ in PVP solution with different chemical compositions (Continued).

$Ce_{1-x}Cu_xO_2$

Doping level	$Ce(NO_3)_3 .6H_2O$ (g)	$Cu(N_2O_6).5H_2O$ (g)	PVP (g)	Chemical compositions
x = 0	1	-	2.30	CeO_2
x = 0.04	1.064	0.012	2.30	$Ce_{0.96}Cu_{0.04}O_2$
x = 0.06	1.042	0.023	2.30	$Ce_{0.94}Cu_{0.06}O_2$
x = 0.08	1.020	0.035	2.30	$Ce_{0.92}Cu_{0.08}O_2$
x = 0.10	0.999	0.047	2.30	$Ce_{0.90}Cu_{0.10}O_2$

$Ce_{1-x}La_xO_2$

Doping level	$Ce(NO_3)_3 .6H_2O$ (g)	$Cu(N_2O_6).5H_2O$ (g)	PVP (g)	Chemical compositions
x = 0	1	-	2.30	CeO_2
x = 0.04	1.064	0.022	2.30	$Ce_{0.96}La_{0.04}O_2$
x = 0.06	1.042	0.043	2.30	$Ce_{0.94}La_{0.06}O_2$
x = 0.08	1.020	0.065	2.30	$Ce_{0.92}La_{0.08}O_2$
x = 0.10	0.999	0.087	2.30	$Ce_{0.90}La_{0.10}O_2$

Table 3.3 List of weight content of raw materials for the preparation of CeO_2 and $Ce_{1-x}M_xO_2$ in PVP solution with different chemical compositions.

samples	The weight content		
	PAN (g)	$Ce(NO_3)_3 \cdot 6H_2O$ (g)	DMF (mL)
PAN	4	-	40
$Ce(NO_3)_3$/PAN-10wt.%	4	0.40	40
$Ce(NO_3)_3$/PAN-20wt.%	4	0.80	40
$Ce(NO_3)_3$/PAN-40wt.%	4	0.16	40

3.4 Phase identification, structural characterization and morphology

3.4.1 The thermogravimetric analysis and differential scanning calorimetry (TGA/DSC)

TGA and DSC are the techniques used to measure the change in mass of the sample when it is subjected to a heating rate (10 °C/min) and under flowing gas (e.g., dried air, Ar or N_2) in controlled atmosphere. The measurement of changes in the mass of the sample as a function of temperature shows the purity, crystallization, and decomposition behavior. The temperature difference between the sample and reference (e.g. Al_2O_3) was recorded using thermocouple, as both are subjected to the same temperature program. During a temperature program, the temperature of the samples will differ from that of the reference due to the difference in heat capacity between the sample and reference. These techniques are widely used to study the thermal characteristics of substances, especially polymers (PVP and PAN). The weight losses of the sample during heat treatment are evidence of polymer structure deformation or decomposition which is useful for consideration of the proper temperature for calcination of as-spun polymer nanofibers.

In this work, the thermal stability and exothermic reaction of metal oxides were carried out in air atmosphere (60 ml min^{-1}) and N_2 (100 ml min^{-1}) for carbon nanofibers in the temperature range of 35-1000 °C with a heating rate of 10 °C min^{-1}using Mettler TOLEDO, US at SUT.

3.4.2 X-Ray diffraction (XRD)

XRD is a technique that can be used to determine the crystallographic structure and chemical composition of materials. In this technique, a collimated of X-ray is incident on a specimen and diffracted by crystalline phases in the specimen according to Bragg's law, the condition for constructive interference, is given in Equation 3.1.

$$2d \sin\theta = n\lambda \tag{3.1}$$

Where n is an integer, λ is the wavelength of the X-ray radiation and θ is angle of incidence and d is the distance between lattice planes. The Bragg's Law conditions are satisfied by different d-spacings in polycrystalline and single crystalline materials. Plotting the angular positions and intensities of the resultant diffracted peaks of the radiation produces a pattern, which is characteristic of the sample.

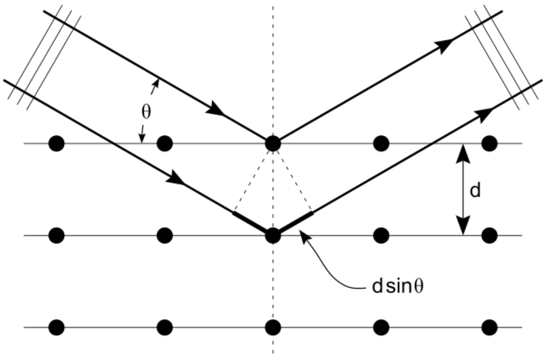

Figure 3.6 (a) The Bragg reflection from a particular set of the lattice planes separated by a distance d and θ is a half of the total angle by which the incident beam is detected.

In this work, crystal structure and phase identification of the prepared samples were determined by XRD using a Bruker D8, Germany, with CuKα radiation (λ= 0.154060 nm). XRD patterns were obtained using X-Ray Diffractometer using a scan rate for 2θ was 20-80°; scan step was 0.02°/s. The crystalline phase identification was carried out by comparison with the Joint Committee on Powder Diffraction Standard (JCPDS) diffraction files. The X-ray diffraction pattern for CeO_2 at room temperature was performed using X Pert High Score Plus program to determine the average crystalline size. In this thesis, the crystallite size (D) was calculated according to Scherer's equation;

$$D = \frac{0.89\lambda}{\beta \cos\theta} \tag{3.2}$$

where λ is the wavelength of the X-ray radiation, θ is the diffraction angle and β is the full width at half maximum (FWHM).

Figure 3.7 X-ray diffraction (XRD; Brucker D8, SUT).

3.4.3 Raman spectroscopy (RAMAN)

Raman spectroscopy is a spectroscopic technique which gives information on molecular vibrations and rotations and crystal structures. This technique is widely used to study the vibration properties, the microstructure of graphitic crystals and various disordered carbon materials (Kim et al., 2004, Wang and Golden, 2016). The basic principle is based on inelastic scattering of monochromatic light from a laser source. Photons of the laser light are absorbed by the sample and then reemitted, where the frequency of the reemitted photons is shifted up or down in comparison with original monochromatic frequency. This shift provides information about rotation and vibration molecular. The plotting of the shift light intensity with the frequency provides the Raman spectrum. Every band in the Raman spectrum corresponds to a specific vibrational frequency of a bond within the molecule.

In this study, Raman spectroscopy was performed between 200 to 4400 cm^{-1} using BRUKER SENTERRA, UK, laser wavelength of 532 nm, to characterize the crystalline and carbon structures of all samples.

3.4.4 Transmission electron microscopy (TEM)

TEM is an electron microscopy technique used to investigate the morphology, structure and phase composition in submicroscopic detail. In this technique, a beam of electros is transmitted through an ultra-thin specimen, interacting with specimen as it passes though. An image is formed from the interaction of electrons transmitted though the specimen. The image is magnetified and focused onto an imaging device, such as a fluorescent screen to be detected by a sensor such as a CCD camera.

A diffraction pattern is formed on the back focal plane of the objective lens when electron beam passes through a crystalline specimen. In the diffraction mode, a pattern.

$$\lambda = 2d\Theta \tag{3.3}$$

$$\lambda L = Rd \tag{3.4}$$

where L is the camera length of a TEM, the distance between the crystal and photographic plate of camera. L is an equivalent camera length for calculating the spacing of the lattice plane. $\lambda L$is called as the camera constant of the TEM. Eq. (3.3) is the basic equation for electron diffraction in a TEM. The spacing of crystallographic planes can be calculated by measuring R (the distance from the central spot of the transmitted beam to diffraction spot) in photographic film using Eq. (3.4) L can be changed in a TEM.

In this work, the CeO$_2$ and Ce$_{1-x}$M$_x$O$_2$ samples were dispersed in ethanol and sonicated for 30 min. A few drops of suspension were placed onto a carbon coated copper grid. The SEAD patterns and energy dispersive X-ray spectroscopy (EDX) were performed on TECNAI $G^2$20, FEI, USA which were used to compliment XRD Bruker D8 results.

3.4.5 Field emission scanning electron microscopy (FESEM)

FESEM is a powerful microscopy technique which gives information about external morphology chemical composition, and the orientation of materials. In this work, the samples were held on a metal stub and coated with gold for 9 nanometers before SEM analysis. FESEM JEOL 7800F, U.K., was employed to investigate external morphologies, such as surface, diameter size, particles size and fibers arrangement etc. of both the as-spun and calcined sample.

Figure 3.8 Field emission scanning electron microscopy (FESEM; JEOL JSM-7800F, U.K., SUT).

3.5 The specific surface area and pore distribution

In the specific surface area and pore distribution analysis, a sample is exposed to N_2 gas of different pressures at a given temperature (usually at -196 °C, the liquid-nitrogen temperature). Increments of pressure result in increased amounts of N_2 molecules being adsorbed on the surface of the sample. The pressure at which the adsorption equilibrium is established is measured and the universal gas law is applied to determine the quantity of N_2 gas adsorbed. Thus, an adsorption isotherm is obtained (Figure 3.9). If the pressure is systematically decreased to induce desorption of the adsorbed N_2 molecules, then a desorption isotherm is obtained.

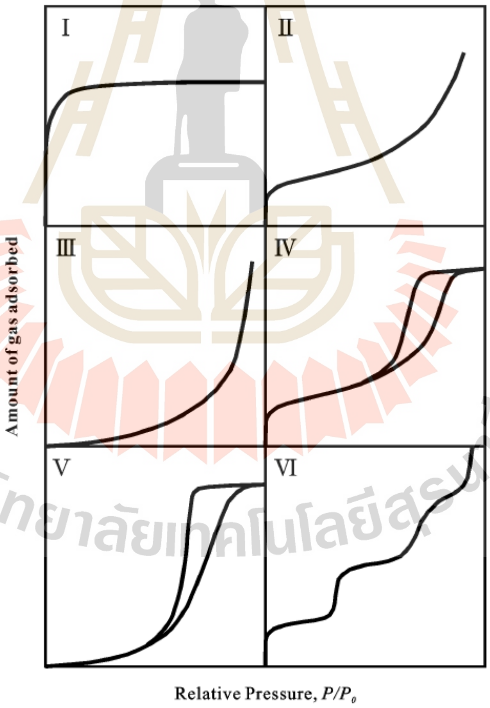

Figure 3.9 IUPAC classification of adsorption isotherm.

Analysis of the adsorption and desorption isotherms in combination with some physical models yields information about the pore structure of the sample, such as surface area, pore volume, pore size and surface nature. The Brunauer-Emmett-Teller (BET) and Barrett-Joyner-Halenda (BJH) methods were used to describe the specific surface area and pore size distribution. The phenomenon of adsorption can be expressed with the following equation.

$$\frac{1}{W\left[\left(\frac{P_0}{P}\right)-1\right]}=\frac{1}{W_\mathrm{m}C}+\frac{C\text{-}1}{W_\mathrm{m}C}\left(\frac{P}{P_0}\right) \tag{3.5}$$

where W_m is the volume of gas adsorbed at standard temperature and STP pressure (273.15 K and 1.103 x 105 Pa) (ml). W_m is the volume of gas adsorbed at STP to produce an apparent monolayer on the sample surface (ml). P_0 is saturated pressure of adsorbate gas (Pa). P is partial vapor pressure of adsorbate gas in equilibrium with the surface at 77.4 K (-195.75 °C). C is dimensionless constant. At the relative pressures (P/P_0) lower than 0.05, N_2 is adsorbed in the form of single molecules. The multi-layer adsorption occurs in some small micropores with increasing in relative pressure. By decrease in relative pressure, desorption nitrogen is observed. When the shapes of the capillary pores are similar, the adsorption and desorption branches of the adsorption isotherm coincide with each other. The specific surface area can be calculated by

$$a_{BET}=\frac{W_m s N_A}{m V_0} \tag{3.6}$$

Where W_m arise from the slop and the intercept of plot between the relative pressure and $1/W[(P_0/P)-1]$, s is the area of the surface occupied by individual gas molecules, N_A is the Avogadro number, m is the sample mass and V_0 is the molar volume of gas (22414 cm^3/molar at atmospheric pressure). The six types of IUPAC standard adsorption isotherms are shown in Figure 3.9.

In this study, the samples were degassed at 300 °C for 6 h and then the N_2 adsorption/desorption isotherms were measured at 77 K using an automatic specific surface area/pore size distribution analyzer BELSORP-mini II. The specific surface area was calculated by BET method.

3.6 Optical properties measurement

3.6.1 UV-visible spectroscopy (UV-Vis)

Ultraviolet-visible spectroscopy or ultraviolet-visible spectrophotometry (UV-Vis) is absorption spectroscopy or reflectance spectroscopy in the ultraviolet-visible spectral region. The UV-Vis uses light in the visible and adjacent (near-UV and near-infrared (NIR)) ranges. The absorption or reflectance in the visible range directly affects the perceived color of the chemicals involved. In this region of the electromagnetic spectrum, molecules undergo electronic transitions. This technique is complementary to fluorescence spectroscopy, in that fluorescence deals with transitions from the excited state to the ground state, while absorption measures transitions from the ground state to the excited state. UV-Vis spectroscopy is routinely used in analytical chemistry for the quantitative determination of different analysis, such as transition metal ions, highly conjugated organic compounds, and biological macromolecules.

In this work, the absorption spectra of the CeO_2 and $Ce_{1-x}M_xO_2$samples were measured in the range of 200-800 nm using a UV-3101PC UV-Vis-NIR scanning spectrometer (Shimadzu, Japan).

3.7 Chemical compositions and electronic states determination

3.7.1 Fourier transform infrared spectroscopy (FTIR)

FTIR is used to obtain an infrared spectrum of absorption, emission, photoconductivity or Raman scattering of a solid, liquid or gas. FTIR spectrometer records the interaction of infrared radiation with a sample by measuring the frequencies at which the sample absorbs the radiation and the intensities of the absorptions. Chemical functional groups are known to absorb light at specific frequencies. Thus, the chemical structure can be determined from the frequencies recorded. When the molecule receives energy from infrared radiation with a frequency corresponding to the frequency of vibrating (stretching) or rotation (bending) of covalent bonds in molecules. The molecules were absorbed IR light and change the dipole moment. Then the instrument will measure the light intensity per frequency or wavelength (Wave number) is the spectrum called "Interferogram" in which each bond of the function group shows different specific wavelengths, such as C = O of ~1,800 cm^{-1}, OH stretching very broad at 3,300-2,500 cm^{-1}, NH stretching ~3500-3300 cm^{-1}, -C = C- Stretching ~1667-1613 cm^{-1}, CH Stretching ~ 3,000-2,840 cm^{-1}.

In this thesis work, FTIR spectra were recorded using Bruker Tensor 27, U.K., with a resolution of 4 cm^{-1} in the wavelength range of 400 - 4000 cm^{-1}. The samples were prepared with potassium bromide mixing (KBr) by ratio 1:9. The carbon samples were prepared without KBr.

3.7.2 X-ray photoelectron spectroscopy (XPS)

X-ray photoelectron spectroscopy (XPS), also known as electron spectroscopy for chemical analysis (ESCA), is a widely used for determination of the elementary and chemical composition of material. The theoretical fundamental of XPS is based on the equation proposed by Einstein to explain the photoelectric effect:

$$h\nu = E_b - E_{kin} \tag{3.7}$$

where $h\nu$ is the quantum energy, E_b is the binding energy of the electron in matter (i.e. energy required to remove an electron) and E_{kin} is the kinetic energy of the ejected electron. XPS spectra are obtained by irradiating a material with a beam of X-rays while simultaneously measuring the kinetic energy and number of electrons that escape from the material being analyzed.

In this work, XPS spectra were collected on a PHI 5000 Versa Probe II XPS system (ULVAC-PHI, Japan) with Al K (1486.4 eV) radiation as the excitation source to determine the element and valence sate of Ce, Fe, Co and La in the CeO_2 and $Ce_{1-x}M_xO_2$ samples.

3.7.3 X-ray absorption near-edge structure (XANES)

XAS is an element specific technique. It can be divided into x-ray absorption near-edge structure (XANES) and extended x-ray absorption fine-structure (EXAFS), which contain related but slightly different information about an element’s local coordination and chemical state. In this technique, an x-ray is absorbed by an atom when the energy of the x-ray is transferred to a core-level electron (K, L, or M shell) which is ejected from the atom. The atom is left in an excited state with an empty electronic level (a core hole). Any excess energy from the X-ray is given to the ejected photo-electron (see Figure 3.10(a)). XAS measures the energy dependence of the x-ray absorption coefficient μ(E) at and above the absorption edge of a selected element. μ(E) can be measured two ways. First way is Transmission mode as shown in Equation 3.8.

The absorption is measured directly by measuring what is transmitted through the sample. Second way is fluorescence mode (see Equation 3.9). The re-filling of the deep core hole is detected. Typically, the fluorescent x-ray is measured (see Figure 3.10(b)).

$$\mu\,(E)t = -\ln(I\,/\,I_0\,) \tag{3.8}$$

$$\mu\,(E)\ \alpha\ I_f\,/\,I_0 \tag{3.9}$$

where I_0 is the X-ray intensity hitting, I is the intensity transmitted, $\mu(E)$ is absorption coefficient, t is a material of thickness, and If is the fluorescence intensity. In this work X-ray absorption near edge spectra (XANES) of Ce *L3*-edges were collected in transmission mode and Fe, Co, Cu K-edges and La *L3*-edges were collected in fluorescence mode (due to very low Fe, Co, Cu and La concentrations in samples) at the SUT-NANOTEC-SLRI XAS beamline (BL5.2) at the Synchrotron Research Institute (Public Organization), Nakhon Ratchasima, Thailand.

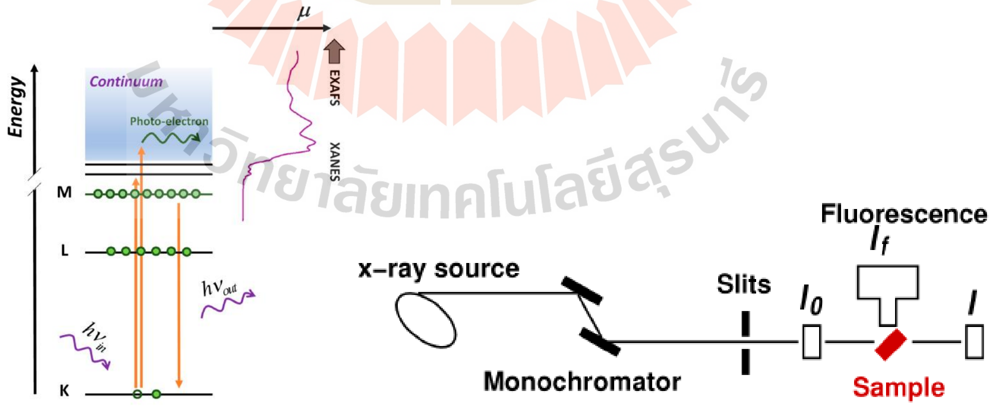

Figure 3.10 (a) Schematic diagram of XAS (Fracchia, Ghigna, Vertova, Rondinini and Minguzzi, 2018) (b) Schematic measured of the XANES.

3.8 Magnetic properties measurement

VSM can measure the magnetic properties of a large variety of materials such as diamagnetic, paramagnetic, ferromagnetic and antiferromagnetic. The VSM technique gives the magnetization (*M*) value at different magnetic field (*H*) providing a *M-H* hysteresis curve. For the measurement, powder was weighed, then place in a small sample holder located at the end of a sample rod mounted in an electromechanical transducer for measurement. The sample is vibrated parallel to the field direction; an electromagnet provides the magnetizing field, a vibrator mechanism to vibrate the sample in the magnetic field, and detection coils which generate signal voltage due to the changing flux emanating from the vibrating sample. The output measurement displays the magnetic moment as function of a magnetic field or the temperature dependent of magnetization. The measurement can be made at RT and above/below RT (350 K to 50K) in field rang of 1000 Oe to 15000 Oe. The VSM is shown schematically in Figure 3.11.

In this work, the magnetic properties of the samples are measured at RT and above/below RT by using a vibrating sample magnetometer (VSM; VersaLab$^{\mathrm{TM}}$, PPMS$^{®}$, KKU).

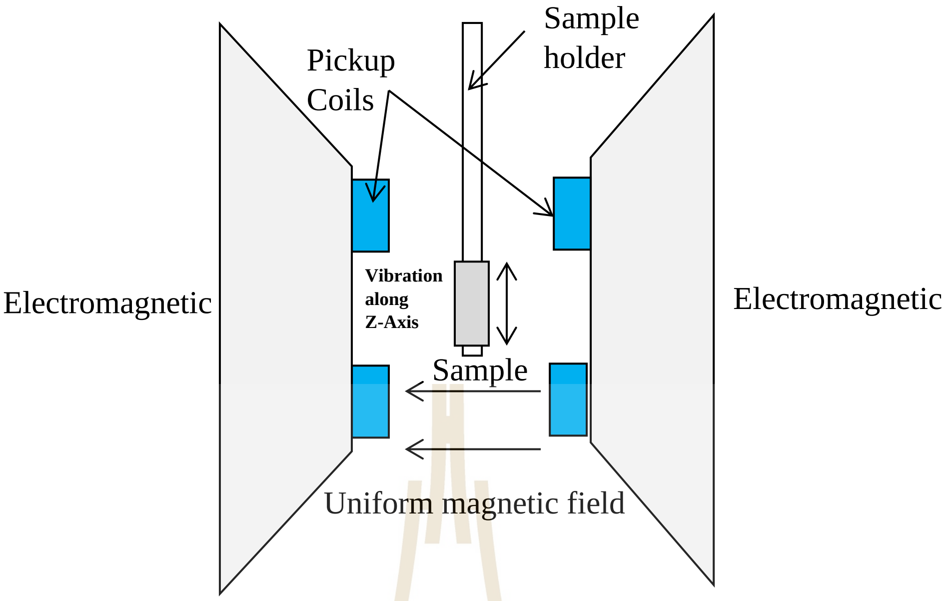

Figure 3.11 Schematic diagram of the VSM (Adapted from Smith, 1956).

3.9 Electrochemical properties measurement

In this study, the electrodes of CeO_2 and $Ce_{1-x}M_xO_2$ samples and C/CeO_2 composite nanofibers and electrolyte were prepared. The electrochemical experiment consisting of three electrodes was set up for CV, GCD and EIS measurements.. The equivalent circuits of the cells were evaluated using Nova 1.11 software, Autolab-PGSTAT302, Netherlands.

3.9.1 Electrode preparation

Two types of electrode were prepared from CeO_2 and $Ce_{1-x}M_xO_2$ samples and C/CeO_2 composite. For the CeO_2 and $Ce_{1-x}M_xO_2$ electrodes, the prepared CeO_2 and $Ce_{1-x}M_xO_2$ samples were mixed with Polyvinylidene fluoride (PVDF) and carbon black at the ratio of 8:1:1, respectively. After that methyl-2-pyrrolidinone 180 µl was added into the mixture and stirred until homogenous solution was received. The mixed solution was dropped on Ni foam 45 µl (about 2 mg), dried at 60 °C for 6 h in the oven and then pressed at 2 kPa as a working electrode (Figure 3.12 (a)). The C/CeO_2 composite electrodes were assembled as working electrodes by using 2 mg of each calcined C/CeO_2 composite sample sandwiched between the nickel foam (1cm (width)×2cm (length)) without any binder and then pressing at 2 kPa for 1 min using an hydraulic press machine following each step in Figure 3.13 (b). The electrodes were kept in a soaked condition in electrolyte for at least 6 h and then were ready for installing in an electrochemical cell.

The specific capacitance of charge/discharge (C_{CD}), energy density (E) and power density (P) of the symmetric device were calculated using the following equations:

$$C_{CD} = \frac{I \times \Delta t}{m \times \Delta V} \tag{3.10}$$

$$E = \frac{1}{2} C_s \Delta V^2 \tag{3.11}$$

$$P = \frac{E}{\Delta t} \tag{3.12}$$

where I (A g^{-1}) is the current density, Δt (s) the discharge time, m (g) is the mass of the active electrode material, and ΔV (V) is the potential window.

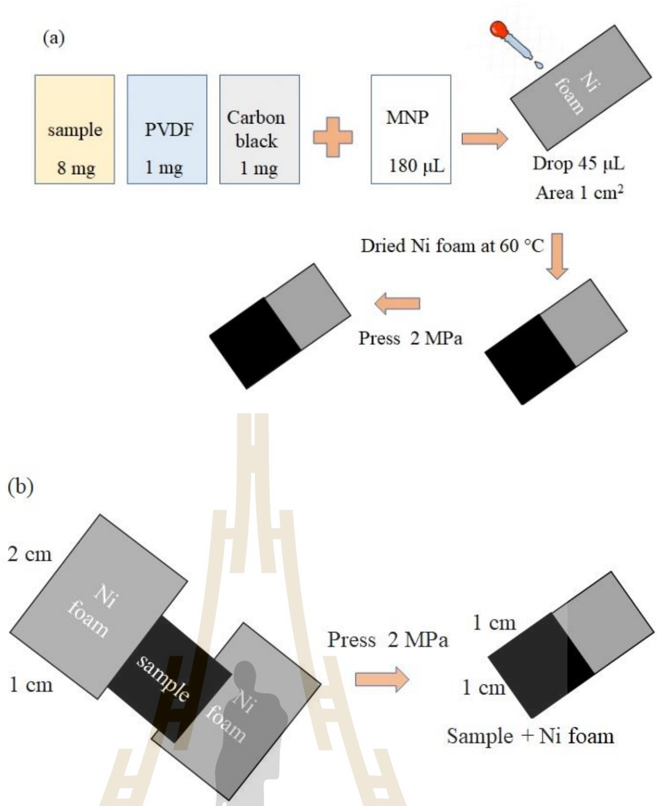

Figure 3.12 Schematic representation of (a) CeO_2 and $Ce_{1-x}M_xO_2$ electrode preparation with binder and (b) C/CeO_2 composite electrode preparation without binder.

3.9.2 Electrolyte preparation

In this experiment, the different concentrations of KOH were used as electrolytes for electrochemical study (shown in table 3.4). They were prepared based on an aqueous solution by dissolving the substrate in distilled water. The concentration was calculated by following equation:

$$\text{Molar concentration} = \frac{\text{Amount in mole}}{\text{Volume of solution}} \tag{3.13}$$

Table 3.4 List of materials used for aqueous electrolyte preparation.

Electrolyte	Substrate (g)	Total volume (ml)
KOH 1 M	14.03	250
KOH 3 M	42.08	250
KOH 6 M	84.15	250

3.9.3 Electrochemical experiment setup

To evaluate the electrochemical performance of the prepared samples, cyclic voltammetry (CV), galvano-statically charge/discharge (GCD) and electrochemical impedance spectroscopy (EIS) techniques were performed in a three-electrode system using Nova 302 N potentiostat at room temperature. Working electrode (WE) is the electrode being studied. Counter electrode (CE) is the electrode that completes the current path and Reference electrode (RE) is the electrodes that serve as experimental reference points. Pt wire and Ag/AgCl were used as CE and RE, respectively.

3.9.4 Cyclic voltammetry (CV)

In this work, the CV measurement was measured within potential windows of -1 to 0 V (Avoidance of oxygen and hydrogen evolution (Conway and Gileadi, 1962)) and scan rates of 2, 5, 10, 20, 50, 100, 200, and 500 mV s^{-1}. The effect of voltage potential windows on specific capacitance was also studied.

3.9.5 Galvanostatic charge/discharge testing (GCD)

The GCD testing was carried out over the same voltage window as same as CV measurement at the current density ranges of 0.5, 1, 2, 5, 10, 15 and 20 A g^{-1}.

3.9.6 Electrochemical impedance spectroscopy

The EIS was monitored over the frequency range, 10 mHz to 100 kHz at 0.1 V using galvanostatic mode.

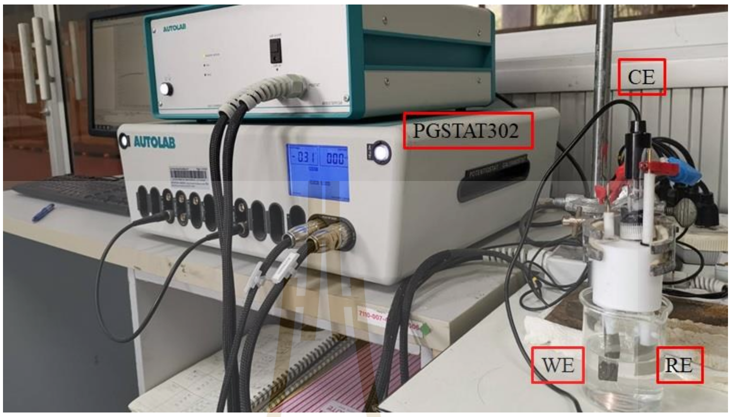

Figure 3.13 Electrochemical experiment setup. Three-electrode electrochemical cell setup. Reference electrode (RE) is Ag/AgCl, counter electrode (CE) is platinum wire, and working electrode (WE) are prepared from the fabricated samples.

CHAPTER IV

CHARACTERIZATION, OPTICAL, MAGNETIC AND ELECTROCHEMICAL PROPERTIES OF UNDOPED CeO_2 AND $Ce_{1-x}M_xO_2$ NANOSTRUCTURES

Chapter IV deals with the characterization results, optical, magnetic and electrochemical properties and the discussion for CeO_2 and $Ce_{1-x}M_xO_2$ nanostructures synthesized by simple solution and electrospinning methods. The weight loss as a function of as-spun CeO_2 and $Ce_{1-x}M_xO_2$ were exanimated by TGA and DSC to estimate the calcination temperature. The morphologies and structures were investigated using SEM and TEM. The crystal structures were identified by XRD. The chemical compositions and electronic states were determined by FT-IR, XPS and XANES. The optical and magnetic measurements were performed using a UV-vis and VSM, respectively. The effect of dopants on the structure, morphology and magnetic structure is briefly discussed based on the VSM measurement. Finally, the electrochemical performances of CeO_2 nanostructures were evaluated by CV and GCD techniques.

4.1 Thermo properties of as-spun CeO_2/PVP and $Ce_{1-x}M_xO_2$/PVP

In this work TGA and DSC were carried out to determine the calcination temperature for the as-spun CeO_2/PVP and $Ce_{1-x}M_xO_2$/PVP. The TGA curves of the asspun CeO_2/PVP and $Ce_{1-x}M_xO_2$/PVP with the metal sources content of 10% mol are shown in Figure 4.1. The measurements were performed by using a heating rate of 10 °C/min in the temperature range of 30 to 1000 °C under air atmosphere. The TGA curves of both as-spun nanofibers show three main steps of weight loss in the range of ~30 to 190, ~190 to 264 and ~264 to 1000 °C suggesting that the decomposition can be divided into three steps. The first step is the initial phase temperature of 30 to 190 °C showing weight loss of ~6 % form initial weight. This step is the decompositions of organic substances such as water, carbon dioxide and nitrate (Keely and Maynor, 1963). The second step is the major weight loss at temperature of ~190 to 264 °C. In this step the polymer (PVP) was burnt out, leaving small amount of polymer in the samples (Šolcová et al., 2014). The third step indicates that the remaining organic residuals and PVP were completely decomposed at temperatures of 293 °C and 366 °C for CeO_2/PVP and $Ce_{1-x}M_xO_2$/PVP, respectively.

The DSC curves of CeO_2/PVP and $Ce_{1-x}M_xO_2$/PVP with the metal sources content of 10% mol are shown in Figure 4.1. The main endothermic reaction peaks were observed at temperature of 254 to 294 °C for both CeO_2/PVP and $Ce_{1-x}M_xO_2$/PVP, which is consistent with the weight losses observed in TGA results. The TGA and DSC results suggest the calcination temperatures of as-spun CeO_2/PVP and $Ce_{1-x}M_xO_2$/PVP in this work which is the range of 500 to 800 °C.

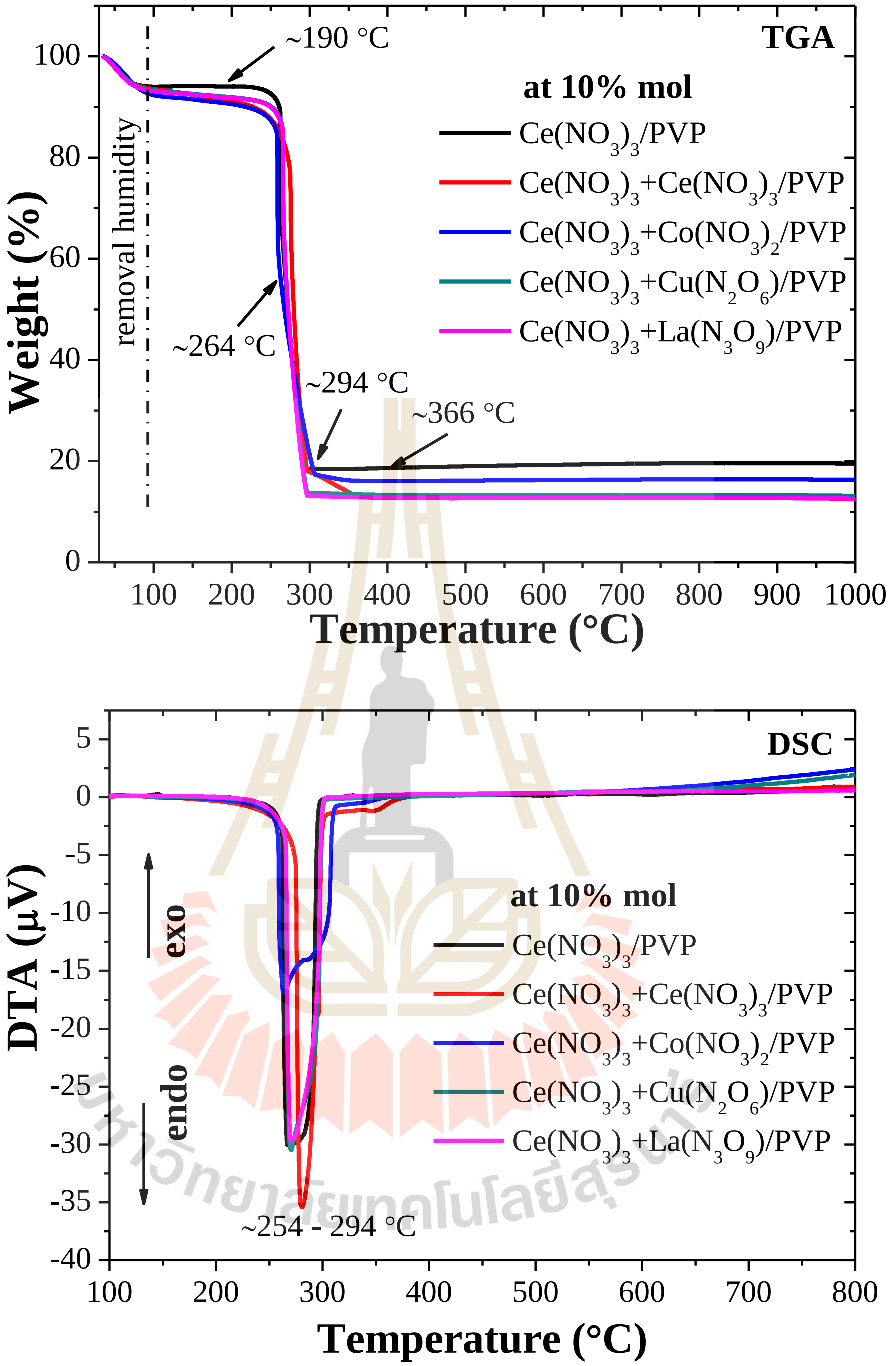

Figure 4.1 TGA and DSC curves of $Ce_{1-x}M_xO_2$/PVP under air atmosphere.

4.2 Characterization of nanoparticles and nanofibers of CeO_2 and $Ce_{1-x}M_xO_2$

4.2.1 Morphology of CeO_2 and $Ce_{1-x}M_xO_2$ nanostructures

The morphologies and structures of CeO_2 and $Ce_{1-x}M_xO_2$ nanostructures were investigated by FESEM and TEM. The SEM images of CeO_2 synthesized by simple solution method and calcined at different temperatures are shown in Figure 4.2. It is seen that CeO_2 synthesized by simple solution method exhibits nanosphere structure including with small particles inside. The size of nanoparticle is ~10-50 nm. It is also observed that the particle size increases with calcination temperature. This is possibly because the nanoparticles were fuse at high temperature. The FESEM images of $Ce_{0.96}Fe_{0.04}O_2$ and $Ce_{0.90}Fe_{0.10}O_2$ synthesized by simple solution method and calcined at different temperatures are shown in Figure 4.3-4.4. The synthesized $Ce_{0.96}Fe_{0.04}O_2$ and $Ce_{0.90}Fe_{0.10}O_2$ exhibit nanosphere structure which is similar to the CeO_2. Similar results were also observed in the other metal doped-CeO_2 nanostructures prepared by simple solution method. This suggests that the addition of metal does not affect the microstructure of CeO_2 nanoparticles.

Figure 4.5 shows the SEM images of the as-spun CeO_2/PVP and $Ce_{0.90}Fe_{0.10}O_2$/PVP before calcination. Both as-spun samples exhibit long straight, smoot, uniform nanofiber (NF) structures with diameter of ~100-220 nm. After calcination, the surfaces of CeO_2 NFs become rough as shown in Figure 4.6. This is because the polymer has been removed from the nanofibers corresponding the TGA results. Small particles were observed in the nanofiber structure. The n other metal doped-CeO_2 nanostructures prepared by electrospinning method as seen in Figure 4.6-4.7 which are the FESEM images of the $Ce_{0.90}Co_{0.10}O_2$ and $Ce_{0.90}Fe_{0.10}O_2$ calcined at

800 °C. The diameter of $Ce_{0.90}Co_{0.10}O_2$ and $Ce_{0.90}Fe_{0.10}O_2$ NFs are slightly different indicating that the added metal does not strongly affect the structure of nanofibers.

The TEM bright field images show that the nanostructures contain both aggregated nanoparticles and nanofibers. The particles sizes obtained from the TEM images were observed to be larger than the crystallite sizes obtained from the XRD pattern. Figure 4.8-4.10 show aggregations of nanoparticles of CeO_2 and $Ce_{1-x}M_xO_2$ samples. The nanoparticles do not have a uniform shape in both CeO_2 and $Ce_{1-x}M_xO_2$ nanostructures and their particle sizes are in range 11-55 nm.

The TEM bright field images of CeO_2 and $Ce_{1-x}M_xO_2$ NFs are shown in Figures 4.11-4.15. It is seen that the nanofibers are uniform and still remain this. structure after calcined at 500-800 °C (Figure 4.11 a-d). The average diameters of nanofibers are 31.4±2, 35.2±2, 46.2±2 and 59.2±2 nm for CeO_2 NFs calcined at 500, 600, 700 and 800 °C, respectively. Figure 4.12-4.15 show the TEM bright field images of $Ce_{0.96}Fe_{0.04}O_2$, $Ce_{0.90}Fe_{0.10}O_2$, $Ce_{0.90}Co_{0.10}O_2$ and $Ce_{0.90}Cu_{0.10}O_2$ NFs calcined at 500-800 °C. The average diameters of $Ce_{0.96}Fe_{0.04}O_2$, $Ce_{0.90}Fe_{0.10}O_2$, $Ce_{0.90}Co_{0.10}O_2$ and $Ce_{0.90}Cu_{0.10}O_2$ NFs are 32.2±2, 38.1±3, 20.3±2 and 55.1±3 nm, 33.4±4, 37.3±1, 48.2±1 and 55.2±1 nm, 34.2±1, 37.2±1, 48.1±3 and 60.1±1 nm and 37.4±1, 40.1±2, 48.2±1 and 53.2±1 nm, respectively, which are very close to the average diameter of CeO_2 NFs.

The selected area electron diffraction (SAED) patterns of the CeO_2 and $Ce_{0.90}Fe_{0.10}O_2$ nanostructures in Figure 4.16-4.17 show spotty and ring patterns corresponding to plane of CeO_2 cubic fluorite structure without secondary phase of dopants in the structure. This result agrees with XRD results. Clarity of spotty indicates that the crystallinity increases when calcination temperature increase. Figure 4.16-4.17 indicate the interplanar spacing distance of 0.270 nm and 0.311 nm correspond to (200),

(111) planes of cubic CeO_2 (JCPDS 750076) which agrees well with the XRD results. This is an indicator of a face-center cubic structure of CeO_2 without any additional diffraction spots and rings of Fe or La-based impurity phases, which is consistent with the XRD results.

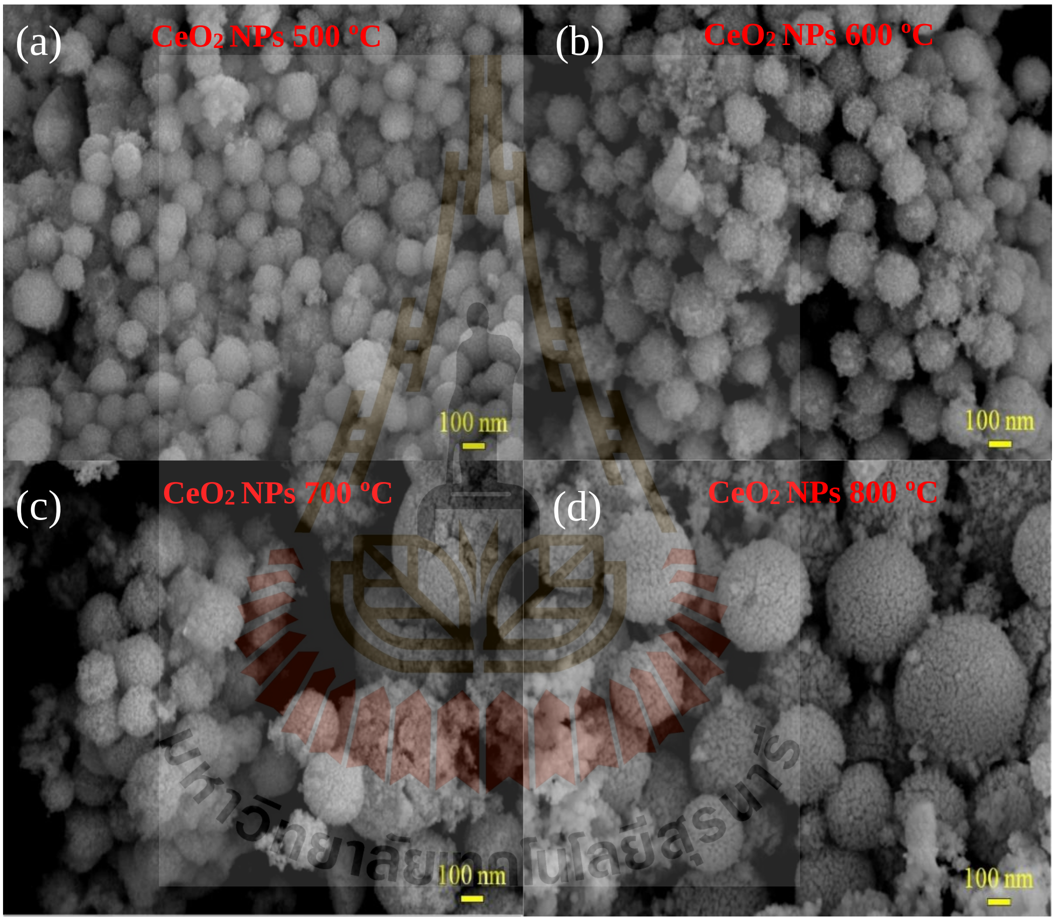

Figure 4.2 FESEM images of CeO_2 NPs synthesized by simple solution method and calcined at (a) 500 °C (b) 600 °C, (c) 700 °C and (d) 800 °C for 2 h in air.

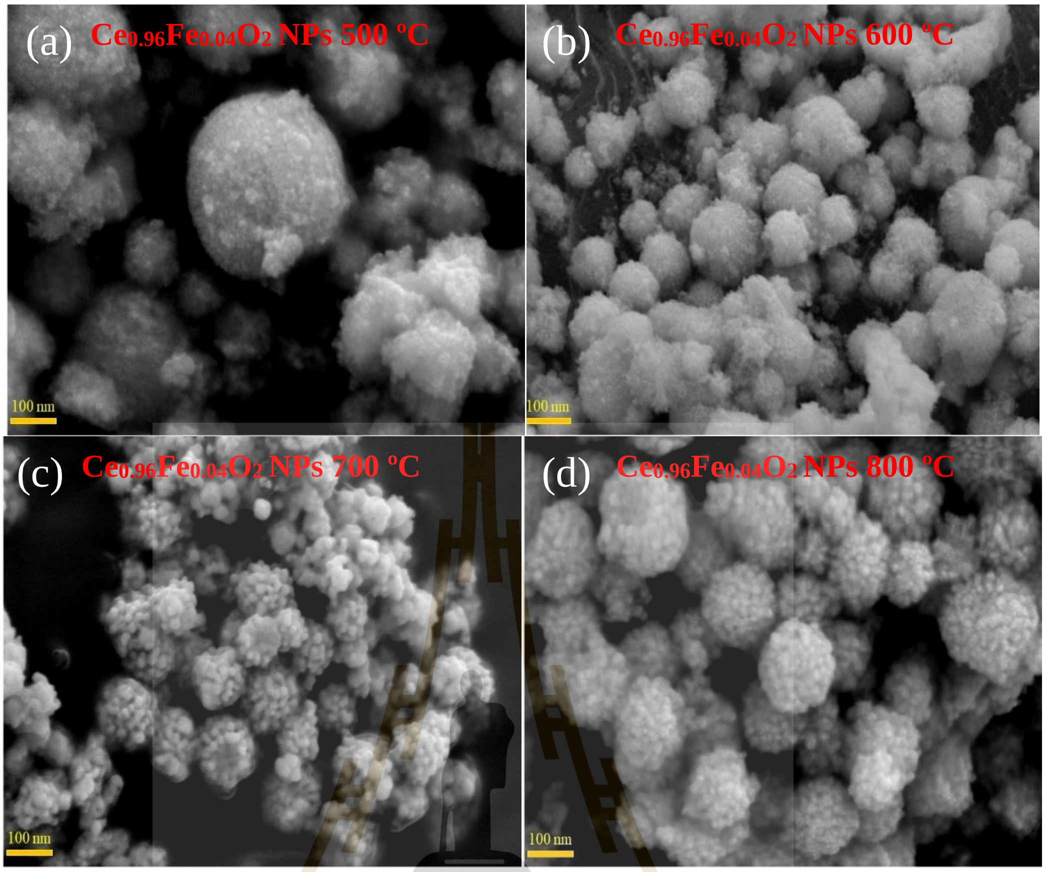

Figure 4.3 FESEM images of $Ce_{0.96}Fe_{0.04}O_2$ NPs synthesized by simple solution method calcined at (a) 500 °C (b) 600 °C, (c) 700 °C and (d) 800 °C for 2 h in air.

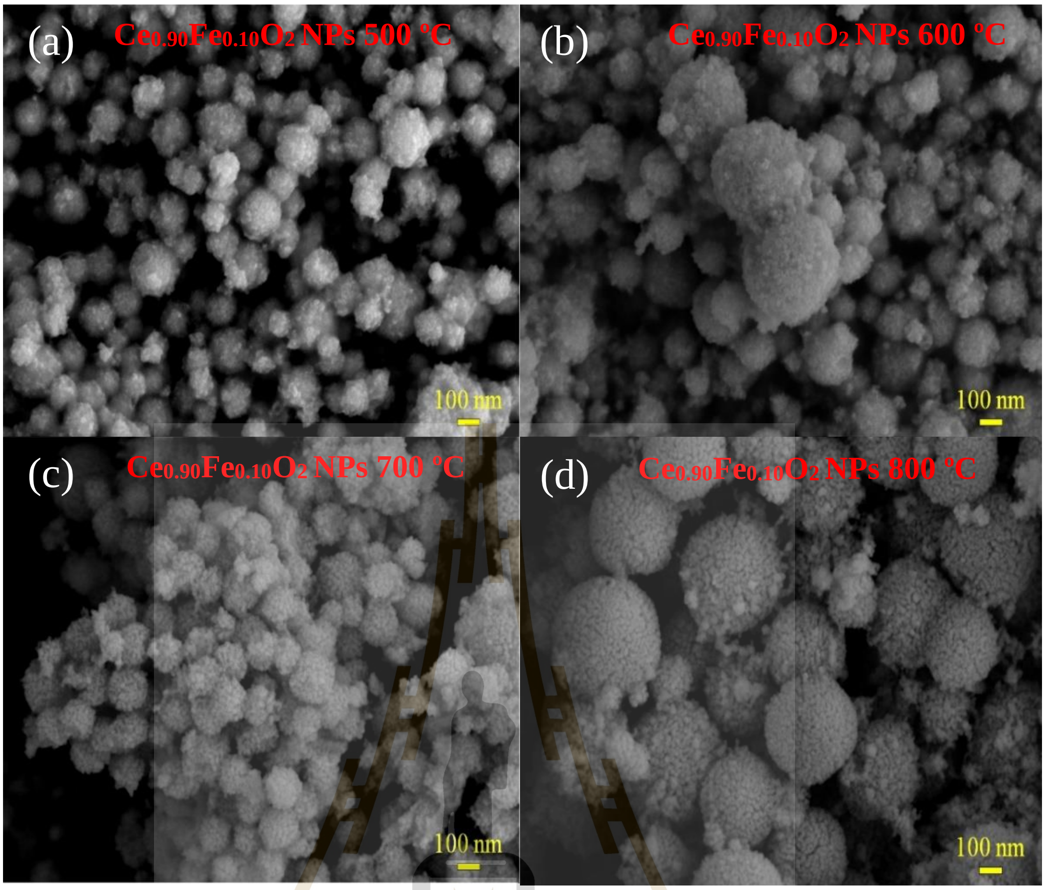

Figure 4.4 FESEM images of $Ce_{0.90}Fe_{0.10}O_2$ NPs synthesized by simple solution method calcined at (a) 500 °C (b) 600 °C, (c) 700 °C and (d) 800 °C for 2 h in air.

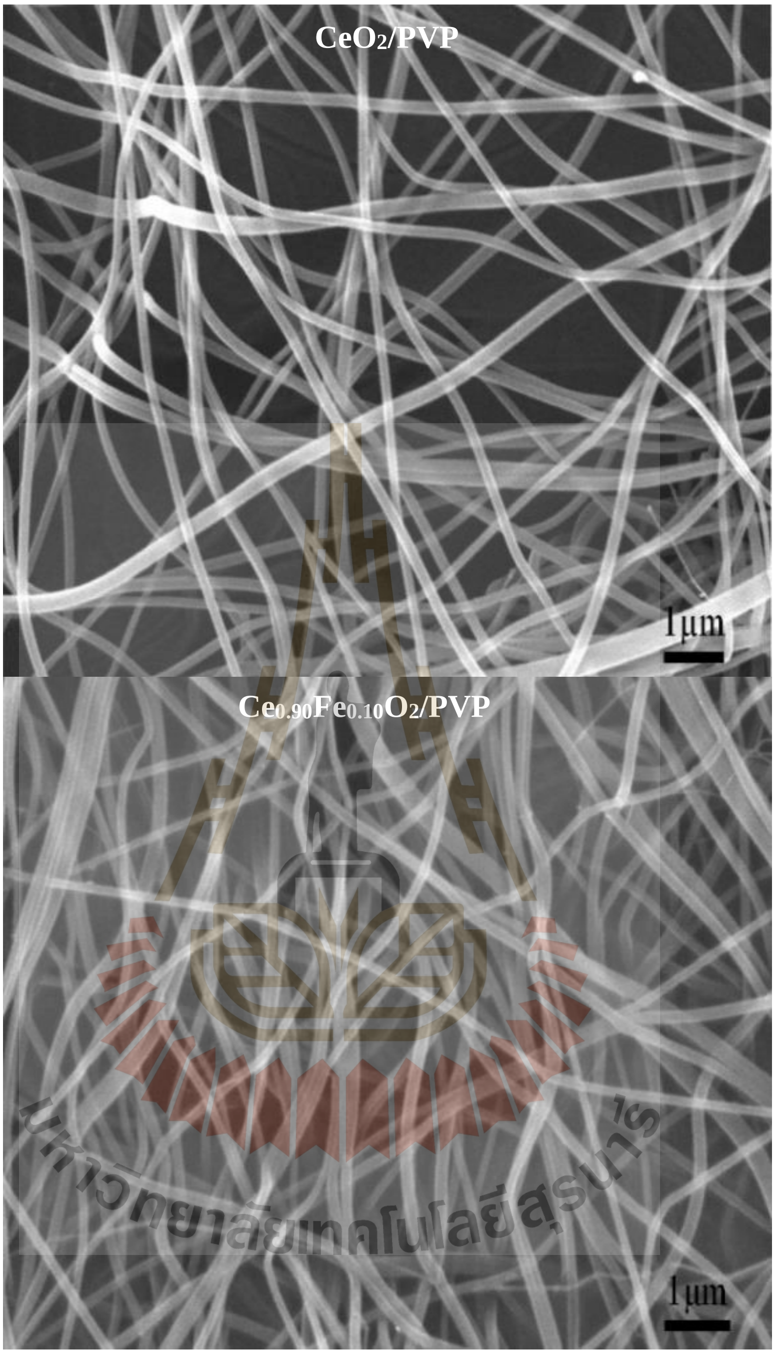

Figure 4.5 SEM images of the as-spun (a) CeO_2/PVP and (b) $Ce_{0.90}Fe_{0.10}O_2$/PVP before calcination.

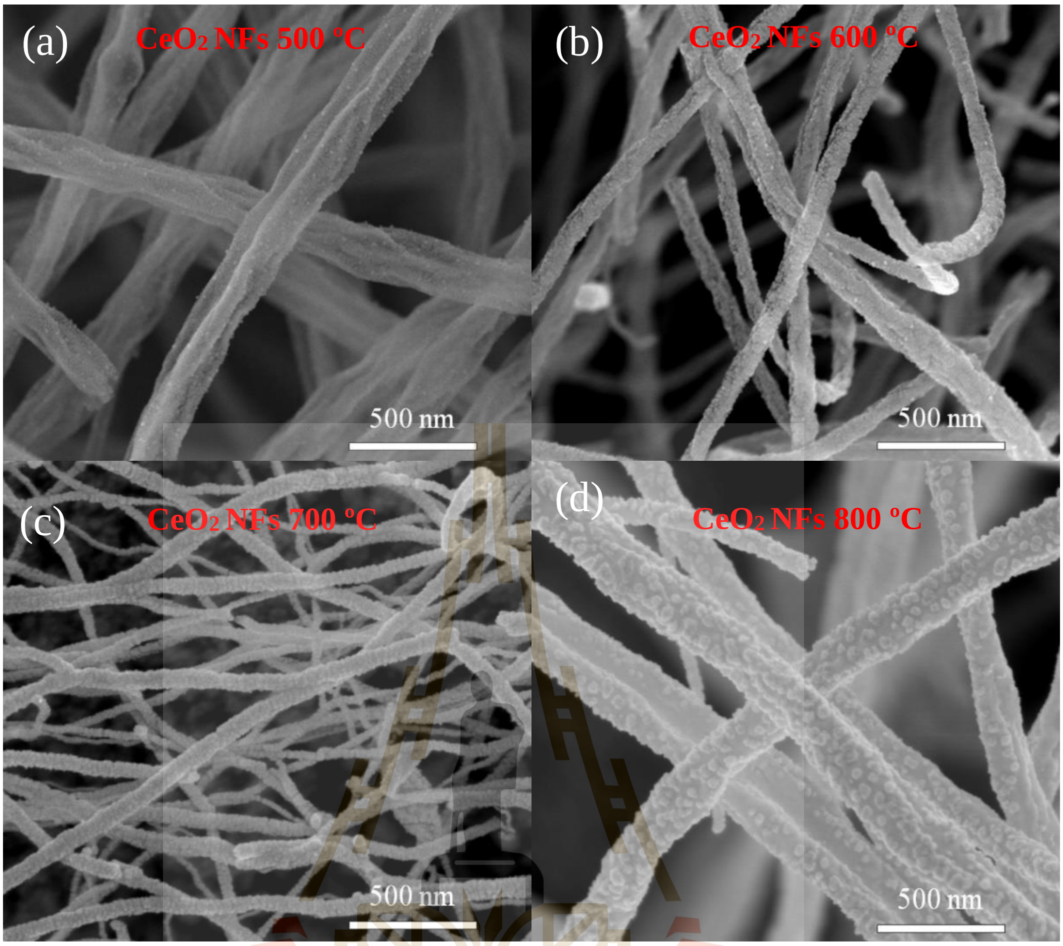

Figure 4.6 FESEM images of CeO_2 NFs synthesized by electrospinning method and calcined at (a) 500 °C (b) 600 °C, (c) 700 °C and (d) 800 °C for 2 h in air.

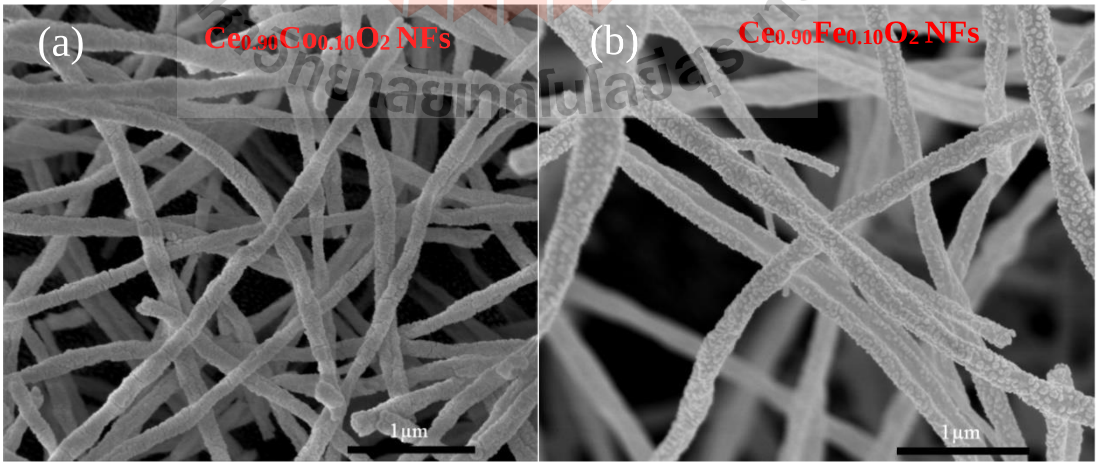

Figure 4.7 FESEM images of the fibers after calcination (b) $Ce_{0.90}Co_{0.10}O_2$ NFs and $Ce_{0.90}Fe_{0.10}O_2$ NFs calcined at 800 °C in air, respectively.

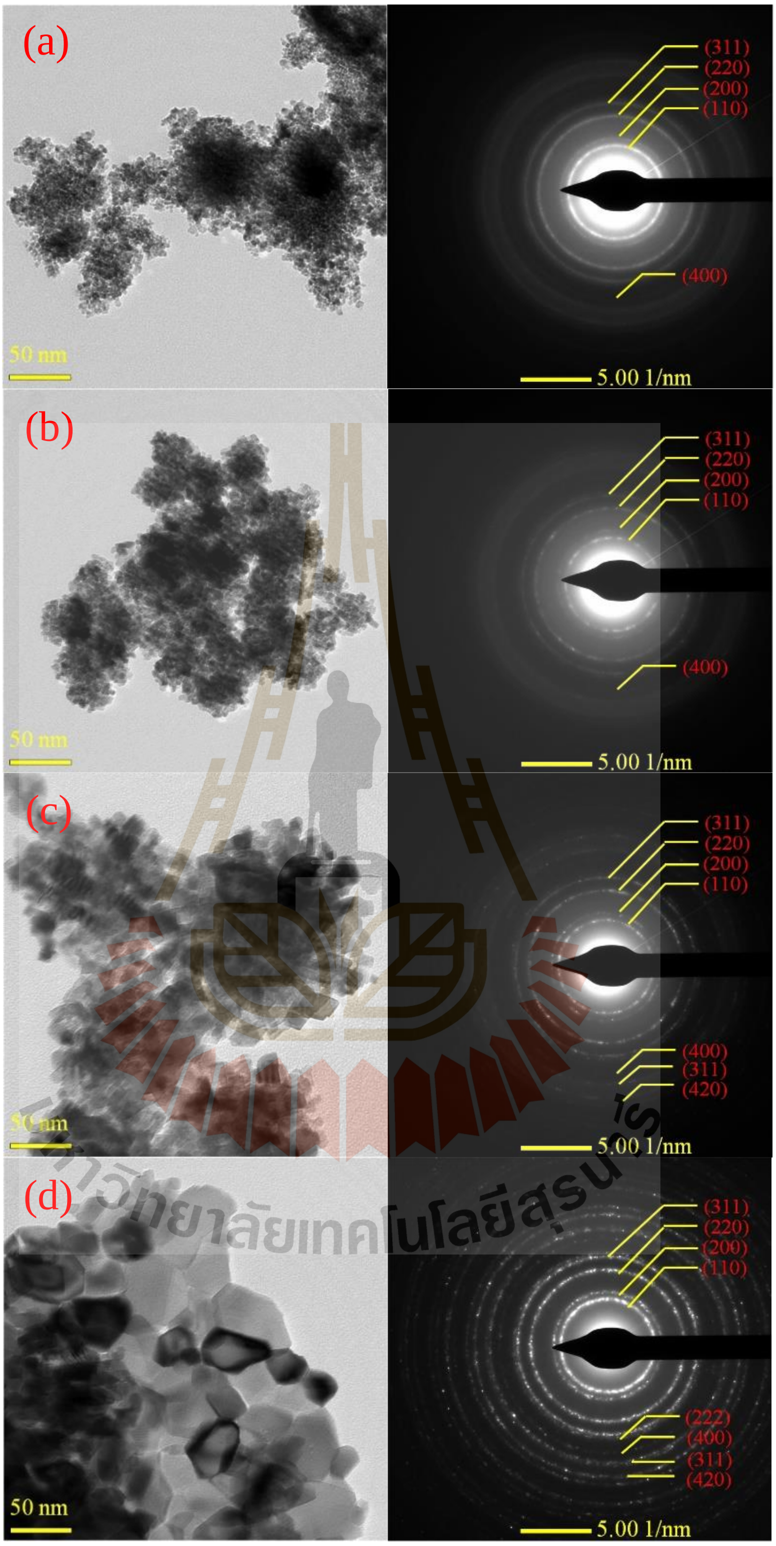

Figure 4.8 TEM bright field images with corresponding SAED patterns of CeO_2 NPs calcined at a) 500 °C, (b) 600 °C, (c) 700 °C, and (d) 800 °C for 2 h in air.

h in air.

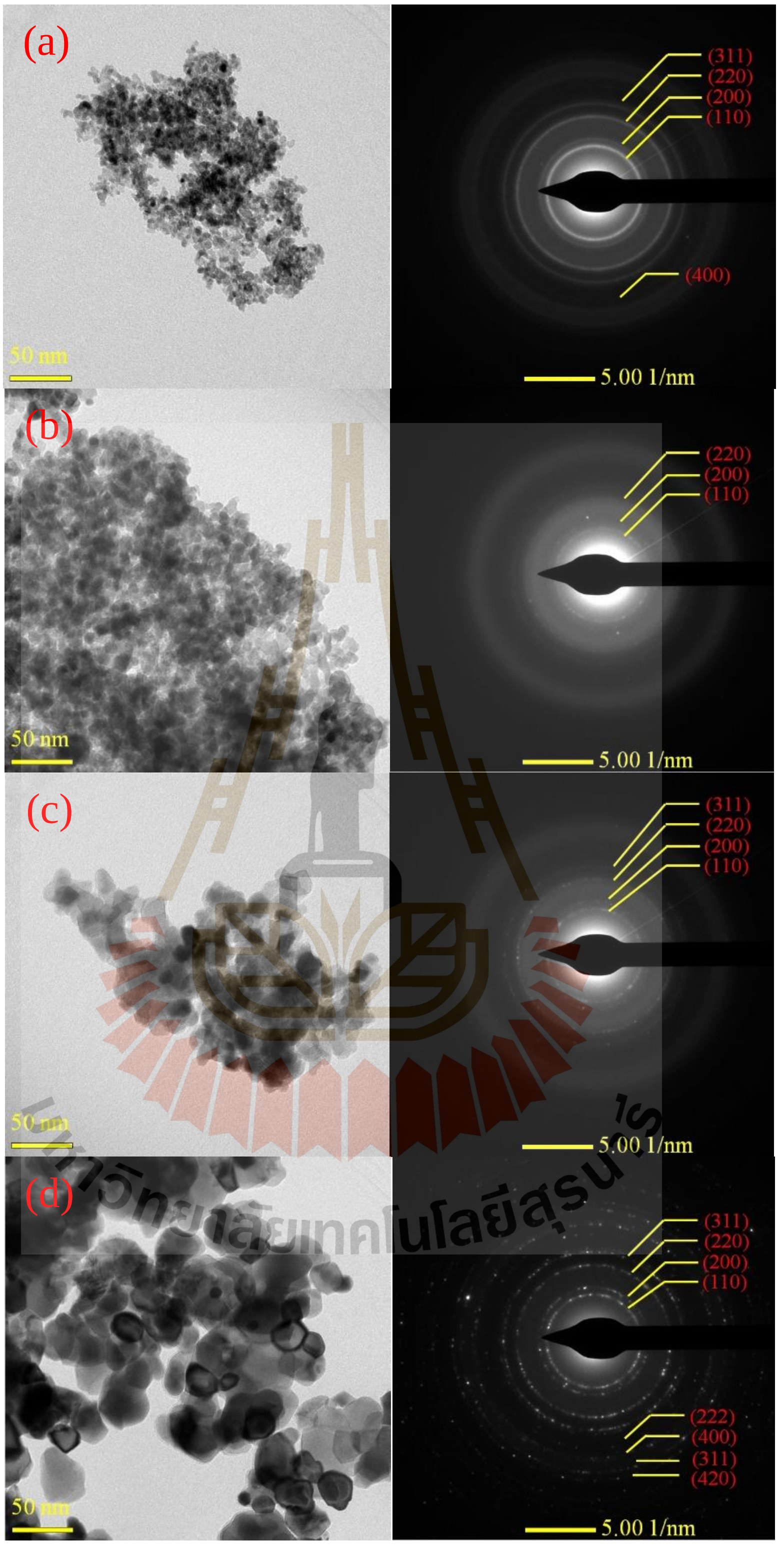

Figure 4.9 TEM bright field images with corresponding SAED patterns of $Ce_{0.90}Co_{0.10}O_2$ NPs calcined at a) 500 °C, (b) 600 °C, (c) 700 °C, and (d) 800 °C for 2 h in air.

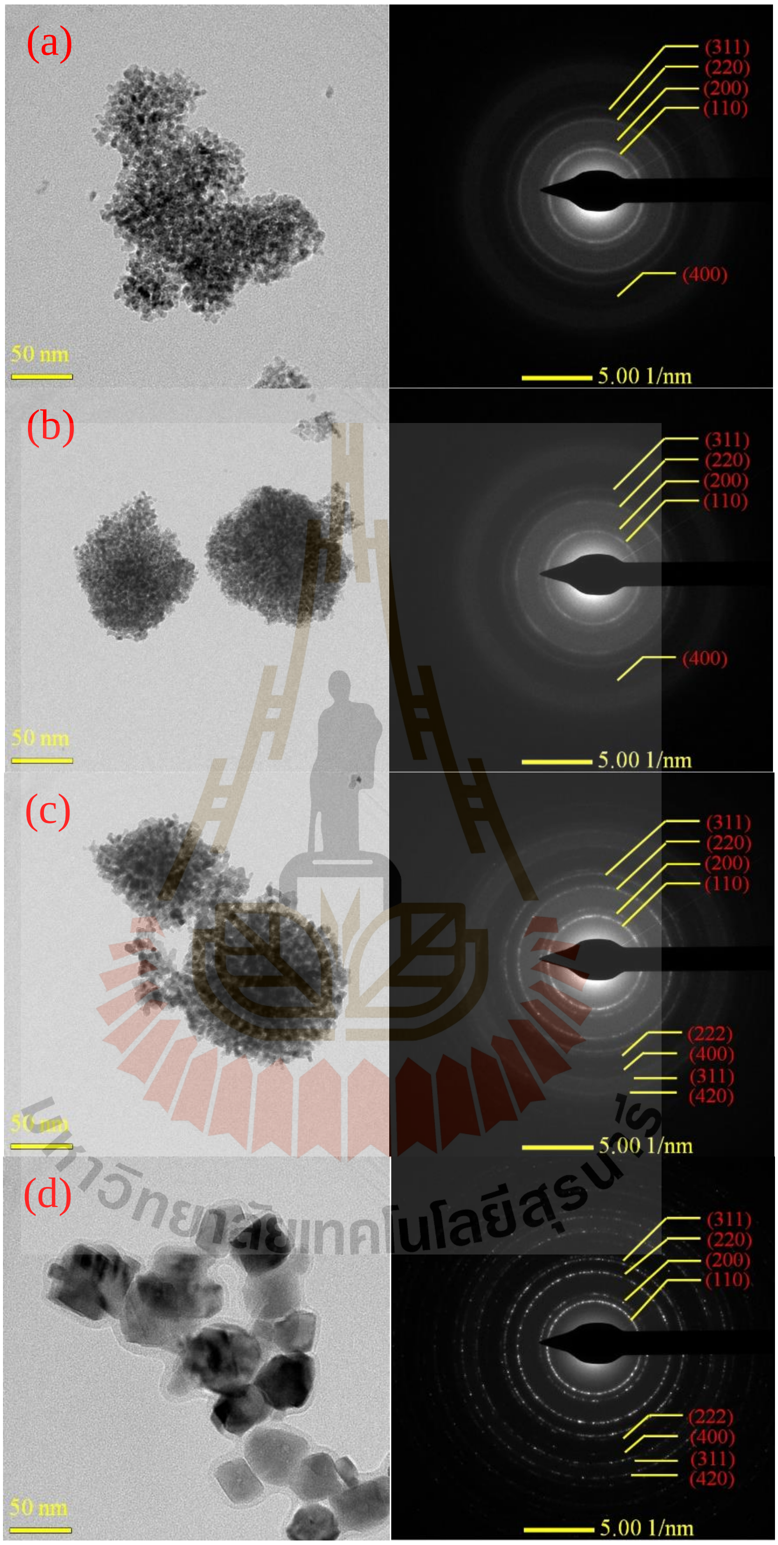

Figure 4.10 TEM bright field images with corresponding SAED patterns of $Ce_{0.90}La_{0.10}O_2$ NPs calcined at a) 500 °C, (b) 600 °C, (c) 700 °C, and (d) 800 °C for 2 h in air.

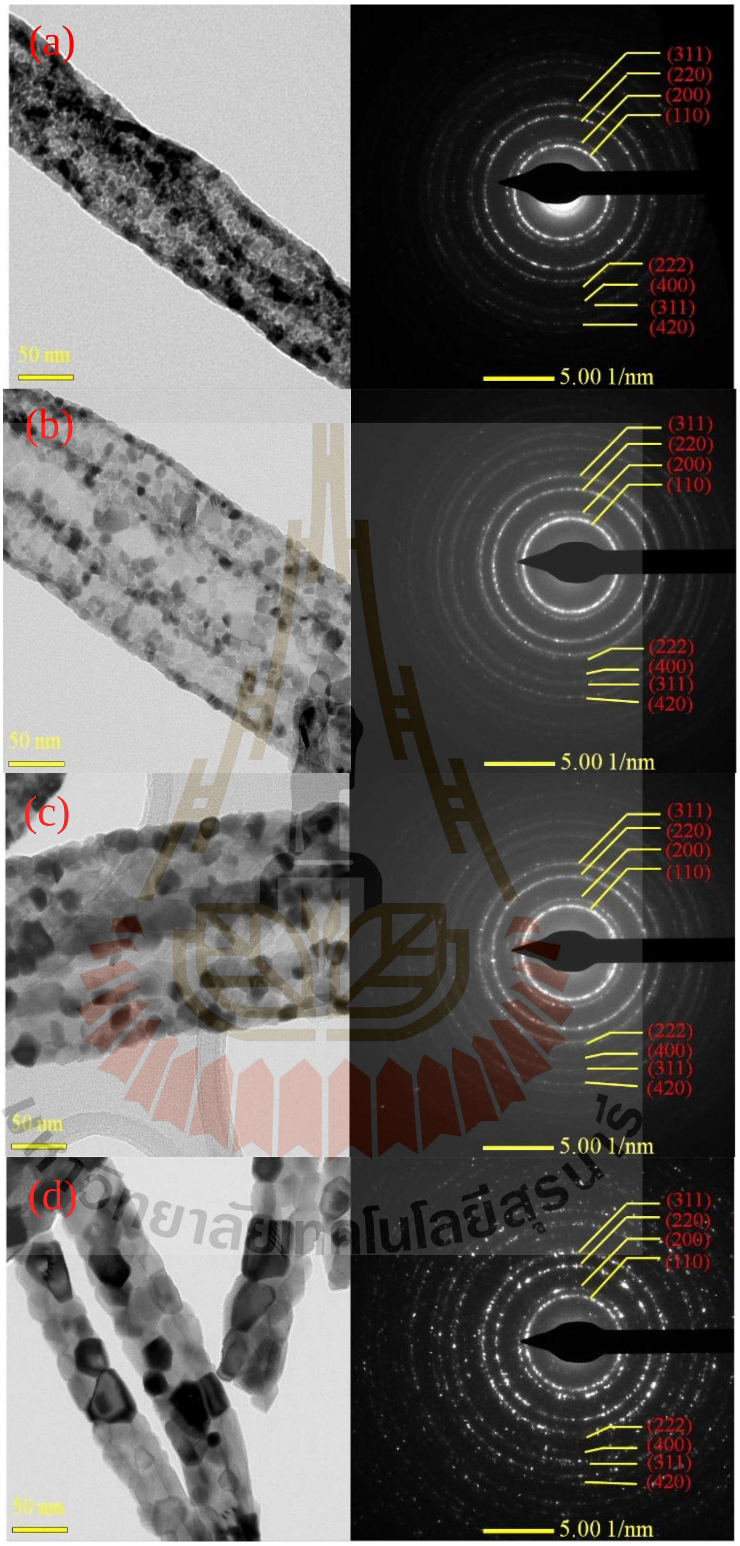

Figure 4.11 TEM bright field images with SAED of CeO_2 NFs calcined at (a) 500 °C, (b) 600 °C, (c) 700 °C, and (d) 800 °C for 2 h in air.

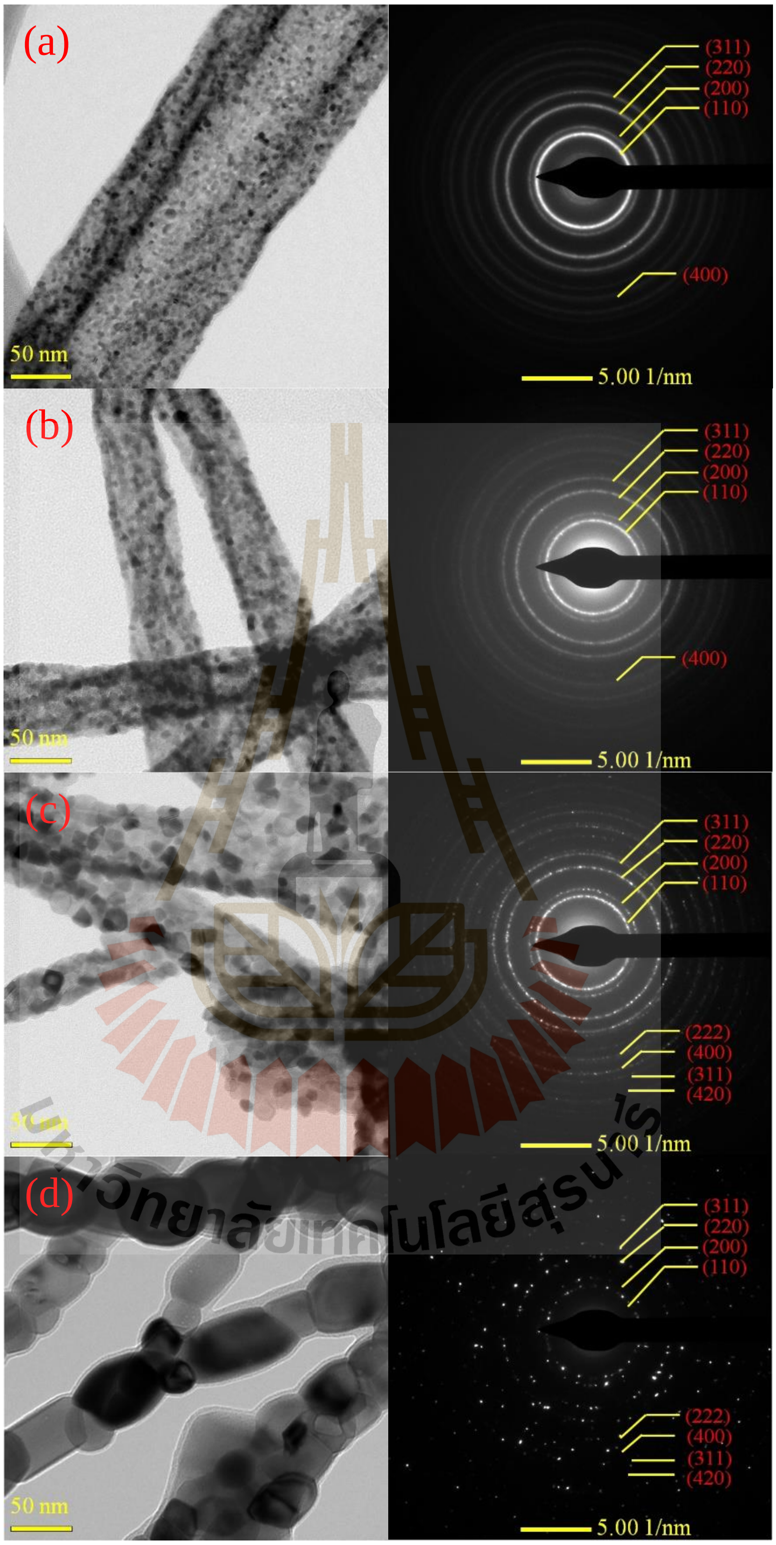

Figure 4.12 TEM bright field images with SAED of $Ce_{0.92}Fe_{0.08}O_2$ NFs calcined at (a) 500 °C, (b) 600 °C, (c) 700 °C, and (d) 800 °C for 2 h in air.

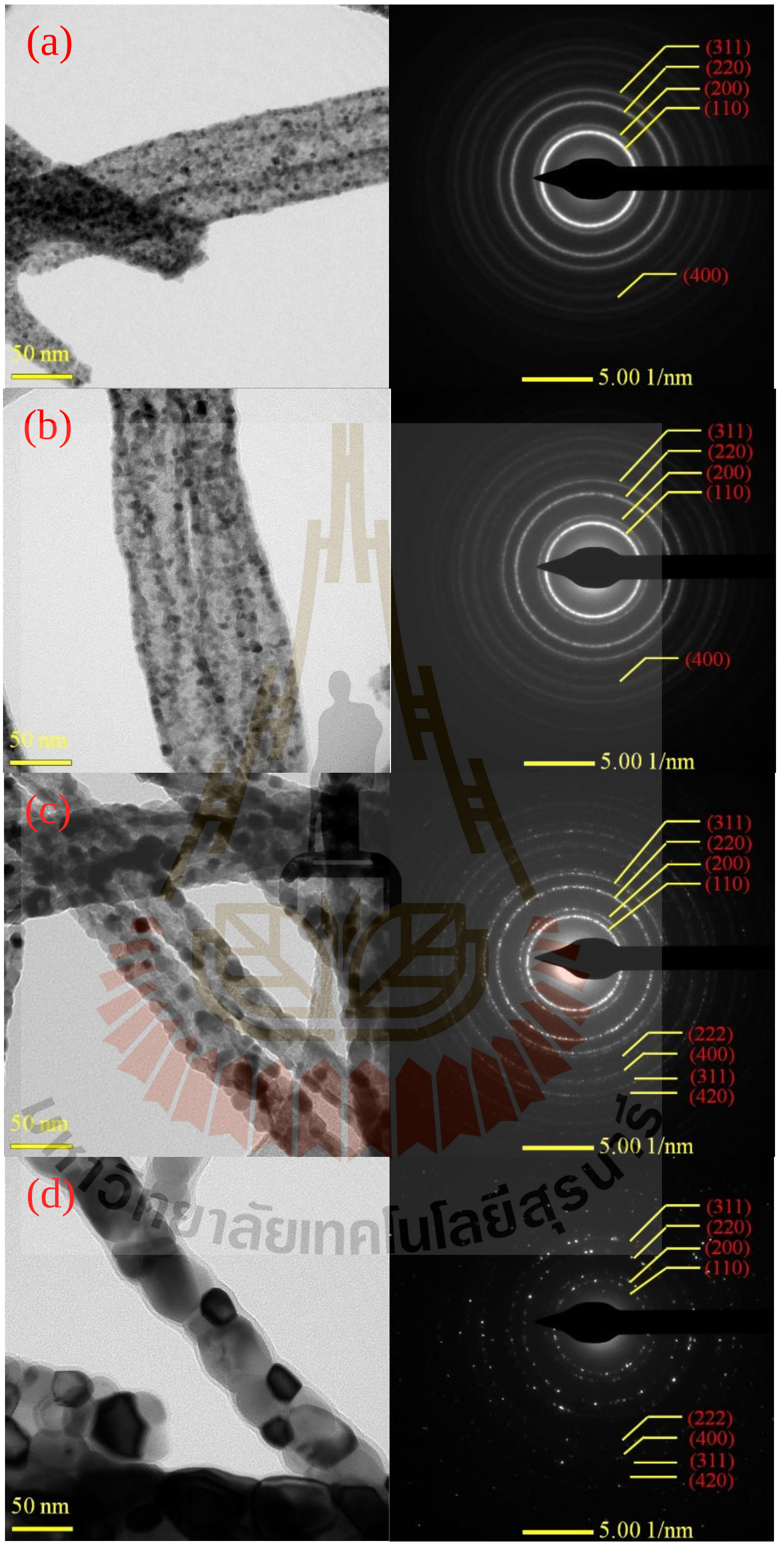

Figure 4.13 TEM bright field images with SAED of Ce$_{0.90}$Fe$_{0.10}$O$_2$ NFs calcined at (a) 500 °C, (b) 600 °C, (c) 700 °C, and (d) 800 °C for 2 h in air.

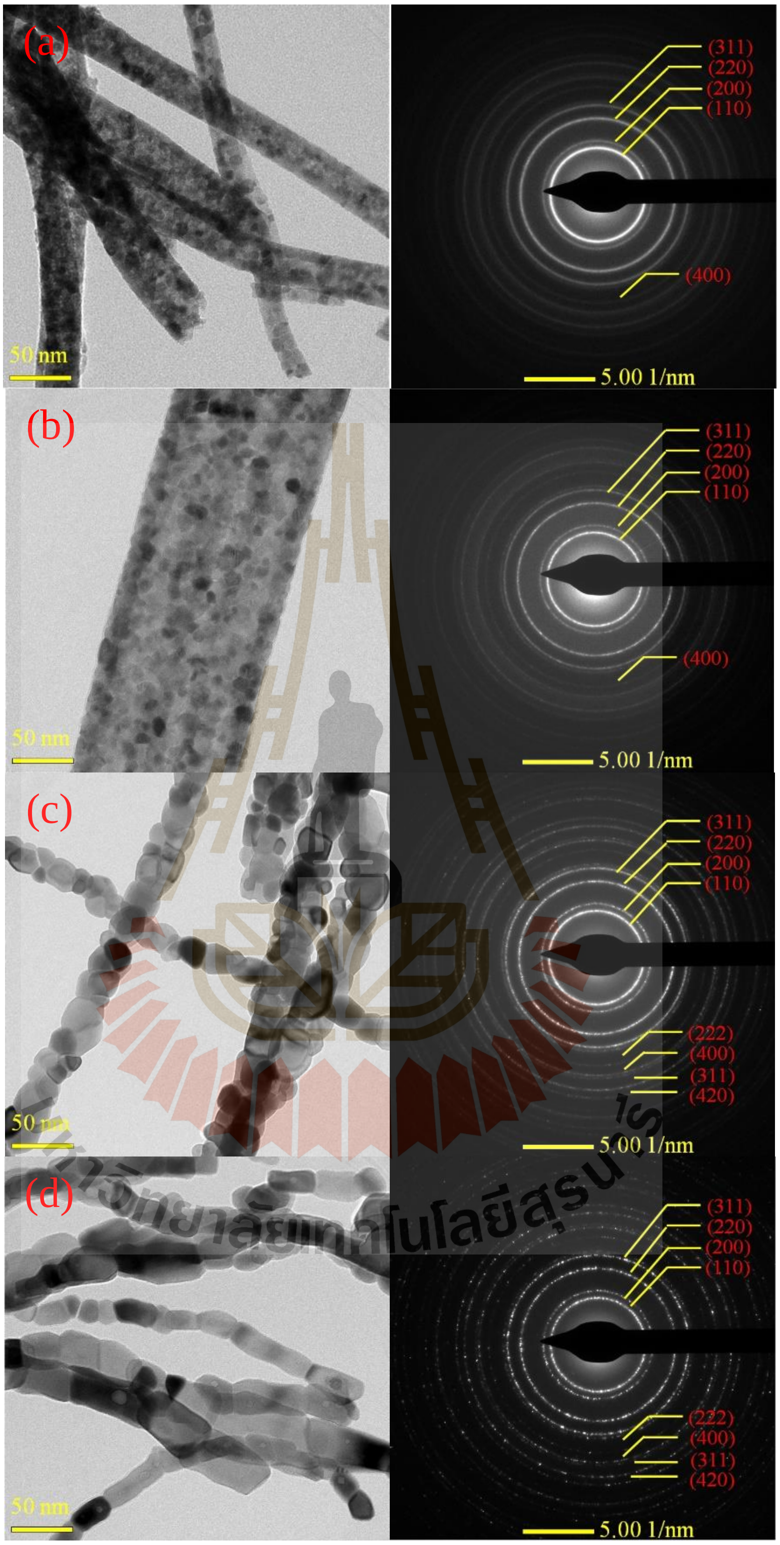

Figure 4.14 TEM bright field images with SAED of $Ce_{0.90}Co_{0.10}O_2$ NFs calcined at (a) 500 °C, (b) 600 °C, (c) 700 °C, and (d) 800 °C for 2 h in air.

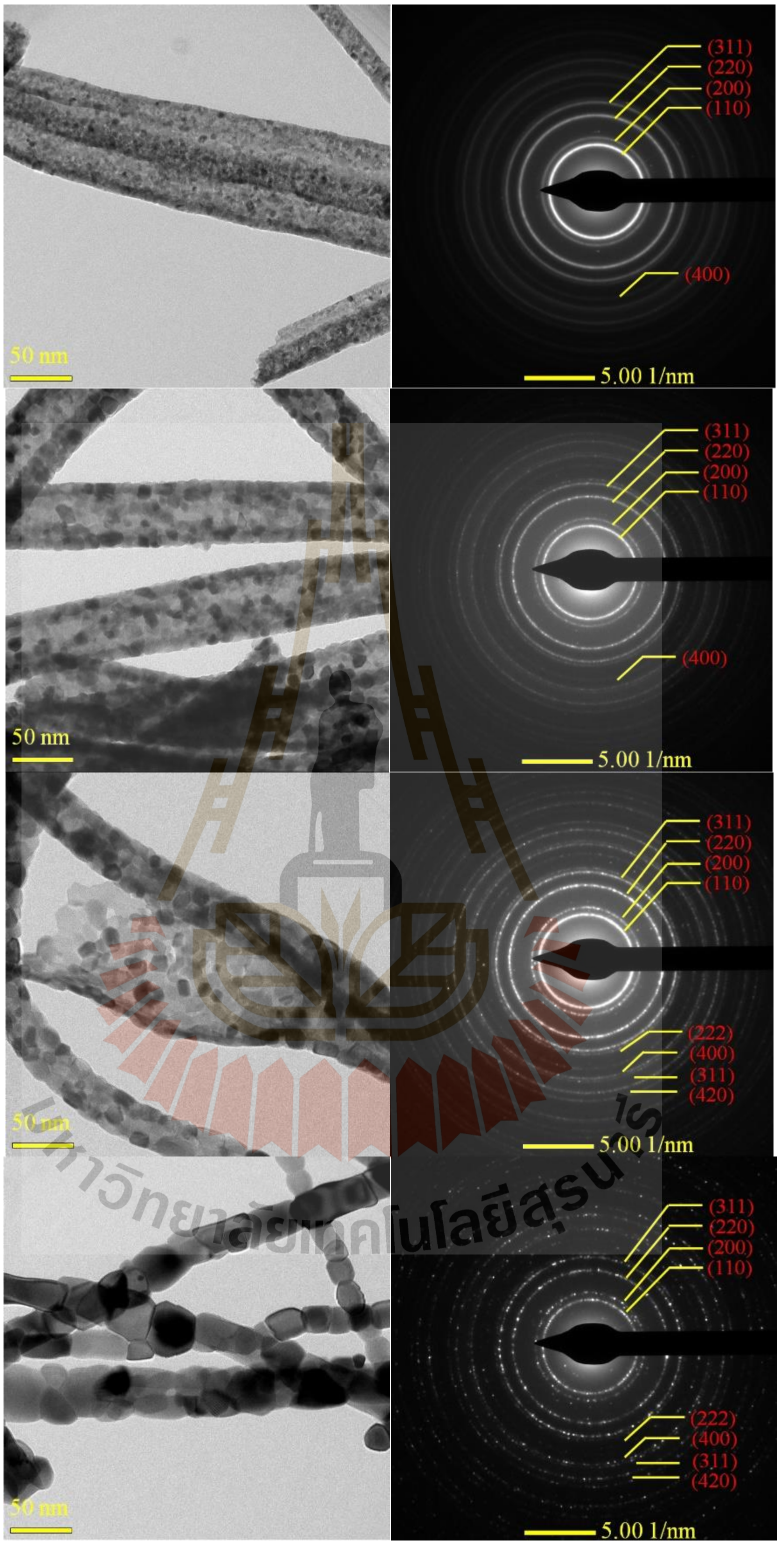

Figure 4.15 TEM bright field images with SAED of $Ce_{0.90}Cu_{0.10}O_2$ NFs calcined at (a) 500 °C, (b) 600 °C, (c) 700 °C, and (d) 800 °C for 2 h in air.

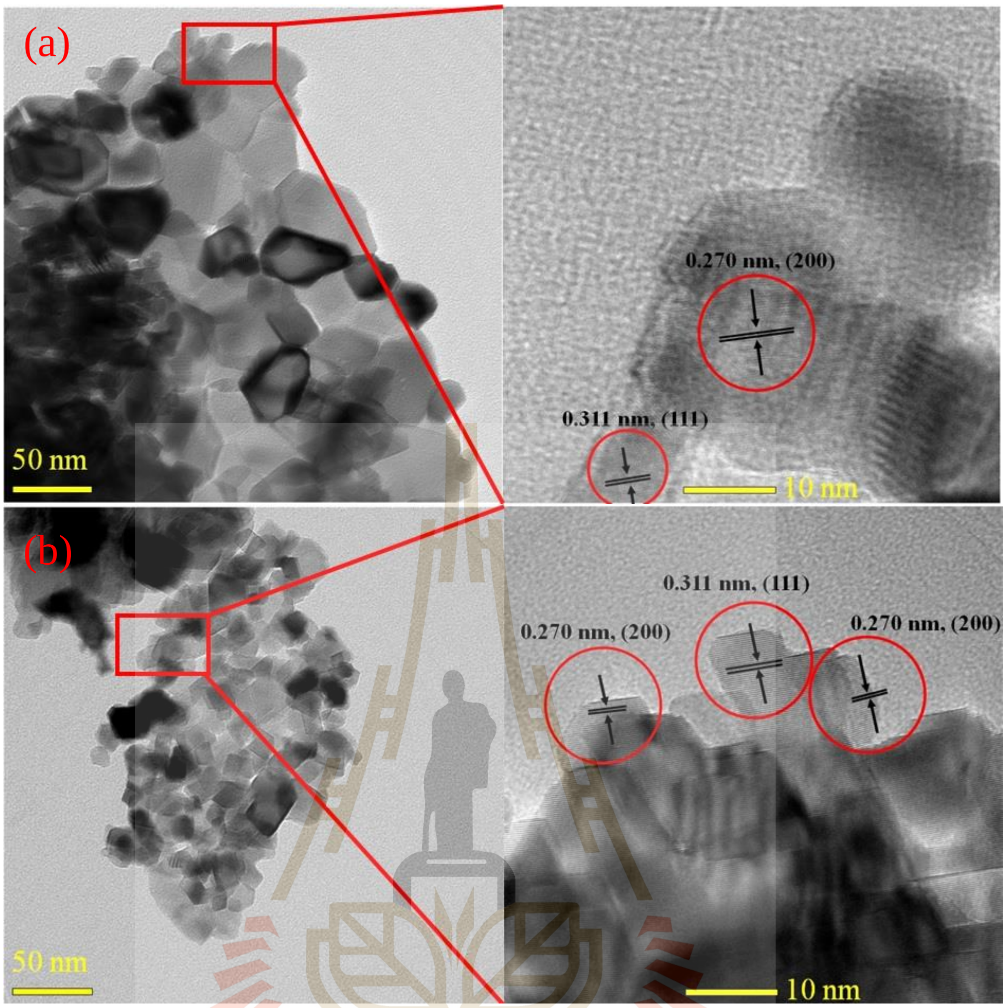

Figure 4.16 HRTEM images of (a) CeO_2 NPs, (b) $Ce_{0.90}La_{0.10}O_2$ NPs calcined at 800 °C for 2 h in air.

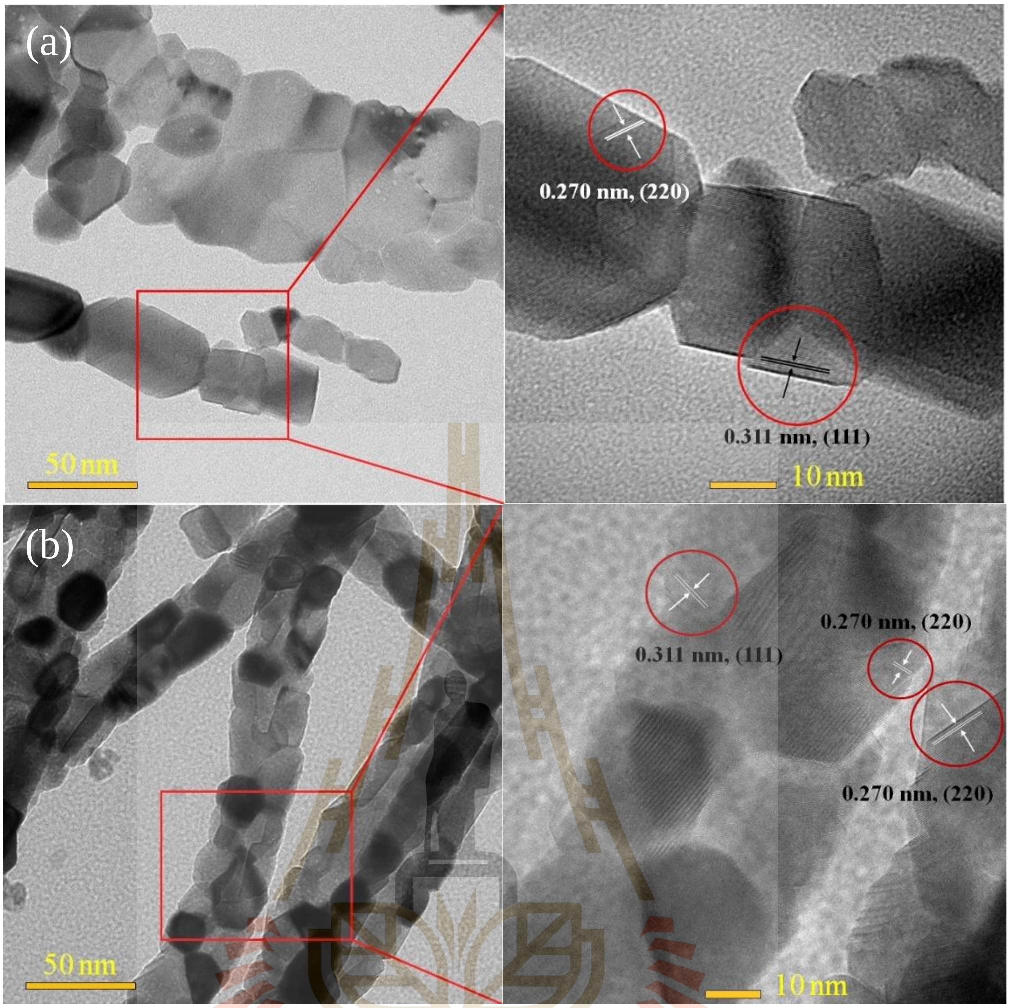

Figure 4.17 HRTEM images of (a) CeO_2 NFs, (b) $Ce_{0.90}Fe_{0.10}O_2$ NFs calcined at 800 °C for 2 h in air.

4.2.2 Phase formation and structure

The structure and phase compositions of CeO_2 and $Ce_{1-x}M_xO_2$ nanostructures were investigated by XRD. Powder X-ray diffraction patterns of the prepared CeO_2 nanostructures are shown in Figure 4.18. Both NPs and NFs show main peaks corresponding to cubic fluorite structure of CeO_2 in the standard data (JCPDS No. 750076). The main peaks become sharper when the calcination temperature increases indicating more crystallinity. The lattice parameters and average crystallites sizes of CeO_2 NPs and NFs are calculated from X-ray line broadening of reflection planes of (111), (200), (220) and (311) using Bragg's law and Debye-Scherrer's equation (see in Equation 3.1, 3.2) (Bernard and Stuart, 2001). The results are summarized in Table 4.1. Crystallite size of CeO_2 nanostructure increases with calcination temperature because the heat treatment made particles condense together. This suggests that the morphologies of NPs and NFs do not affect the crystallinity structures of prepared CeO_2 samples.

The XRD patterns of $Ce_{0.90}M_{0.10}O_2$ (M = Fe, Co, Cu and La) calcined at 800 °C are shown in Figure 4.19. Both $Ce_{0.90}M_{0.10}O_2$ (M = Fe, Co, Cu and La) NPs and NFs show the main peaks corresponding to the cubic fluorite structure of CeO_2. Only the secondary phase of cobalt oxide (Co_3O_4) was observed for $Ce_{0.90}Co_{0.10}O_2$ NPs sample indicating that Co ion might not completely replace Ce ion in the structure. The shift of the peak of plane (111) was also observed because the doping of impurity atom changes the lattice structure. The peak shift in the XRD is based on the dopant size (He et al., 2016). If the dopant size is smaller than the based metal, the d-spacing between the atoms decreases resulting in higher angles shift (2Θ right shift). If the dopant size is larger than the based metal. Lower angles (2Θ left shift) is attained with increase in d-spacing. The lattice parameters of all $Ce_{1-x}M_xO_2$ where $0 \leq x \leq 10$ nanostructures are close to 0.5389 nm which is the value in the standard data (JCPDS No. 750076). This suggests that the addition of metal affect the crystallinity structure of CeO_2 nanostructures.

For $Ce_{1-x}Fe_xO_2$ NPs and NFs where $0 \leq x \leq 10$ calcined at 800 °C in Figure 4.20, the peak shift in the XRD pattern shows the right shift confirming that the larger Ce^{4+} ions were completely replaced by the smaller Fe^{3+} ions or Fe^{2+} ions in the crystal lattice. The calculated crystallite sizes and lattice parameters are also summarized in Table 4.4. The crystallite sizes of $Ce_{1-x}Fe_xO_2$ NPs and NFs show similar characteristics. The lattice parameters are slightly different from 0.5389 nm, which confirms the complete replacement in the structure.

The replacement of the larger Ce^{4+} ions (0.092 nm) by the smaller Fe^{3+} ions (0.065 nm) or Fe^{2+} ions (0.078 nm) or Cu (0.072 nm) in the crystal lattice causes the change in the Ce-O bond length (lattice distortion) and the overall lattice parameter. This has been observed in the earlier studies on the Fe-doped CeO_2 nanoparticles (Gogoi, Navgire, Sarma and Gogoi, 2017, Wang, Zhu, Dai and Wang, 2017). In the case of $Ce_{0.90}La_{0.10}O_2$, the lattice constant values are higher than 0.5389 nm. There was the change in the Ce-O bond length (lattice distortion) (see in Figure 4.22). This is possibly due to the replacement of the smaller Ce^{4+} ions (0.092 nm) by the larger La^{3+} ions (0.106 nm) in the crystal lattice. This result confirms La^{3+} completely inserted into CeO_2 crystal lattice (Shiyou and Tianxi, 2007).

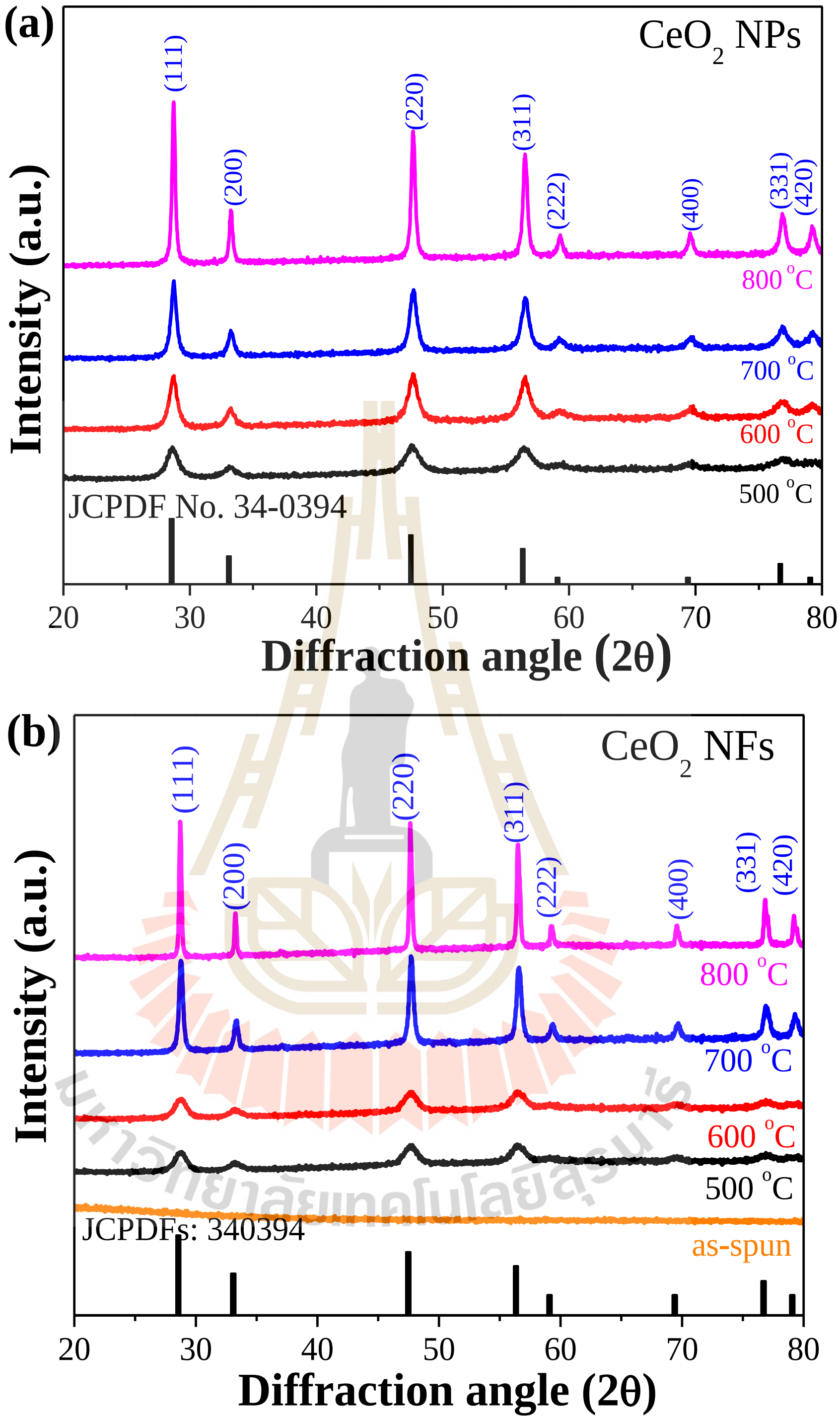

Figure 4.18 XRD patterns of (a) CeO_2 NPs and (b) CeO_2 NFs calcined at 500 - 800 °C in air.

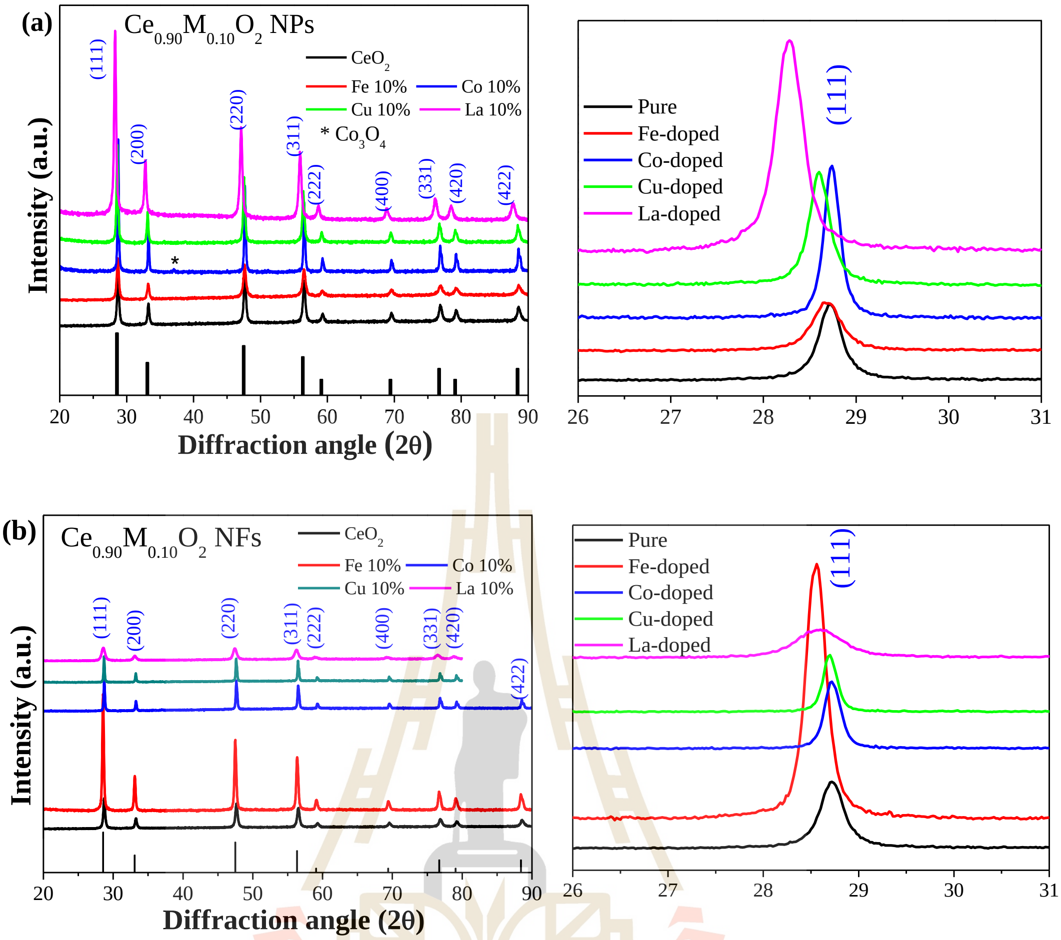

Figure 4.19 XRD patterns of $Ce_{0.90}M_{0.10}O_2$ (M = Fe, Co, Cu and La) (a) NPs and (b) NFs calcined at 800 °C in air.

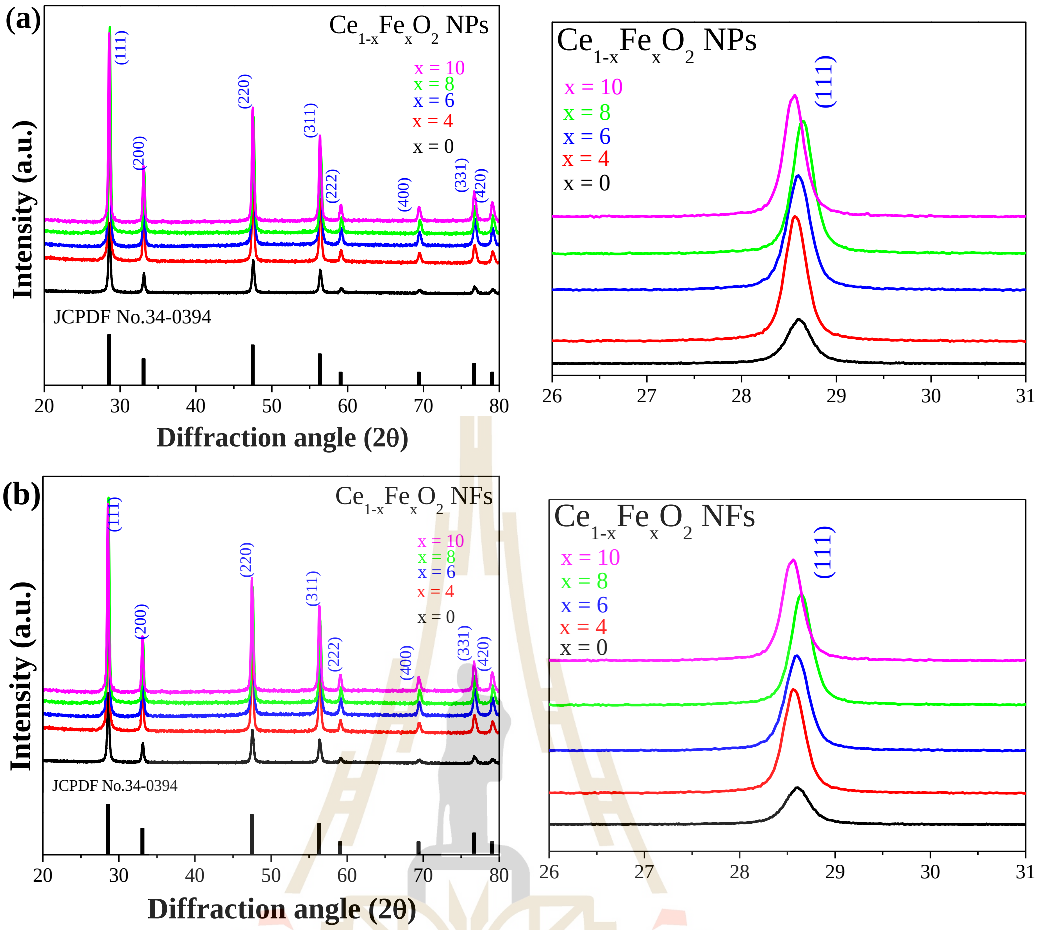

Figure 4.20 XRD patterns of $Ce_{1-x}Fe_xO_2$ ($0 \leq x \leq 10$) (a) NPs and (b) NFs calcined at 800 °C in air.

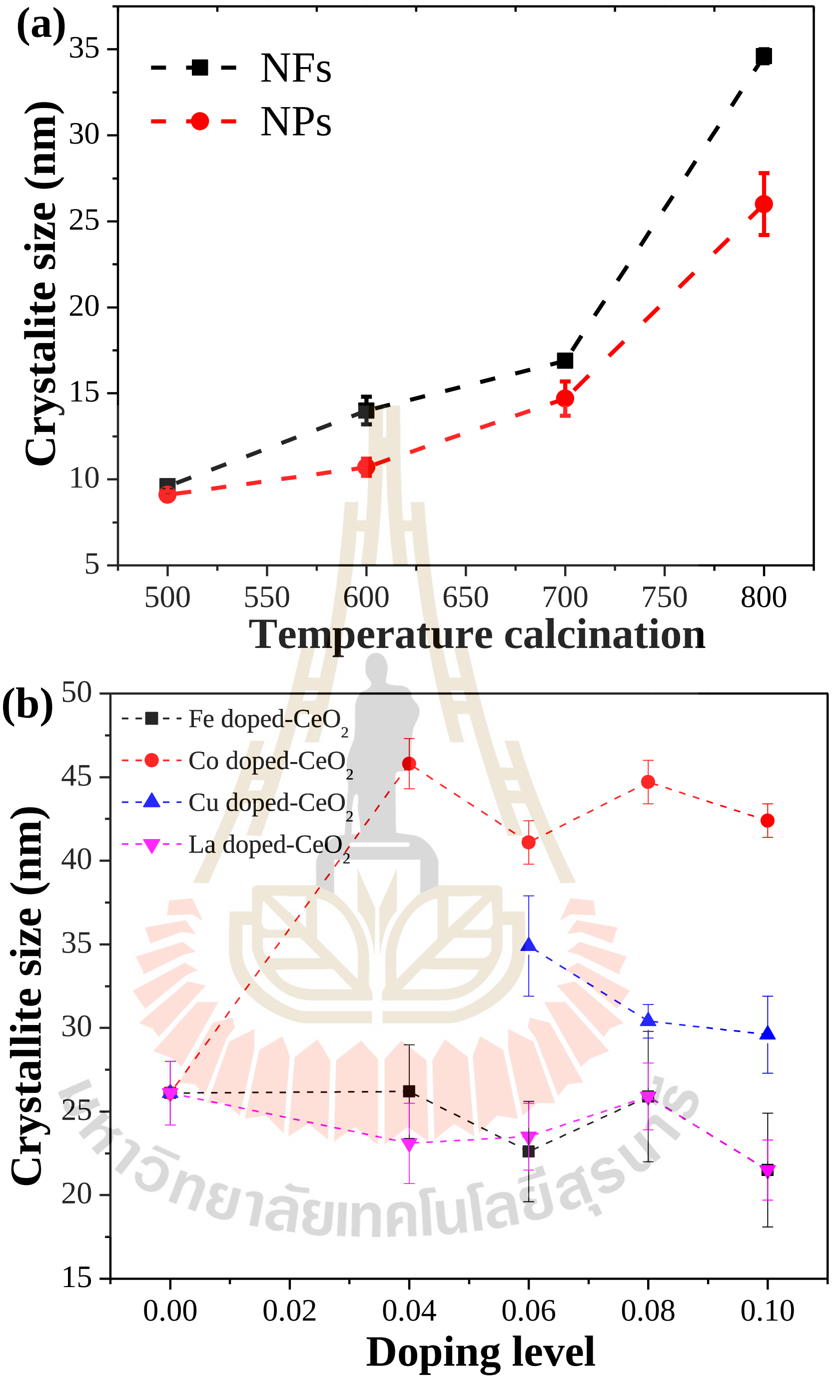

Figure 4.21 An average crystallites size of (a) CeO_2 NPs and NFs calcined at 500-800 °C for 2 h in air and (b) $Ce_{0.90}M_{0.10}O_2$ NPs calcined at 800 °C in air.

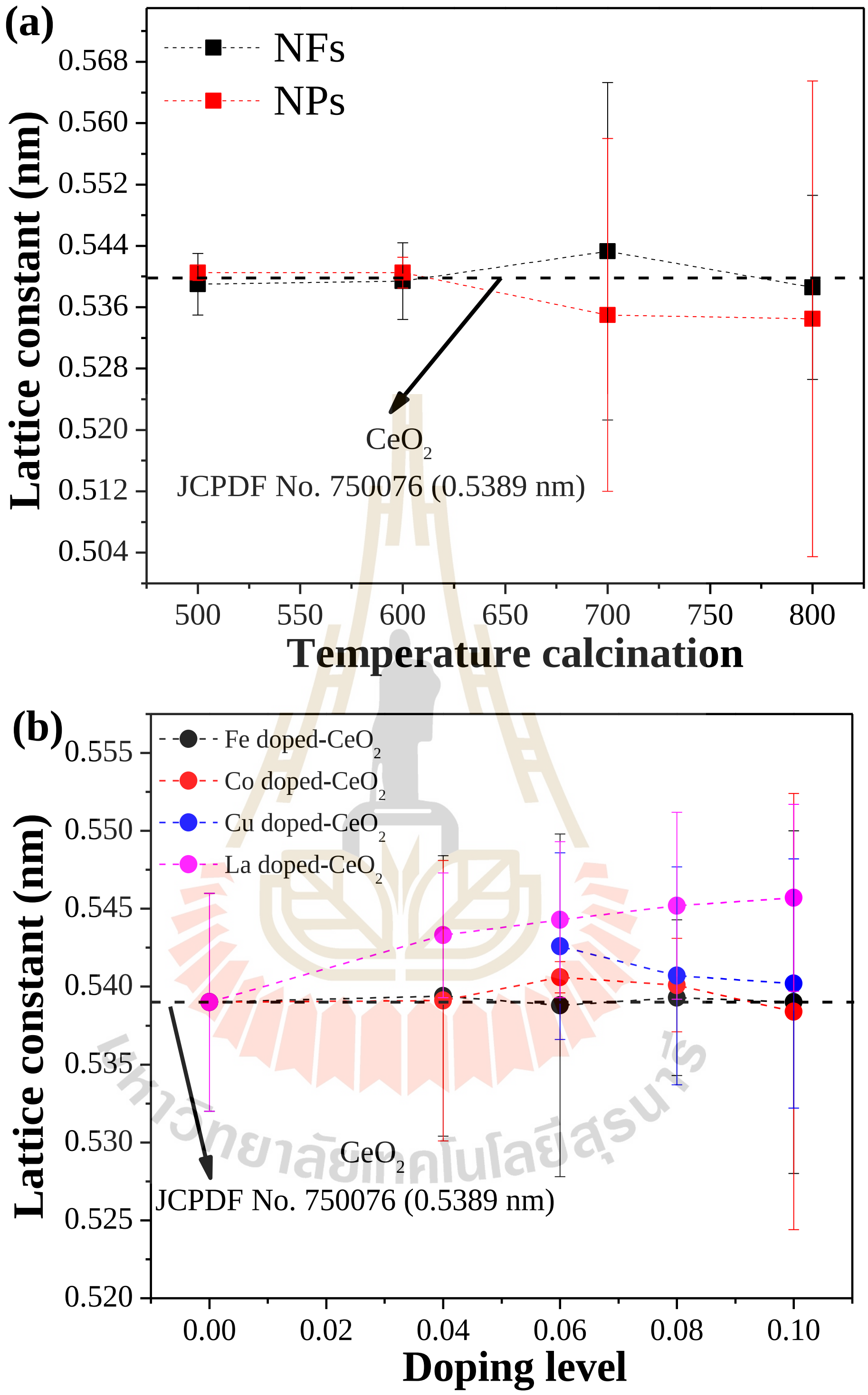

Figure 4.22 Lattice constant of a) CeO_2 NPs and NFs calcined at 500-800 °C for 2 h in air (b) $Ce_{0.90}M_{0.10}O_2$ NPs calcined at 800 °C in air.

Table 4.1 Summary of crystallite size of CeO_2 nanostructures calcined at 500-800 °C for 2 h in air.

Temperature of calcination (°C)	Crystallite size (nm)		Lattice parameter (nm)	
	NPS	NFs	NPs	NFs
500	9.1 ± 0.2	9.6 ± 0.3	0.5390 ± 0.004	0.5405 ± 0.001
600	10.7 ± 0.5	14.0 ± 0.8	0.5394 ± 0.005	0.5405 ± 0.002
700	14.7 ± 1.0	16.9 ± 0.3	0.5433 ± 0.022	0.5350 ± 0.023
800	25.9 ± 2	34.6 ± 0.4	0.5386 ± 0.012	0.5345 ± 0.031

Table 4.2 Summary of crystallite size of CeO_2 and $Ce_{1-x}M_xO_2$ nanostructures calcined at 800 °C for 2 h in air.

Doping level	Crystallite size (nm)			
	Fe	Co	Cu	La
X = 0	26.1 ± 1.9	26.1 ± 1.9	26.1 ± 1.9	26.1 ± 1.9
X = 0.04	26.2 ± 2.8	45.8 ± 1.5	-	23.1 ± 2.4
X = 0.06	22.6 ± 3.0	41.1 ± 1.3	34.9 ± 3.0	23.5 ± 2.0
X = 0.08	25.9 ± 3.9	44.7 ± 1.3	30.4 ± 1.0	25.9 ± 2.0
X = 0.10	21.5 ± 3.4	42.4 ± 1.0	29.6 ± 2.3	21.5 ± 1.8

Table 4.3 Summary of lattice parameter (*a*) of CeO_2 and $Ce_{1-x}M_xO_2$ nanostructures calcined at 800 °C for 2 h in air.

Doping level	Lattice parameter (nm)			
	Fe	Co	Cu	La
X = 0	0.5390 ± 0.007	0.5390 ± 0.007	0.5390 ± 0.007	0.5390 ± 0.007
X = 0.04	0.5394 ± 0.009	0.5391 ± 0.009	-	0.5433 ± 0.004
X = 0.06	0.5388 ± 0.011	0.5406 ± 0.001	0.5426 ± 0.006	0.5443 ± 0.005
X = 0.08	0.5393 ± 0.005	0.5401 ± 0.003	0.5407 ± 0.007	0.5452 ± 0.006
X = 0.10	0.5390 ± 0.011	0.5384 ± 0.014	0.5402 ± 0.008	0.5457 ± 0.006

Table 4.4 Summary of crystallite size which lattice parameter of CeO_2 and $Ce_{1-x}Fe_xO_2$ nanostructures calcined at 800 °C for 2 h in air.

Doping level	Crystallite size (nm)		Lattice parameter (nm)	
	NPS	NFs	NPs	NFs
X=0	26.1±1.9	26.1±1.7	0.5390±0.007	0.5390±0.007
X=0.04	26.2±2.8	31.8±0.9	0.5394±0.009	0.5409±0.001
X=0.06	22.6±3.0	29.7±0.4	0.5388±0.011	0.5405±0.001
X=0.08	25.9±3.9	33.3±1.2	0.5393±0.005	0.5399±0.004
X=0.10	21.5±3.4	34.1±0.9	0.5390±0.011	0.5412±0.001

4.2.3 Specific surface area and pore size distribution

The specific surface area and pore size distribution were analyzed by nitrogen adsorption-desorption isotherms at 77 K. Nitrogen adsorption-desorption isotherms of both CeO_2 NPs and CeO_2 NFs samples correspond to the type II capillary condensation mode (see in Figure 4.23). The summary of BET specific surface areas (SBET), pore volume and diameter mesopore size (D_m) of CeO_2 NPs and CeO_2 NFs samples are shown in Table 4.5. The SBET value of CeO_2 NPs decreases when the calcination temperature increases due to the agglomeration of nanoparticles confirmed by the FESEM results.

The results show that SBET of CeO_2 NPs is higher than CeO_2 NFs. The specific surface area of CeO_2 NPs calcined at 500 °C (135.80 m^2 g^{-1}) prepared by simple solution method is higher than that of CeO_2 NFs 500 °C (73.51 m^2 g^{-1}) prepared by electrospinning method. These values are also higher than those found in the literature for CeO_2. Zheng et. al, (2017) have reported SBET values ranging from 27.2-42.7 m^2 g^{-1} of CeO_2 nanocrystalline synthesized by hydrothermal route assisted by polyvinyl pyrrolidone (Zheng et al., 2017).

CeO_2 NPs and NFs doped with Fe, Cu or La exhibit higher SBET values than undoped CeO_2 because of the replacement of the larger Ce^{4+} ions (0.092 nm) by the smaller Fe^{3+} ions or Fe^{2+} ions or Cu in the crystal lattice. $Ce_{0.90}Cu_{0.10}O_2$ NPs calcined at 500 °C show the highest SBET of 159.76 m^2 g^{-1}. This result indicates that doping causes the change in the CeO_2 structure, corresponding lattice parameter results. Doping metal makes the structure smaller. The pore structure as well as large specific surface area is beneficial for the access of dye molecules to CeO_2 intra-particles and to photodegradation the adsorbed dye pollutants under UV-visible light region, leading to the superior photocatalytic activity (Channei et al., 2014).

Table 4.5 Summary of BET specific surface areas (SBET), pore volumes and diameter mesopore sizes (D_m) of CeO_2 NPs and $Ce_{1-x}M_xO_2$ NPs calcined at 500-800 °C for 2 h in air.

Samples	Temperature (°C)	SBET (m^2g^{-1})	Pore volume (cm^3g^{-1})	D_m (nm)
CeO_2 NPs	500	135.80	0.28	6.56
CeO_2 NPs	600	86.45	0.26	6.56
CeO_2 NPs	700	52.97	0.26	16.12
CeO_2 NPs	800	21.32	0.052	6.56
$Ce_{0.90}Co_{0.10}O_2$ NPs	600	70.22	0.23	3.28
$Ce_{0.90}Co_{0.10}O_2$ NPs	700	34.18	0.15	2.43
$Ce_{0.90}Co_{0.10}O_2$ NPs	800	11.27	0.058	2.43
$Ce_{0.90}Cu_{0.10}O_2$ NPs	500	159.76	0.19	2.43
$Ce_{0.90}Cu_{0.10}O_2$ NPs	600	129.79	0.17	3.28
$Ce_{0.90}Cu_{0.10}O_2$ NPs	700	72.76	0.16	3.28
$Ce_{0.90}Cu_{0.10}O_2$ NPs	800	11.69	0.046	3.28
$Ce_{0.92}La_{0.08}O_2$ NPs	700	68.33	0.29	7.05
$Ce_{0.92}La_{0.08}O_2$ NPs	800	33.23	0.27	3.78
$Ce_{0.90}La_{0.10}O_2$ NPs	800	45.15	0.15	2.43

Table 4.6 Summary of BET specific surface areas (SBET), pore volumes and diameter mesopore sizes (D_m) of CeO_2 NFs and $Ce_{1-x}M_xO_2$ NFs calcined at 500-800 °C for 2 h in air.

Samples	Temperature (°C)	SBET ($m^2\ g^{-1}$)	Pore volume ($cm^3\ g^{-1}$)	D_m (nm)
CeO_2 NFs	500	73.51	0.27	3.28
CeO_2 NFs	600	60.26	0.26	3.28
CeO_2 NFs	700	62.32	0.22	3.28
CeO_2 NFs	800	50.32	0.18	3.28
$Ce_{0.90}Fe_{0.10}O_2$ NFs	500	110.32	0.23	2.42
$Ce_{0.90}Fe_{0.10}O_2$ NFs	600	69.46	0.21	3.28
$Ce_{0.90}Fe_{0.10}O_2$ NFs	700	48.15	0.17	3.28
$Ce_{0.90}Fe_{0.10}O_2$ NFs	800	29.42	0.072	3.28
$Ce_{0.90}Cu_{0.10}O_2$ NFs	500	67.26	0.21	3.28
$Ce_{0.90}Cu_{0.10}O_2$ NFs	600	47.63	0.19	3.28
$Ce_{0.90}Cu_{0.10}O_2$ NFs	700	38.15	0.17	3.28
$Ce_{0.90}Cu_{0.10}O_2$ NFs	800	31.20	0.072	6.28
$Ce_{0.90}La_{0.10}O_2$ NFs	500	81.27	0.20	2.43
$Ce_{0.92}La_{0.08}O_2$ NFs	700	33.43	0.12	2.43

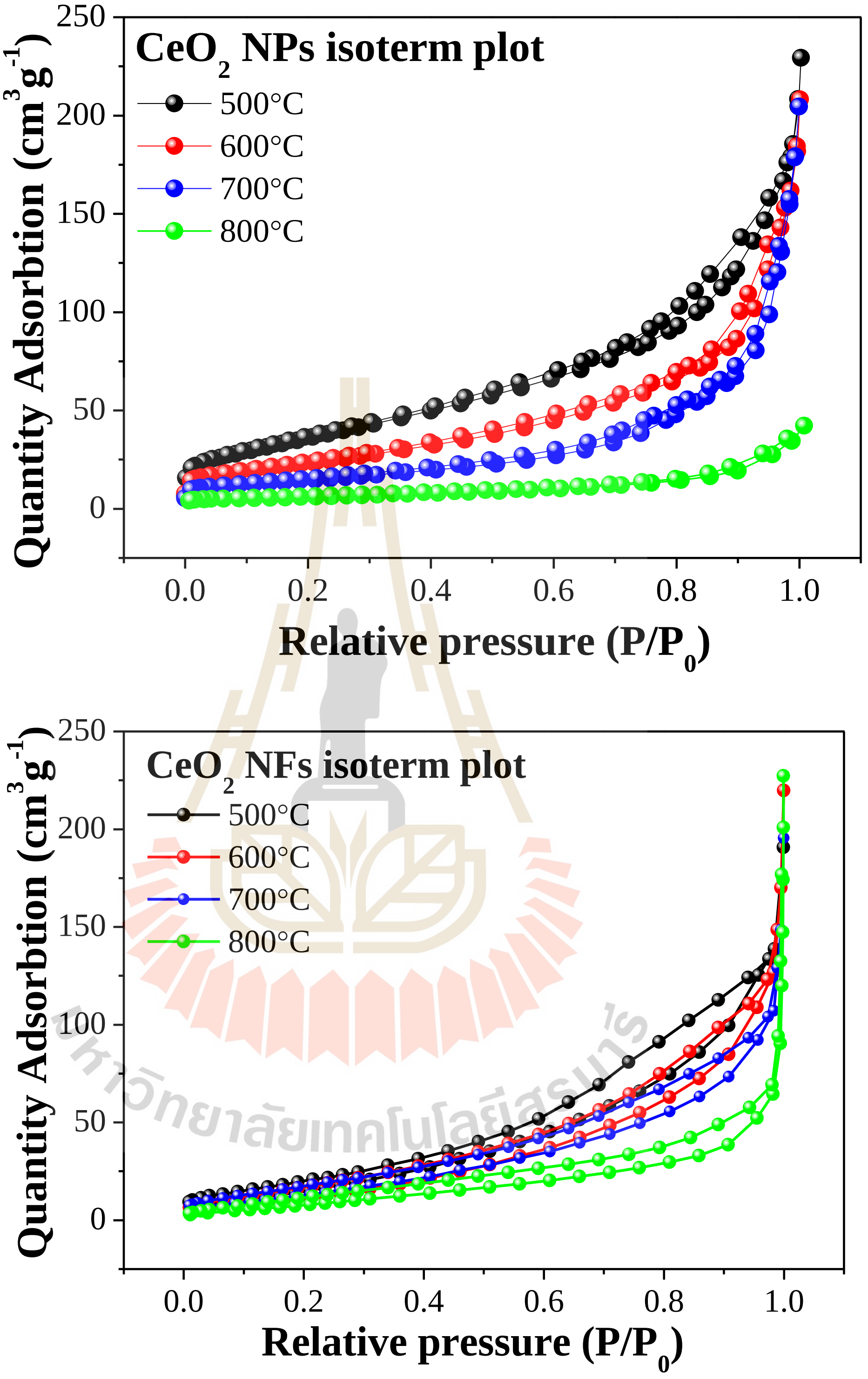

Figure 4.23 N_2 adsorption-desorption isotherms of CeO_2 NPs and CeO_2 NFs.

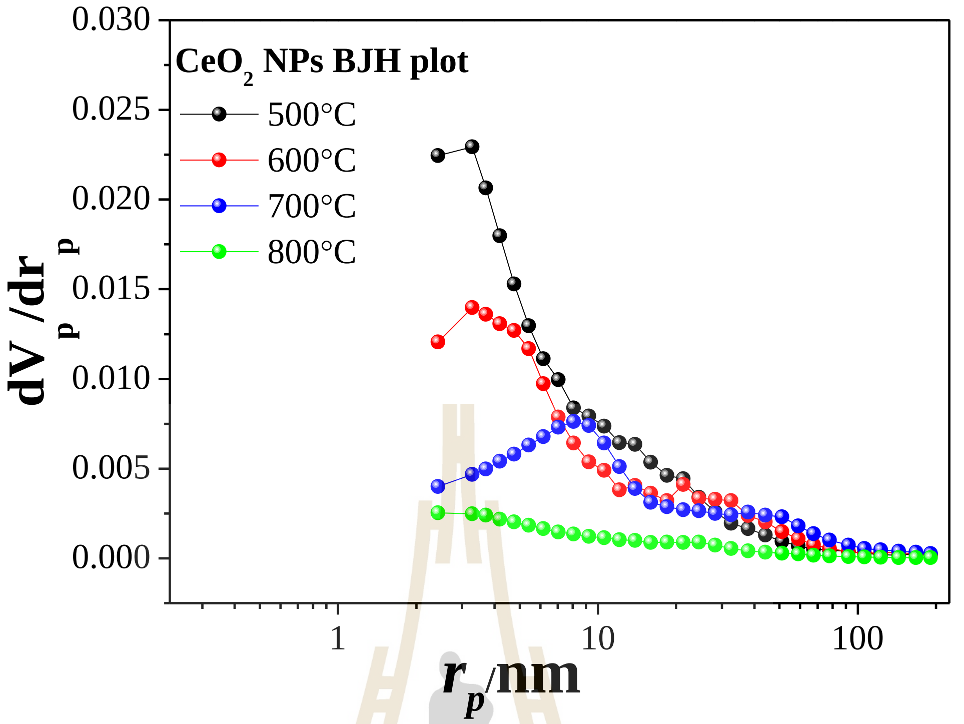

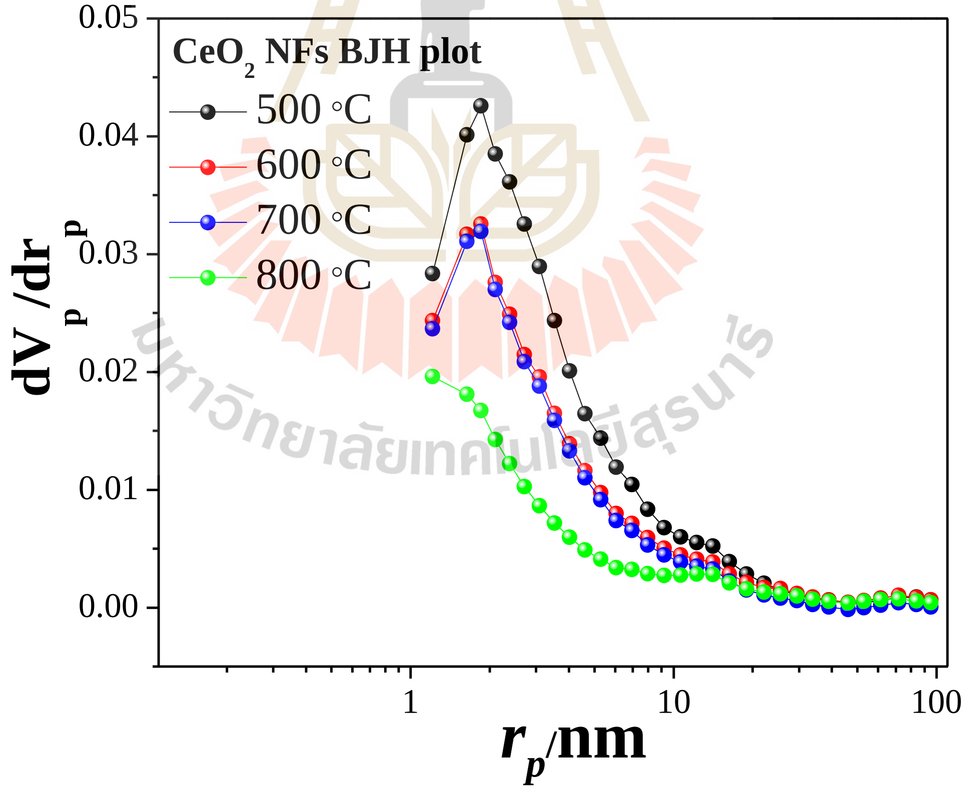

Figure 4.24 Pore size distribution curves of CeO_2 NPs and CeO_2 NFs.

4.2.4 Chemical composition and chemical state

The chemical compositions and oxidation states were studied by XPS, FTIR and XAS. XPS survey spectra of as-spun CeO_2, CeO_2 and metal doped-CeO_2 are shown in Figure 4.25-4.26. Figure 4.25 shows main binding energy peaks indicating the presence of C, N, O, Ce observed at approximately 284.8, 400.5, 530.7, 880 in as-spun CeO_2. The result indicate that as-spun CeO_2 still have polymer (PVP) and nitrate in sample. However, the intensity of C, O decrease and nitrate signal is not observed in the XPS survey spectra of prepared CeO_2 NPs and NFs. This result indicates that the polymer was burnt out after calcination, leaving small amount of C, O in the samples which is consistent with the TGA/DSC results.

Additional main binding energy peaks attributing to Fe, Co, La and Cu were observed for $Ce_{1-x}Fe_xO_2$, $Ce_{1-x}Co_xO_2$, $Ce_{1-x}La_xO_2$ and $Ce_{1-x}Cu_xO_2$, respectively. This result confirms the chemical compositions of the synthesized nanostructures.

The high resolution XPS spectra of Ce *3d* peaks of CeO_2 NPs and NFs are shown in Figure 4.27-4.28. The Ce3d peaks of both CeO_2 NPs and NFs can be fitted with 5 sets of spin-orbit split doublets of Ce *3d* ($3d_{5/2}$ and $3d_{3/2}$) with a Gaussian-Lorentzian peak shape after the subtraction of a Shirley-type background. The three final states of Ce^{4+}, containing Ce $3d^9$ $4f^0$ O $2p^6$, Ce $3d^9$ $4f^1$ O $2p^5$, and Ce $3d^9$ $4f^2$ O $2p^4$, are expressed as $U^{///}$, $U^{//}$, U (for $Ce3d_{3/2}$), $V^{///}$, $V^{//}$ and V (for $Ce3d_{5/2}$) respectively. Two final states of Ce^{3+} containing $3d^9$ $4f^1$ O $2p^6$ and Ce $3d^9$ $4f^1$ O $2p^5$, are expressed as $U^{/}$, U_0 (for $Ce3d_{3/2}$) $V^{/}$ and V_0 (for $Ce3d_{5/2}$) (Sonsupap et al., 2016). These peaks are observed in all samples with the minor variation in the positions in accordance to those reported previously (Li and Xia, 2004). This result indicates that both Ce^{4+} and Ce^{3+} are present in the samples the detailed information can be found in the Table 4.7-4.14. The percent concentration of Ce^{4+} and Ce^{3+} ions can be calculated from the ratio of the sum of the integrated areas of the XPS 3d peaks related to Ce^{4+} and Ce^{3+} to the total integral area for the whole Ce *3d* region integrated areas of the XPS 3d peaks related to Ce^{4+} to the total integral area for the whole Ce *3d* region. (see in the result reveals that Ce^{3+} content in CeO_2 NPs are higher than CeO_2 NFs.

The XPS spectra of Ce3d peak of CeO_2 metal doped with Fe, Cu or La, also indicate that both Ce^{4+} and Ce^{3+} are present in the samples as shown in Figure 4.29. The variation of the peak-shape in the different calcination temperatures is observed, indicating that there is a transition between Ce^{4+} and Ce^{3+}. This transition from Ce^{4+} to Ce^{3+} lead to the introduction of oxygen vacancies to the lattice and plays an important role on magnetism in Fe-doped CeO_2 nanostructures (Phokha et al., 2013, Wang et al., 2015).

The XPS spectra in the Fe *2p*, Co *2p*, La *3d*, and Cu *2p* regions of Fe, Co, Cu or La-doped CeO_2 NPs are shown in Figure 4.30-4.31. The spectra show the presences of Fe^{2+} ($2p_{1/2}$ BE = 722.5 eV, $2p_{1/2}$ BE = 714.7 eV) and Fe^{3+} ($2p_{1/2}$ BE = 724.5 eV, $2p_{1/2}$ BE = 711.1 eV) states in $Ce_{0.90}Fe_{0.10}O_2$, Co^{2+} ($2p_{3/2}$ BE = 779.7 eV) states in $Ce_{0.90}Co_{0.10}O_2$, Cu^{2+} ($2p_{3/2}$ BE = 933.4 eV, $2p_{1/2}$ BE = 952.55 eV, ΔE = 19.2 eV) states in $Ce_{0.90}Cu_{0.10}O_2$, and La^{3+} ($2p_{5/2}$ BE = 833.3 eV, 837.81 eV, ΔE = 4.4 eV) state in the, , $Ce_{0.90}La_{0.10}O_2$.

The XPS spectra in the Fe *2p* region of the $Ce_{1-x}Fe_xO_2$ where $0 \leq x \leq 10$ NPs are also shown in Figure 4.31. The spectra show the mixture of Fe^{2+} ($2p_{3/2}$) and Fe^{3+} ($2p_{3/2}$) states in all the samples calcined at 800 °C (Yamashita and Hayes, 2008). Moreover, the samples calcined at 800 °C also show a clear evidence of Fe_3O_4 phases (Lin, Seshadri and Kelber, 1997). We believed that this is a mean of magnetic properties observed in the samples.

The XPS spectra of O1s region of CeO_2 and $Ce_{1-x}M_xO_2$ nanostructures are shown in Figure 4.32-4.36. The O1s peaks of all samples can be deconvoluted into three peaks at approximately ~528.8 eV, ~531.1 eV, and ~533.2 eV. The binding energy at ~528.8 eV (OI) is corresponded to O^{2-} ions on the cubic structure. The binding energy at ~531.1 eV (OII) can be attributed to O^{2-} ions in the oxygen deficient regions, indicating the presence of the oxygen vacancies in matrix of CeO_2 nanostructures. The binding energy at ~532.2 eV (OIII) can be assigned to the bound oxygen, such as hydroxyl group on the surface (Caglar and Yakuphanoglu, 2012). The observation of V_o in the O *1s* XPS spectra supports the results obtained from the Ce *3d* XPS spectra because Ce^{3+} can be created V_o in structure. This observed V_o is the origin of magnetism in samples. However, the evidence of V_o was not observed in the O1s peak of $Ce_{0.90}Cu_{0.10}O_2$

This is possibly because of the surface sensitivity of XPS. It can measure to the depth of only 10 nm from the surface of the sample. The XPS technique is also unsuitable to compare the amount of oxygen in each sample. This is a reason that the measured V_o from the surface of the nanosphere is still unclear. The amount of V_o detected by XPS technique may not be the V_o of all oxygen vacancies in the nanosphere. We believed that this is a mean of magnetic properties observed in the samples.

Table 4.7 Peak position, full width at half maximum (FWHM), and integrated peak area of the deconvolution of Ce *3d* ($3d_{5/2}$ and $3d_{3/2}$) peaks of CeO_2 NPs calcined at 500 °C and the percentage of Ce^{4+} and Ce^{3+} cations.

Peak assignment	Origin of Cerium contribution	Reference peak position from CeO_2 and Ce_2O_3 samples	Peak decomposition		
			Peak	FWHM	Area
V_0	Ce^{3+}	880.50	880.2	2.30	1477
V	Ce^{4+}	882.10	882.24	2.73	5706
$V^{/}$	Ce^{3+}	884.90	884.77	2.80	3346
$V^{//}$	Ce^{4+}	888.60	887.87	5.10	6285
U	Ce^{4+}	898.00	897.59	2.30	3909
$V^{///}$	Ce^{3+}	898.90	899.29	2.50	1836
U_0	Ce^{4+}	900.50	900.14	2.73	4039
$U^{/}$	Ce^{3+}	903.30	902.73	3.57	4054
$U^{//}$	Ce^{4+}	907.00	906.93	4.90	4457
$U^{///}$	Ce^{4+}	916.30	916.32	3.00	4585
Ce^{4+} %					**73.01**
Ce^{3+} %					**26.99**

Table 4.8 Peak position, full width at half maximum (FWHM), and integrated peak area of the deconvolution of Ce *3d* ($3d_{5/2}$ and $3d_{3/2}$) peaks of CeO_2 NPs calcined at 600 °C and the percentage of Ce^{4+} and Ce^{3+} cations.

Peak assignment	Origin of Cerium contribution	Reference peak position from CeO_2 and Ce_2O_3 samples	Peak decomposition		
			Peak	FWHM	Area
V_0	Ce^{3+}	880.50	880.20	2.30	1311
V	Ce^{4+}	882.10	882.24	2.05	4145
$V^{/}$	Ce^{3+}	884.90	884.82	2.45	2322
$V^{//}$	Ce^{4+}	888.60	887.87	5.10	5166
U	Ce^{4+}	898.00	897.93	2.30	5178
$V^{///}$	Ce^{3+}	898.90	899.80	2.50	918
U_0	Ce^{4+}	900.50	900.82	1.70	2902
$U^{/}$	Ce^{3+}	903.30	903.20	3.57	2606
$U^{//}$	Ce^{4+}	907.00	907.38	4.90	3804
$U^{///}$	Ce^{4+}	916.30	916.46	2.29	3625
Ce^{4+} %					**77.62**
Ce^{3+} %					**22.38**

Table 4.9 Peak position, full width at half maximum (FWHM), and integrated peak area of the deconvolution of Ce *3d* ($3d_{5/2}$ and $3d_{3/2}$) peaks of CeO_2 NPs calcined at 700 °C and the percentage of Ce^{4+} and Ce^{3+} cations.

Peak assignment	Origin of Cerium contribution	Reference peak position from CeO_2 and Ce_2O_3 samples	Peak decomposition		
			Peak	FWHM	Area
V_0	Ce^{3+}	880.50	880.20	2.30	3836
V	Ce^{4+}	882.10	882.59	2.05	8903
$V^{/}$	Ce^{3+}	884.90	885.07	2.51	5921
$V^{//}$	Ce^{4+}	888.60	888.38	5.10	10788
U	Ce^{4+}	898.00	898.10	2.30	10353
$V^{///}$	Ce^{3+}	898.90	899.80	2.50	2685
U_0	Ce^{4+}	900.50	900.99	2.20	6232
$U^{/}$	Ce^{3+}	903.30	903.38	3.75	5981
$U^{//}$	Ce^{4+}	907.00	907.30	4.90	7448
$U^{///}$	Ce^{4+}	916.30	916.37	2.78	7247
Ce^{4+} %					**73.45**
Ce^{3+} %					**26.55**

Table 4.10 Peak position, full width at half maximum (FWHM), and integrated peak area of the deconvolution of Ce *3d* ($3d_{5/2}$ and $3d_{3/2}$) peaks of CeO_2 NPs calcined at 800 °C and the percentage of Ce^{4+} and Ce^{3+} cations.

Peak assignment	Origin of Cerium contribution	Reference peak position from CeO_2 and Ce_2O_3 samples	Peak decomposition		
			Peak	FWHM	Area
V_0	Ce^{3+}	880.50	880.54	2.3	4570
V	Ce^{4+}	882.10	881.90	2.05	6969
$V^{/}$	Ce^{3+}	884.90	884.18	2.76	5389
$V^{//}$	Ce^{4+}	888.60	887.87	5.1	10099
U	Ce^{4+}	898.00	897.24	2.3	9964
$V^{///}$	Ce^{3+}	898.90	898.95	2.5	3199
U_0	Ce^{4+}	900.50	900.40	2.06	4878
$U^{/}$	Ce^{3+}	903.30	902.52	3.75	5691
$U^{//}$	Ce^{4+}	907.00	906.79	4.9	7274
$U^{///}$	Ce^{4+}	916.30	915.83	2.44	6975
Ce^{4+} %					**71.01**
Ce^{3+} %					**28.99**

Table 4.11 Peak position, full width at half maximum (FWHM), and integrated peak area of the deconvolution of Ce *3d* ($3d_{5/2}$ and $3d_{3/2}$) peaks of CeO_2 NFs calcined at 500 °C and the percentage of Ce^{4+} and Ce^{3+} cations.

Peak assignment	Origin of Cerium contribution	Reference peak position from CeO_2 and Ce_2O_3 samples	Peak decomposition		
			Peak	FWHM	Area
V_0	Ce^{3+}	880.50	880.20	2.30	1660
V	Ce^{4+}	882.10	882.24	2.73	17155
$V^{/}$	Ce^{3+}	884.90	884.66	1.80	2584
$V^{//}$	Ce^{4+}	888.60	887.87	5.10	18421
U	Ce^{4+}	898.00	897.59	2.30	15025
$V^{///}$	Ce^{3+}	898.90	899.29	2.50	1162
U_0	Ce^{4+}	900.50	900.11	2.63	12009
$U^{/}$	Ce^{3+}	903.30	902.77	3.57	8035
$U^{//}$	Ce^{4+}	907.00	907.19	4.77	12278
$U^{///}$	Ce^{4+}	916.30	916.1	3.00	13742
Ce^{4+} %					**86.83**
Ce^{3+} %					**13.17**

Table 4.12 Peak position, full width at half maximum (FWHM), and integrated peak area of the deconvolution of Ce *3d* ($3d_{5/2}$ and $3d_{3/2}$) peaks of CeO_2 NFs calcined at 600 °C and the percentage of Ce^{4+} and Ce^{3+} cations.

Peak assignment	Origin of Cerium contribution	Reference peak position from CeO_2 and Ce_2O_3 samples	Peak decomposition		
			Peak	FWHM	Area
V_0	Ce^{3+}	880.50	881.60	2.40	2851
V	Ce^{4+}	882.10	882.81	2.3	11653
$V^{/}$	Ce^{3+}	884.90	884.73	3.2	6651
$V^{//}$	Ce^{4+}	888.60	889.29	5.1	12924
U	Ce^{4+}	898.00	898.32	2.3	12543
$V^{///}$	Ce^{3+}	898.90	899.35	2.5	1996
U_0	Ce^{4+}	900.50	900.88	2.39	8157
$U^{/}$	Ce^{3+}	903.30	902.95	3.34	6271
$U^{//}$	Ce^{4+}	907.00	907.70	4.9	10734
$U^{///}$	Ce^{4+}	916.30	917.07	3.37	12856
Ce^{4+} %					**79.49**
Ce^{3+} %					**20.51**

Table 4.13 Peak position, full width at half maximum (FWHM), and integrated peak area of the deconvolution of Ce *3d* ($3d_{5/2}$ and $3d_{3/2}$) peaks of CeO_2 NFs calcined at 700 °C and the percentage of Ce^{4+} and Ce^{3+} cations.

Peak assignment	Origin of Cerium contribution	Reference peak position from CeO_2 and Ce_2O_3 samples	Peak decomposition		
			Peak	FWHM	Area
V_0	Ce^{3+}	880.50	881.11	2.2	2954
V	Ce^{4+}	882.10	882.98	2.5	7958
$V^{/}$	Ce^{3+}	884.90	885.54	3.2	3287
$V^{//}$	Ce^{4+}	888.60	888.95	4.9	8629
U	Ce^{4+}	898.00	898.49	2.3	7087
$V^{///}$	Ce^{3+}	898.90	899.35	2.3	2068
U_0	Ce^{4+}	900.50	901.05	2.2	5571
$U^{/}$	Ce^{3+}	903.30	906.37	3.34	5053
$U^{//}$	Ce^{4+}	907.00	908.93	4.09	3509
$U^{///}$	Ce^{4+}	916.30	917.00	2.9	7941
Ce^{4+} %					**75.28**
Ce^{3+} %					**24.72**

Table 4.14 Peak position, full width at half maximum (FWHM), and integrated peak area of the deconvolution of Ce *3d* ($3d_{5/2}$ and $3d_{3/2}$) peaks of CeO_2 NFs calcined at 800 °C and the percentage of Ce^{4+} and Ce^{3+} cations.

Peak assignment	Origin of Cerium contribution	Reference peak position from CeO_2 and Ce_2O_3 samples	Peak decomposition		
			Peak	FWHM	Area
V_0	Ce^{3+}	880.50	881.62	2.30	1915
V	Ce^{4+}	882.10	882.81	2.73	11000
$V^{/}$	Ce^{3+}	884.90	885.20	3.20	5233
$V^{//}$	Ce^{4+}	888.60	889.29	5.10	12095
U	Ce^{4+}	898.00	898.32	2.30	12371
$V^{///}$	Ce^{3+}	898.90	899.29	2.50	1341
U_0	Ce^{4+}	900.50	900.88	2.20	7700
$U^{/}$	Ce^{3+}	903.30	902.70	2.90	4974
$U^{//}$	Ce^{4+}	907.00	907.70	4.90	15060
$U^{///}$	Ce^{4+}	916.30	916.64	3.00	12156
Ce^{4+} %					**83.94**
Ce^{3+} %					**16.06**

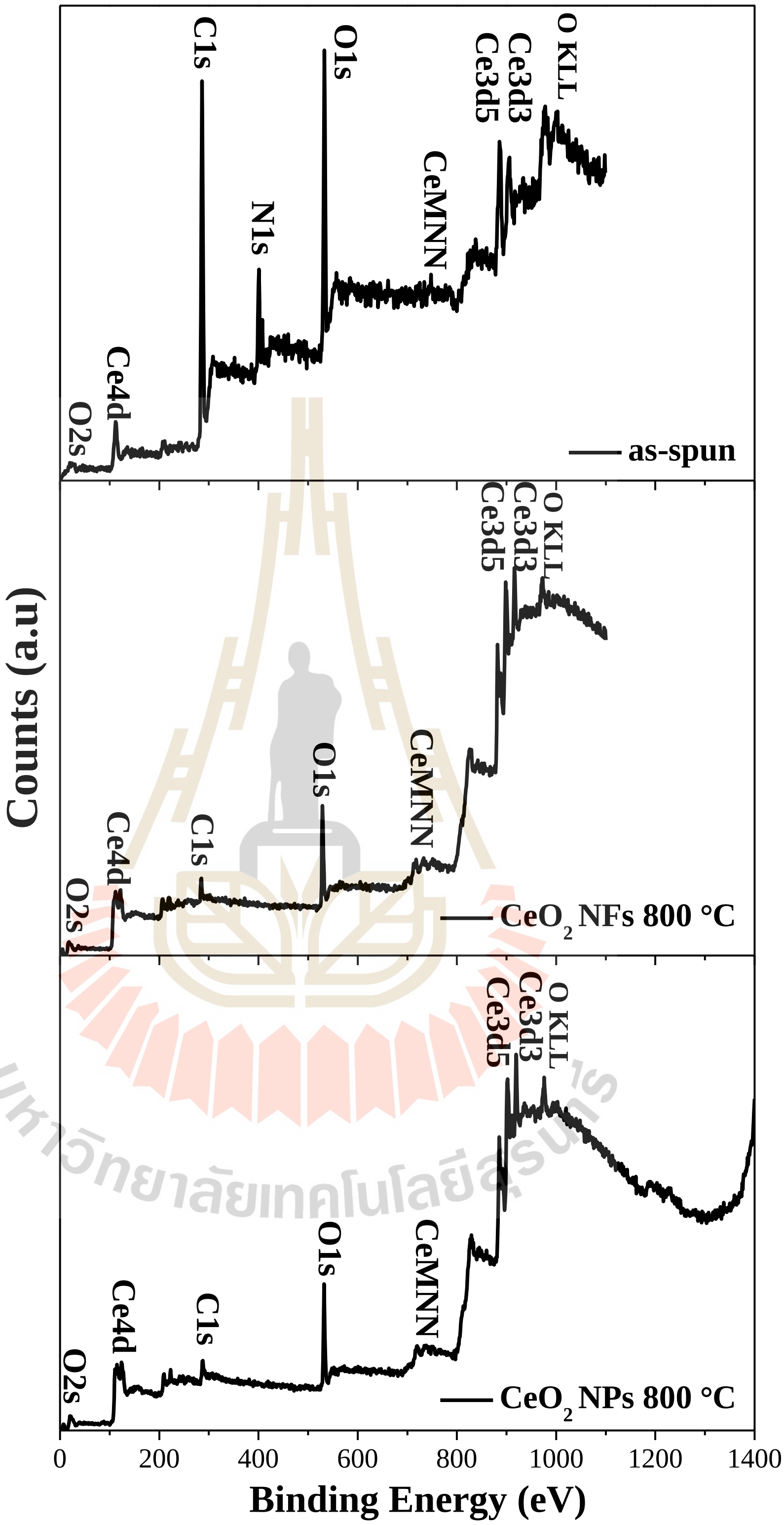

Figure 4.25 XPS spectra of as-spun, CeO_2 NPs and CeO_2 NFs calcined at 800 °C with the survey scan mode.

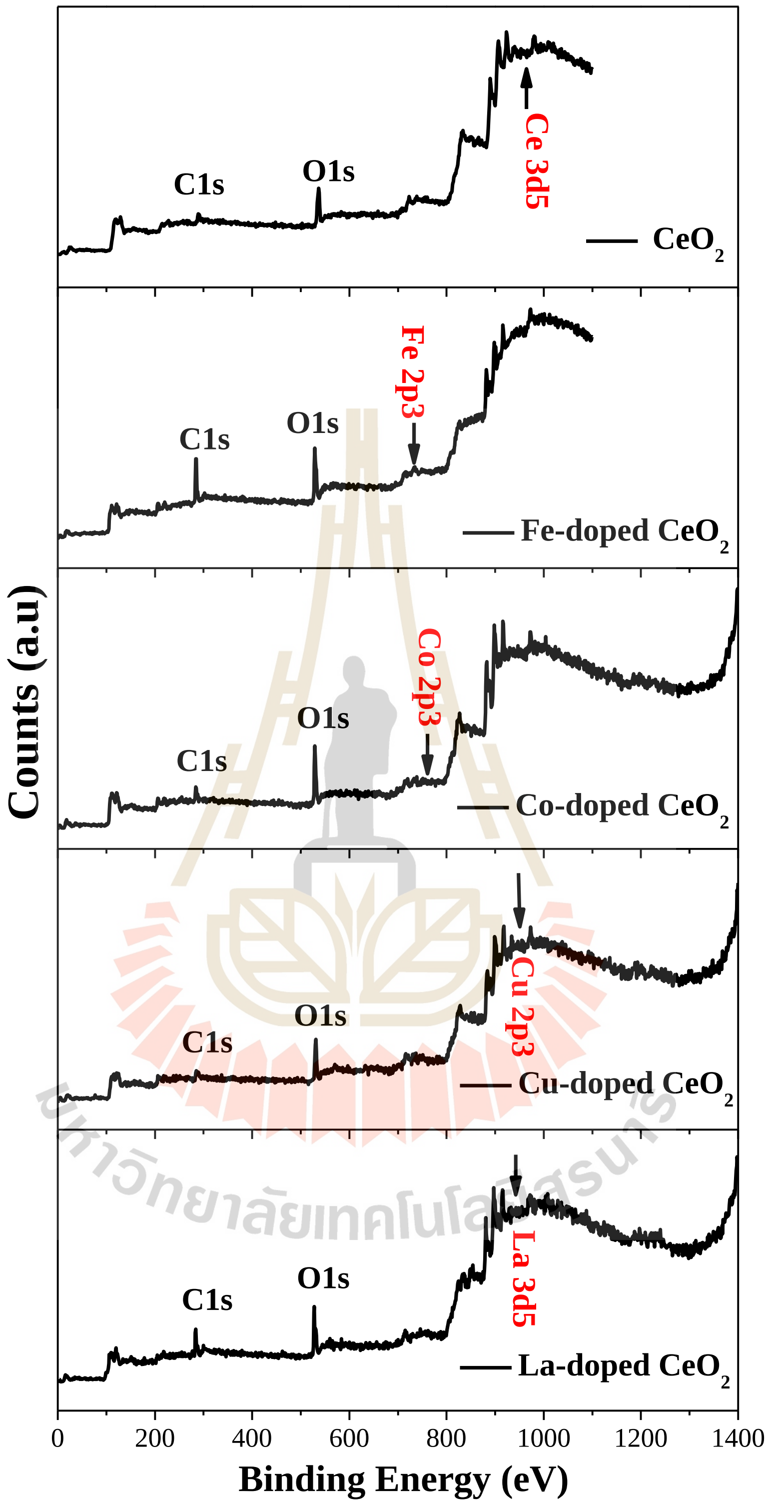

Figure 4.26 XPS spectra of as-spun, CeO$_2$ NPs and doped-CeO$_2$ NPs calcined at 800 °C with the survey scan mode.

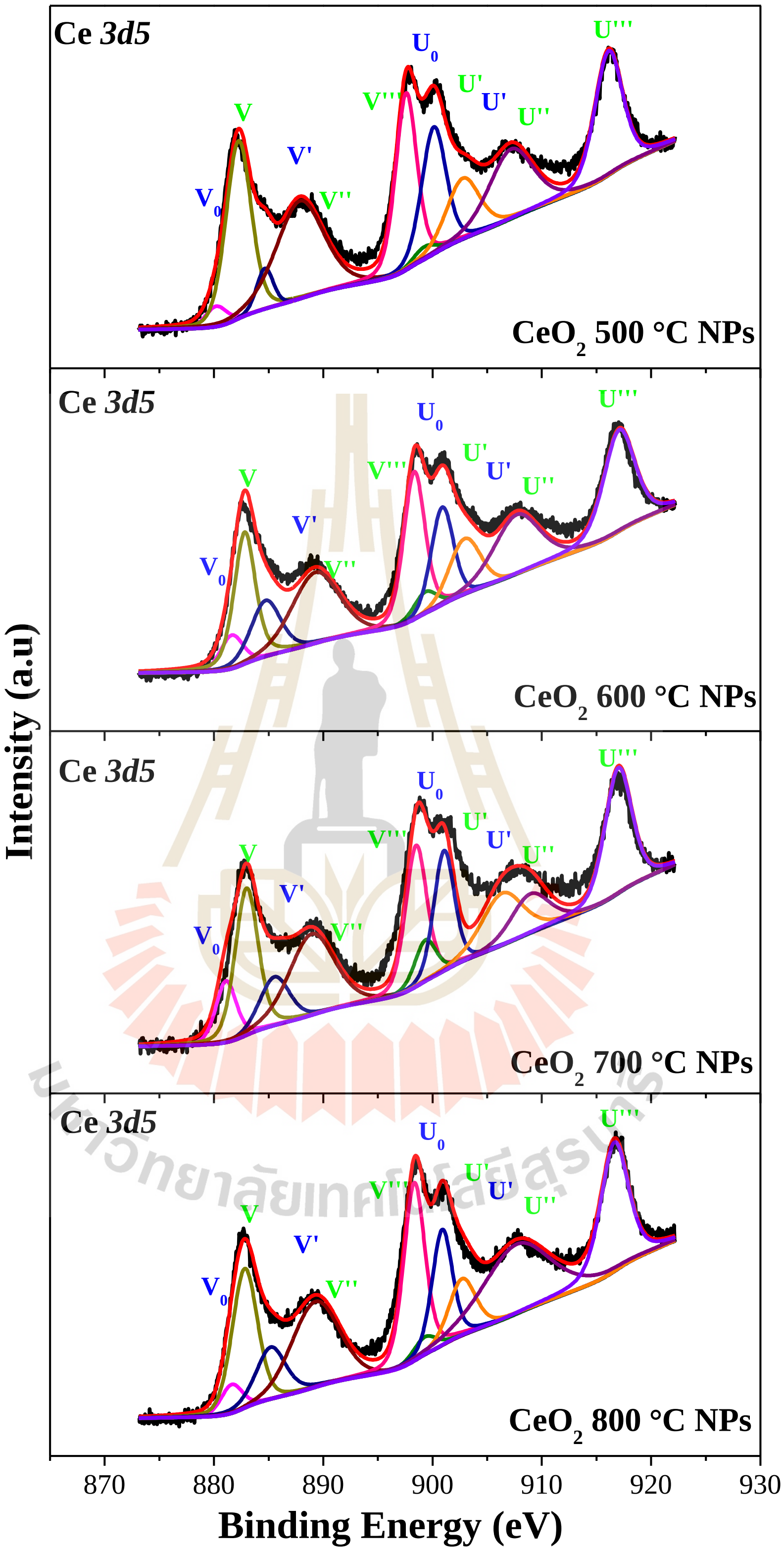

Figure 4.27 Curve-fitting for Ce 3d XPS spectrum of CeO_2 NPs.

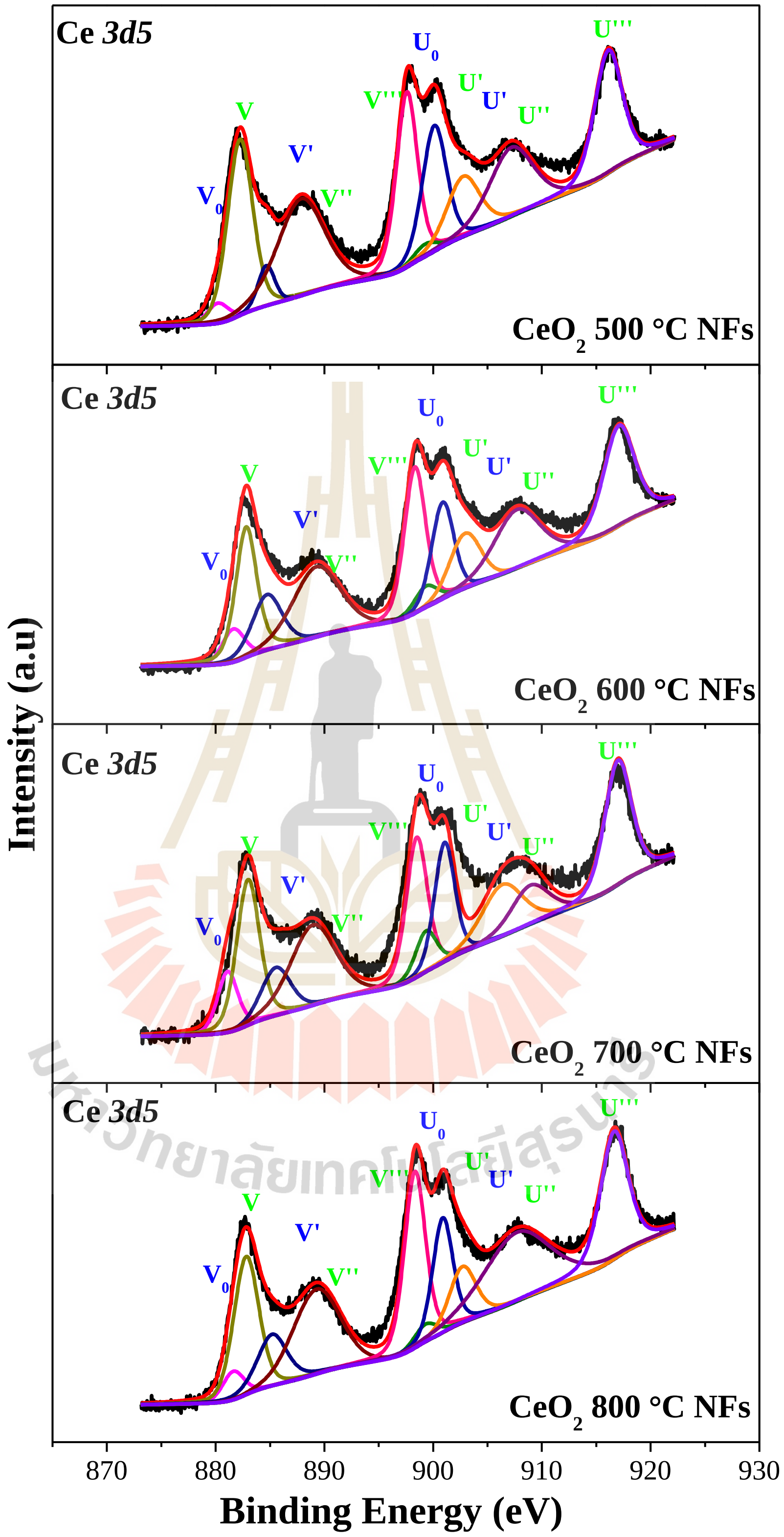

Figure 4.28 Curve-fitting for Ce 3d XPS spectrum of CeO_2 NFs.

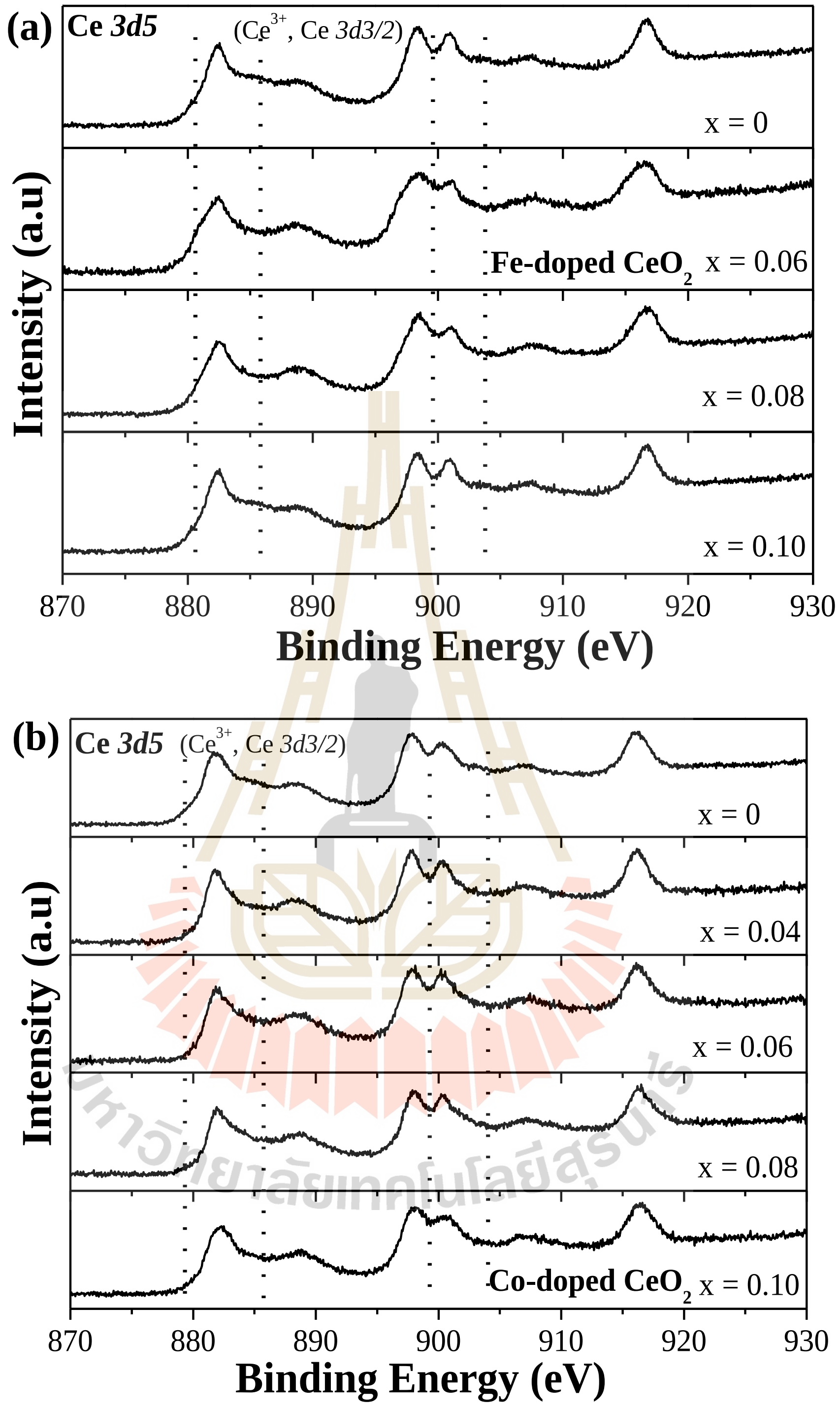

Figure 4.29 XPS integral spectra of $Ce_{1-x}M_xO_2$ samples (a) Ce *3d* of $Ce_{0.90}Fe_{0.10}O_2$ and (b) $Ce_{0.90}Co_{0.10}O_2$ sample.

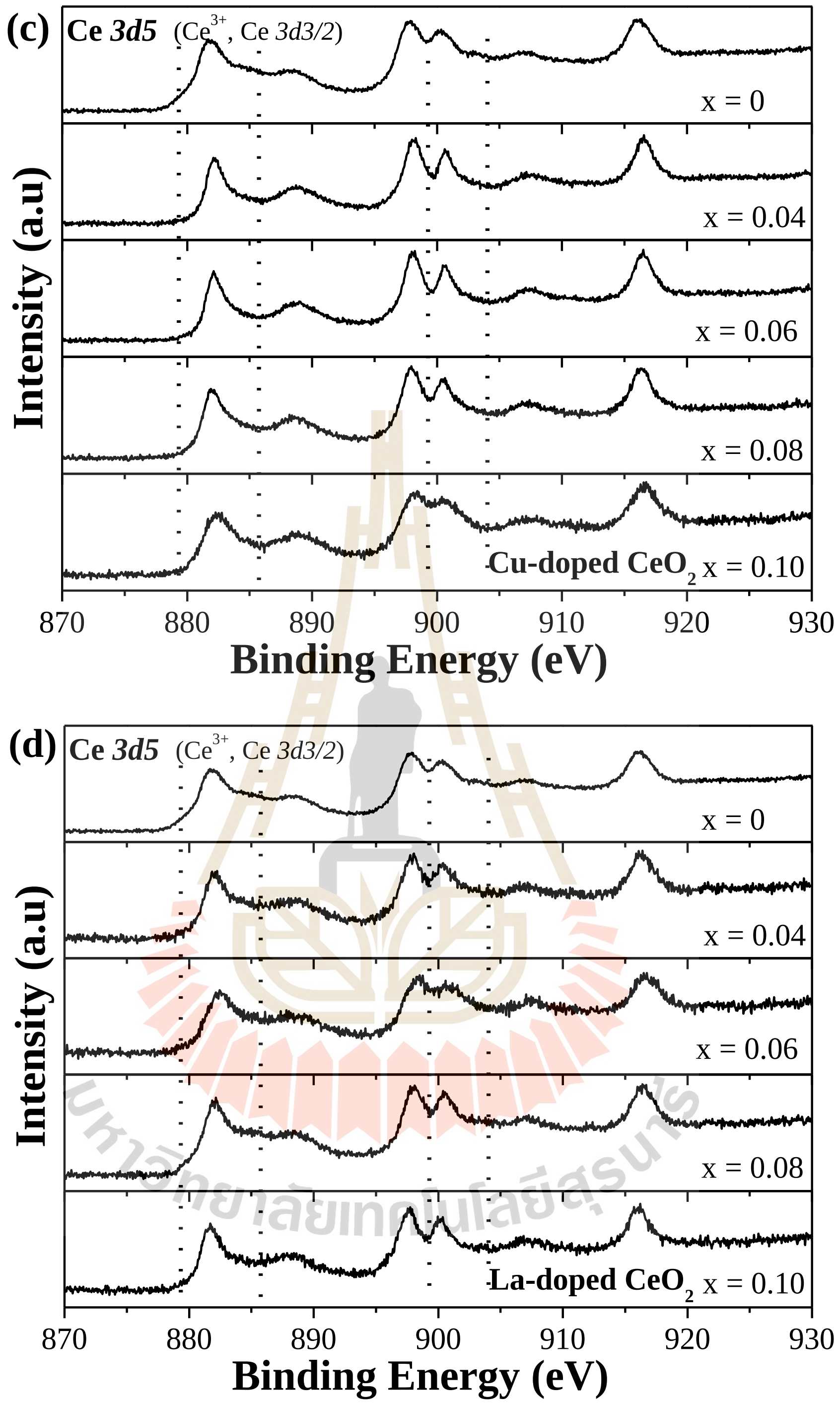

Figure 4.29 XPS integral spectra of $Ce_{1-x}M_xO_2$ samples (c) $Ce_{0.90}Cu_{0.10}O_2$ and (d) $Ce_{0.90}La_{0.10}O_2$ sample.

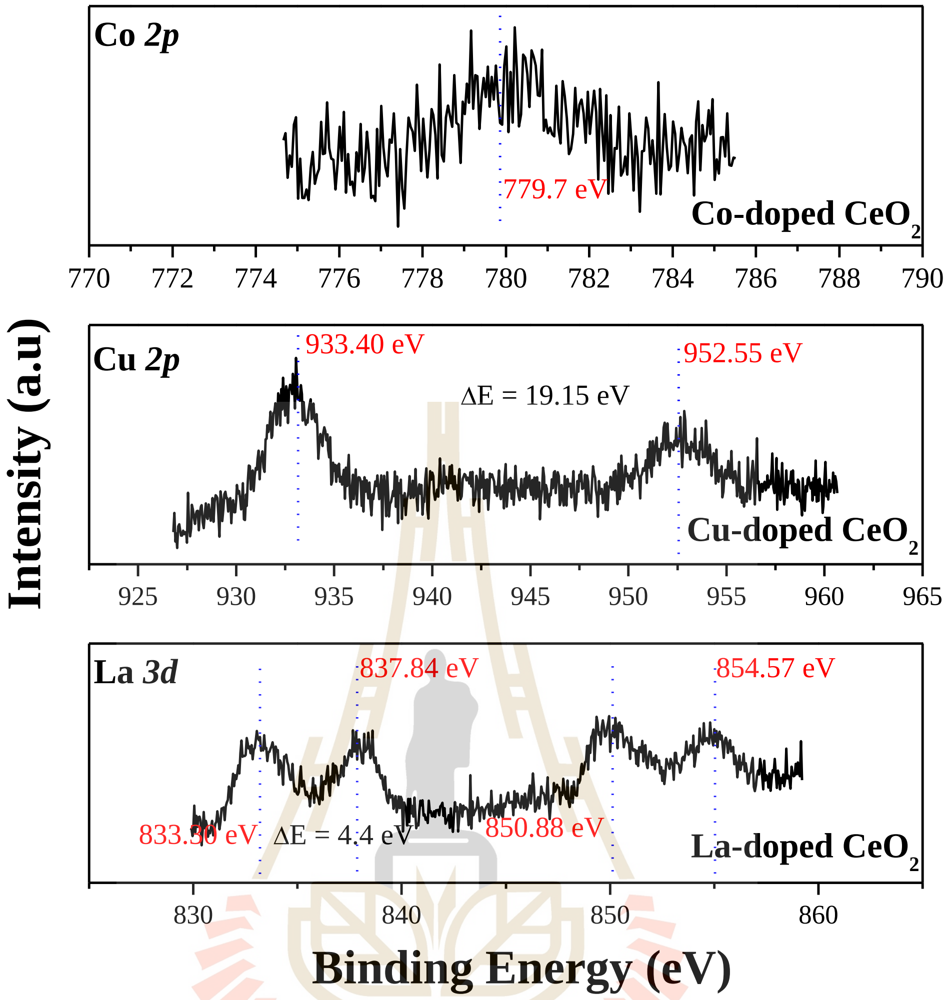

Figure 4.30 XPS integral spectra of samples (a) Co *2p* (b) Cu *2p* and (c) La *3d* of $Ce_{0.90}Co_{0.10}O_2$, $Ce_{0.90}Cu_{0.10}O_2$ and $Ce_{0.90}La_{0.10}O_2$, respectively.

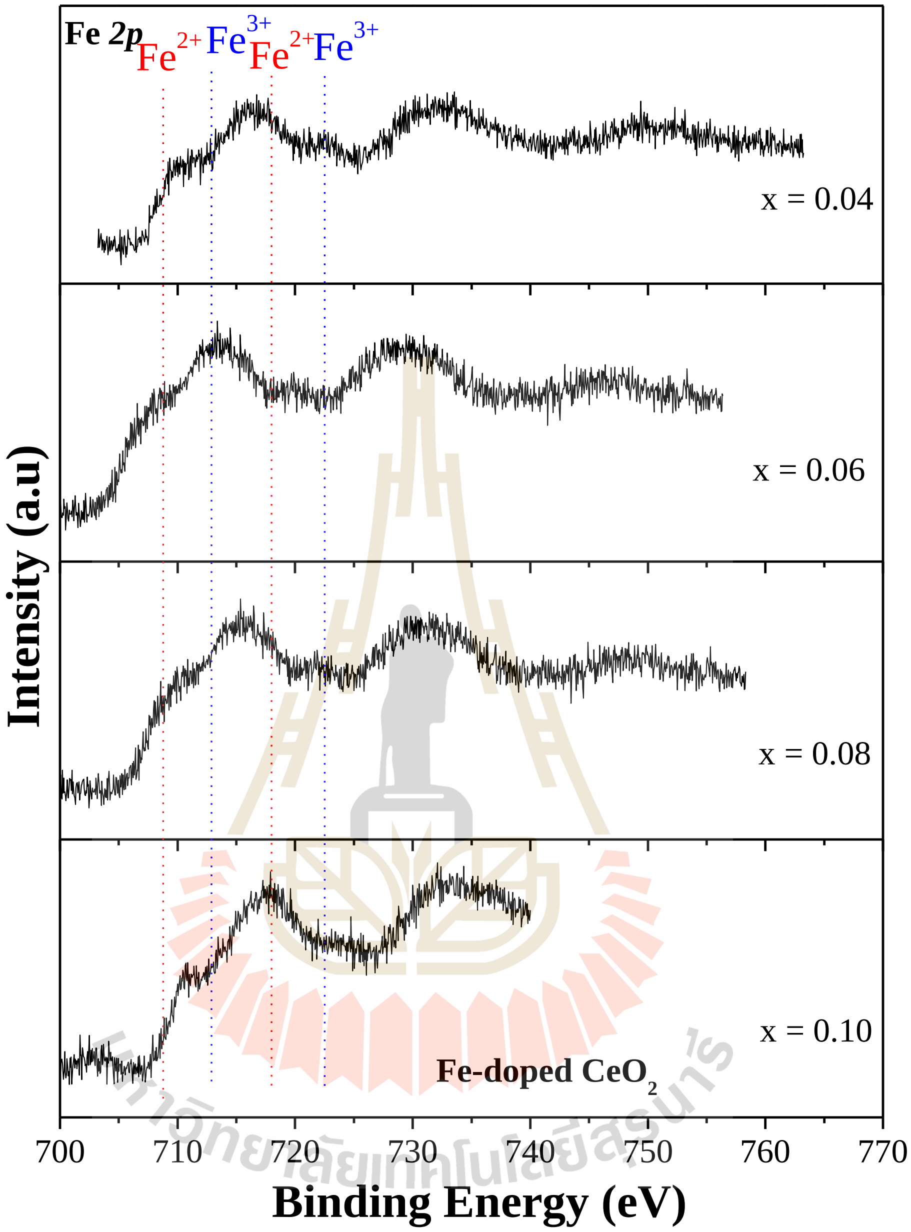

Figure 4.31 Fe 2p XPS of $Ce_{1-x}Fe_xO_2$ samples.

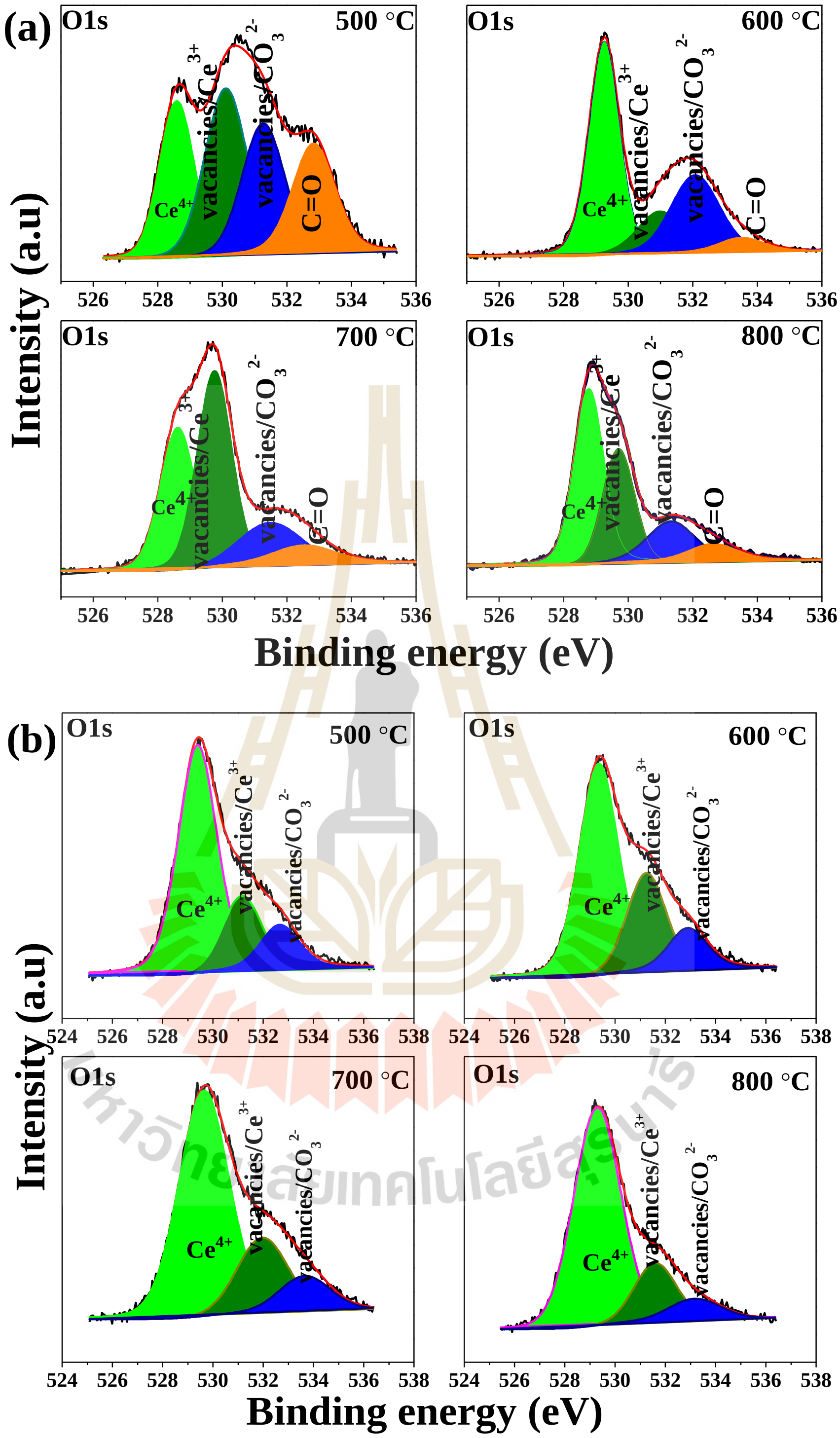

Figure 4.32 XPS integral O *1s* spectra of (a) CeO$_2$ NPs (b) CeO$_2$ NFs.

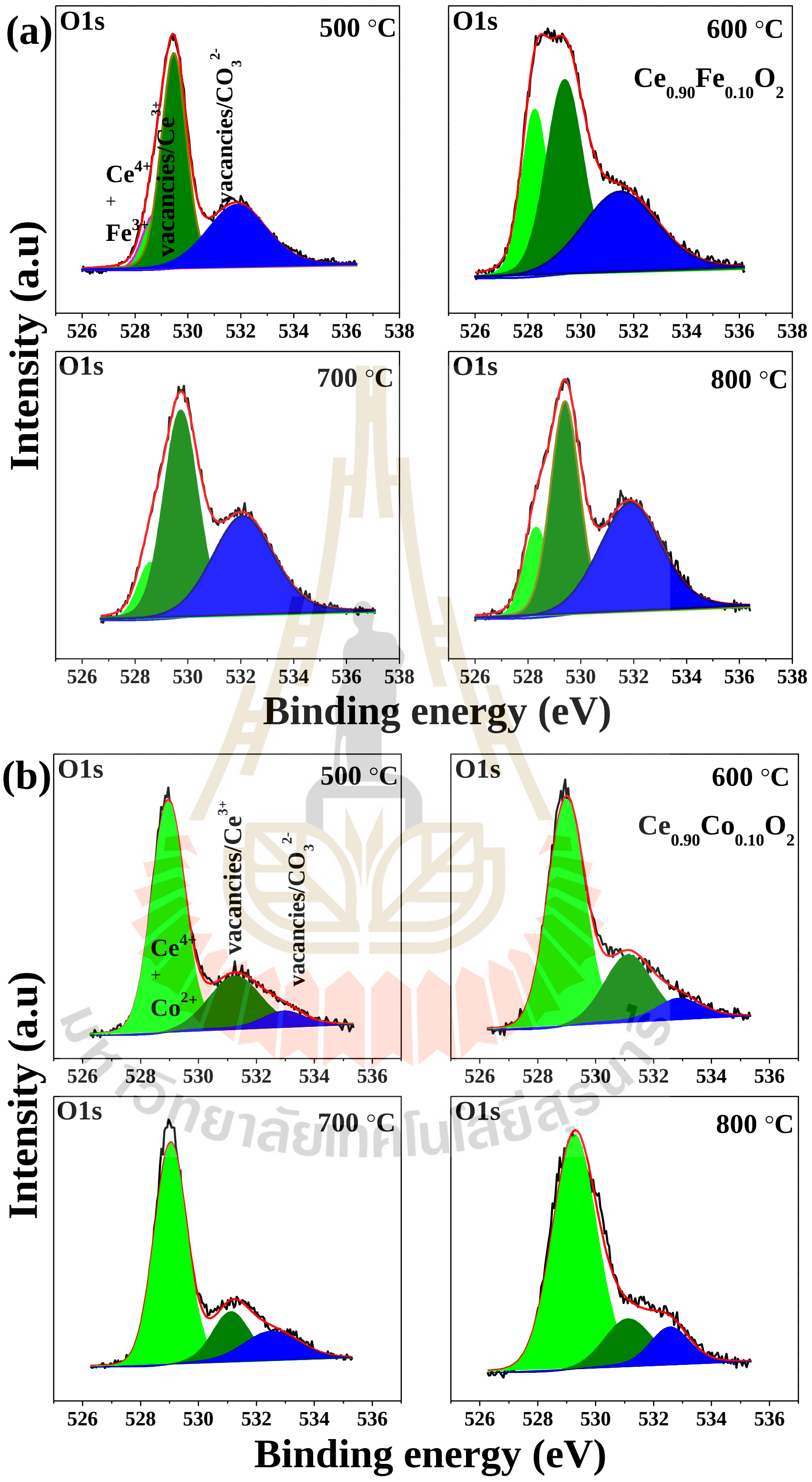

Figure 4.33 XPS integral O *1s* spectra of (a) $Ce_{0.90}Fe_{0.90}O_2$ NPs (b) $Ce_{0.90}Co_{0.90}O_2$ NPs.

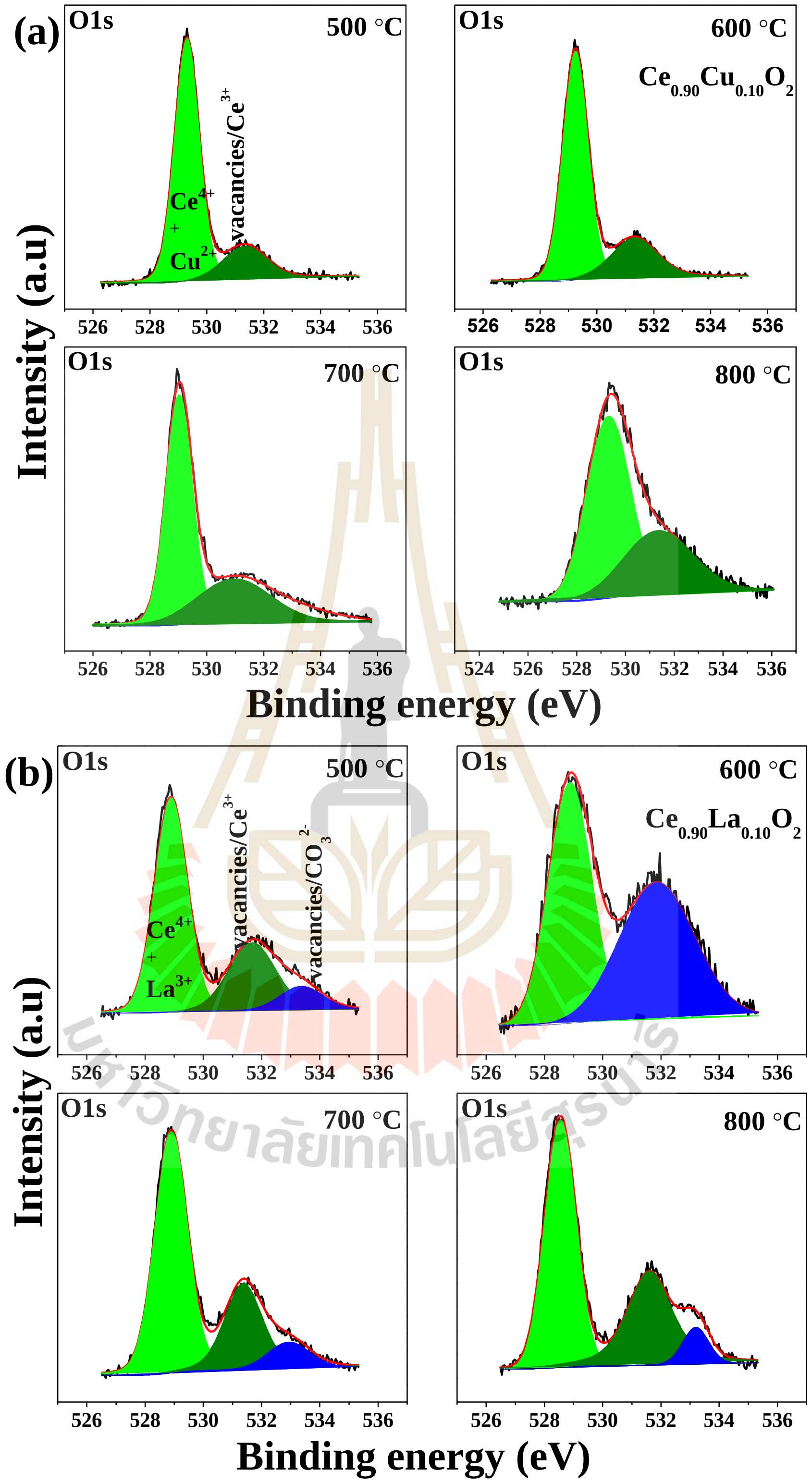

Figure 4.34 XPS integral O *1s* spectra of (a) $Ce_{0.90}Cu_{0.90}O_2$ NPs (b) $Ce_{0.90}La_{0.90}O_2$ NPs.

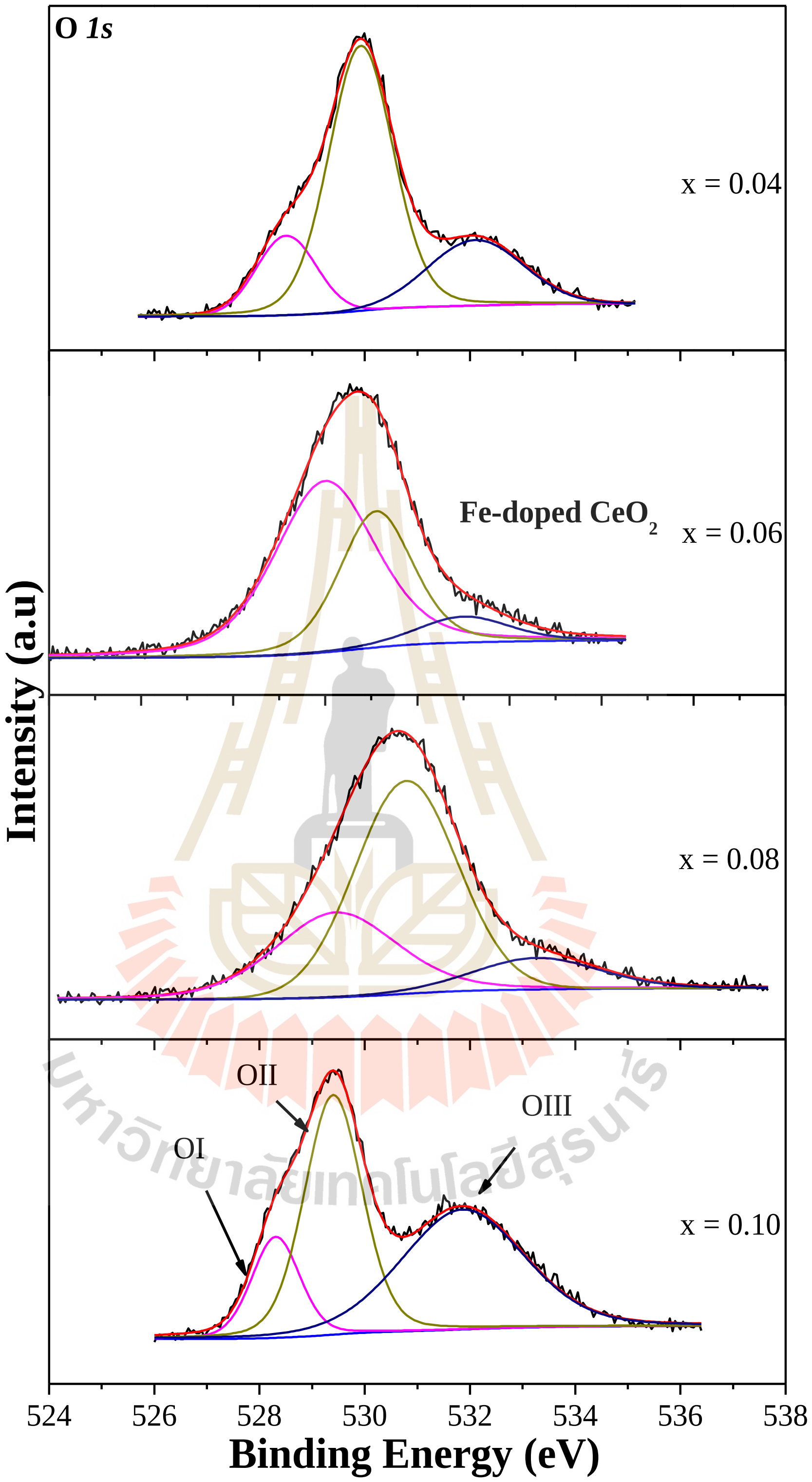

Figure 4.35 O *1s* XPS of $Ce_{1-x}Fe_xO_2$ samples.

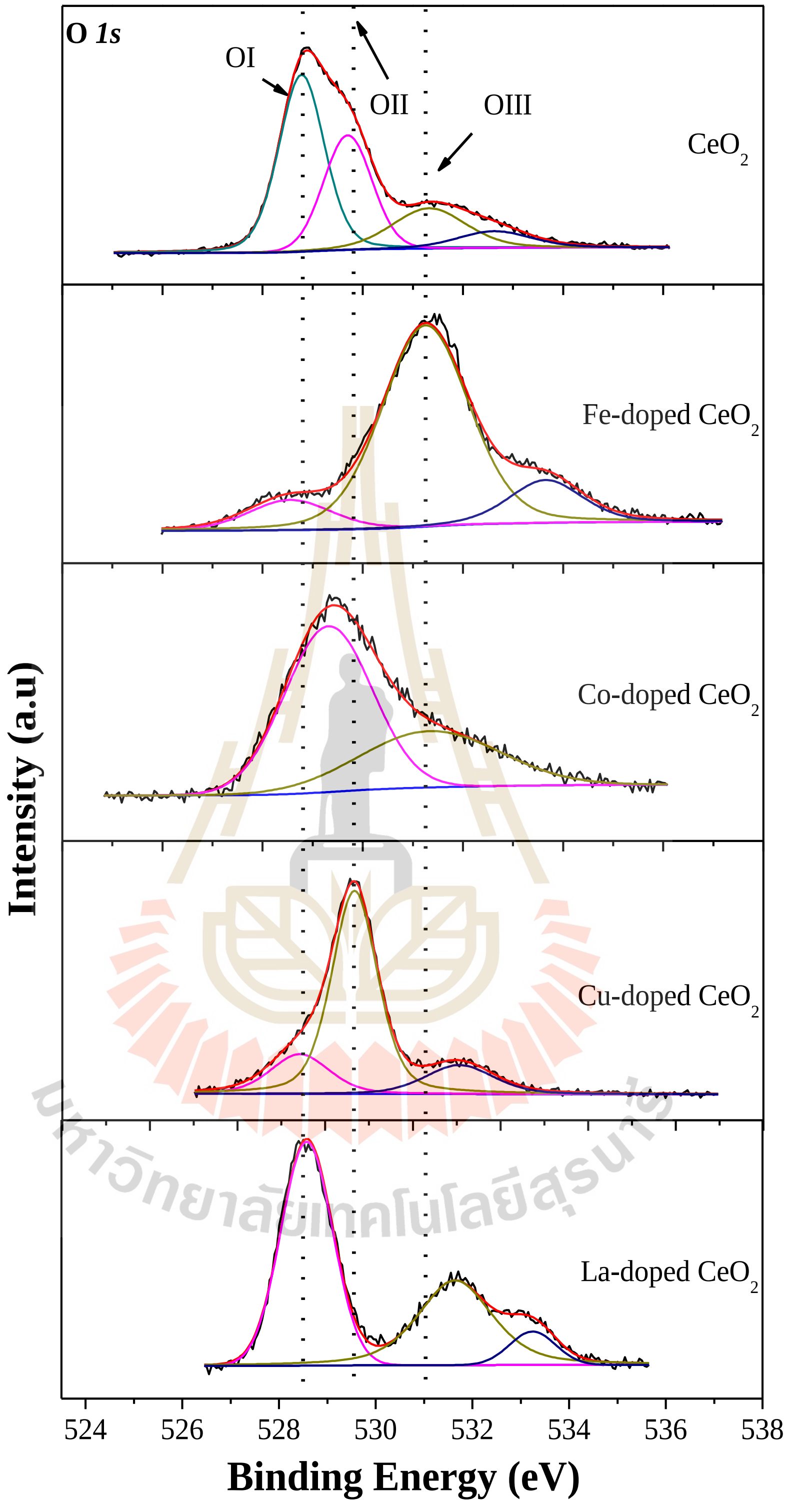

Figure 4.36 High resolution XPS spectra of O *1s* peak of CeO_2 and $Ce_{1-x}M_xO_2$ NPs.

Figure. 4.37 show FT-IR spectra of the as-spun nanofibers, CeO_2 and $Ce_{1-x}Fe_xO_2$ NFs calcined for 2 h in air. All of sample are observed that the absorption peaks ascribing to Ce-O or Ce-Fe-O stretching modes lower than 600 cm^{-1} appear in all temperatures (Vantomme, Yuan, Du and Su, 2005, Wang and Sun, 2008). The absorption bands located at around 3407, 2944, 1647, 1440, and 1033 cm^{-1} belong to PVP. The large region of band at ~3407 cm^{-1} indicates the presence of residual water, which has stretching vibrations of hydroxyl group (Cui, Dong, Wang and Li, 2008). The band at ~2944 and ~1440 cm^{-1} may be assigned to the C–H bond stretching mode corresponding to the carbonyl group, and they shift to ~1390 and ~2898 cm^{-1} for a polymer concentration of before and after calcination. The band at ~1644 cm^{-1} corresponds to the carbonyl group (Li and Xia, 2004). Furthermore, the less intense peak at ~1033 cm^{-1} is identified to C–N and/or C–O. However, carbon and humidity contamination from the environment do easily occur in the samples.

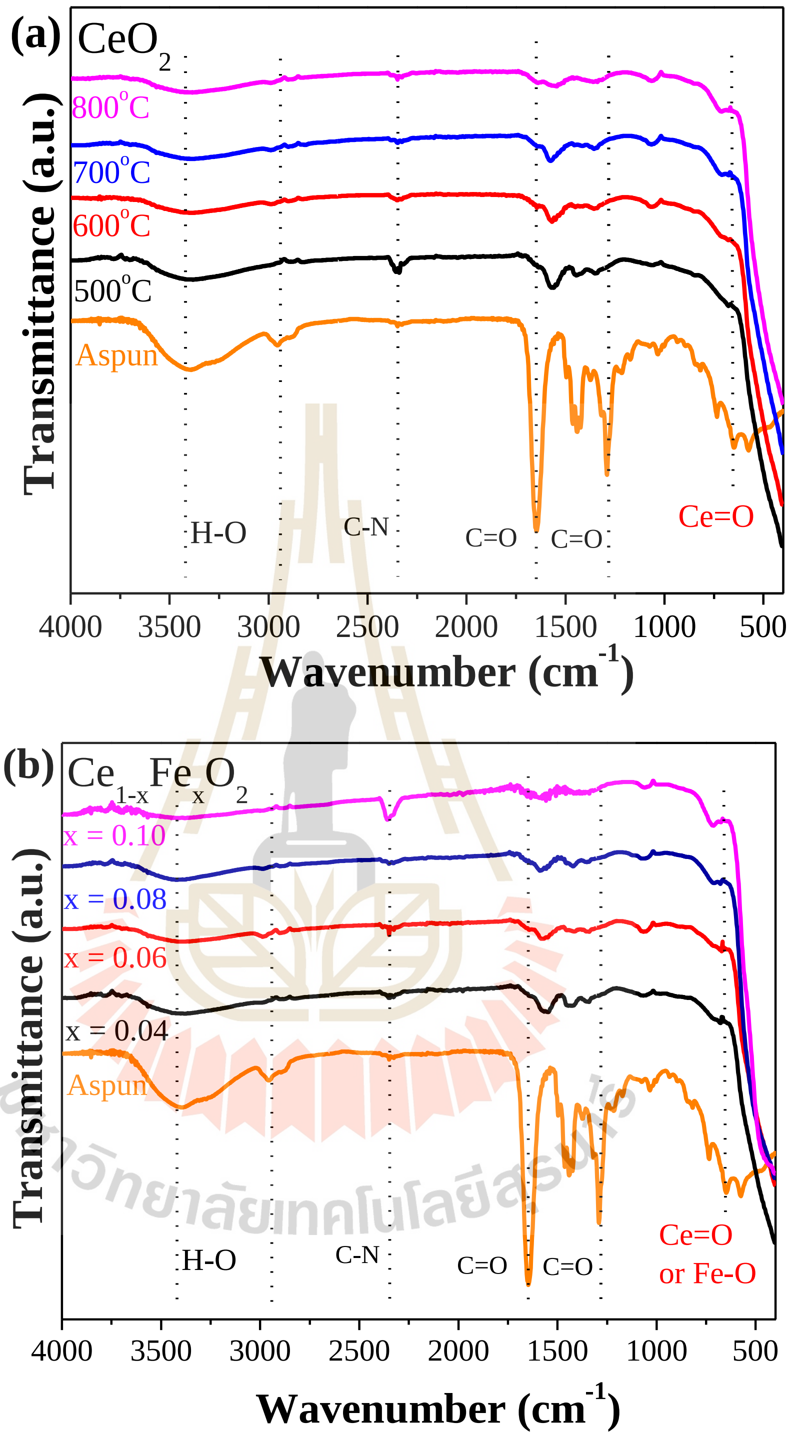

Figure 4.37 FTIR spectra of as spun (a) CeO_2/PVP calcined at 500, 600, 700 and 800 °C in air and (b) $Ce_{1-x}Fe_xO_2$/PVP where $0 \leq x \leq 10$ calcined at 800 °C in air.

The X-ray Absorption Near-Edge structure (XANES) spectra of CeO_2 and $Ce_{1-x}M_xO_2$ samples at the Ce *L* edge (5720 eV) were measured at room temperature in transmission mode, and the TM *K* edge (included Fe, Co, and Cu *K* edge) XANES spectra of the samples were measured in Fluorescent mode to study the valent states of Ce ions in the structures. XANES were measured at energy the energy edges were evaluated using Athena software. The normalized absorption Ce *L*-edge of XANES spectra for CeO_2 and $Ce_{1-x}M_xO_2$ samples compared with those of reference materials for Ce are presented in Figure 4.38. To explain the Ce oxidation state of all samples, standard of $Ce(NO_3)_3.6H_2O$ was used as a reference for oxidation state of Ce^{3+} and CeO_2 was used as reference for oxidation state of Ce^{4+}. Figure 4.38 shows the edge energy of the Ce atoms in $Ce_{0.90}M_{0.10}O_2$ samples comparing with CeO_2 (Ce^{4+}) standard, and Cerium nitrate (Ce^{3+}) standard. From a very precise analysis, after background correction and normalization using the ATHENA software which is included in an IFEFFIT package (Newville, 2001, Ravel and Newville, 2005), the edge energies are shown in Table 4.15. These edge energies are consistent with a coupling valence states of Ce^{3+} and Ce^{4+}. Furthermore, the semi-qualitative analysis of the valence state of Ce in each of samples was determined using an empirical calculation as recently reported by Daengsakul et al. (Daengsakul et al., 2015). The average and percentages of Ce^{4+} and Ce^{3+} in all samples are calculated from Eq. (4.1), (4.2) and (4.3). Qualitatively, from these calculations, we can obtain the valence states of Ce atoms according to the edge energy shift positions as shown in Table 4.15. From this calculation, it is clear that the highest percentages of Ce^{4+} are approximate 98.55 % in the CeO_2 samples calcined at 600 °C. With increasing a calcination temperature, doping with Fe, Co, Cu and La the percentage of Ce^{4+} oxidation states are found to be decreased. The evidence of coupling of Ce valence states can be used to clearly address and confirm a phenomenon of oxygen vacancies occurred in samples.

$$\langle \text{Ce oxidation state} \rangle = 4 \times \frac{\Delta \text{E of sample}}{\Delta \text{E of Ce}^{3+} \text{and Ce}^{4+}} + \left(3 \times \left(1 - \frac{\Delta \text{E of sample}}{\Delta \text{E of Ce}^{3+} \text{and Ce}^{4+}}\right)\right) \qquad (4.1)$$

$$\% \text{ of Ce}^{3+} = \left(1 - \frac{\Delta \text{E of sample}}{\Delta \text{E of Ce}^{3+} \text{and Ce}^{4+}}\right) \times 100\% \qquad (4.2)$$

$$\% \text{ of Ce}^{4+} = \left(\frac{\Delta \text{E of sample}}{\Delta \text{E of Ce}^{3+} \text{ and Ce}^{4+}}\right) \times 100\% \qquad (4.3)$$

Figure 4.38-4.39 also demonstrate that the local environment of Ce rather than of Fe, Co, Cu and La. The intensity of the Ce *L3*-edge white line decreases monotonically with Fe, Co, Cu and La contents, which is consistent with a uniform reduction in coordination number. The XANES spectra for the Ce *L3*-edge (Figure 4.39) are more complex. In first case, the Ce *L3*-edge white line comprises two peaks A(2p f^0 5d state) and B(2 p f^1 5d$*$L state), (Takahashi, Shimizu, Usui, Kagi and Nomura, 2000, Zhang, Wang, Koberstein, Khalid and Chan, 2004), where 2p denotes the empty state in the 2p shell and L denotes an empty state in the oxygen orbital. Since the appearance of peak B originates from the transfer of charge from the oxygen to the Ce *4f* orbital, the relative decrease in the intensity of peak B with increased doping should be attributed to the larger concentration of oxygen vacancies around Ce. In second case the combined Ce *L3*-edge peak intensity decreases with Fe and La contents. This is consistent with an increase in the concentration of vacancies introduced by Fe and La doping. This marked change in the local environment of the Ce ion maybe related to the fact that oxygen sites that are equivalent in the fluorite phase become nonequivalent in the phase and/or to the increased ordering of the near neighbor oxygen vacancies which accompany increased levels of Fe and La doping.

For the original doping, FeO was used as reference state of Fe^{2+} while Fe_2O_3 and Fe_3O_4 was used as references for oxidation state of Fe^{3+} and mix Fe^{2+} and Fe^{3+}, respectively. Figure 4.41 also shows XANES spectra after data correction at Fe K-edge of $Ce_{1-x}Fe_xO_2$ samples, for comparison, FeO (Fe^{2+}) standard and Fe_2O_3 (Fe^{3+}) standard are plotted. The edge energies of all samples are found with a slight increase and very closed to Fe^{3+} standard at 7125.42, 7125.38, 7125.40 and 7126.42 eV for 0.04, 0.06, 0.08 and 0.10 °C of $Ce_{1-x}Fe_xO_2$ samples, respectively. These edge energy values imply a coupling of Fe^{2+}/Fe^{3+} in samples. In addition, the semi-qualitative analysis of the valence states of Fe atoms in each sample were also calculated using the same procedure as Ce atoms. By empirical calculation, the percentage of mixed valence states of Fe atoms are also shown in Table 4.16 with the highest percentages of Fe^{3+} are approximate 89.85 % in the $Ce_{0.90}Fe_{0.10}O_2$ calcined at 800 °C. As clearly seen in the calculation, the percentage of Fe^{3+} increases with increasing calcination temperature and concentration of doping. This is in a good agreement with XPS results where samples calcined at 800 °C have outstanding traces of Fe_3O_4 (Fe^{2+}/Fe^{3+}) comparing to other samples. It is possible to note that the existence of Fe^{3+} play an important role in the ferromagnetism interaction of our $Ce_{0.90}Fe_{0.0}O_2$ samples.

The XANES spectra at Co *k*-edge of Co doped samples exhibits the Co^{2+} and Co^{3+} valences and the absorption edge (Figure 4.42). The absorption edge position and edge shift are summarized in Table 4.17. In the case of XANES spectra at Cu *k*-edge of Cu doped samples exhibits the Cu^{2+} valences and the absorption edge (Figure 4.43). The absorption edge position and edge shift are summarized in Table 4.17.

Table 4.15 Absorption edge and oxidation state at Ce *L*-edge of CeO_2 and $Ce_{1-x}M_xO_2$ samples at room temperature.

samples	Energy (eV) of sample	Energy (eV) of Ce^{4+} std	Energy (eV) of Ce^{3+} std	Δ E	% of Ce^{3+}	% of Ce^{4+}	Ce oxidation state
Cerium nitrate		-	5724.35	-	100	-	3+
CeO_2 STD		5728.5	-	-	-	100	4+
CeO_2 NPs							
500 °C	5728.22	5728.50	5724.35	4.15	6.75	93.25	3+, 4+
600 °C	5728.44	5728.50	5724.35	4.15	1.45	98.55	3+, 4+
700 °C	5728.38	5728.50	5724.35	4.15	2.89	97.11	3+, 4+
800 °C	5727.93	5728.50	5724.35	4.15	13.73	86.27	3+, 4+
$Ce_{0.90}Fe_{0.10}O_2$							
500 °C	5727.34	5728.50	5724.35	4.15	27.95	72.05	3+, 4+
600 °C	5727.21	5728.50	5724.35	4.15	31.08	68.92	3+, 4+
700 °C	5726.69	5728.50	5724.35	4.15	43.61	56.39	3+, 4+
800 °C	5727.22	5728.50	5724.35	4.15	30.84	69.16	3+, 4+
$Ce_{0.90}Co_{0.10}O_2$							
500 °C	5727.75	5728.50	5724.35	4.15	18.07	81.93	3+, 4+
600 °C	5727.85	5728.50	5724.35	4.15	15.66	84.34	3+, 4+
700 °C	5727.89	5728.50	5724.35	4.15	14.70	85.30	3+, 4+
800 °C	5727.85	5728.50	5724.35	4.15	15.66	84.34	3+, 4+
$Ce_{0.90}Cu_{0.10}O_2$							
500 °C	5728.09	5728.50	5724.35	4.15	9.88	90.12	3+, 4+
600 °C	5727.82	5728.50	5724.35	4.15	16.39	83.61	3+, 4+
700 °C	5727.86	5728.50	5724.35	4.15	15.42	84.58	3+, 4+
800 °C	5727.95	5728.50	5724.35	4.15	13.25	86.75	3+, 4+

Table 4.15 Absorption edge and oxidation state at Ce *L*-edge of CeO_2 and $Ce_{1-x}M_xO_2$ samples at room temperature (Continued).

$Ce_{0.90}La_{0.10}O_2$							
500 °C	5727.42	5728.50	5724.35	4.15	26.02	73.98	3+, 4+
600 °C	5727.41	5728.50	5724.35	4.15	26.27	73.73	3+, 4+
700 °C	5727.62	5728.50	5724.35	4.15	21.20	78.80	3+, 4+
800 °C	5727.62	5728.50	5724.35	4.15	21.20	78.80	3+, 4+

Table 4.16 Absorption edge and oxidation state at Fe *K*-edge of $Ce_{1-x}Fe_xO_2$ 800 °C samples at room temperature.

samples	Energy (eV) of sample	Energy (eV) of Fe^{2+} std	Energy (eV) of Fe^{3+} std	Δ E	% of Fe^{2+}	% of Fe^{3+}	Fe oxidation state
FeO		-	7120.19	-	100	-	2+
Fe_2O_3		7126.30	-	-	-	100	3+
Fe_3O_4		7124.20					2+/3+
$Ce_{1-x}Fe_xO_2$							
X =0.04	7125.42	7126.30	7120.19	6.11	14.40	85.60	2+, 3+
X = 0.06	7125.38	7126.30	7120.19	6.11	15.06	84.94	2+, 3+
X = 0.08	7125.45	7126.30	7120.19	6.11	13.91	86.09	2+, 3+
X = 0.10	7125.68	7126.30	7120.19	6.11	10.15	89.85	2+, 3+

Table 4.17 Absorption edge and oxidation state at Co *K*-edge of $Ce_{1-x}Co_xO_2$ 800 °C samples at room temperature.

Sample	Absorption edge at Co (eV)	Edge shift at Co (eV)	Co oxidation state
CoO	7718.12	0	2+
Co_3O_4	7722.13	4.01	2+, 3+
X = 0.04	7720.27	2.15	2+
X = 0.06	7723.36	5.42	2+, 3+
X = 0.08	7722.15	4.03	2+, 3+
X = 0.10	7722.18	4.06	2+, 3+

Table 4.18 Absorption edge and oxidation state at Cu *K*-edge of $Ce_{1-x}Cu_xO_2$ 800 °C samples at room temperature.

Sample	Absorption edge at Cu (eV)	Edge shift at Cu (eV)	Valence state at Cu
CuCl	8981.50	0	1+
CuO	8983.87	2.46	2+
$Cu(NO_3)_2$	8984.96	3.17	2+
X = 0.04	8983.12	1.62	2+
X = 0.10	8983.28	1.78	2+,

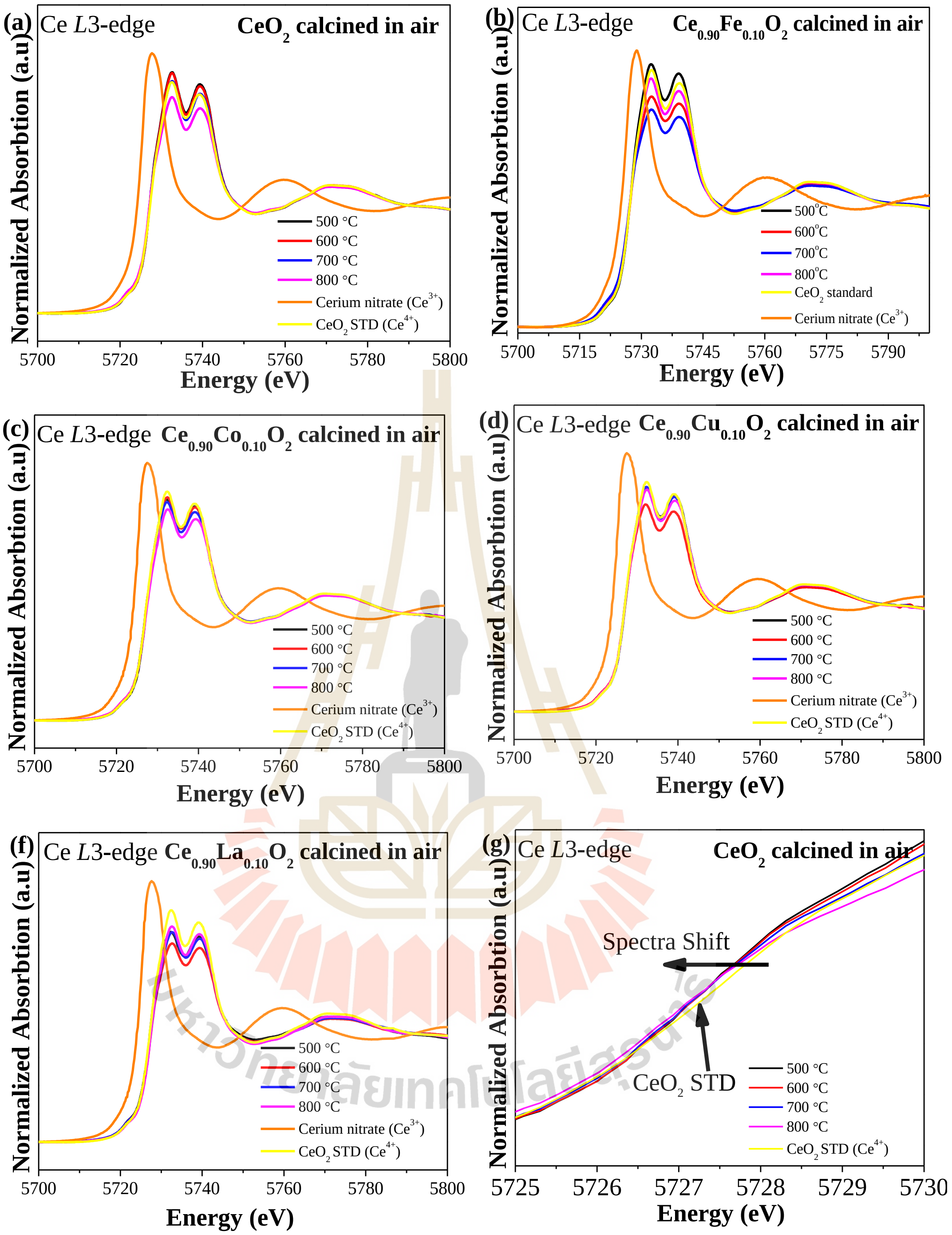

Figure 4.38 XANES spectra at the Ce *L3*-edge for CeO_2 standard, and XANES spectra of $Ce_{0.90}M_{0.10}O_2$ samples calcined at 500-800 °C for 2 h in air.

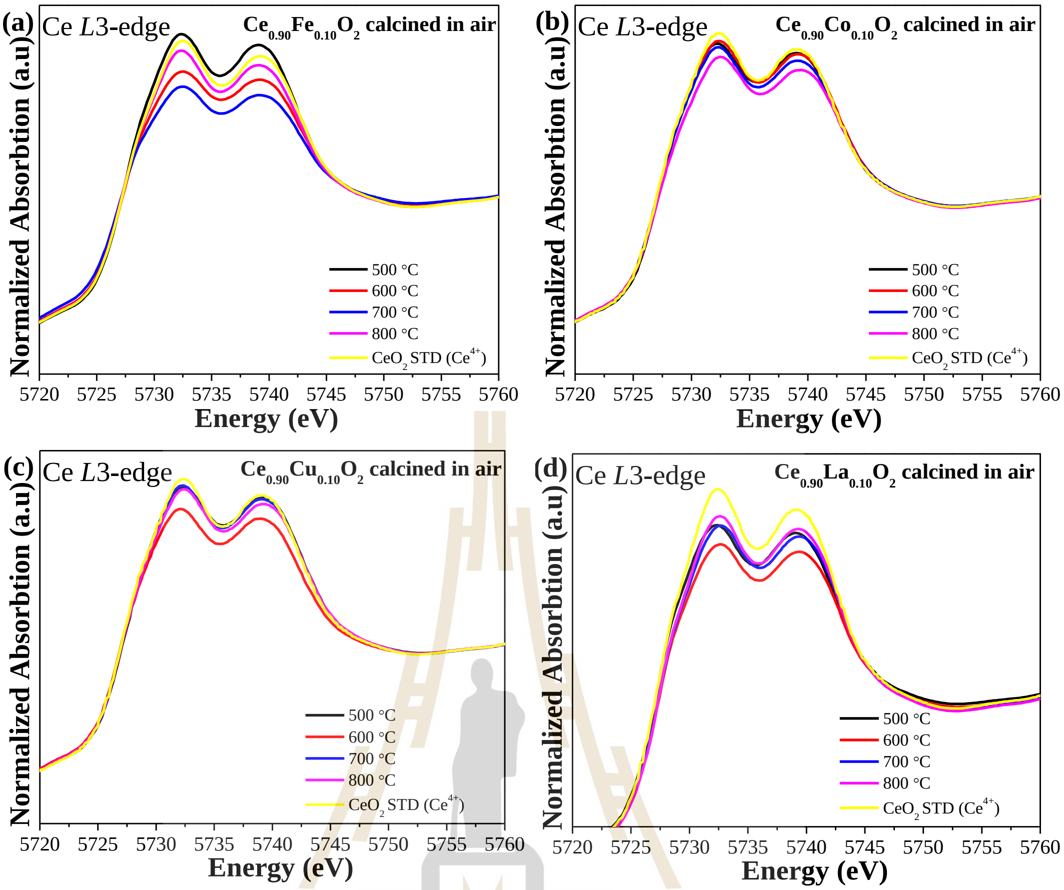

Figure 4.39 Ce *L*3-edge XANES spectra blow up of the white line peaks CeO_2 standard, and $Ce_{0.90}M_{0.10}O_2$ samples calcined at 500-800 °C for 2 h in air.

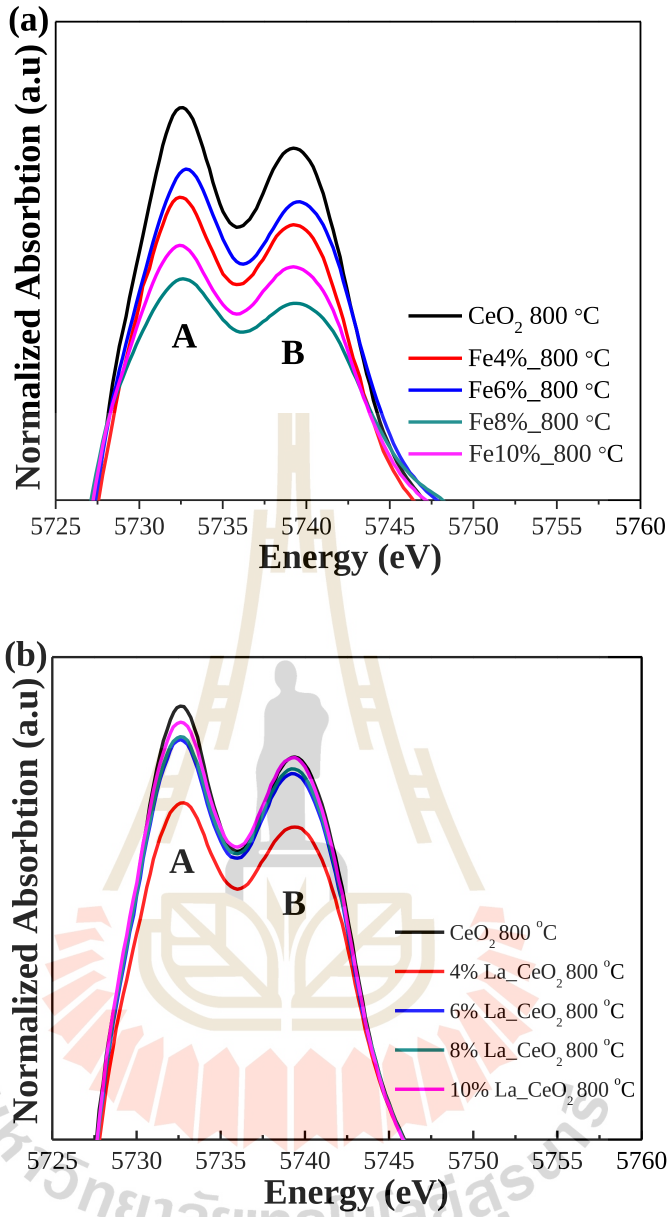

Figure 4.40 Ce *L3*-edge XANES spectra blow up of the white line peaks of CeO_2 (a) $Ce_{1-x}Fe_xO_2$ and (b) $Ce_{1-x}La_xO_2$ samples calcined at 800 °C for 2 h in air.

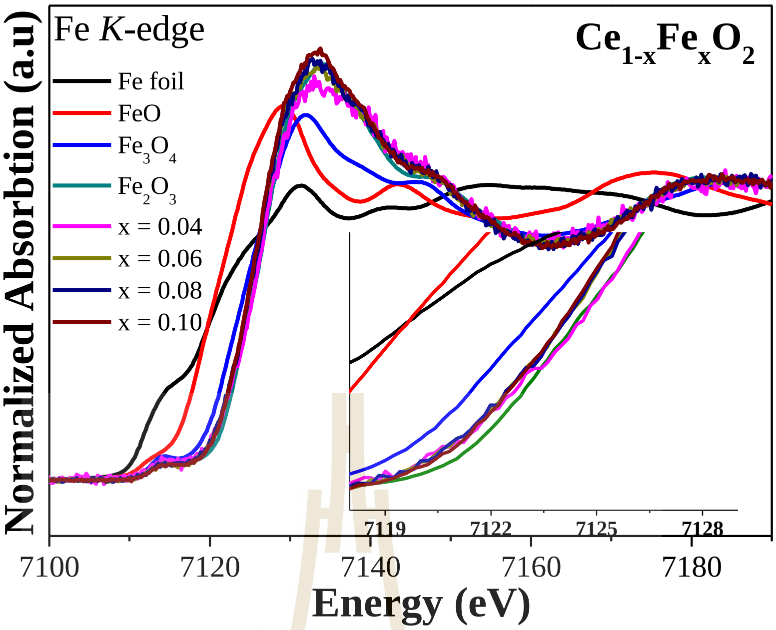

Figure 4.41 XANES spectra at the Fe K-edge for Fe Foil, FeO, Fe_2O_3, Fe_3O_4 standard, and XANES spectra of $Ce_{1-x}Fe_xO_2$ samples calcined at 800 °C for 2 h in air.

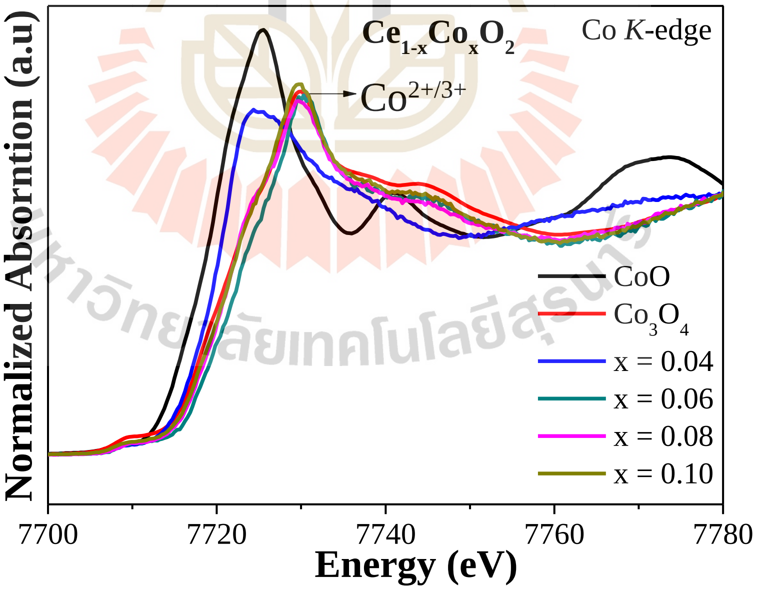

Figure 4.42 XANES spectra at the Co *K*-edge for CoO and Co_3O_4 standard, and XANES spectra of $Ce_{1-x}Co_xO_2$ samples calcined at 800 °C for 2 h in air.

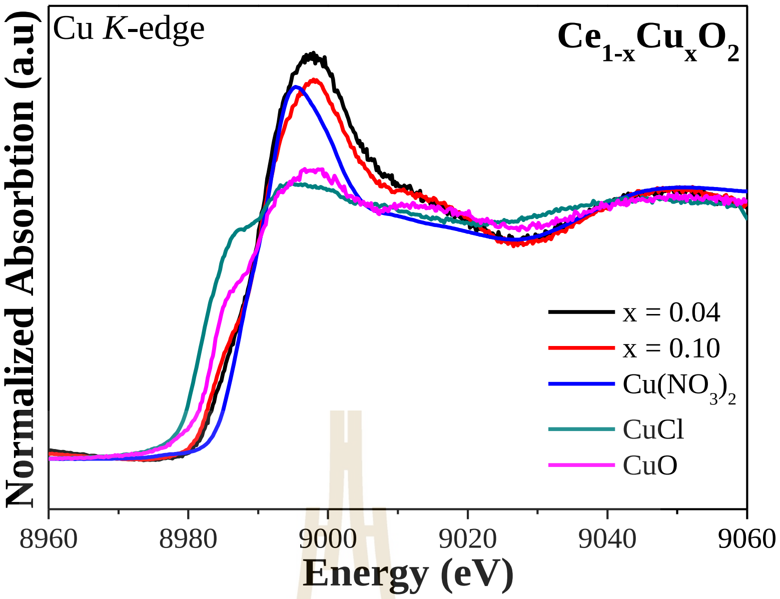

Figure 4.43 XANES spectra at the Co *K*-edge for $Cu(NO_3)_2$, CuCl and CuO standard, and XANES spectra of $Ce_{1-x}Cu_xO_2$ samples calcined at 800 °C for 2 h in air.

4.3 Optical property

The UV-Vis absorption spectra of the CeO_2 NPs and NFs calcined at different temperatures are shown in Figure 4.44. The spectra of all nanostructures show a strong absorption in the ultraviolet region centered at 285 nm (4.35 eV). Both CeO_2 NPs and NFs exhibit similar absorption spectra. The optical absorbance spectra of $Ce_{1-x}M_xO_2$ $Ce_{1-x}Co_xO_2$ and $Ce_{1-x}Cu_xO_2$ NPs are shown in Figure 4.45-4.46. Additional weak absorption peaks were observed at approximately 350 nm (3.54 eV), 350 nm (3.54 eV), 550 nm (2.72 eV) and 360 nm (3.50 eV) for $Ce_{1-x}Co_xO_2$, $Ce_{1-x}Cu_xO_2$, $Ce_{1-x}Fe_xO_2$ and $Ce_{1-x}La_xO_2$ NPs, respectively. The observed additional absorption peaks are the result of the formation of sub-levels within the band gap due to the defects or the impurities. The direct band gap energy (E_g) was determined by fitting the absorption data to the direct transition as equation 4.4,

$$\alpha h\nu = A\left(h\nu\text{-}E_g\right)^{\frac{1}{2}} \tag{4.4}$$

where α is the optical absorption coefficient, $h\nu$ is the photon energy, E_g is the direct band gap, and A is a constant (Khan et al., 2014). The extrapolation of the linear portions of the curves toward absorption equal to zero (y=0) gives E_g for direct transitions (see Figure 4.47-4.49). The estimated direct band gaps of CeO_2 NPs, CeO_2 NFs and $Ce_{1-x}M_xO_2$ NPs are shown in Table 4.19-4.20. There is no significant difference between their band gaps. However, it was observed that the band gap slightly decreases when TMs are doped into the CeO_2 nanostructure and the band gap decreases when TM content increases CeO_2 samples. This decrease exhibits the redshifts in the absorption spectra. The decrease in band gap is because the TM ions size is smaller than the Ce ion which causes the decrease in the lattice parameter corresponding XRD results. In the case of La-doped CeO_2, La ions is larger than Ce ions and therefore the E_g increases as the lattice parameter is larger confirmed by XRD result.

The band edge absorption of nanometer-sized semiconductor materials is mainly related to two factors: a quantum size effect and a surface and interface effect. The quantum size effect leads to the blue shift of E_g with decrease of particle size down to less than a few nanometers, while the surface and interface effect induces the redshift (Barreca, Bruno, Gasparotto, Losurdo and Tondello, 2003). In this work, the CeO_2 and $Ce_{1-x}M_xO_2$ nanostructures have crystallite sizes in the range of 10-36 nm, the difference of the absorption band edge due to the quantum size effect is not observable. Clearly, the surface and interface effect should be responsible for the variation of the absorption band edge. The specific surface area from BET confirm the change of interface between particles according to doping and contamination temperature. When a divalent or trivalent of TM ion is substituted in CeO_2, the V_o is naturally formed to ensure charge neutrality. By introducing Ce^{3+} ions, these ions create the level deep in the band gap between the valence band of full oxygen *2p* states and the conduction band of empty cerium *4f* states. Thus, energy band shifts to the Ce^{3+} band with occupied $4f^1$ state due to oxygen vacancies/defects (Barreca et al., 2003), which reduces the band gap of TM or La ion substitution in CeO_2 lattice and introduces a redshift tendency in the absorption band edge. Similar results have been obtained in some other systems (Shanmuga Sundari, Sugan and Pabitha, 2018, Dhara, Sain, Sadhukhan, Das and Pradhan, 2019). These values are lower than those found in the previous literatures for CeO_2. Dhara et al. (2019) reported the direct band gap values ranging from 3.63 eV observed in CeO_2 nanocrystalline synthesized by ball mill method. Babitha et al. (2015) reported the direct band gap values ranging from 3.33 to 3.50 eV observed in CeO_2 nanoparticles synthesized by chemical precipitate using cerium nitrate and ammonium carbonate as precursor (K Babitha, Sreedevi, K P, Sabu and Varghese, 2015). These band gaps of 3.24 eV are close to those of around 3.2 eV observed in CeO_2, which is an n-type semiconductor (Yin et al., 2016). From the above studies, discussion and proposed photodecomposition mechanism are illustrated as the diagram in Figure 4.51. It is obvious that an energy band gab is an effective tool for narrowing the band gap energy of semiconductor metal oxides, making it photoactive for the decomposition of toxic chemicals under visible light irradiation.

Table 4.19 Summary of band gap energies (E_g) of CeO_2 NPs and CeO_2 NFs calcined at 500-800 °C for 2 h in air.

Temperature (°C)	**E_g (eV) of CeO_2**	
	NFs	**NPs**
500	3.24	3.01
600	3.23	2.98
700	3.28	3.14
800	3.03	3.16

Table 4.20 Summary of band gap energies (E_g) of CeO_2 and $Ce_{1-x}M_xO_2$ NPs calcined at 800 °C for 2 h in air.

Doping Level	**E_g (eV) of CeO_2 and $Ce_{1-x}M_xO_2$ NPs**			
	Fe	**Co**	**Cu**	**La**
X = 0	3.16	3.16	3.16	3.16
X = 0.04	2.77	2.85	2.86	3.15
X = 0.06	-	3.10	2.77	3.12
X = 0.08	253	2.63	2.75	3.11
X = 0.10	2.68	2.73	-	3.10

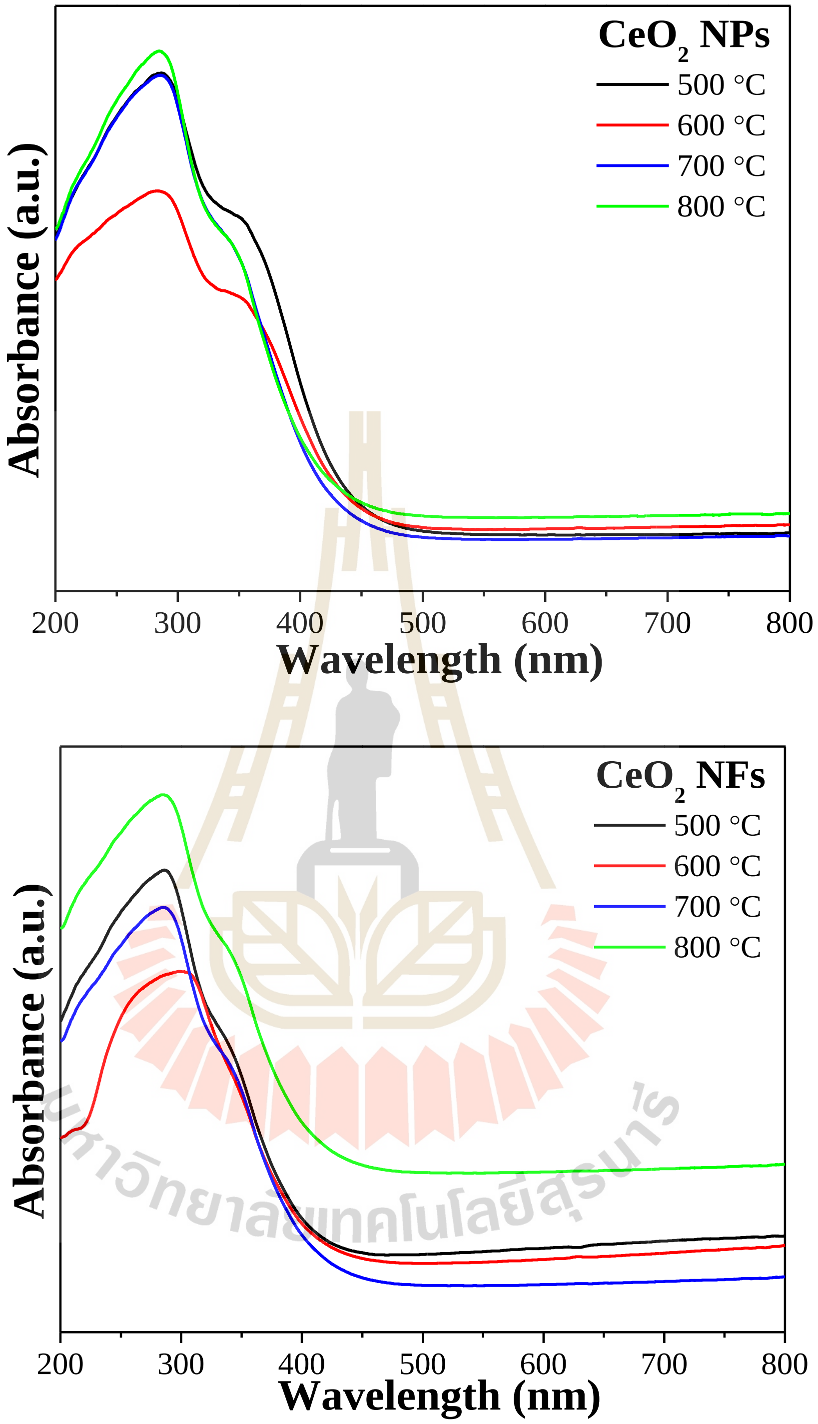

Figure 4.44 Room-temperature optical absorbance spectra of CeO$_2$ NPs and CeO$_2$ NFs calcined at 500-800 °C for 2 h in air.

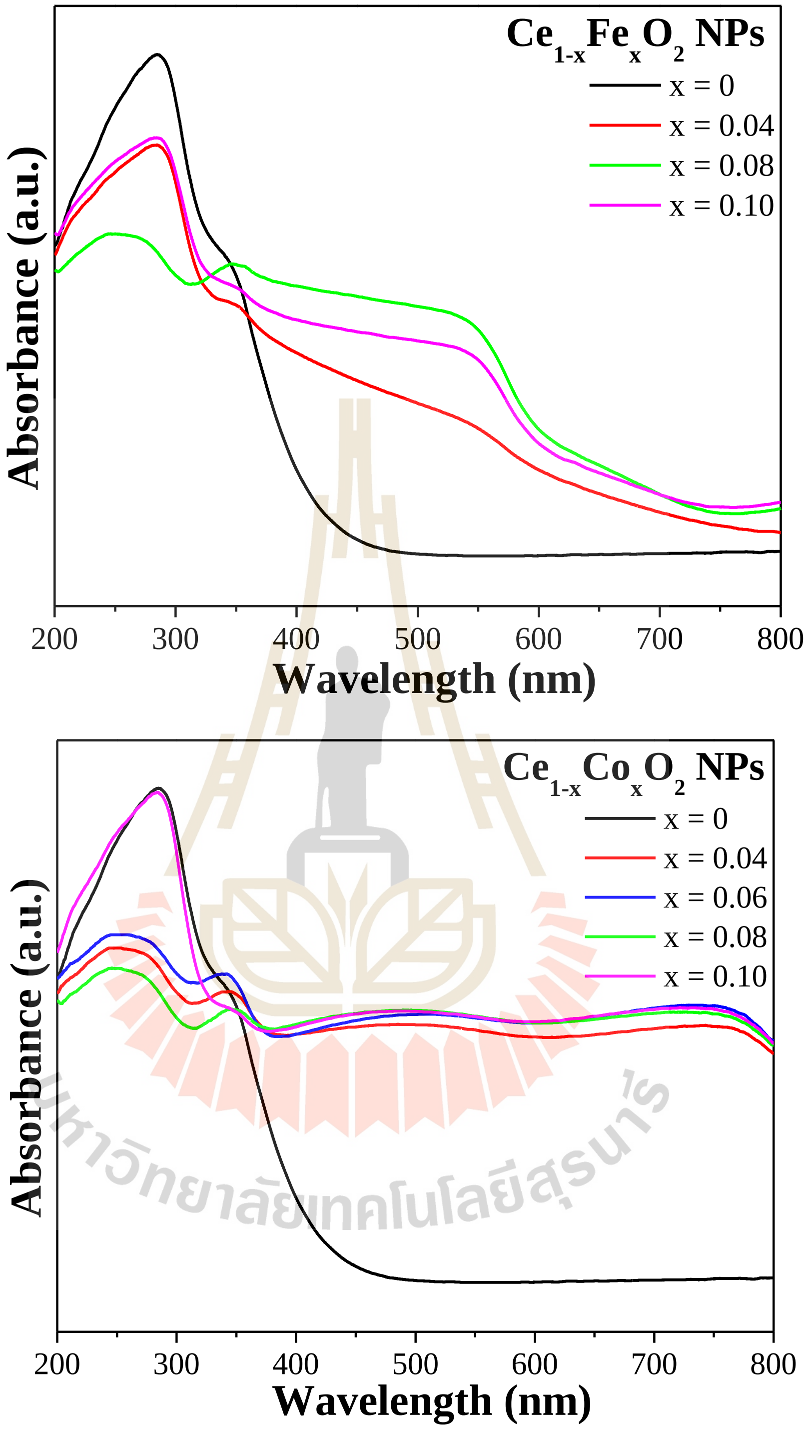

Figure 4.45 Room-temperature optical absorbance spectra of $Ce_{1-x}Fe_xO_2$ and $Ce_{1-x}Co_xO_2$ NPs calcined at 800 °C for 2 h in air.

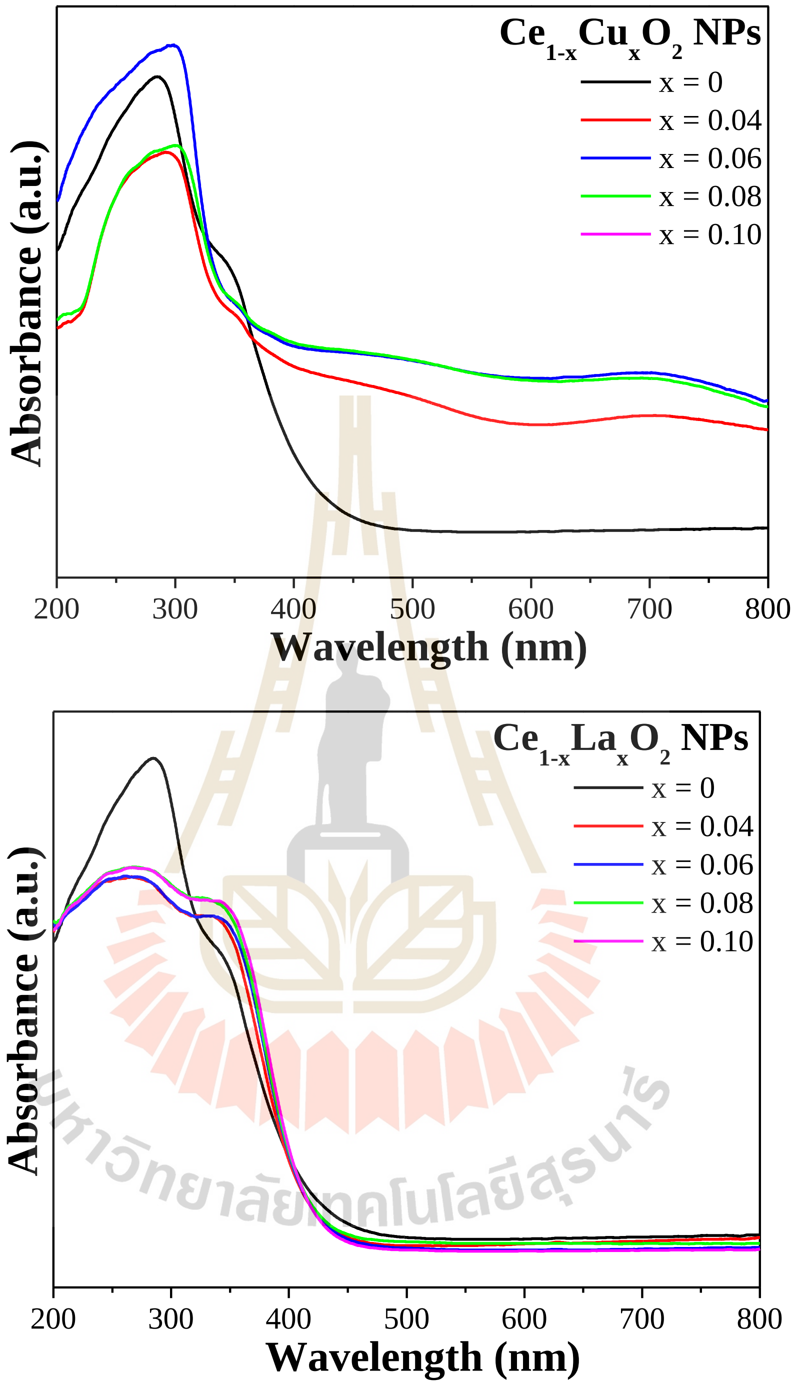

Figure 4.6 Room-temperature optical absorbance spectra of Ce$_{1-x}$Cu$_x$O$_2$ and Ce$_{1-x}$La$_x$O$_2$ NPs calcined at 800 °C for 2 h in air.

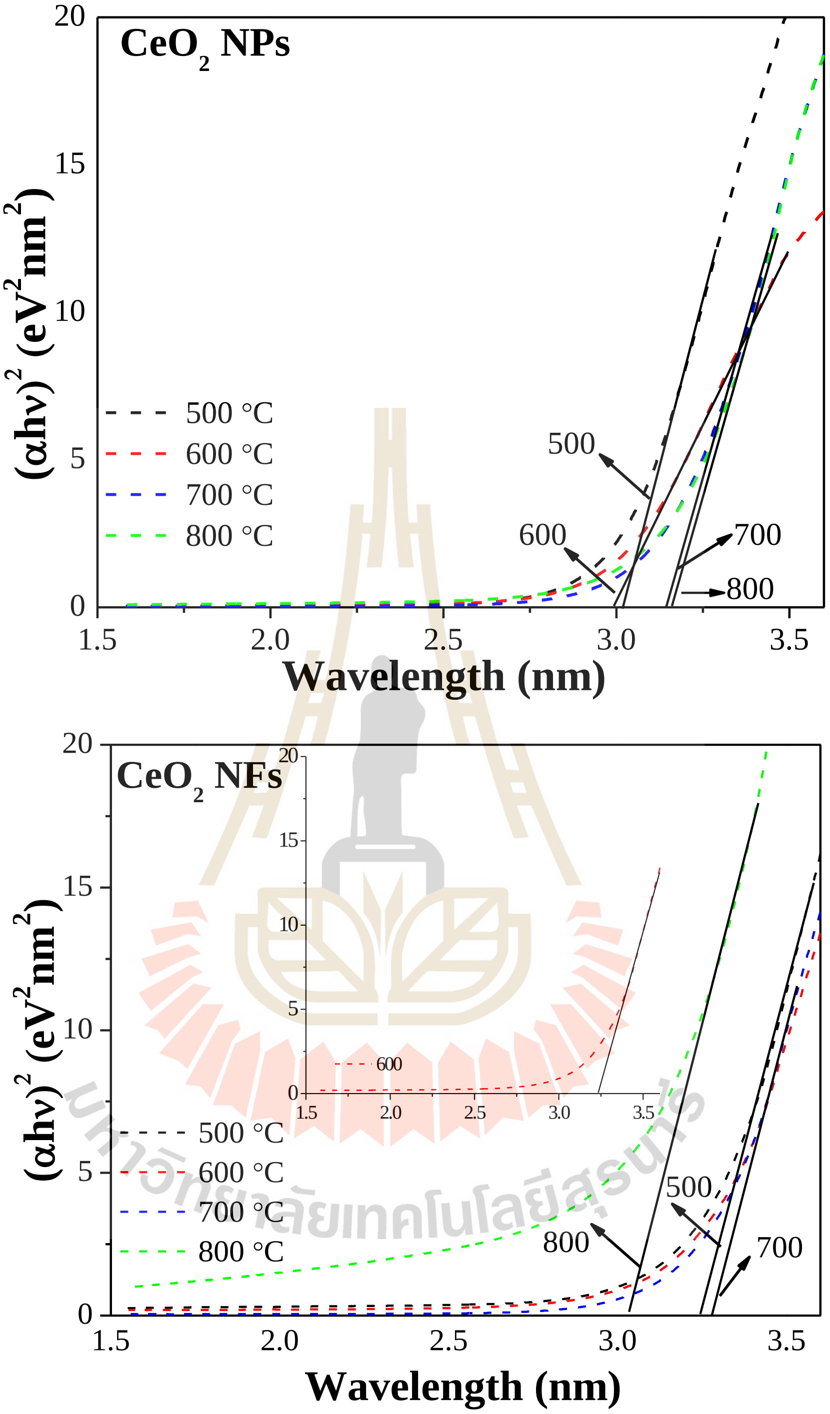

Figure 4.47 Plot of $(\alpha h\nu)^2$ as a function of photon energy for CeO$_2$ NPs and CeO$_2$ NFs calcined at 500-800 °C for 2 h in air.

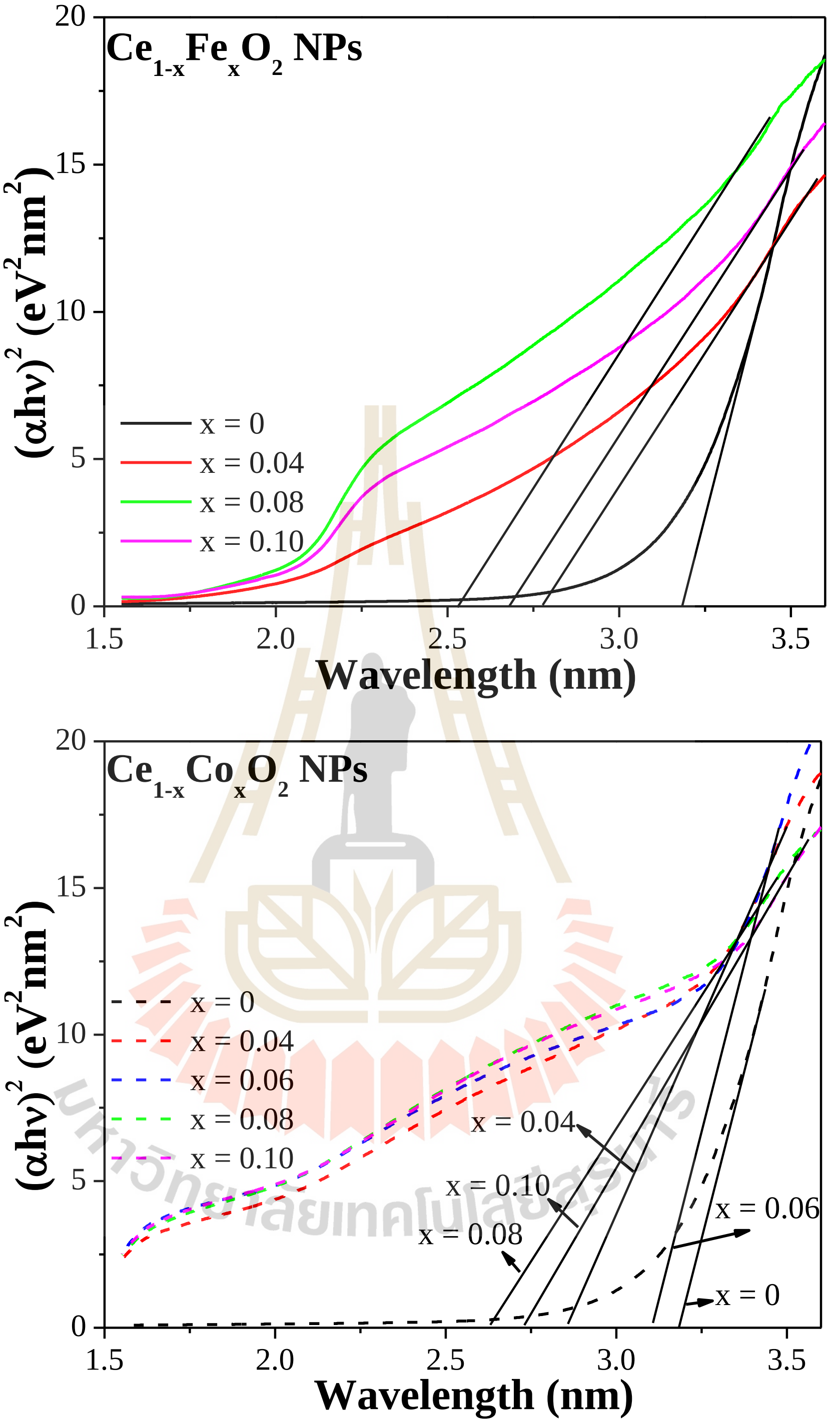

Figure 4.48 Plot of $(\alpha h\nu)^2$ as a function of photon energy for $Ce_{1-x}Fe_xO_2$ and $Ce_{1-x}Fe_xO_2$ NPs calcined at 800 °C for 2 h in air.

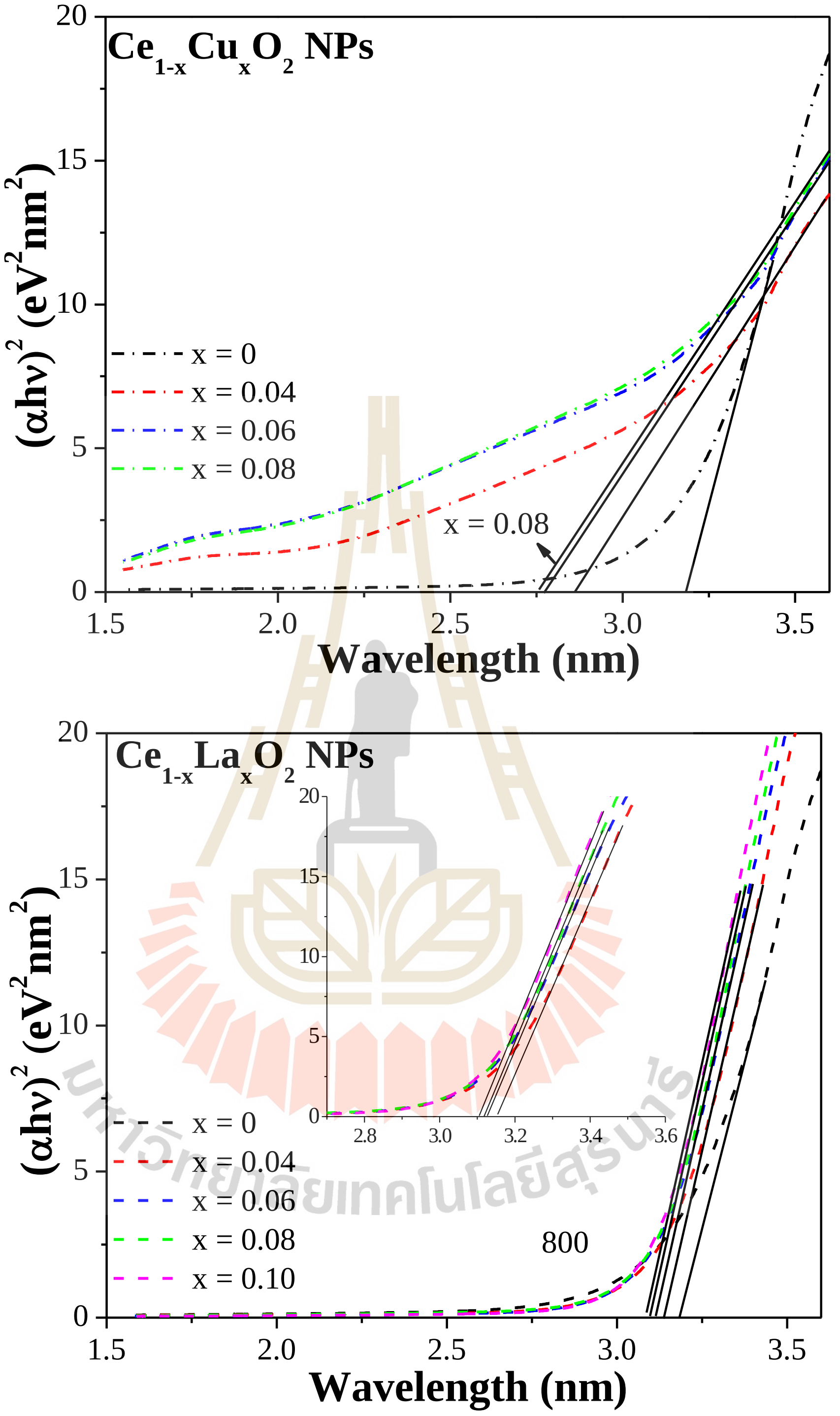

Figure 4.49 Plot of ($\alpha h\nu$)^2 as a function of photon energy for $Ce_{1-x}Cu_xO_2$ and $Ce_{1-x}La_xO_2$ NPs calcined at 800 °C for 2 h in air.

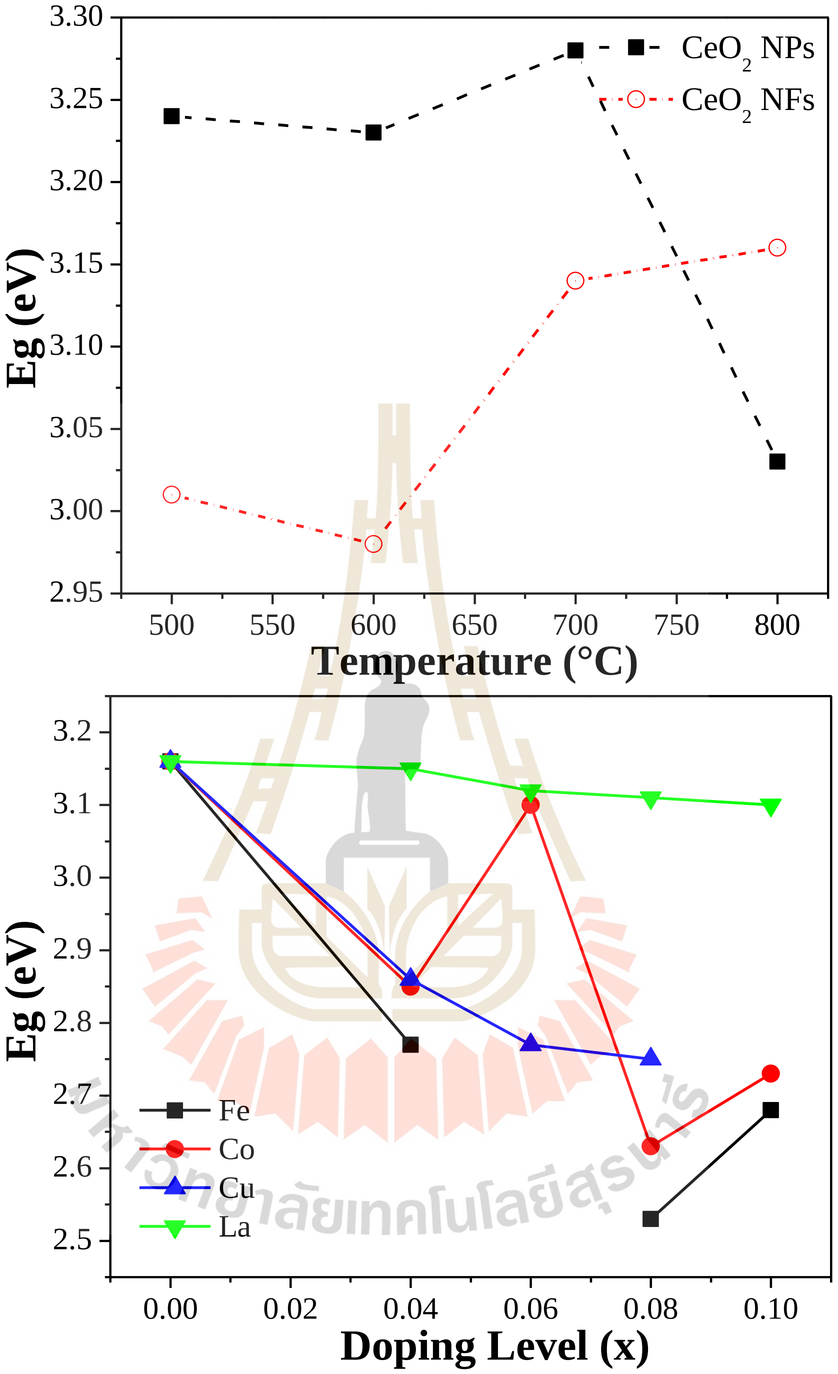

Figure 4.50 Band gaps as estimated from the absorption data of (a) CeO$_2$ NPs and NFs and (b) Fe-, Co-, Cu- and La-doped CeO$_2$ NPs calcined at 800 °C for 2 h.

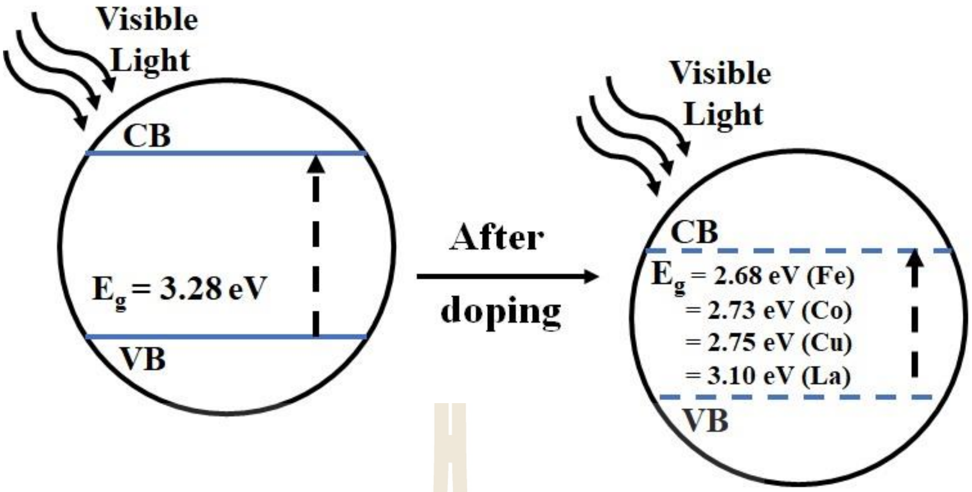

Figure 4.51 Proposed mechanism for the photodegradation of CeO_2 and $Ce_{0.90}M_{0.10}O_2$ calcined at 800 °C nanostructures under visible light irradiation.

4.4 Magnetic properties

Figure 4.52 shows the field dependence of magnetization (*M*–H curve) of the CeO_2 NPs and CeO_2 NFs calcined at 500-800 °C for 2 h in air obtained from room-temperature VSM measurement (with the removal of any diamagnetic contribution). Both CeO_2 nanostructures exhibits weak ferromagnetic mixed with diamagnetic behavior with magnetization (*M*) of approximately 0.002-0.026 emu/g at an applied field of 10 kOe. These values are higher than those found in the literatures for CeO_2. Phokha et al. (2013) reported *M* for CeO_2 nanocrystalline (0.0026 emu/g) synthesized by hydrothermal method (Phokha et al., 2013). Moreover, CeO_2 NFs exhibit *M* higher than CeO_2 NPs. Because of on surface CeO_2 NFs give V_o and Ce^{3+} more than CeO_2 NPs correspond to SEM, XAS and XPS results. SEM results show nanofibers dispersed without aggregation, but nanoparticles show aggregation of particles. For this reason, NPS makes the opportunity to create V_o is more difficult when comparing the two structures. So, the magnetic signals for the samples synthesized by electrospinning technique were attributed to enhanced Ce^{3+} content at surface and correlated with oxygen vacancies, which create more Ce^{3+}, as measured by XANES at the Ce absorption edge and XPS O *1s* spectra. These results show that the magnetic properties of CeO_2 NFs were related to the preparation methods. The magnetic properties generally depend on the size, shape, crystallinity, magnetization direction and so on.

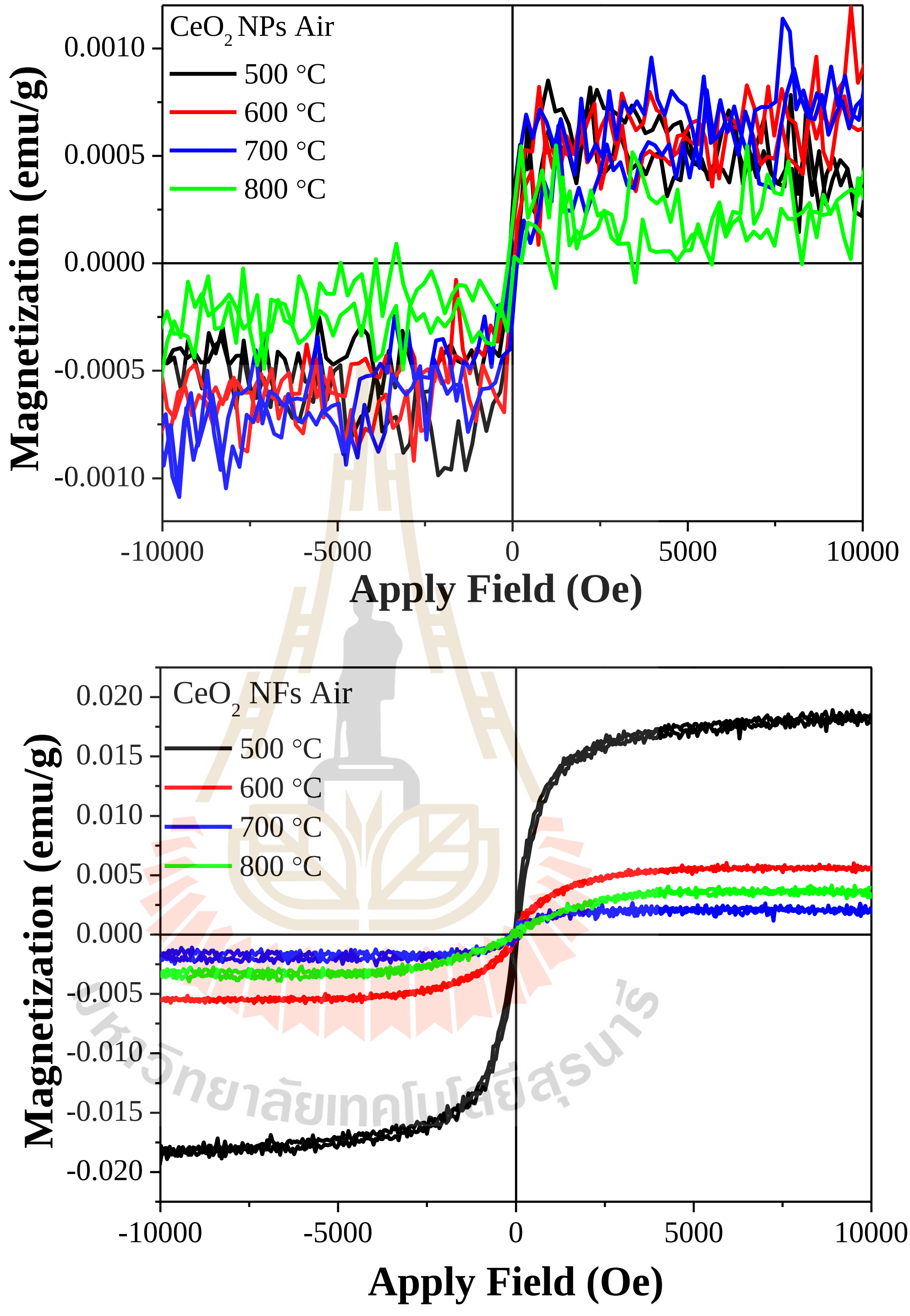

Figure 4.52 *M*-H curve at 300 K obtained from VSM measurements of CeO_2 NPs and CeO_2 NFs calcined at 500-800 °C for 2 h in air (removal of any diamagnetic contribution).

4.4.1 Effect of transition metal doping

The *M*–H curves of $Ce_{1-x}Fe_xO_2$ where 0≤x≤10 NPs and NFs are shown in Figure 4.53. Both $Ce_{1-x}Fe_xO_2$ nanostructures exhibit room-temperature ferromagnetism (FM). The *M* and coercivity increases with concentration of Fe ions. This may be because of the increase of Fe^{3+} content participating in the ferromagnetism interaction which is clearly seen from our qualitative and quantitative XANES data (Table 4.15). The highest *M* of approximately 0.305 emu/g was observed for the $Ce_{0.90}Fe_{0.10}O_2$ nanofibers. The *M* and coercivity values are listed in Table 4.21. The ferromagnetism in $Ce_{1-x}Fe_xO_2$ samples might be contributed from the long-range Fe ions and the vacancies/defects in the samples which can be activated in the nanostructures and induced during the calcination process. These phenomena have been observed in Fe-doped In_2O_3 (Yan, Ge, Zuo, Qiao and Zhang, 2009). The magnetizations $Ce_{1-x}Co_xO_2$ where x = 0.04, 0.06, and 0.08 NPs shown in Figure 4.46 exhibit both room-temperature FM and paramagnetism (PM) which increase with magnetic field in the range of ±10 kOe. The $Ce_{0.90}Co_{0.10}O_2$ NPs shows highest *M* value of approximately 0.010 emu/g. The PM in sample is from the magnetism of CoO in the structure which is in a good agreement with XRD results.

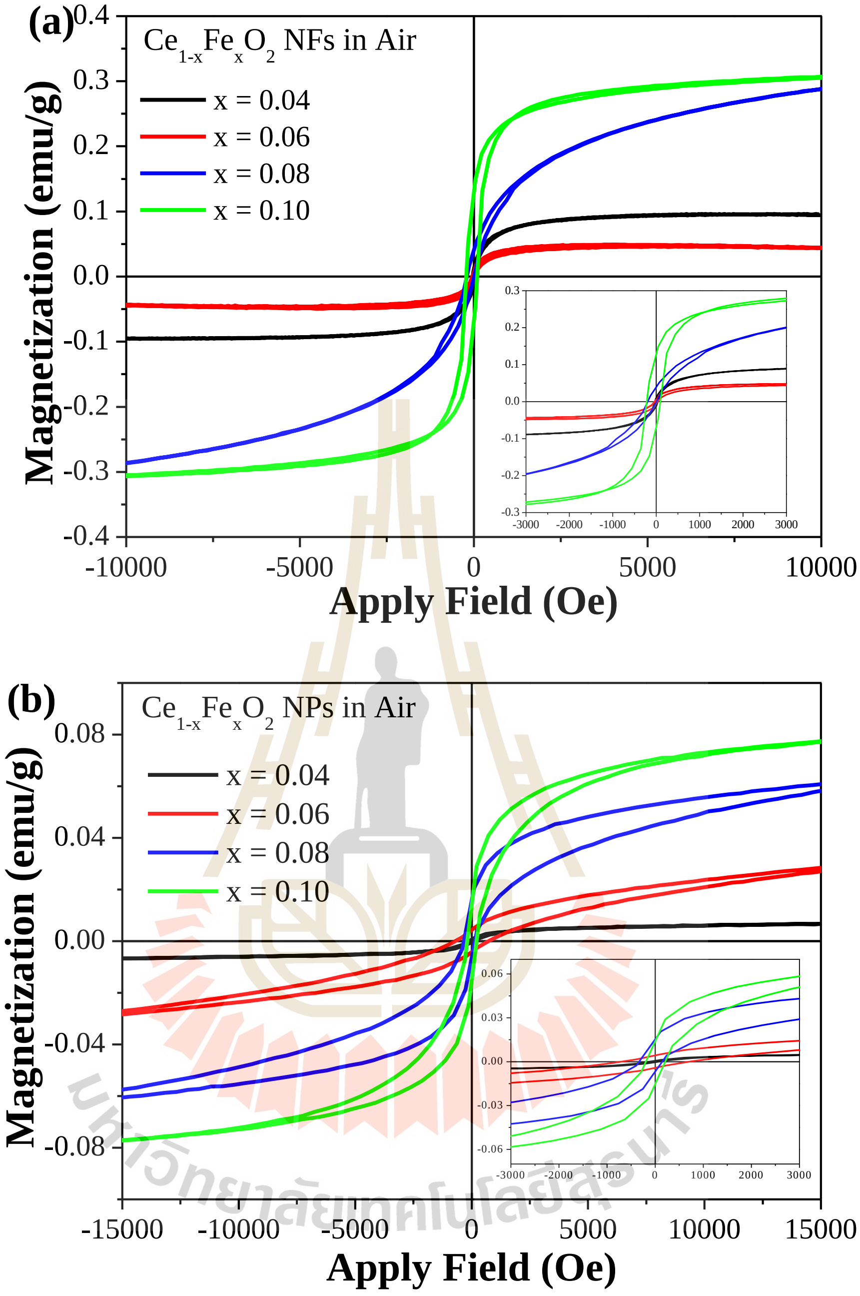

Figure 4.53 *M*-H curve at 300 K obtained from VSM measurements of Ce$_{1-x}$Fe$_x$O$_2$ where $0 \leq x \leq 10$ (a) nanofibers and (b) nanoparticles calcined at 800 °C for 2 h in air.

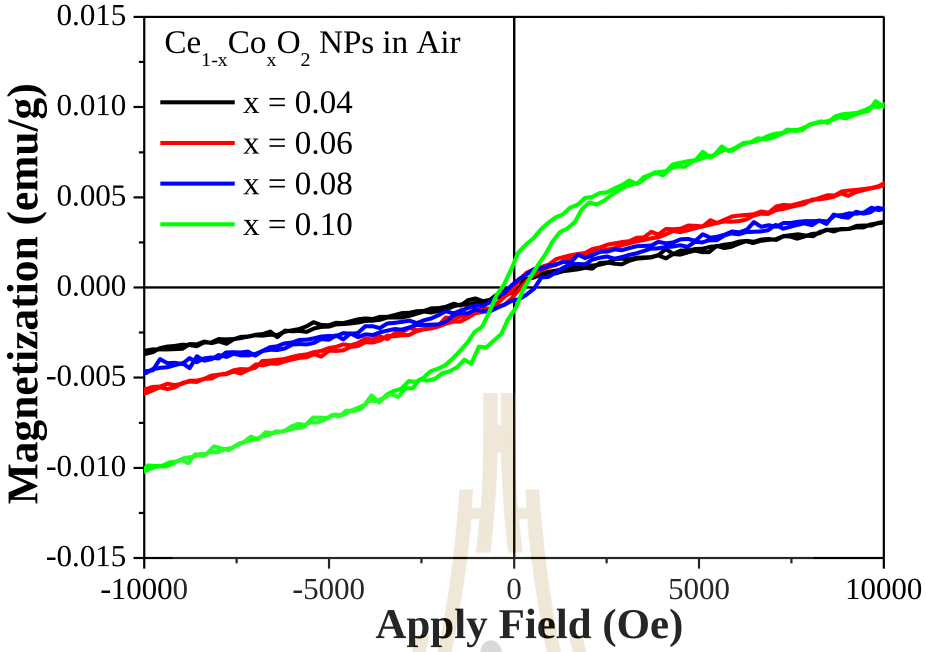

Figure 4.54 *M*-H curve at 300 K obtained from VSM measurements of $Ce_{1-x}Co_xO_2$ NPs where 0≤ x ≤10 calcined at 800 °C.

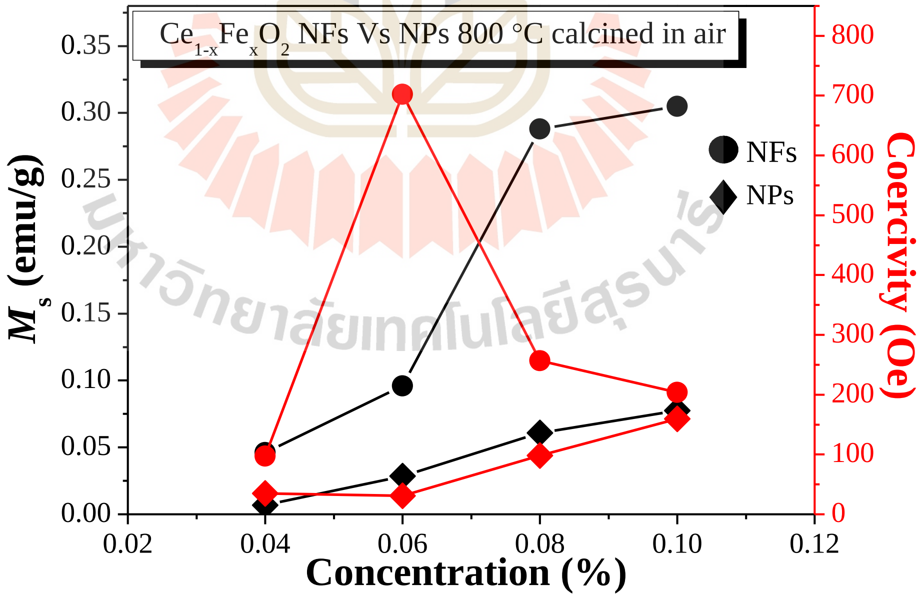

Figure 4.55 Comparison between magnetization and coercivity of $Ce_{1-x}Fe_xO_2$ nanoparticles and nanofibers at 300 K.

To explain the origin of the ferromagnetic contribution in Fe-doped CeO_2 nanostructures, the following reasons are proposed. Two main mechanisms are responsible for the RTFM of the $Ce_{1-x}Fe_xO_2$ nanostructures which are the V_o and the carrier-induced FM mechanism (Wang et al., 2017). The theoretical studies suggest that V_o can cause change of the band structure of host oxides and makes a significant contribution to the ferromagnetism (Coey et al., 2005). The formation of bound magnetic polarons (BMPs), which includes electrons locally trapped by oxygen vacancy, with the trapped electron occupying an orbital overlapping with the d shells of TM neighbors, has also been proposed to explain the origin of ferromagnetism (Durst et al., 2002). In this work, the $Ce_{1-x}Fe_xO_2$ nanofibers have the nanofibrous structure which has a large surface area (Ponhan, Amornkitbamrung and Maensiri, 2014). Therefore, the oxygen vacancies are easily presence on the surface of the nanofibers, which is confirmed by the XPS results. This results in the RTFM exhibited in the $Ce_{1-x}Fe_xO_2$ NFs.

Phokha et al. (Phokha et al., 2013) have proposed that the ferromagnetism in nanospheres monodisperse is explained by the exchange interaction between electron spin moment of ions metal and V_o at the particle surface. This direct ferromagnetic coupling is called the F-center exchange (FCE) (Coey et al., 2005, Coey, 2006, Venkatesan et al., 2007). In this work, the XANES spectra show the evidence of Fe^{3+} substitution in CeO_2, and the Ce^{3+}/Ce^{4+} transition, which can be attributed to V_o in $Ce_{1-x}Fe_xO_2$ structure. Another possibility is the creation of defects with the formation of two V_o about Co^{2+} each transferring one electron to Co^{4+} to form Co^{2+} and one electron to neighboring Ce^{4+} ions, leading to the formation of two Ce^{3+} ions. The RTFM in these samples can be explained by the FCE of Fe^{3+}-V_o-Fe^{3+} complex in the nanostructures.

This FCE forms bound magnetic polarons (BMP). The neighboring BMPs are overlapping and this results in the long-range Fe-Fe ferromagnetic coupling in CeO_2. Therefore, the $Ce_{1-x}Fe_xO_2$ nanostructures exhibit room temperature ferromagnetism.

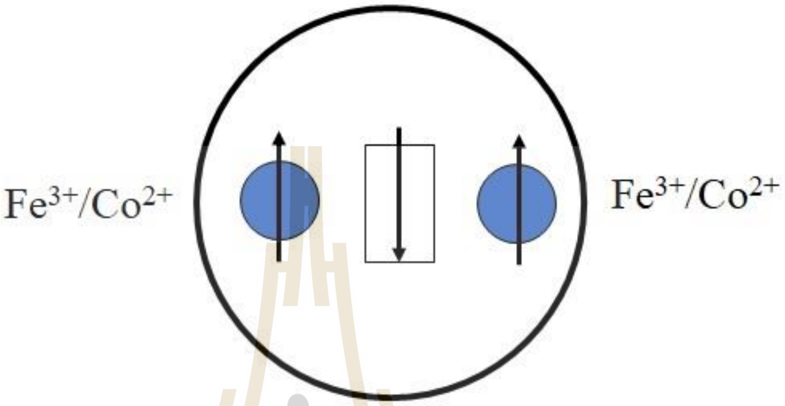

Figure 4.56 Schematic diagrams showing the F-center exchange mechanism in TM-doped CeO_2 nanostructures (adopted from Coey et al., 2004).

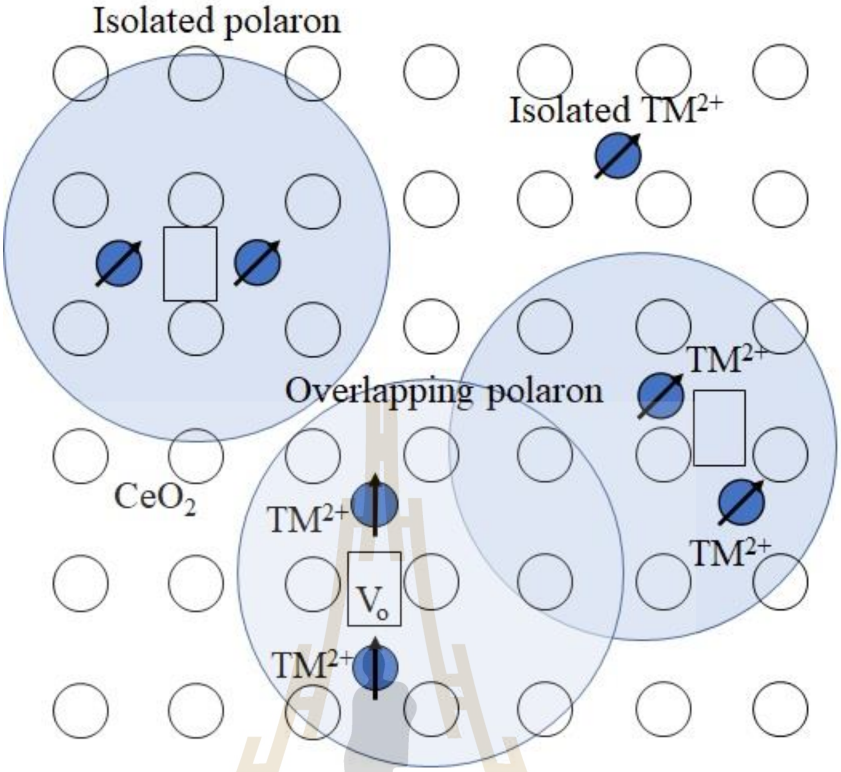

Figure 4.57 Schematic diagram of oxygen-vacancy-induced ferromagnetism through overlapping of polarons (adopted from Coey et al., 2005).

Table 4.21 Summary of magnetization (*M*) and coercivity of CeO_2 and $Ce_{1-x}Fe_xO_2$ samples calcined at 800 °C for 2 h in air.

Doping level	$Ce_{1-x}Fe_xO_2$ nanofibers		$Ce_{1-x}Fe_xO_2$ nanoparticles	
	M at 10 KOe (emu/g)	Coercivity (Oe)	*M* at 10 KOe (emu/g)	Coercivity (Oe)
X = 0	0.42	-	-	-
X = 0.04	0.046	35	0.067	97
X = 0.06	0.096	31	0.028	702
X = 0.08	0.288	98	0.061	257
X = 0.10	0.305	159.5	0.078	204

4.4.2 Effect of nonmagnetic doping

Figure 4.58 shows the *M*-H curve at 300 K of $Ce_{1-x}La_xO_2$ NPs. The $Ce_{1-x}La_xO_2$ NPs exhibit room-temperature weak ferromagnetism. The magnetization (*M*) increases with the La ions doping content, but it decreases when x = 0.08. This may be because of the increase of La^{3+} participating in the ferromagnetism interaction which is clearly seen from our qualitative and quantitative XANES data. The highest *M* of approximately 0.015 emu/g was observed for the sample $Ce_{0.90}La_{0.10}O_2$ calcined at 700 °C (considered by calcine temperature). The *M* and coercivity values of La doped CeO_2 NPs are shown in Table 4.22.

The decrease of magnetization after x = 0.08 is because La ions in structure are over the maximum doping level, which reduces oxygen vacancy in the structure as confirmed by XPS results (Coey, Ackland, Venkatesan and Sen, 2016). The ferromagnetism in $Ce_{1-x}La_xO_2$ NPs might be contributed from the long-range La ions alone for $Ce_{1-x}La_xO_2$ and the vacancies/defects in the samples which can be activated in the nanostructures and induced during the calcination process. Also, the coercivity value of $Ce_{1-x}La_xO_2$ increases with i La concentration. Main mechanisms which responsible for the RT-FM of the $Ce_{1-x}La_xO_2$ are the oxygen vacancies and the carrier-induced FM mechanism (in these cases carrier-induced is La ions).

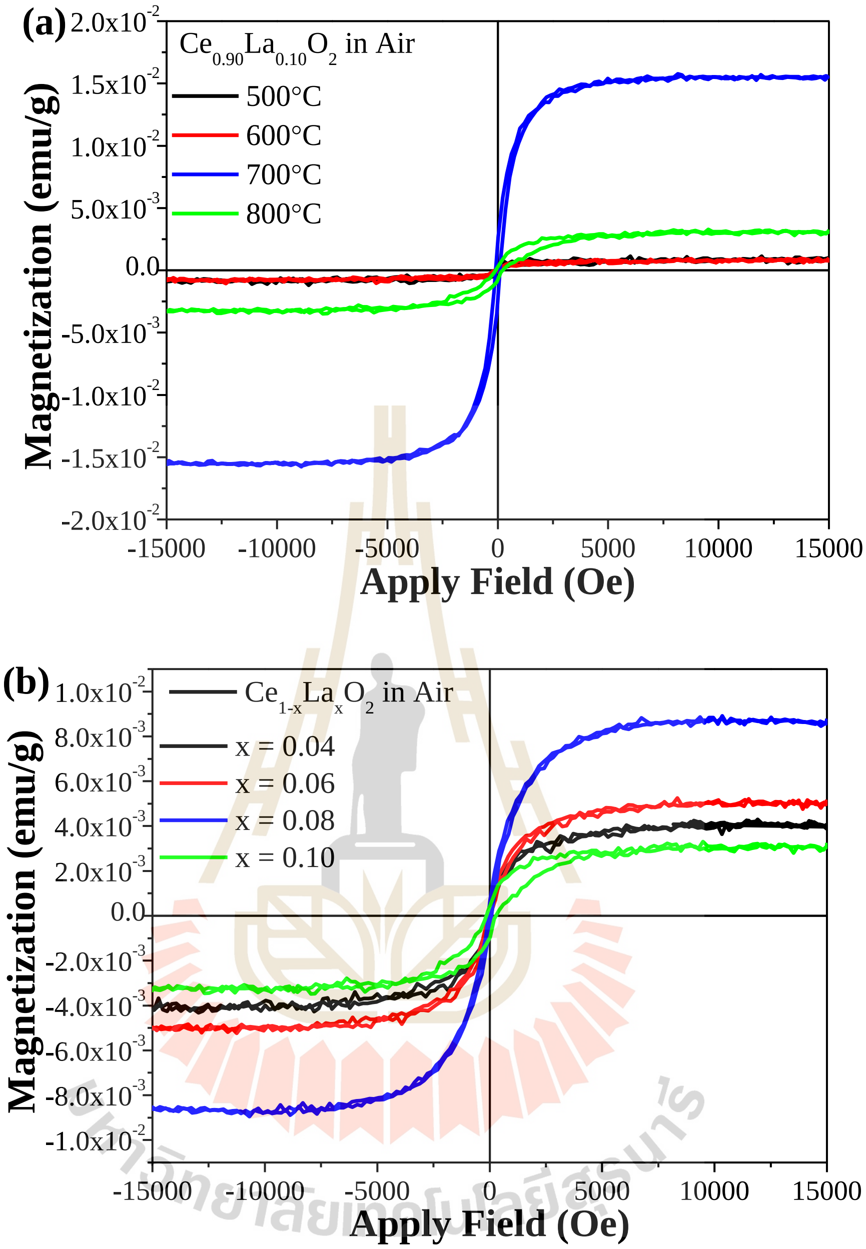

Figure 4.58 *M*-H curve at 300 K obtained from VSM measurements of (a) $Ce_{0.90}La_{0.10}O_2$ NPs calcined at 500-800 °C for 2 h in air and (b) $Ce_{1-x}La_xO_2$ NPs where 0≤x≤ 10 calcined at 800 °C.

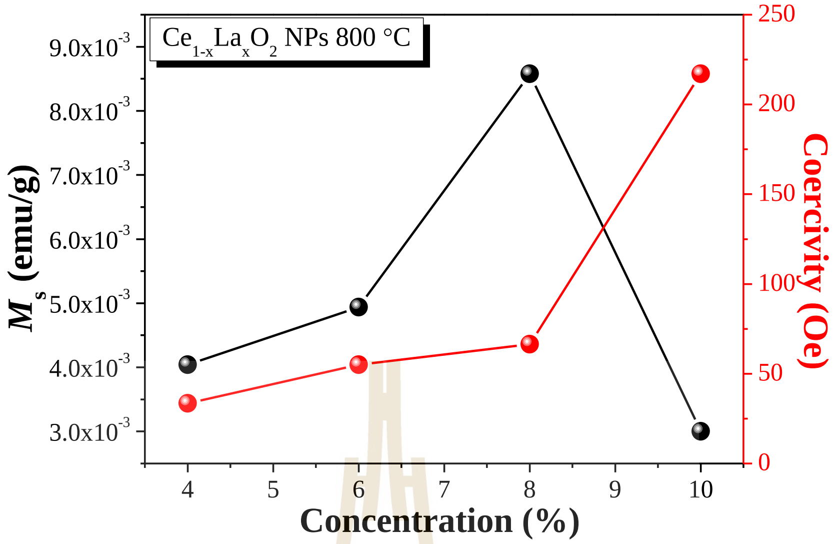

Figure 4.59 Comparison between magnetization and coercivity of $Ce_{1-x}La_xO_2$ NPs at 300 K.

Table 4.22 Summary of magnetization (*M*) and coercivity of CeO_2 and $Ce_{1-x}La_xO_2$ NPs calcined at 800 °C for 2 h in air.

Doping level	$Ce_{1-x}La_xO_2$ nanoparticles *M* at 15 KOe (emu/g)	Coercivity (Oe)
X = 0	0.0042	90.25
X = 0.04	0.0041	33.50
X = 0.06	0.00494	55.00
X = 0.08	0.00858	66.50
X = 0.10	0.003	217.00

4.4.3 Zero field cooling (ZFC) and field cooling (FC) measurement

The low temperature magnetic behavior was investigated by zero- field-cooled (ZFC) and field-cooled (FC) measurements. Figure 4.60 shows ZFC-FC curves of $Ce_{1-x}Fe_xO_2$ NPs calcined at 800 °C recorded from 50 to 350 K temperature range. The ZFC curve was obtained by initially cooling the sample from 350 to 50 K in the absence of magnetic field and heating up in 500 Oe field while recording magnetization. For the FC measurements, sample was cooled down in the same field and magnetization was recorded while heating-up (FC). It is observed that Curie transition temperature (T_c) of $Ce_{1-x}Fe_xO_2$ NPs calcined at 800 °C is above 390 K. FC curves of s $Ce_{1-x}Fe_xO_2$ NPs also show absence of T_c below 350 K. The XRD results measured at room temperature in the previous subsection show no evidence for the presence of possible oxide phase of iron.

M-T curves of CeO_2, $Ce_{0.96}Fe_{0.04}O_2$ and $Ce_{0.90}Fe_{0.10}O_2$ NPs are different as shown in Figure 4.60. The FC of $Ce_{0.96}Fe_{0.04}O_2$ NPs exhibit ferromagnetic behavior without secondary phase from FeO or Fe_2O_3. This also confirm that Fe ions were completely substituted into $Ce_{0.96}Fe_{0.04}O_2$ NPs in structure. However, *M*-T curves of $Ce_{0.90}Fe_{0.10}O_2$ NPs shows curve at 90 K exhibiting the antiferromagnetic effect from FeO. This is not detectable in the XRD results because of detection limit of XRD. This result indicates that the magnetic behavior of $Ce_{0.90}Fe_{0.10}O_2$ NPs is the combination of double exchange interaction (from Fe^{3+}-V_o-Fe^{3+}) and FeO. The inverse magnetic susceptibility versus temperature ($\chi^{-1}(T)$) curves in temperature range of 50 K to 350 K is illustrated in Figure 4.61. The para/antiferromagnetic behavior and the magnetic susceptibility can be simply fitted to the modified Curie-Weiss law (Amoretti and Fournier, 1984) quite well in high temperature region (300 K – 350 K).

$$\chi = \frac{C}{T-\theta} + \chi_0 \qquad (4.5)$$

Where χ, χ_0, θ and C are the susceptibility, temperature independent susceptibility (sum of Pauli, Landau and core susceptibilities), the Curie-Weiss temperature and Curie constant, respectively. Using $C=N\mu_{eff}^2/3k_B=Ng^2\mu_B^2 s(s+1)/3k_B$, with N = number of magnetic ions/g, k_B = Boltzmann constant, μ_{eff} = effective magnetic moment; $\mu_{eff}=g\mu_B\sqrt{s(s+1)}$. In the case of Fe-doped CeO_2, θ and C are estimated to be 140 K and 0.0328 emu g^{-1} Oe^{-1}. The effective magnetic moment $\mu_{eff} \sim 1.51$ μ_B for Fe ion. In principle, a $Fe^{3+}(d^5)$ ion at the high-spin (HS) are configured as (↑↑↑↑↑; $s = 5/2$) or Low-spin (LS) configuration (↑↑↑↑↑; $s = 1/2$). A number of studies suggest that the Fe^{3+} ions of Fe-doped CeO_2 adopt the LS configuration. Our results are close to the values of LS Fe^{3+} ($s = 1/2$, $\mu_{eff} \sim 1.73\ \mu_B$). This result suggests the ferromagnetic interactions in structure of $Ce_{1-x}Fe_xO_2$ system.

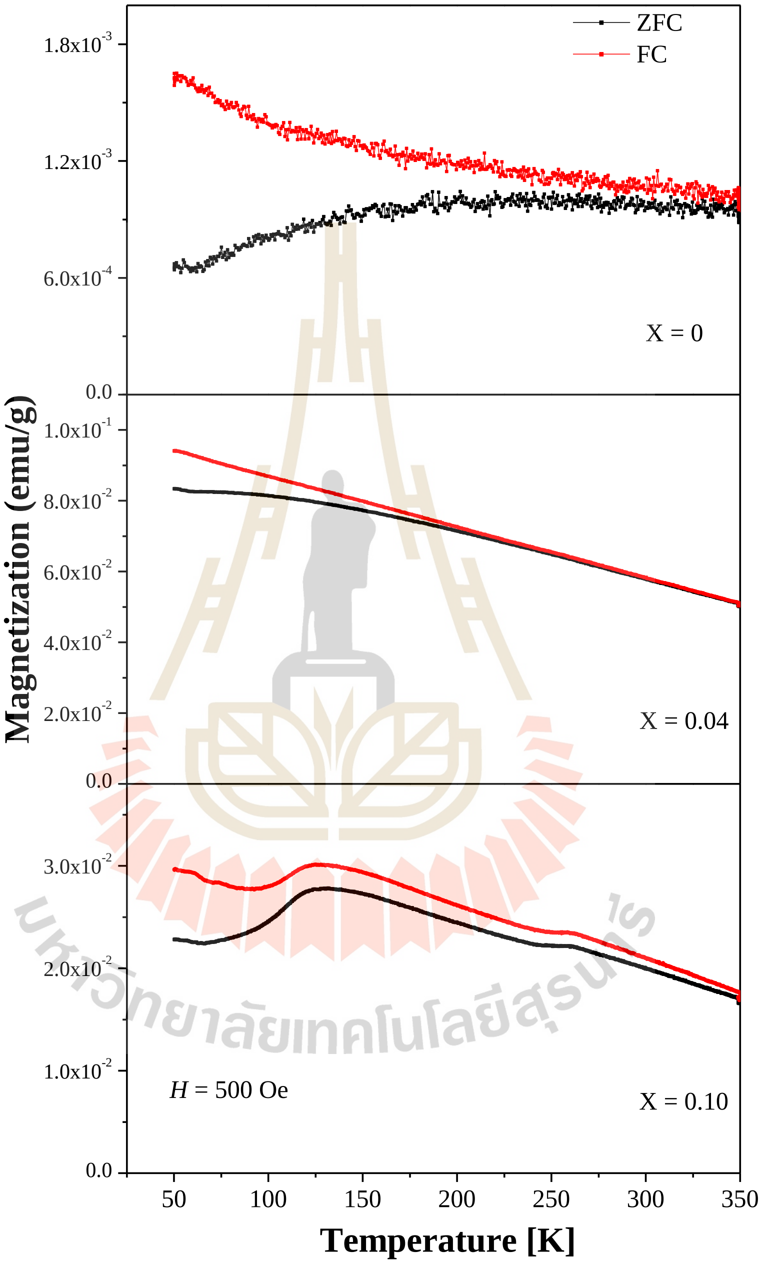

Figure 4.60 *M*-T curves at 500 Oe of samples $Ce_{1-x}Fe_xO_2$ nanoparticles calcined at 800 °C in air.

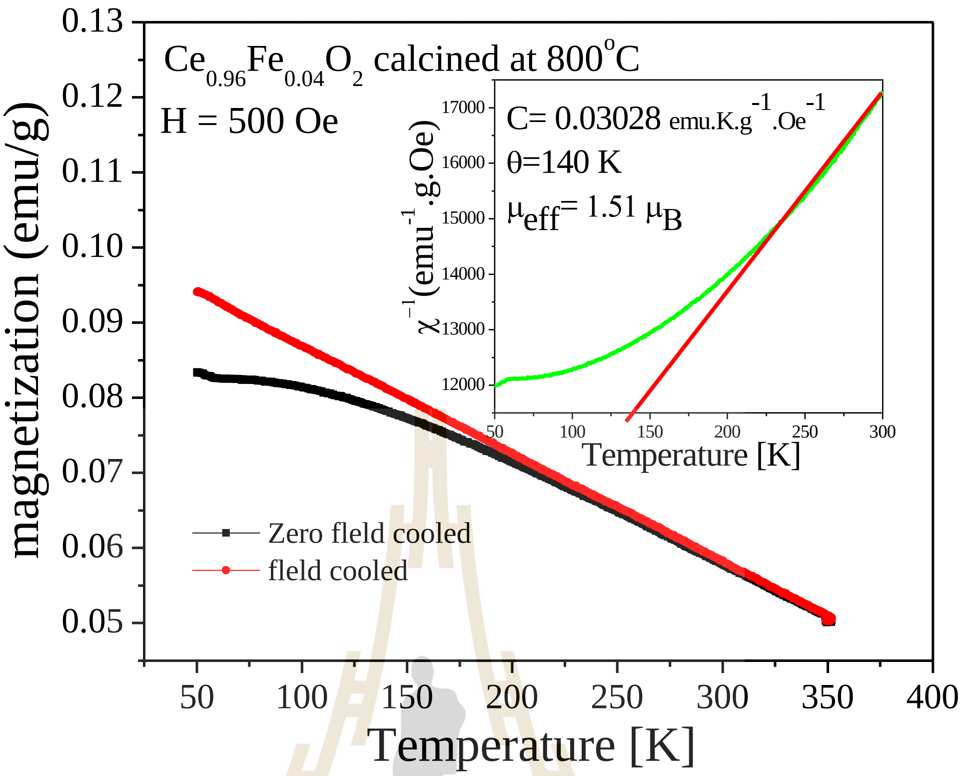

Figure 4.61 Modified Curie-weiss fitting to the data between 50 K and 350 K under 500 Oe as a function of temperature and fitting result using the modified Curei-weiss law.

4.5 Electrochemical properties

In this section, the electrochemical properties and the capacitive performance of CeO_2 electrode were evaluated using cyclic voltammetry (CV), galvanostatic charge/discharge (GCD) techniques in 6 M KOH electrolyte solution. The CV measurement was performed in the potential range of -1.2-0 V in scan rate 2-200 mV s^{-1}. The galvanostatic charge/discharge test was run at the current density of 0.5, 0.75, 1 and 2 A g^{-1}.

4.5.1 Cyclic Voltammetry measurement

Figure 4.62-4.63 show cyclic voltammograms of CeO_2 NP and NF electrodes in 6 M KOH electrolyte. The measured currents were normalized with the electrode mass. The charged/discharged current of all the electrodes strongly increased with the large scan rate. The CV curve areas of CeO_2 NF electrode are close to those of CeO_2 NP electrode. The characteristics of redox peaks indicating to the electron reduction/oxidation transition were observed in the CV curve of both CeO_2 NP and CeO_2 NF electrodes. No cathodic peak was observed during the selected potential window, while the positive current peak in which arises from the anodic reduction was clearly observed at around -0.6 V for both CeO_2 NP and NF electrodes. This result indicates that CeO_2 nanoparticles create the pseudo capacitance. It was confirmed that in, the comparison of CV curves between CeO_2 NFs and Ni foam electrodes is also shown in Figure 4.64. This anodic peak is probably associated with the reduction of Ce^{4+} (0.6 V) of the CeO_2 (Wen et al., 2011). This result suggests the potential of CeO_2 nanoparticles for an electrode material. This give us the idea to synthesize the composites of CeO_2 nanoparticle and carbon nanofiber electrode presented in Chapter 5.

4.5.2 Galvanostatic charge/discharge measurements

Figure 4.65-4.66 show the galvanostatic charge/discharge curves of CeO_2 NFs and CeO_2 NPs electrodes in 6 M KOH aqueous solution. The cut-off voltage of charging/discharging was -1.0-0 V. The measurement was performed at different current density of 0.5, 0.75, 1 and 2 A g^{-1} in a three-electrode system. It was found that the shape of charge/discharge curve for all electrodes is not linear and symmetric. The specific capacitance was calculated from a half-maximum region as suggested by Stoller and Ruoff method (Stoller and Ruoff, 2010), thus the specific capacitances of all electrodes tend to decrease when the current density increased. The GDC curve was used to evaluate the specific capacitance according to Equation (3.9), which shows that the specific capacitance values of the CeO_2 NFs and CeO_2 NPs are a function of current density (Figure 6.67). The specific capacitance of CeO_2 NFs calcined at 500 °C electrode yields a value of ~44 F g^{-1} at current density of 0.5 A g^{-1} that appears to be much higher than the other electrodes.

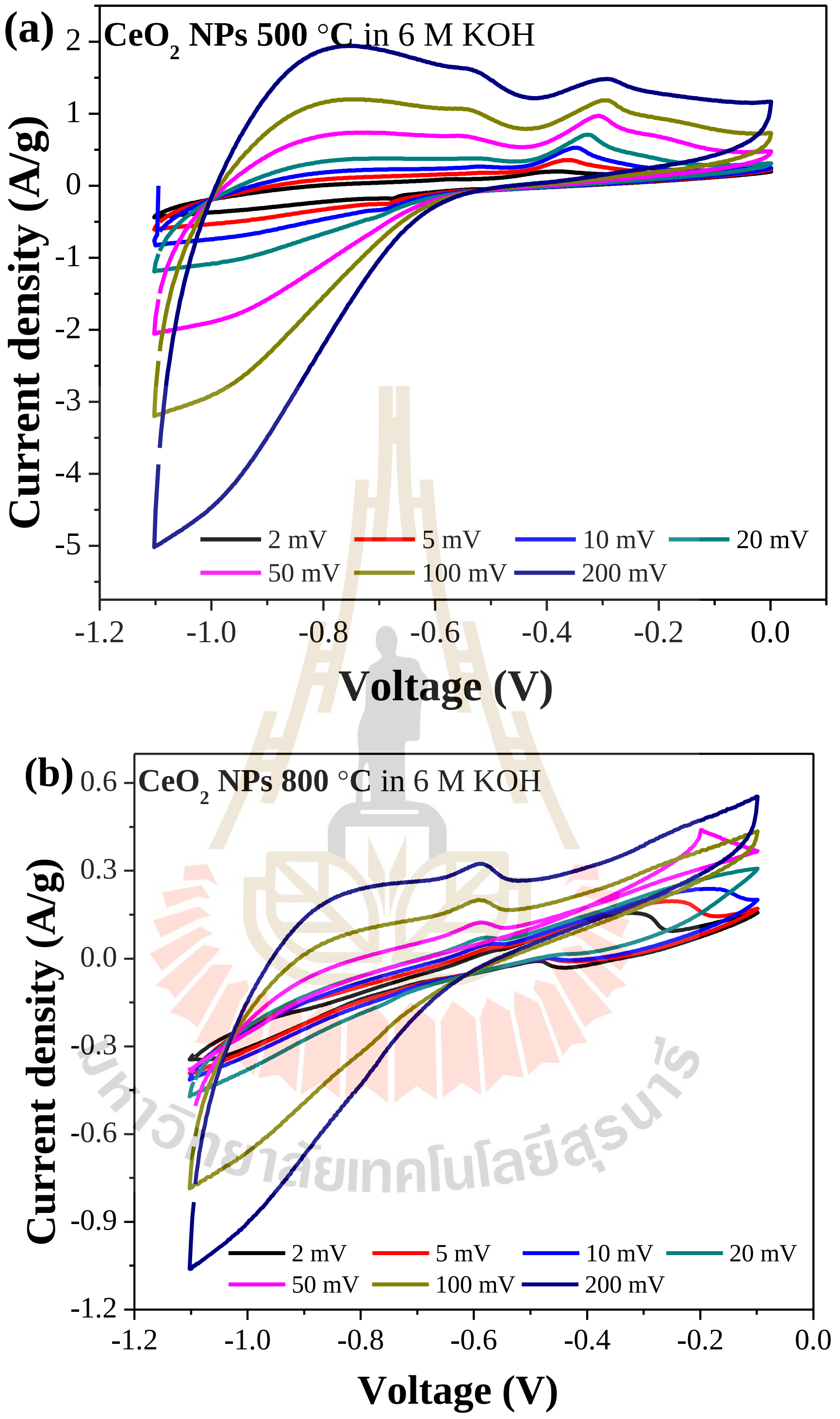

Figure 4.62 CV curves of CeO_2 NPs calcined at (a) 500 °C and (b) 800 °C by vary scan rate.

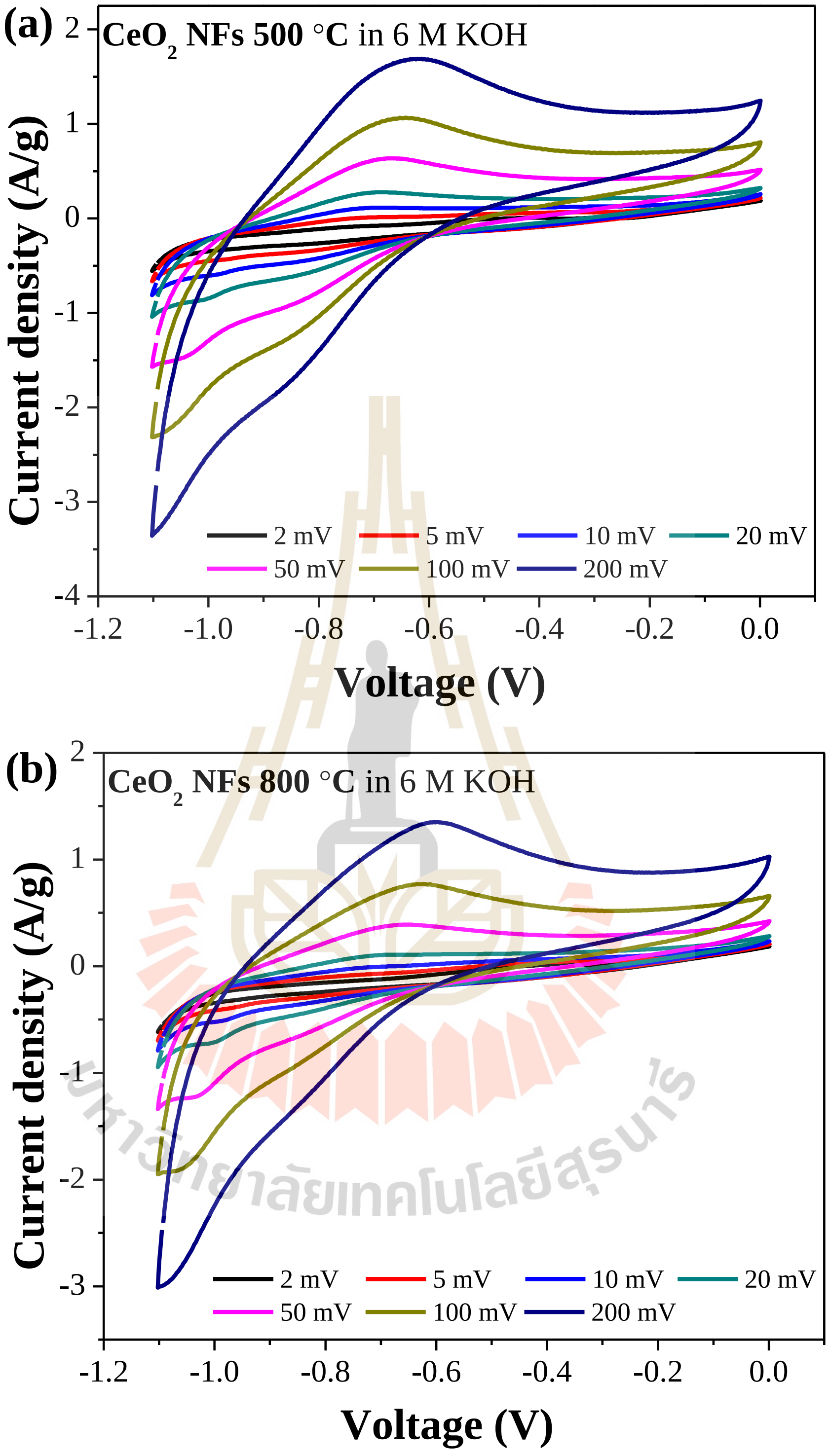

Figure 4.63 CV curves of CeO$_2$ NFs calcined at (a) 500 °C and (b) 800 °C by vary scan rate.

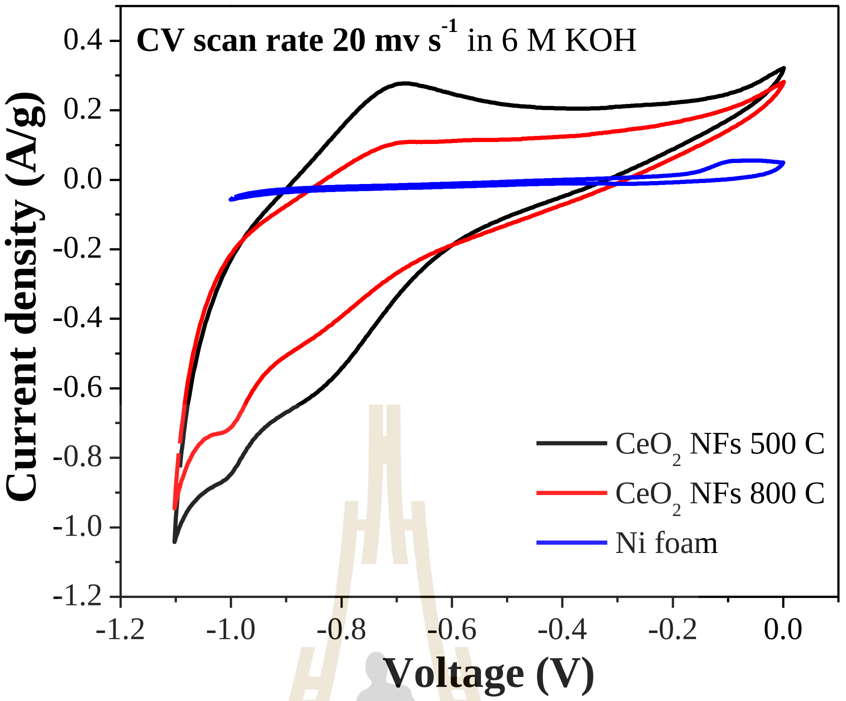

Figure 4.64 Comparison of CV curves between CeO_2 NFs calcined at 500 °C, 800 °C and Ni foam at scan rate 20 mV s^{-1}.

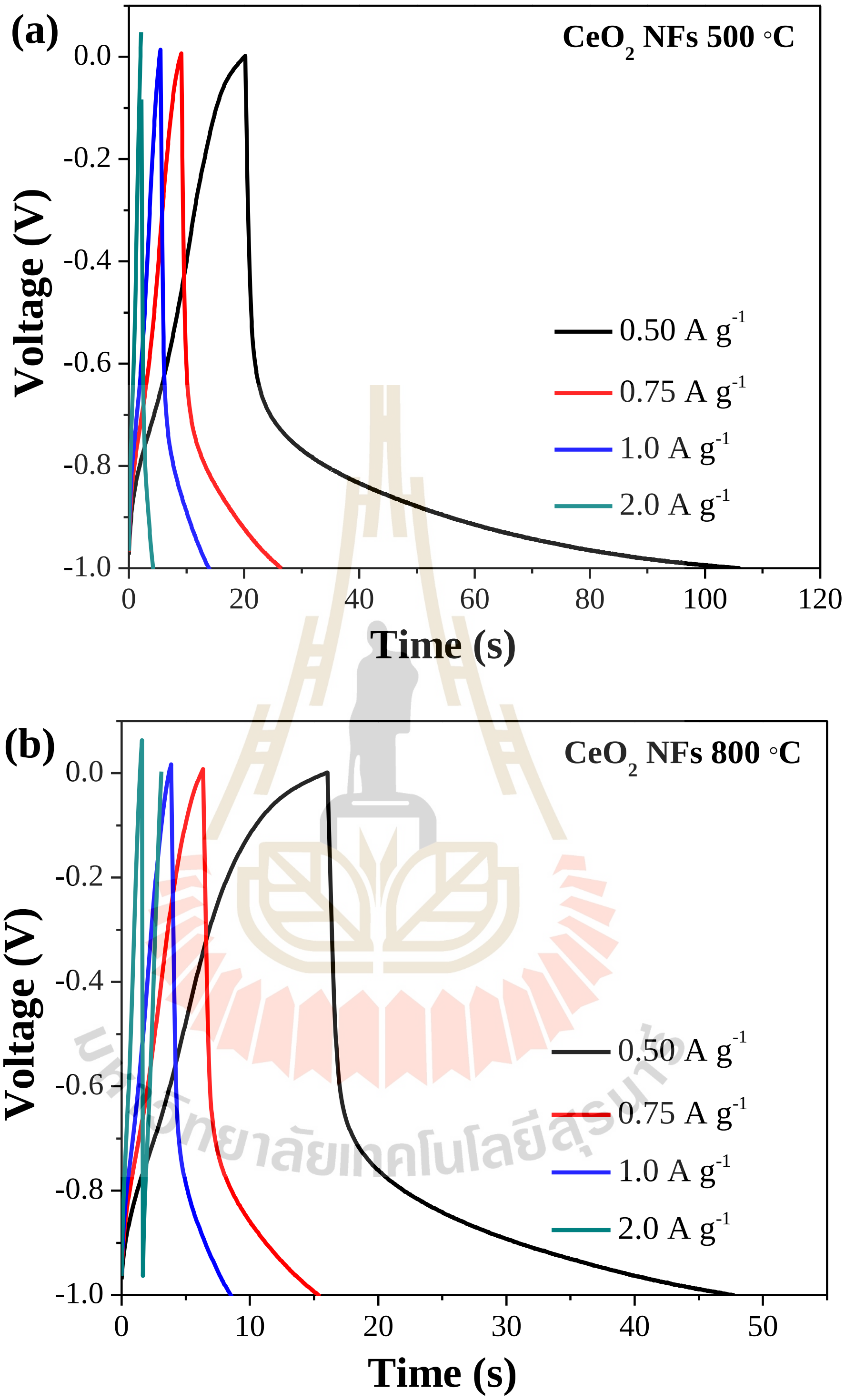

Figure 4.65 CDC of CeO$_2$ NFs samples at 0.5, 0.75, 1 and 2 A g^{-1} (a) calcined at 500 °C and (b) 800 °C.

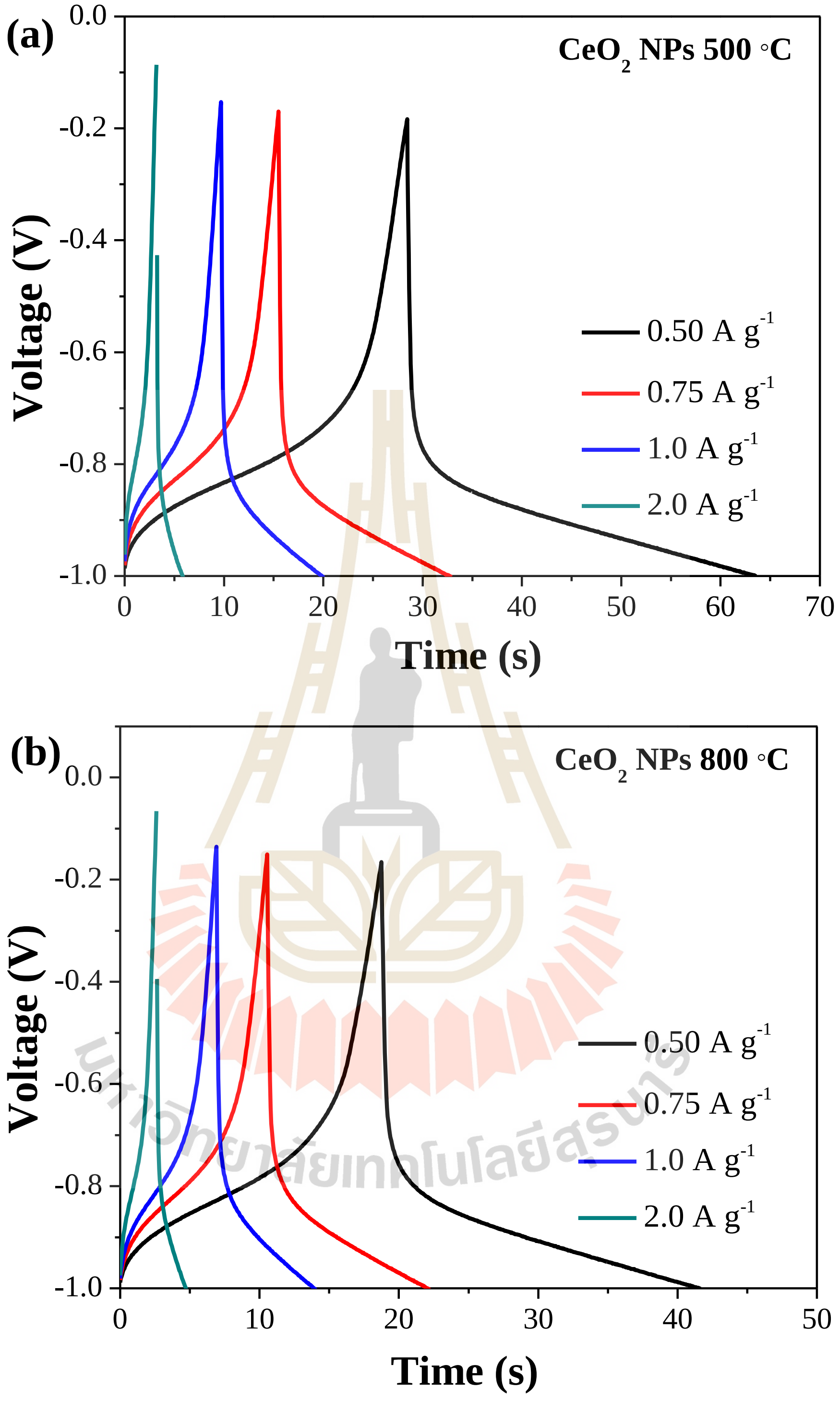

Figure 4.66 CDC of CeO_2 NPs samples at 0.5, 0.75, 1 and 2 A g^{-1} (a) calcined at 500 °C and (b) 800 °C.

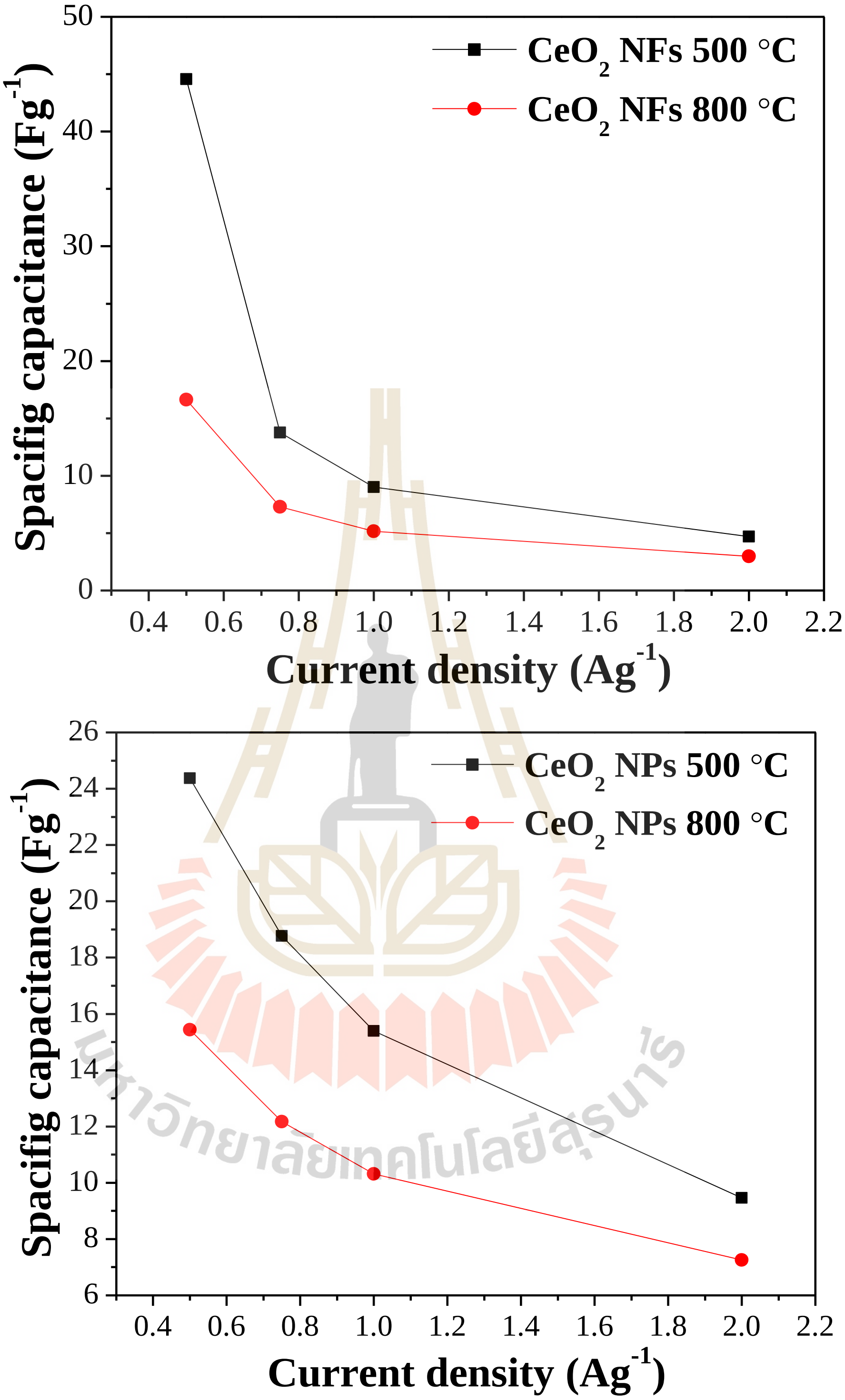

Figure 4.67 Specific capacitance of CeO_2 nanostructures calcined at 500 °C and 800 °C in air.

4.5.3 Effect of metal doping in CeO_2 nanostructure

Figure 4.68(a-d) shows the voltammogram (CV) of $Ce_{0.90}Fe_{0.10}O_2$, $Ce_{0.90}Co_{0.10}O_2$, $Ce_{0.90}Cu_{0.10}O_2$ and $Ce_{0.90}La_{0.10}O_2$ electrodes recorded over the potential window of -1.1 to 0 V in 6 M KOH. It was found that the area surrounded by CV curves for the $Ce_{0.90}Fe_{0.10}O_2$ electrode is larger than that of other electrodes suggesting the largest induced current and thus supporting the high cell capacitance. In addition, a redox peak was observed at around 0.50 V for $Ce_{0.90}Fe_{0.10}O_2$ electrode as shown in Figure 4.60 (e). This redox peak suggests that the charge storage mechanism is via the reduction/oxidation transition of $Ce_{0.90}Fe_{0.10}O_2$ showing the pseudocapacitance behavior. During oxidation reaction, ions are transferred from electrolyte to the electrode (generated positive current), while the ions are released back into the electrolyte during reduction reaction (generated negative current).

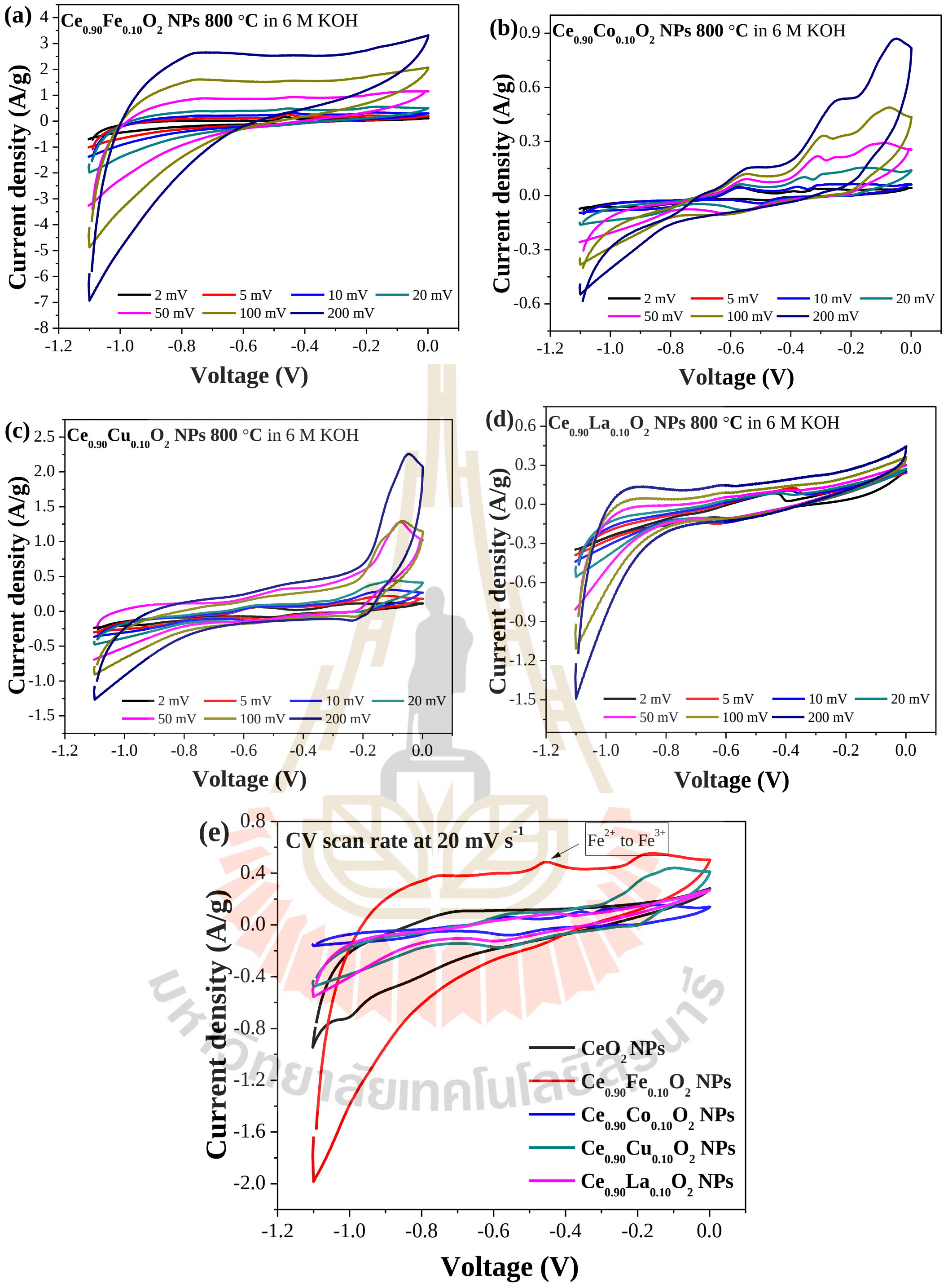

Figure 4.68 CV curves of (a) $Ce_{0.90}Fe_{0.10}O_2$, (b) $Ce_{0.90}Co_{0.10}O_2$, (c) $Ce_{0.90}Cu_{0.10}O_2$, (d) $Ce_{0.90}La_{0.10}O_2$ at different scan rates (e) Comparison of CV curves of all samples.

CHAPTER V

CHARACTERIZATION AND ELECTROCHEMICAL PROPERTIES OF C/CeO_2 COMPOSITE NANOFIBERS

This work investigates the introduction of CeO_2 NPs into carbon nanofibers (CNFs) to enhance EDLC capacitance. The C/CeO_2 composite nanofibers with different content of CeO_2 were prepared by electrospinning technique. TGA/DSC were carried out to study and thermo properties and estimate the calcination temperature for the as-spun C/CeO_2 composite nanofibers. The successfully prepared C/CeO_2 composite nanofibers were characterized by XRD, SEM, TEM, RAMAN and XPS. The electrochemical properties were examined by using CV, GCD and EIS methods.

5.1 Structural and morphology characterization

Thermal behavior of as-spun C/CeO_2 composite nanofibers was evaluated using TGA and DSC., The experiments were performed under air in the temperature range of 30 °C to 1000 °C with the heating rate of 10 °C min $^{-1}$. The weight loss of samples calculated from the TGA results are shown in Figure 5.1 (a). The weight content of as-spun/$Ce(NO_3)_3$ 10, 20 and 40 wt.% are 7, 14 and 34%, respectively. This result is in good agreement with the EDX results presented in the next section. Figure 5.1 (b) shows the DSC curves of all the samples. The main exothermic peaks are observed at about 320, 354 and 360 °C for the as-spun/$Ce(NO_3)_3$ 10, 20 and 40 wt.%, respectively. The shift of the main exothermic peaks suggests that the embedding of $Ce(NO_3)_3$ enhance the cyclization reaction of nitride groups in samples.

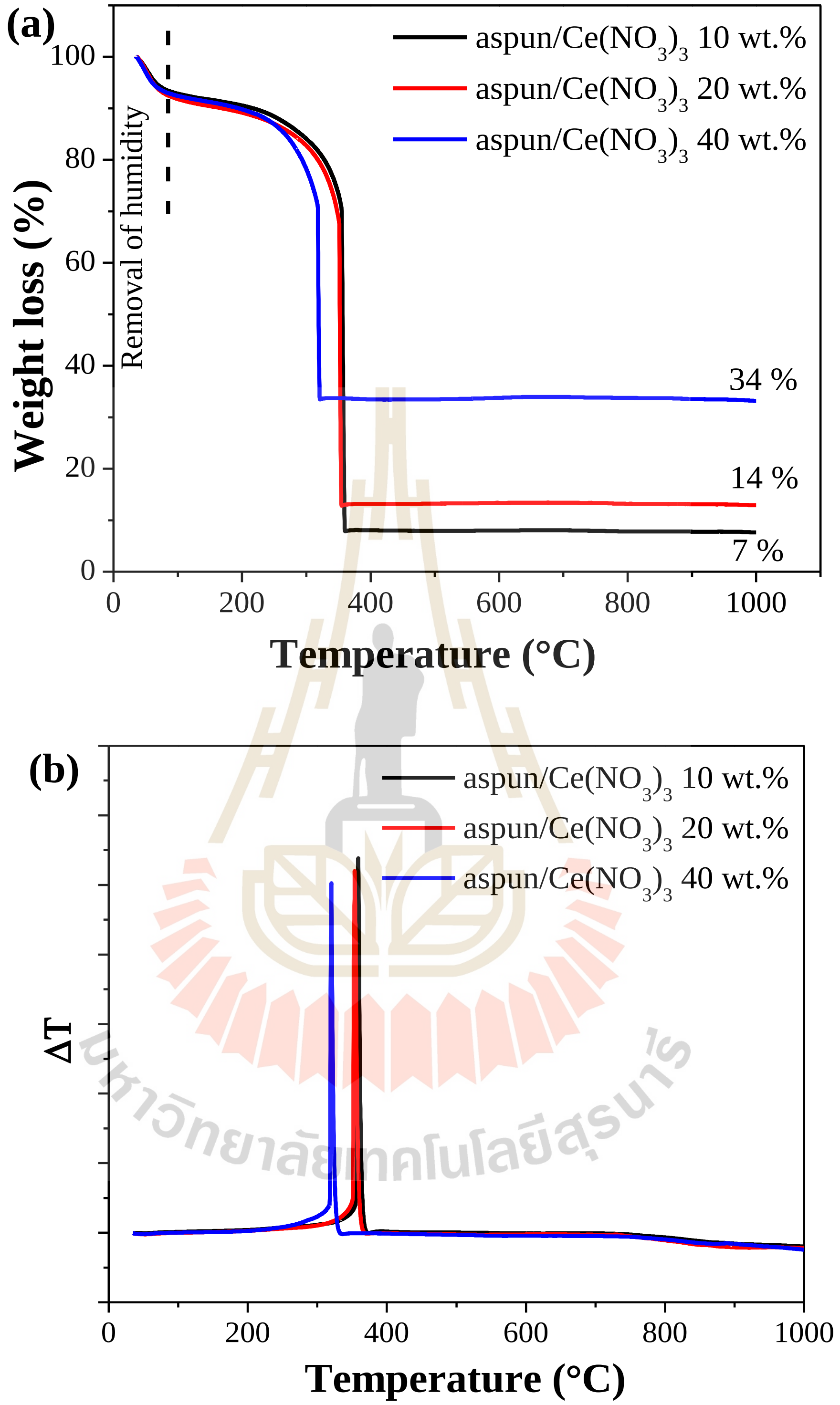

Figure 5.1 (a) TGA and (b) DSC curves of as-spun samples.

5.2 Characterizations of C/CeO$_2$ composite nanofibers

X-ray diffraction patterns of the CNF and C/CeO$_2$ composite nanofibers are presented in Figure 5.2. The main peaks at 29.13º, 33.48º, 47.98º, 56.76º, 59.52º, 68.87º, 77.09º, 79.48º and 88.72º were observed and matched well with crystallite planes of (111), (200), (220), (311), (222), (400), (331), (420) and (420), respectively, of the cubic fluorite structure of CeO$_2$ (JCPDS No. 340394) (Désaunay et al., 2013). An additional broad peak at 25.4º observed along with the other CeO$_2$ peaks indicates the presence of amorphous carbon in CNF (Cuesta, Dhamelincourt, Laureyns, Martínez-Alonso and M. D. Tascón, 1998). This result clearly confirms the formation of C/CeO$_2$ nanocomposite. The average crystallite sizes (D) of CeO$_2$ in CNF/CeO$_2$ samples were calculated from X-ray line broadening of reflection planes of (111), (200), (220) and (311) using Debye-Scherrer's equation (Eq. (3.2)) (Bernard and Stuart, 2001).

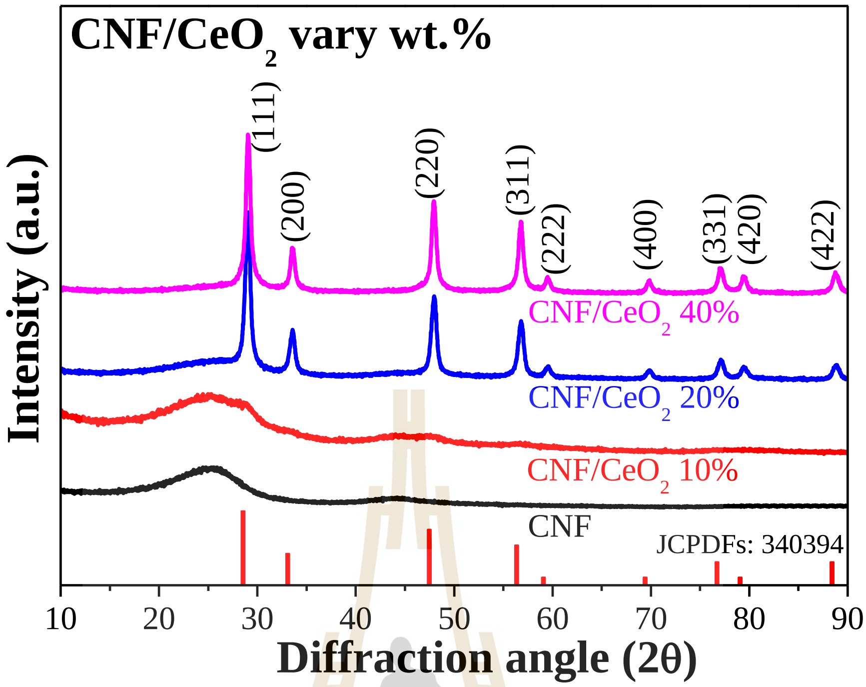

Figure 5.2 XRD patterns of CNFs and C/CeO$_2$ composite nanofibers (CeO$_2$ = 10, 20 and 40 wt.%) calcined at 900 °C for 2 h in argon.

FESEM and TEM were performed to investigate the formation and structure of the C/CeO$_2$ nanocomposites. Figure 5.3(a-b) illustrate the SEM cross-section images of as-spun CNFs before and after calcination, showing the formation of CNFs nanostructure. The obtained as-spun nanofiber sheets had a thickness of approximately 250 µm and slight down to approximately 80 µm after calcination. This is due to the loss of solvent from the nanofiber after calcination. The reduction in size and thickness of the as-spun nanostructure C/CeO$_2$ sheet produces the impact as-spun sheet which is considered as a facile method for electrode fabrication. The FESEM images of all C/CeO$_2$ composite nanofibers before and after calcination are shown Figure 5.4(a-e). The sizes of nanofibers are in the range of 242 to 1038 nm. TEM images of CNF and C/CeO$_2$ composite nanofibers shown in Figure 5.5(a-d) reveal that the CeO$_2$

nanoparticles are aggregated both on the surface and inside the CNFs nanofibers. This formation of CeO_2 nanoparticles is different from other preparation techniques in which the nanoparticles are formed only on the surface of nanostructures (Chen and Xue, 2015, Vanitha, Keerthi, Cao and Balasubramanian, 2015, Deng et al., 2017). This formation can possibly enhance the specific capacitance of the C/CeO_2 composite nanofibers. The SAED patterns of the C/CeO_2 composite nanofibers corresponding to the planes (111), (200), (220) and (311) of CeO_2 (JCPDS No. 340394) are shown in Figure 5.5(e-h). Energy dispersive X-ray spectroscopy (EDX) was carried out to confirm the chemical composition of C/CeO_2 composite nanofibers and the results are shown in (Figure5.5(i-l)). The result confirms that the wt.% and at.% of CeO_2 in the as-spun nanofibers, in good agreement with TGA results. The summary of wt.% and at.% of elements is show in the Table 5.1. Figure5.5(m-n), display typical high resolution TEM (HRTEM) images of C/CeO_2 composite nanofibers. The interplanar spacing distance of 0.270 nm and 0.311 nm correspond to (200), (111) planes of cubic CeO_2 (JCPDS 340394) which agrees well with the XRD results.

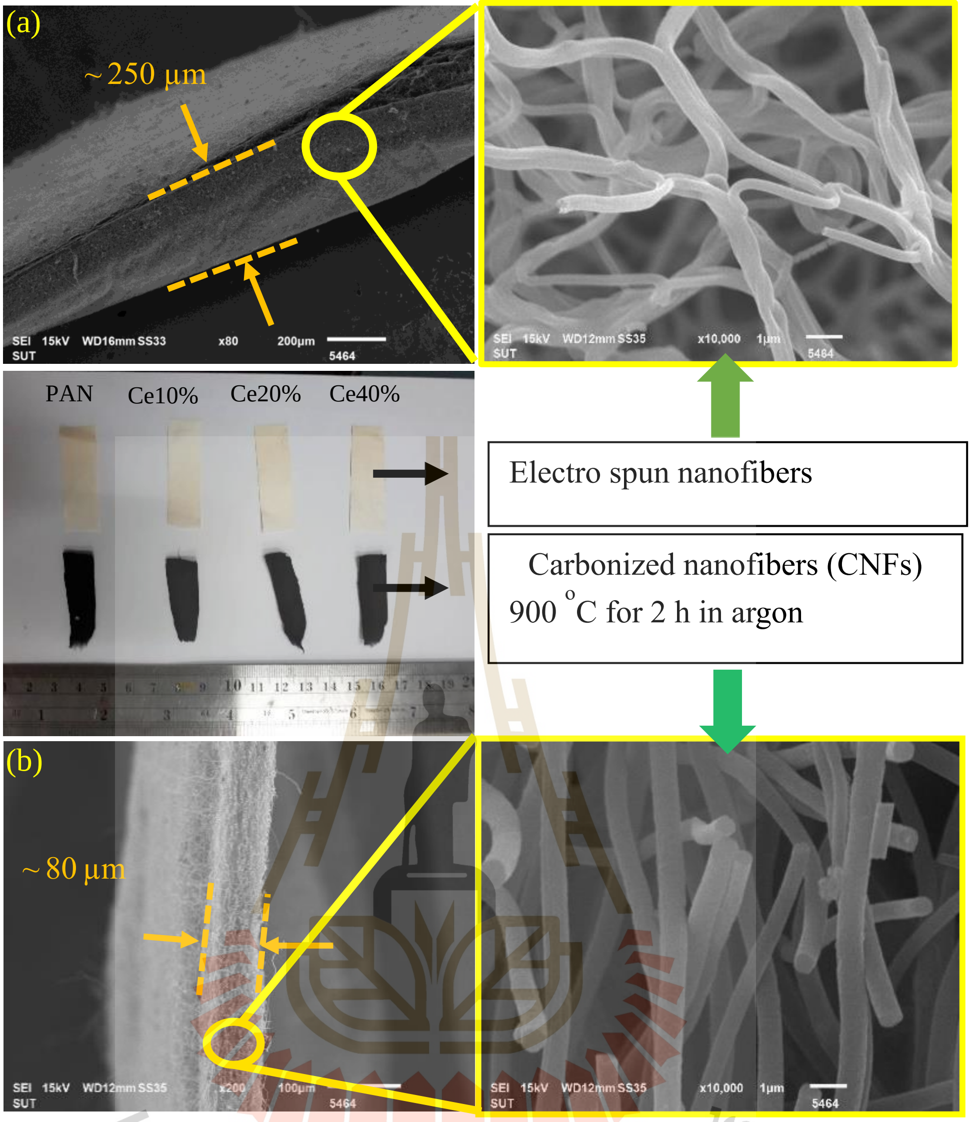

Figure 5.3 SEM Cross section image of (a) as-spun and (b) carbonized nanofibers (c) SEM images of CNFs.

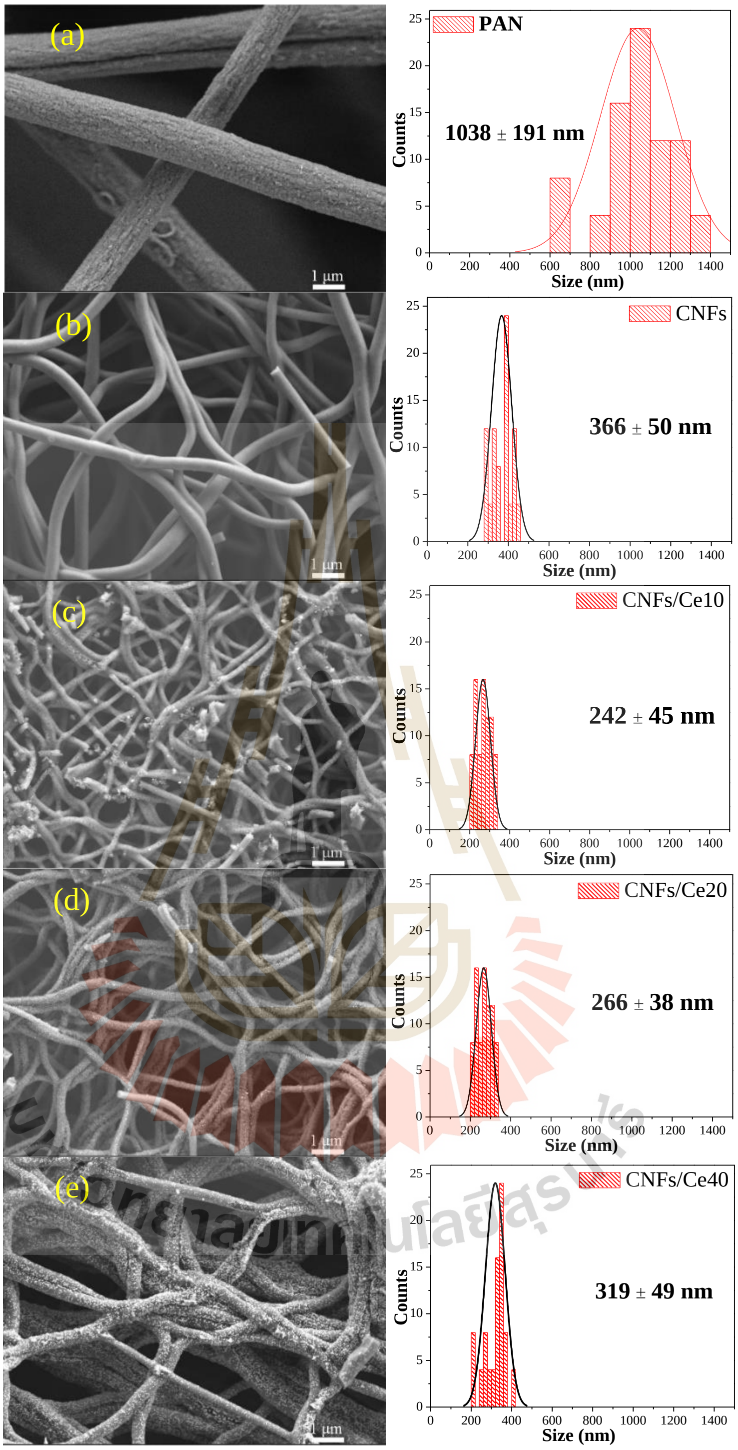

Figure 5.4 FESEM images of (a) as-spun (before calcination) and C/CeO_2 composite nanofibers (CeO_2 = (b) 10, (c) 20 and (e) 40 wt.%) calcined at 900 °C for 2 h in argon.

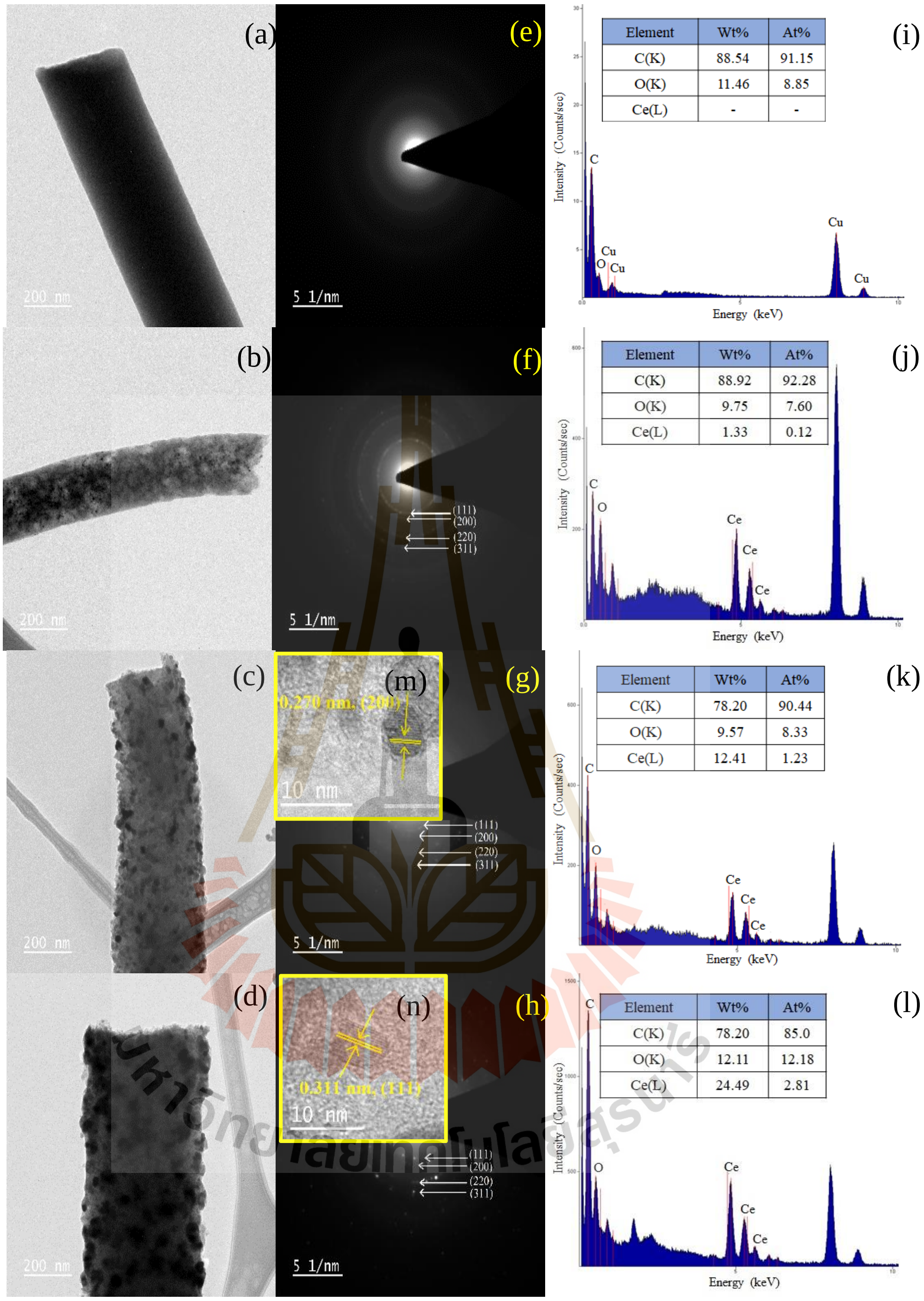

(i)

Element	Wt%	At%
C(K)	88.54	91.15
O(K)	11.46	8.85
Ce(L)	-	-

(j)

Element	Wt%	At%
C(K)	88.92	92.28
O(K)	9.75	7.60
Ce(L)	1.33	0.12

(k)

Element	Wt%	At%
C(K)	78.20	90.44
O(K)	9.57	8.33
Ce(L)	12.41	1.23

(l)

Element	Wt%	At%
C(K)	78.20	85.0
O(K)	12.11	12.18
Ce(L)	24.49	2.81

Figure 5.5 TEM bright field images with the SAED pattern and EDX spectra of (a, e, i) CNF and (b, f, j) C/CeO_2 composite nanofibers 10% wt.% , (c, g, k) 20% wt.% (d, h, l) 40 wt.% with and (m, n) HRTEM images.

Raman spectroscopy was used to study the structural characteristics of CNFs and C/CeO_2 composite nanofibers. Raman spectra of the CNF and C/CeO_2composite nanofibers are shown in Figure 5.6. The peaks observed at 1359, 1580, and 2695 cm^{-1} represent D, G, and 2D bands of CNF, respectively. The D band is a first-order zone boundary phonon mode associated with the defects in the CNF and G band is show C-C stretching mode of sp^2 bonded carbon (Cuesta et al., 1998, Fujisawa et al., 2014). The intensity ratio of D band to G band (ID/IG) reflects the degree of the defects in the CNFs. The strongest intensity mode at around 455 cm^{-1} shows the optical Raman F_{2g} mode, which is originated from oxygen stretching vibrations surrounding the Ce^{4+} (F_{2g}) in the cubic fluorite ceria (Suzuki, Kosacki, Anderson and Colomban, 2001). This mode peak of C/CeO_2compositenanofibers increases with the percentage of CeO_2. The C/CeO_2 40 wt.% composite nanofibers exhibits the strongest F_{2g} mode peak because of rich Ce-O mode in the structure. The Raman measurement confirms the formation of C/CeO_2 nanocomposite.

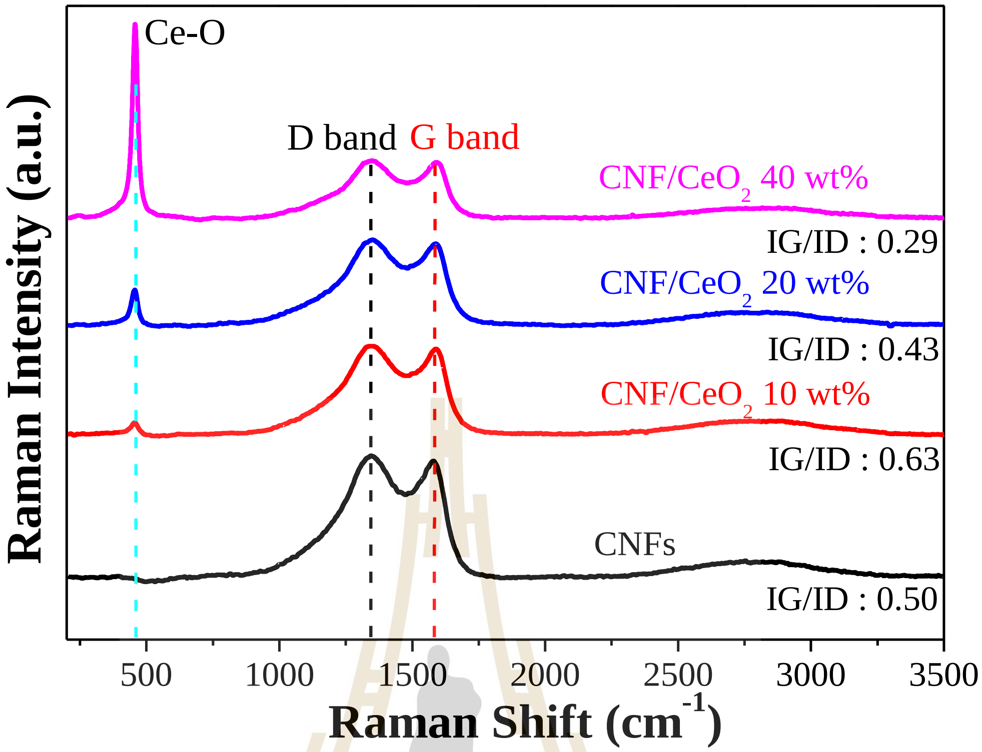

Figure 5.6 RAMAN spectra of CNFs and C/CeO$_2$ (CeO$_2$ = 10, 20 and 40 wt.%) composite nanofibers calcined at 900 °C for 2 h in argon.

The surface chemical compositions of the C/CeO$_2$ 20 wt.% was further investigated by XPS, as shown in Figure 5.7. The survey spectrum in Figure 5.7(a) shows the binding energy peaks at 287.3, 530.7 and 885.8 eV, which are attributed to C1s, O 1s and Ce3d, respectively. Figure 5.7(b-d) show high-resolution XPS spectra of Ce3d, C1s and O1s peaks. The Ce3d spectrum in Figure 5.7(b) can be deconvoluted into 10 peaks (Tsunekawa, Wang and Kawazoe, 2006). The Ce3d main peaks of Ce^{4+} including Ce3d^9 4f^0 O2p^6, Ce3d^9 4f^1 O2p^5, and Ced^9 4f^2 O2p^4, are expressed as U$^{///}$, U$^{//}$, U (for Ce3d$_{3/2}$), V$^{///}$, V$^{//}$ and V (for Ce3d$_{5/2}$) respectively. The Ce^{3+} peaks containing 3d^9 4f^1 O2p^6 and Ce 3d^9 4f^1 O2p^5, are shown as U$^{/}$, U$_0$ (for Ce3d$_{3/2}$) V$^{/}$ and V$_0$ (for Ce3d$_{5/2}$), respectively (Sonsupap et al., 2016). The C1s XPS spectrum can be fitted into four peaks as shown in Figure 5.7(c). The peak at 284.8 eV indicates the non-oxygenated C-C present in CNF. The peak at 286.5 eV is related to the C atoms bonded directly to the oxygen of hydroxyl group (C-OH). The peaks at 289.0 eV and 291.1 eV correspond to carbonyl (C=O) and carboxyl (O=C-OH) groups, respectively (Ganguly, Sharma, Papakonstantinou and Hamilton, 2011, Joung et al., 2011). The O 1s spectrum (Figure 5.7(d)) can be deconvoluted into three components at 529.8 eV, 531.8 eV and 533.9 eV corresponding to the Ce-O bond, carboxylate C-OH and C=O group, respectively (Wang, Jiang, Zheng, Xie and Zheng, 2012).

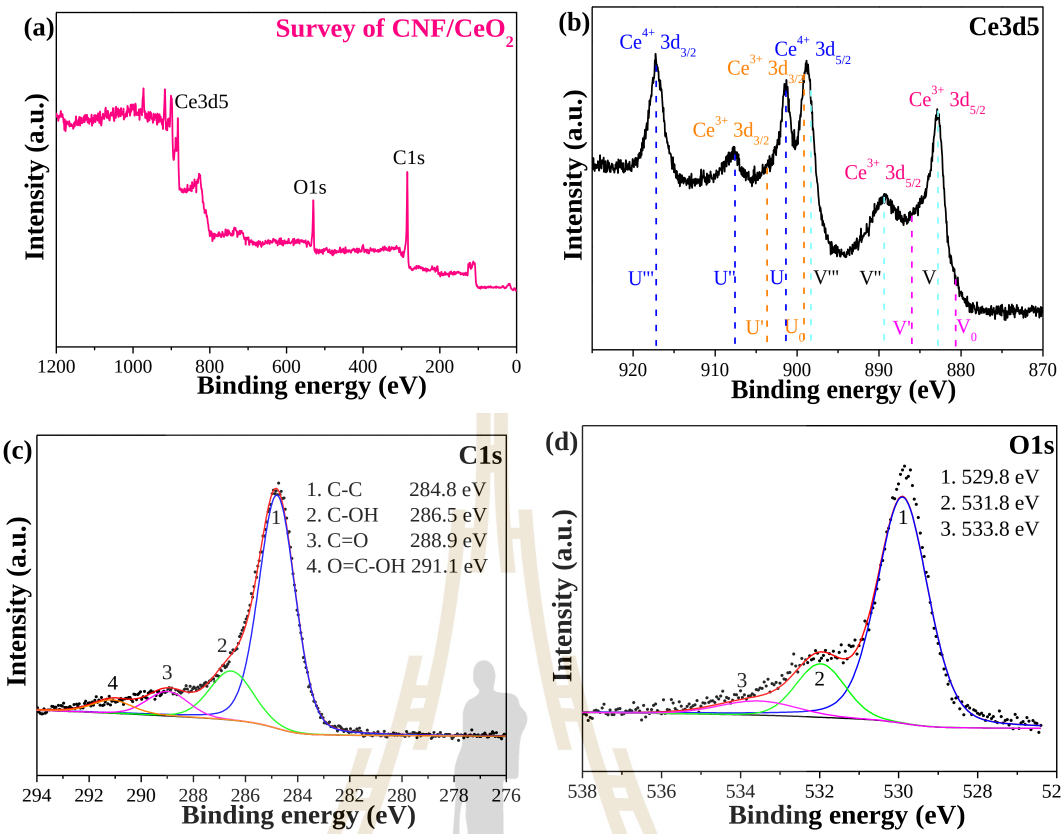

Figure 5.7 XPS spectra of C/CeO$_2$ 20 wt.% (a) survey scan (b) Ce3d5 (c) C1s and (d) O1s calcined 900 °C in argon.

The specific surface area and pore size distribution were analyzed by nitrogen adsorption-desorption isotherms at 77 K. The pure CNF exhibits a typical type I (microporous structure) isotherm, while the C/CeO$_2$composite nanofibers exhibits a mixed type between I and IV (mesoporous structure) isotherm. The interaction between the sample surfaces and adsorbates were relatively strong at low P/P_0 (<0.1) (Figure 5.8 (a)). The pore size distributions were determined by the BJH method as shown in Figure 5.8(b). The micropore size distributions of CNF and C/CeO$_2$ composite nanofibers exhibit peaks at 1.5-3 nm indicating the presence of microporous structure. The summarized porosity parameters of the samples are shown in Table 5.1. The surface area and total pore volume of the CNF and C/CeO_2 composite nanofibers are in the ranges of 211-754 m^2 g^{-1} and 0.18-0.78 cm^3g^{-1}, respectively. The specific surface area and pore volume also increase with the CeO_2 mass ratio (at 10 and 20 wt.%). This indicates that micro porosity could be adjusted by varying the ratio of CeO_2. The C/CeO_2 10 and 20 wt.% composite nanofibers have higher porous volume with high specific surface area and mesoporous feature compared to pure CNFs. This can provide more accessible sites of electrolyte ions between the reversible ion adsorption onto the carbon surface (Nilmoung et al., 2016).

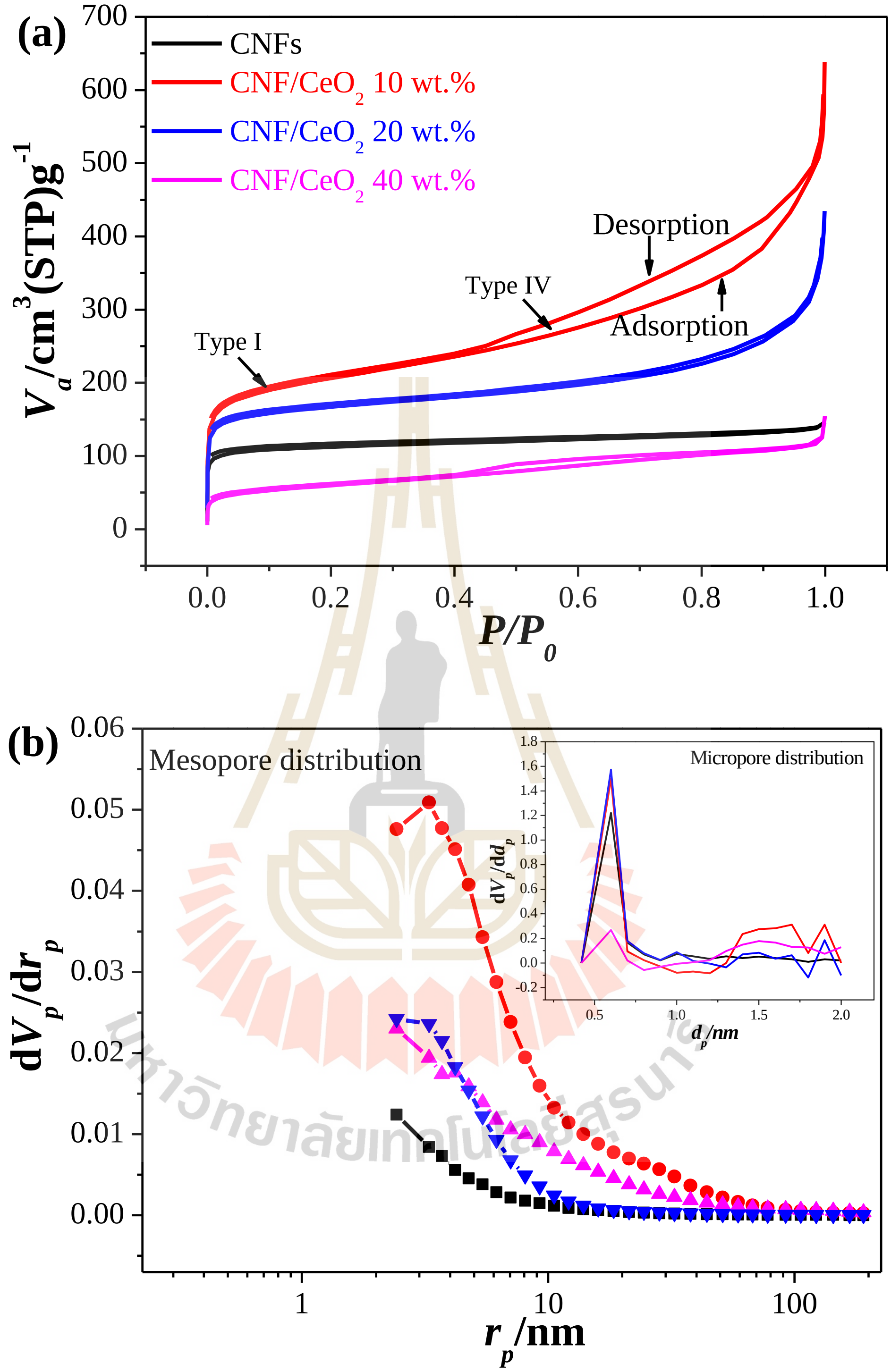

Figure 5.8 (a) N_2 adsorption/desorption isotherms and (b) pore size distributions of CNFs and C/CeO_2 composite nanofibers.

5.3 Electrochemical performances of C/CeO_2 composite nanofibers

To evaluate the electrochemical performance of CNFs and C/CeO_2 composite nanofibers. CV, GCD, and EIS techniques were applied in a three-electrode system. The CV tests were carried out in an aqueous electrolyte of 6 mol L^{-1} KOH in the potential range from -1 to 0 V at a scan rate of 10 mV s^{-1}. The CV curves in Figure 5.9 (a) of all samples exhibit a rectangular shape, similar to the ideal behavior of the EDLCs (Wang, Song and Xia, 2016). The charge storage mechanisms of the CNFs and C/CeO_2 composite nanofibers is the reversible adsorption of electrolyte ions onto the carbon surface at the electrolyte/electrode interface (Burke, 2000). It is also observed that the rectangular shape of the CV curves of C/CeO_2 20 wt.% does not change with different scan rates (Figure 5.9 (b)). This indicates good stability in the charge storing process. The GCD curves of the CNFs and C/CeO_2 composite nanofibers measured at a current density of 1.0 A g^{-1} are shown in Figure 5.10. The linear behavior of the GCD curves also demonstrates the EDLC nature of the C/CeO_2 composite nanofibers as an electrode material. The asymmetric between the charging and discharging of the GDC curves indicates that discharging time is longer than the charging time (Graydon, Panjehshahi and Kirk, 2014). The GDC curves curve was used to evaluate the specific capacitance according to Equation (3.9), which shows that the specific capacitance values of the CNFs and CNF/CeO_2 are a function of current density (Figure 5.11). The C/CeO_2 20 wt.% exhibits the specific capacitance values of 232.86, 219.5, 211.84, 197.88, 180.80, 166.55, 157.13, and 150.08 F g^{-1} at 0.5, 0.75, 1, 2, 3, 4, 5, 10, 15, and 20 A g^{-1}, respectively, which represent the highest specific capacitance among the other C/CeO_2 composite nanofibers samples as shown in Table 5.2. This may be due to its larger specific surface area than the other sample (Figure 5.8(a and b)). The CeO_2

nanoparticles inside CNFs also have a reasonable amount to enhance electron transport around surface of electrode materials. There is evident that the ternary nanocomposite had a higher value of specific capacitance than binary nanocomposite (Stoller and Ruoff, 2010, Aravinda et al., 2013, Vanitha et al., 2015). The specific capacitance of CeO_2 nanostructure are reported in Table 5.3. The discharge specific capacitance values of C/CeO_2 20 wt.% measured density at 1 A g^{-1} (211.84 F g^{-1}) was higher than another structure such as Graphene/CeO_2 89 F g^{-1}, carbon/CeO_2 61 F g^{-1} (Phokha, Hunpratub, Chanlek, Sonsupap and Maensiri, 2018), porous Carbon/CeO_2 75 F g^{-1} (Shuvo et al., 2015).

The EIS measurement was carried out in frequency range from 0.1 Hz to 100 kHz at amplitude of 0.1 V. The plot of imaginary part (-Z″) versus the real part (Z′) is shown in Figure 5.11. The intercept of the real axis indicates the solution resistance (R_s) which is the total resistance of pore-electrolyte resistance, bulk resistance, and contact resistance due to electrode and current collector surfaces. The solution resistances of 1.84, 1.66, 1.91 and 1.55 Ω were obtained for CNF, C/CeO_2 10, 20 and 40 wt.%, respectively. The EIS plots of all samples exhibit a small semicircle section in the low frequency domain corresponding to Warburg impedance (Vanitha et al., 2015). The fitting semi-circular section in the Nyquist plot can identify the charge transfer behavior in the same frequency range. The charge transfer resistance (R_{ct}) extracted from the plots are 0.23, 0.22, 0.14 and 0.26Ω for CNF, C/CeO_2 10, 20 and 40 wt.%, respectively. The C/CeO_2 20wt.% electrode exhibited the lowest R_{ct} suggesting low ion diffusion and its transportation in the electrolyte (Sarpoushi et al., 2014). The enhanced electrochemical performance in C/CeO_2 20wt.% electrode is a result of high surface area. The large surface area not only provides more electron ions insertion/extraction sites, but also facilitates fast ion transfer between electrode and electrolyte, thus leading to a large reversible specific capacity of the nanocomposite electrode (Snook, Kao and Best, 2011, Zhu, Zhu, Murali, Stoller and Ruoff, 2011). The result indicates that the incorporation of CNFs and C/CeO_2 composite nanofibers could significantly improve the electrochemical performance of electrodes.

The cycle stability of supercapacitors is of great importance for their practical applications. The cycling performance of CNFs and C/CeO_2 10, 20 and 40 wt.% nanocomposite electrodes were further investigated by galvanostatic charge-discharge tests for 1000 cycles at the current density of 5 A g^{-1}. It is shown in Figure 5.12 that the capacitance of C/CeO_2 20 wt.% electrode is still reached at 175.10 F g^{-1} and maintain at approximately 97.33% of its initial capacitance (179.89 F g^{-1}) after 1000 cycles. Figure 5.13 shows the Ragone plot for all of samples. The overall performance of the samples is excellent; the C/CeO_2 20 wt.%, shows superior energy and power density compared with the other samples.

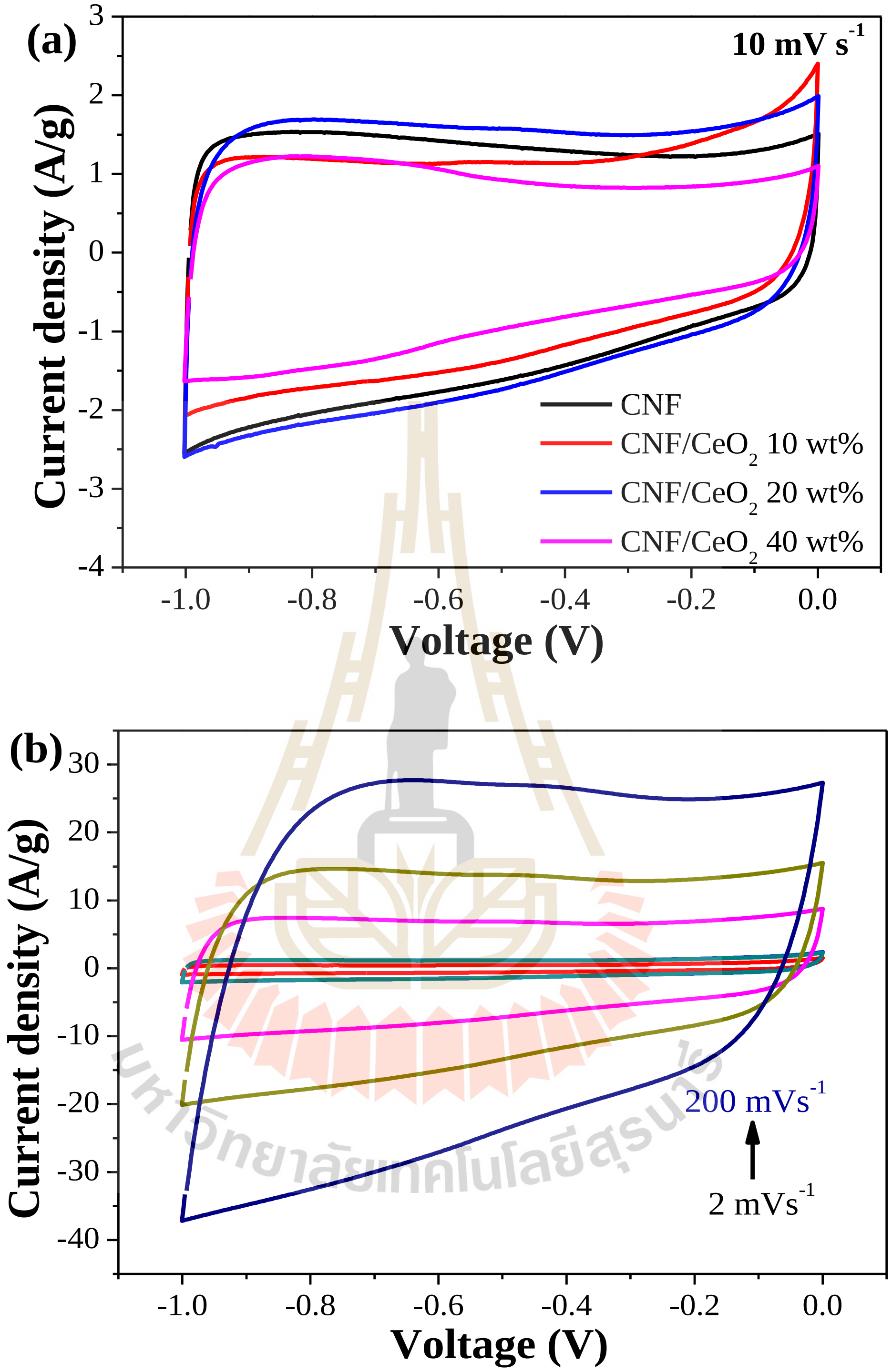

Figure 5.9 (a) CV curves of CNFs and C/CeO$_2$ composite nanofibers at 10 mV s^{-1}, (b) CV curves of C/CeO$_2$ 20 wt.% composite nanofibers with different scan rates.

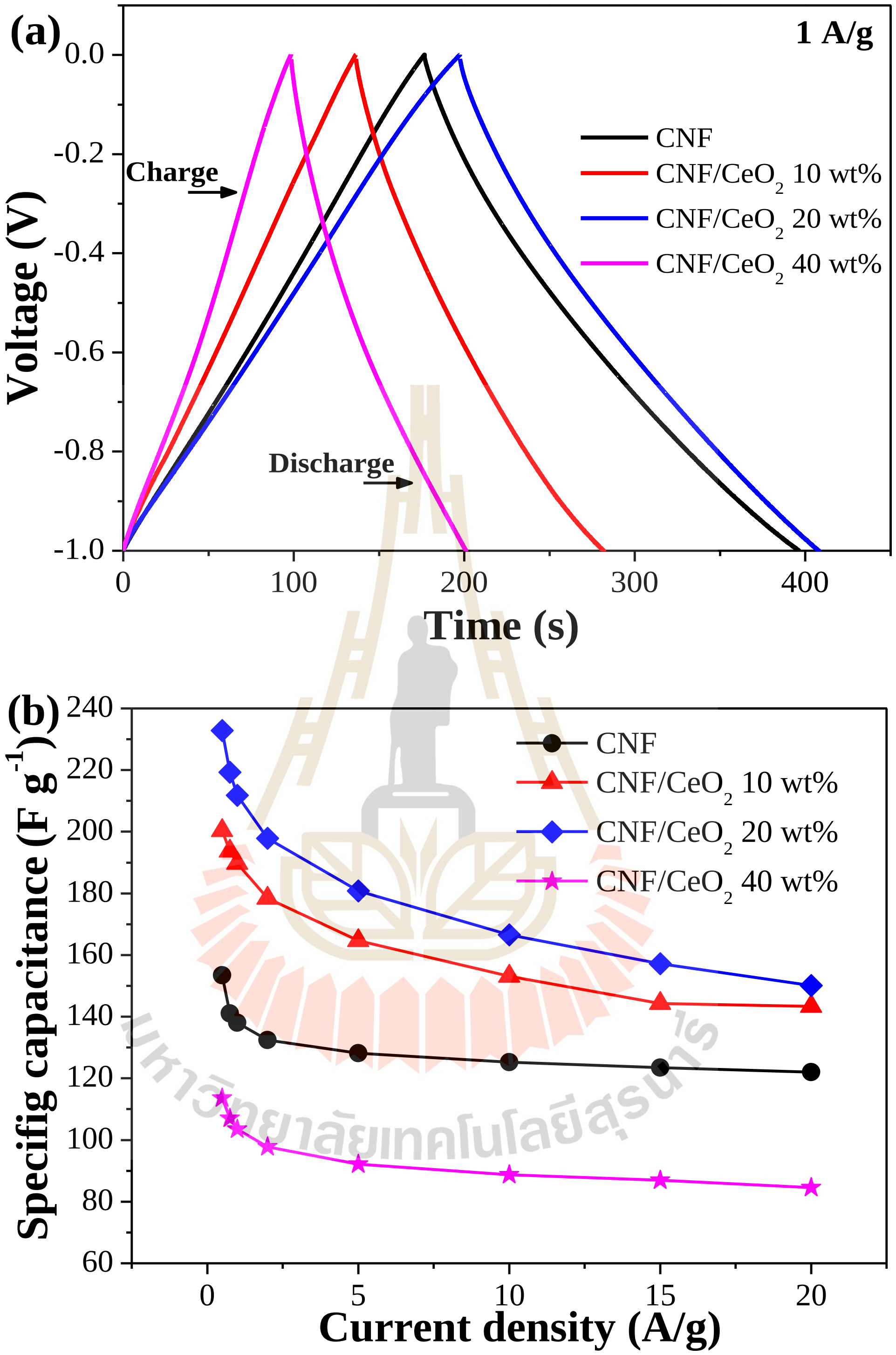

Figure 5.10 (a) CDC at 1 A/g and (b) specific capacitance of CNFs and C/CeO$_2$ composite nanofibers.

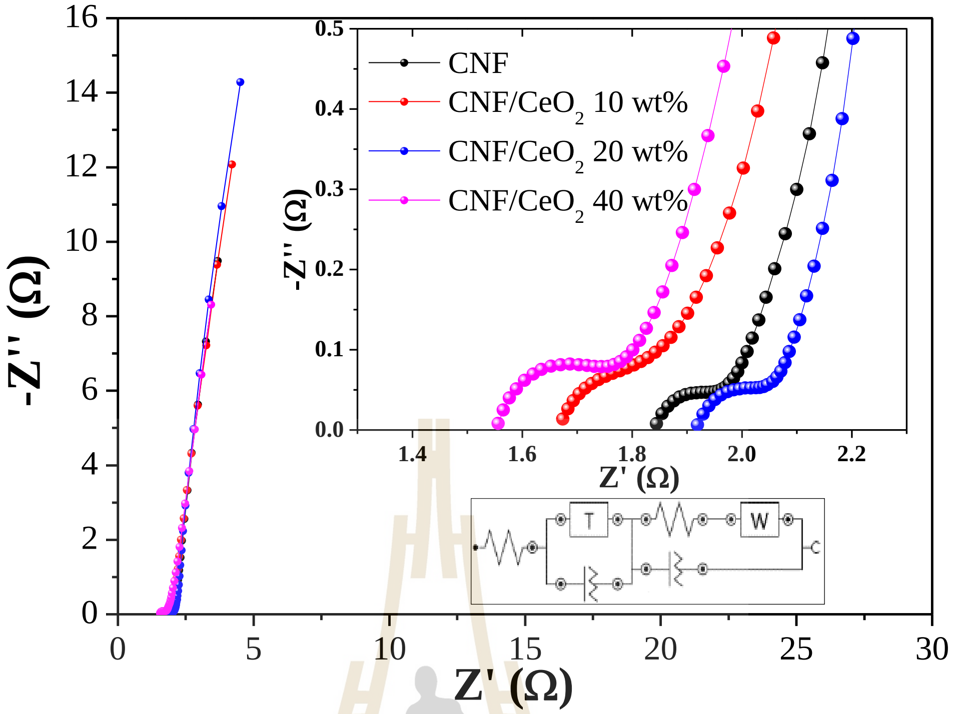

Figure 5.11 EIS curves of CNFs and C/CeO$_2$ composite nanofibers.

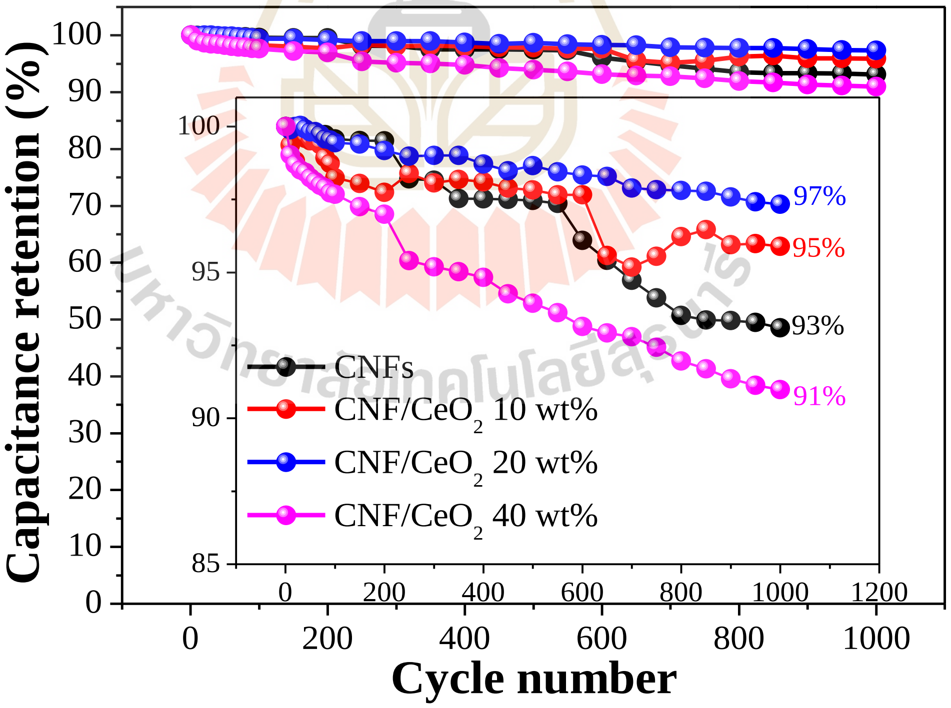

Figure 5.12 Cycle stability of CNFs and C/CeO$_2$ composite nanofibers after 1000 cycles.

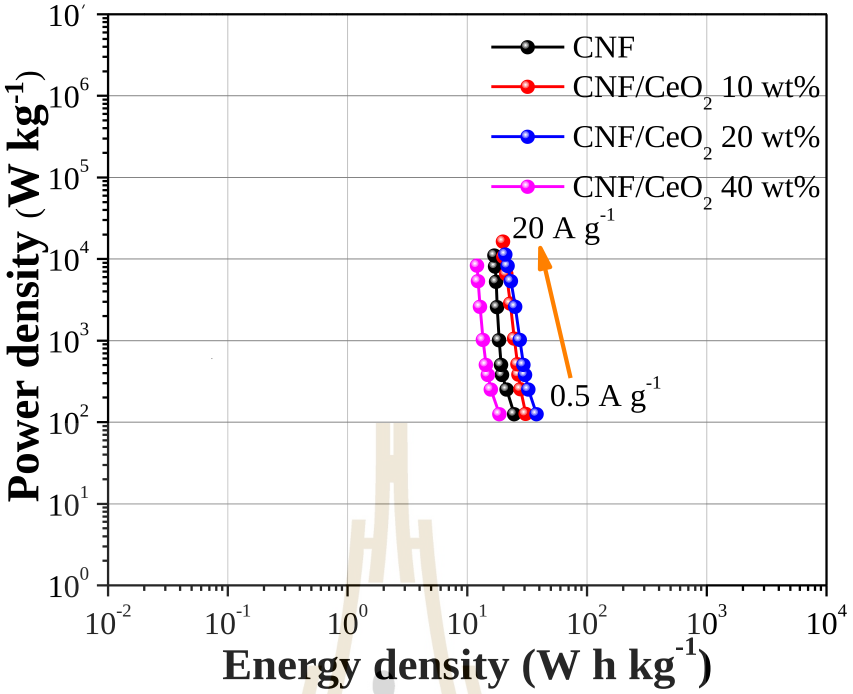

Figure 5.13 Ragone plot showing energy density in relation to the power density of CNFs and C/CeO$_2$ composite nanofibers at different current densities from 0.5 A g^{-1} to 20 A g^{-1}.

Table 5.1 Summary of crystallite sizes from XRD, cubic lattice constants, BET specific surface areas (SBET), pore volumes and diameter mesopore sizes (D_m) of CNF and C/CeO_2 composite nanofibers (CeO_2 = 0, 10, 20 and 40 wt.%) calcined 900 °C for 2 h in argon.

Samples	Crystallite size (nm)	Cubic lattice constant a (nm)	SBET (m^2g^{-1})	Pore volume (cm^3g^{-1})	D_m (nm)
CNFs	-	-	422.30	0.22	2.43
C/CeO_2 10%	-	-	754.86	0.79	3.28
C/CeO_2 20%	14.70	0.535±0.002	631.03	0.55	2.43
C/CeO_2 40%	15.90	0.535±0.003	211.47	0.19	2.43

Table 5.2 Summary of specific capacitances (C_s) obtained from CD curves at various current densities of CNFs and C/CeO_2 composite nanofibers (CeO_2 = 0, 10, 20 and 40 wt.%) calcined 900 °C for 2 h in argon

parameter	CNFs/CeO_2 composite weight %			
	0	10	20	40
C_{CD} (F g^{-1}) at current densities of:				
(A/g)				
0.50	153.41	200.35	232.86	113.60
0.75	141.01	193.71	219.25	107.01
1.0	138.05	189.73	211.84	103.47
2.0	132.45	178.36	197.88	97.75
5.0	128.13	164.63	180.80	92.12
10.0	125.24	153.11	166.55	88.69
15.0	123.48	144.25	157.13	86.95
20.0	121.99	143.33	150.08	84.56

Table 5.3 Summary of performance analysis based on specific capacitance of the electrode materials.

Sample	Electrolyte	Specific capacitance ($F\ g^{-1}$)	Scan rate ($m\ V^{-1}$) or current density ($A\ g^{-1}$)	References
Graphene/CeO_2	2 M KOH	89	1 A g^{-1}	(Chen and Xue, 2015)
Carbon/CeO_2	6 M KOH	61	1 A g^{-1}	(Shuvo et al., 2015)
Porous carbon/CeO_2	-	75	1 A g^{-1}	(Stoller and Ruoff, 2010)
Graphene-ceria	1 M H_2SO_4	110	10 mV s^{-1}	(Saravanan et al., 2015)
CeO_2	6 M KOH	73.70	1 A g^{-1}	(Deng et al., 2017)
CeO_2	3 M KOH	57	5 mV s^{-1}	(Wang et al., 2011)
CNFs	6 M KOH	153.41	0.5 A g^{-1}	This work
C/CeO_2 10 wt.%	6 M KOH	200.35	0.5 A g^{-1}	This work
C/CeO_2 20 wt.%	6 M KOH	232.86	0.5 A g^{-1}	This work
C/CeO_2 40 wt.%	6 M KOH	113.60	0.5 A g^{-1}	This work

CHAPTER VI

CONCLUSIONS AND SUGGESTIONS

6.1 Conclusions

CeO_2 and transition metal-doped (Fe, Co, Cu and La) $Ce_{1-x}M_xO_2$ nanostructures where $0 \le x \le 10$ have been successfully fabricated by simple solution method and electrospinning technique using PVP as a polymer solution. The XRD and SEAD results indicate that all the samples had a cubic fluorite structure of CeO_2 without secondary phase, which indicates that Fe^{3+} ions Co^{2+} ions La^{3+} ions are substituted in Ce^{4+} sites. The average crystallite size was obtained to be 11.50±1.8 to 34.1±0.9 nm. The morphology of nanostructures prepared by simple solution method shows agglomerate nanoparticles look like nanosphere, while that fabricated by electrospinning technique compose of uniform long length nanofibers. The optical properties of $CeO_2$and $Ce_{1-x}M_xO_2$ nanostructures were exhibits UV-vis absorption in the range of 285 to 350 nm (E_g = 2.68 to 3.28eV). UV-Vis spectra showed a redshift of band gap energy which is originated from defects/oxygen vacancy caused by TM substitution. The present of oxygen vacancy is confirmed by XANES and XPS measurements, which reveals that most of the Fe^{3+} ions Co^{2+} ions La^{3+} ions are in the 3+, 2+ and 3+ state, respectively, and that some Ce ions transform to the 3+ state. The Ce^{3+} and Fe^{3+}, $Co^{2+}$and La^{3+}spin electrons are induced weak RTFM in transition metal-doped (Fe, Co, Cu and La) $Ce_{1-x}M_xO_2$ nanostructures. This behavior indicates that the ferromagnetism is essentially related to oxygen vacancy/defects. The RT-FM in

The sample is suggested to the exchange interactions between Fe^{3+} or Fe^{2+} or^{+}, Co^{2+} or La^{3+}or Ce^{3+} and oxygen vacancy on the surface of sample. In addition, the C/CeO_2 composite nanofibers with 10, 20 and 40 wt.% of CeO_2 were successfully fabricated by electrospinning method. The formation of CNF/CeO_2 composites was studied by XRD, Raman, SEM and TEM results. The chemical composition was confirmed by XPS and EDS results. The specific surface area and pore volume were investigated by BET. The diameter of CNF and CNF/CeO_2 composite nanostructures were in the range of 400 to 720 nm with CeO_2 nanoparticles around 10 to 70 nm. The C/CeO_2 20 wt.% electrode exhibited the highest specific capacitance of 232.86 F g^{-1} at the current density of 0.50 A g^{-1}, which is 51% higher than that of CNFs electrode synthesized by the same method. Furthermore, it exhibits good specific capacitance retention of 97% after 1000 continuous charge-discharge cycles, resulting a better cyclic stability than the pure CNFs. The C/CeO_2 20 wt.% could be a promising electroactive material for supercapacitor applications.

6.2 suggestions

The findings in this research suggest the future works as follows: Investigation of the stoichiometry of $Ce_{1-x}M_xO$ (M = Fe, Co, Cu and La) using Energy Dispersive Spectroscopy (EDS) is required to confirm the fraction of constituent elements of Ce, O, Fe, Co, Cu and La ions in the prepared samples. Along with studying of the dielectric constant on materials will be necessary to explain of ferromagnetism based on BMP model. This model constitutes from the magnetic ions via *F*-center exchange. The orbital radius of the trapped electron is determined by ~ $a_0\varepsilon$, where a_0 is the Bohr radius and ε is the dielectric constant of the material. Although the room temperature ferromagnetic with high Curie temperature of materials has the potential for developing spintronics devices. Moreover, local structures using EXAFS is important to confirm the substitution of dopants in ferromagnetic metal-doped CeO_2 system. Finally, update application of C/CeO_2 composite nanofibers for energy storage device using asymmetric supercapacitor process.

REFERENCES

REFERENCES

Abbas, F., Jan, T., Iqbal, J., Ahmad, I., Naqvi, M. S. H. and Malik, M. (2015). Facile synthesis of ferromagnetic Ni doped CeO_2 nanoparticles with enhanced anticancer activity. **Applied Surface Science** 357, Part A: 931-936.

Abbas, F., Jan, T., Iqbal, J. and Naqvi, M. S. H. (2015). Fe doping induced enhancement in room temperature ferromagnetism and selective cytotoxicity of CeO_2 nanoparticles. **Current Applied Physics** 15(11): 1428-1434.

Amoretti, G. and Fournier, J. M. (1984). On the interpretation of magnetic susceptibility data by means of a modified Curie-Weiss law. **Journal of Magnetism and Magnetic Materials** 43(3): L217-L220.

Anderson, P. W. (1950). Antiferromagnetism. Theory of Superexchange Interaction. **Physical Review** 79(2): 350-356.

Aravinda, L. S., Udaya Bhat, K. and Ramachandra Bhat, B. (2013). Nano CeO_2/activated carbon based composite electrodes for high performance supercapacitor. **Materials Letters** 112: 158-161.

Bamwenda, G. R. and Arakawa, H. (2000). Cerium dioxide as a photocatalyst for water decomposition to O_2 in the presence of Ce_{aq}^{4+} and Fe_{aq}^{3+} species. **Journal of Molecular Catalysis A: Chemical** 161(1–2): 105-113.

Barreca, D., Bruno, G., Gasparotto, A., Losurdo, M. and Tondello, E. (2003). **Nanostructure and optical properties of CeO_2 thin films obtained by plasma-enhanced chemical vapor deposition**.

Bäumer, M. and Freund, H.-J. (1999). Metal deposits on well-ordered oxide films. **Progress in Surface Science** 61(7–8): 127-198.

Bednarski, H. (2014). The origin of ferromagnetic interaction between bound magnetic polarons in diluted magnetic semiconductors: A minimal model. **Journal of Magnetism and Magnetic Materials** 349: 281-283.

Bernard, D., Cullity and Stuart, R., Stock (2001). **Elements of X-ray diffraction**. Prentice Hall, Englewood Cliffs, N.J.

Bryan, J. D., Heald, S. M., Chambers, S. A. and Gamelin, D. R. (2004). Strong Room-Temperature Ferromagnetism in Co^{2+}-Doped TiO_2 Made from Colloidal Nanocrystals. **Journal of the American Chemical Society** 126(37): 11640-11647.

Burke, A. (2000). Ultracapacitors: why, how, and where is the technology. **Journal of Power Sources** 91(1): 37-50.

Caglar, M. and Yakuphanoglu, F. (2012). Structural and optical properties of copper doped ZnO films derived by sol–gel. **Applied Surface Science** 258(7): 3039-3044.

Channei, D., Inceesungvorn, B., Wetchakun, N., Ukritnukun, S., Nattestad, A., Chen, J. and Phanichphant, S. (2014). Photocatalytic Degradation of Methyl Orange by CeO_2 and Fe–doped CeO_2 Films under Visible Light Irradiation. **Scientific Reports** 4: 5757.

Chen, K. and Xue, D. (2015). In-situ electrochemical route to aerogel electrode materials of graphene and hexagonal CeO_2. **Journal of Colloid and Interface Science** 446: 77-83.

Chenguo, H., Zuwei, Z., Hong, L., Puxian, G. and Zhong Lin, W. (2006). Direct synthesis and structure characterization of ultrafine CeO_2 nanoparticles. **Nanotechnology** 17(24): 5983.

Choi, J.-K., Hwang, I.-S., Kim, S.-J., Park, J.-S., Park, S.-S., Jeong, U., Kang, Y. C. and Lee, J.-H. (2010). Design of selective gas sensors using electrospun Pd-doped SnO_2 hollow nanofibers. **Sensors and Actuators B: Chemical** 150(1): 191-199.

Coey, J. M. D. (2006). Dilute magnetic oxides. **Current Opinion in Solid State and Materials Science** 10(2): 83-92.

Coey, J. M. D., Ackland, K., Venkatesan, D. M. and Sen, S. (2016). Collective magnetic response of CeO_2 nanoparticles. **Nature Physics** 12: 694–699.

Coey, J. M. D., Douvalis, A. P., Fitzgerald, C. B. and Venkatesan, M. (2004). Ferromagnetism in Fe-doped SnO_2 thin films. **Applied Physics Letters** 84(8): 1332-1334.

Coey, J. M. D., Venkatesan, M. and Fitzgerald, C. B. (2005). Donor impurity band exchange in dilute ferromagnetic oxides. **Nature Materials** 4(2): 173-179.

Coey, J. M. D., Venkatesan, M. and Fitzgerald, C. B. (2005). Donor impurity band exchange in dilute ferromagnetic oxides. **Nat Mater** 4(2): 173-179.

Cuesta, A., Dhamelincourt, P., Laureyns, J., Martínez-Alonso, A. and M. D. Tascón, J. (1998). Comparative performance of X-ray diffraction and Raman microprobe techniques for the study of carbon materials. **Journal of Materials Chemistry** 8(12): 2875-2879.

Cui, Q., Dong, X., Wang, J. and Li, M. (2008). Direct fabrication of cerium oxide hollow nanofibers by electrospinning. **Journal of Rare Earths** 26(5): 664-669.

Daengsakul, S., Kidkhunthod, P., Soisang, O., Kuenoon, T., Bootchanont, A. and Maensiri, S. (2015). The effect of Gd doping in $La_{1-x-y}Gd_xSr_yMnO_3$ compound on nanocrystalline structure by X-ray Absorption Spectroscopy (XAS) technique. **Microelectronic Engineering** 146: 38-42.

Deng, D., Chen, N., Li, Y., Xing, X., Liu, X., Xiao, X. and Wang, Y. (2017). Cerium oxide nanoparticles/multi-wall carbon nanotubes composites: Facile synthesis and electrochemical performances as supercapacitor electrode materials. **Physica E: Low-dimensional Systems and Nanostructures** 86: 284-291.

Désaunay, T., Bonura, G., Chiodo, V., Freni, S., Couzinié, J. P., Bourgon, J., Ringuedé, A., Labat, F., Adamo, C. and Cassir, M. (2013). Surface-dependent oxidation of H_2 on CeO_2 surfaces. **Journal of Catalysis** 297: 193-201.

Dhara, A., Sain, S., Sadhukhan, P., Das, S. and Pradhan, S. K. (2019). Effect of lattice distortion in optical properties of CeO_2 nanocrystals on Mn substitution by mechanical alloying. **Journal of Alloys and Compounds** 786: 215-224.

Dietl, T., Ohno, H., Matsukura, F., Cibert, J. and Ferrand, D. (2000). Zener Model Description of Ferromagnetism in Zinc-Blende Magnetic Semiconductors. **Science** 287(5455): 1019.

Durst, A. C., Bhatt, R. N. and Wolff, P. J. P. R. B. (2002). Bound magnetic polaron interactions in insulating doped diluted magnetic semiconductors. **Physical Review** 65(23): 235205.

E. Angelescu, D. and N. Bhatt, R. (2001). Effective Interaction Hamiltonian of Polaron Pairs in Diluted Magnetic Semiconductors. **Physical Review B** 65: 075211.

El-Hagary, M., Shaaban, E. R., Moustafa, S. H. and Gad, G. M. A. (2019). The particle size-dependent optical band gap and magnetic properties of Fe-doped CeO_2 nanoparticles. **Solid State Sciences** 91: 15-22.

Fitzgerald, C. B., Venkatesan, M., Douvalis, A. P., Huber, S., Coey, J. M. D. and Bakas, T. (2004). SnO_2 doped with Mn, Fe or Co: Room temperature dilute magnetic semiconductors. **Journal of Applied Physics** 95(11): 7390-7392.

Fracchia, M., Ghigna, P., Vertova, A., Rondinini, S. and Minguzzi, A. (2018). Time-Resolved X-ray Absorption Spectroscopy in (Photo)Electrochemistry. **Surfaces** 1(1).

Fujisawa, K., Cruz-Silva, R., Yang, K.-S., Kim, Y. A., Hayashi, T., Endo, M., Terrones, M. and Dresselhaus, M. S. (2014). Importance of open, heteroatom-decorated edges in chemically doped-graphene for supercapacitor applications. **Journal of Materials Chemistry A** 2(25): 9532-9540.

Galperin, F. M. (1975). Electron Structure of Atoms of the 3d Transition Metals. 70(1): 227-236.

Ganguly, A., Sharma, S., Papakonstantinou, P. and Hamilton, J. (2011). Probing the Thermal Deoxygenation of Graphene Oxide Using High-Resolution In Situ X-ray-Based Spectroscopies. **The Journal of Physical Chemistry C** 115(34): 17009-17019.

Gogoi, A., Navgire, M., Sarma, K. C. and Gogoi, P. (2017). Fe_3O_4-CeO_2 metal oxide nanocomposite as a Fenton-like heterogeneous catalyst for degradation of catechol. **Chemical Engineering Journal** 311: 153-162.

Graydon, J. W., Panjehshahi, M. and Kirk, D. W. (2014). Charge redistribution and ionic mobility in the micropores of supercapacitors. **Journal of Power Sources** 245: 822-829.

Grover, V., Shukla, R., Kumari, R., Mandal, B. P., Kulriya, P. K., Srivastava, S. K., Ghosh, S., Tyagi, A. K. and Avasthi, D. K. (2014). Effect of grain size and microstructure on radiation stability of CeO_2: an extensive study. **Physical Chemistry Chemical Physics** 16(48): 27065-27073.

Gupta, R. K., Ghosh, K. and Kahol, P. K. (2010). Room temperature ferromagnetic multilayer thin film based on indium oxide and iron oxide for transparent spintronic applications. **Materials Letters** 64(18): 2022-2024.

He, D., Hao, H., Chen, D., Liu, J., Yu, J., Lu, J., Liu, F., Wan, G., He, S. and Luo, Y. (2016). Synthesis and application of rare-earth elements (Gd, Sm, and Nd) doped ceria-based solid solutions for methyl mercaptan catalytic decomposition. **Catalysis Today** 281.

He, H.-W., Wu, X.-Q., Ren, W., Shi, P., Yao, X. and Song, Z.-T. (2012). Synthesis of crystalline cerium dioxide hydrosol by a sol–gel method. **Ceramics International** 38: S501-S504.

He, X., Hu, Y., Shen, Z., Chen, R., Wu, K., Cheng, Z., Zhang, X. W. and Pan, P. (2017). Channelized carbon nanofiber with uniform-dispersed GeO_2 as anode for long-lifespan lithium-ion batteries. **Journal of Alloys and Compounds** 729: 313-322.

Hou, J., You, G., Xu, Y., Wang, C., Wang, P., Miao, L., Ao, Y., Li, Y. and Lv, B. (2015). Effects of CeO_2 nanoparticles on biological nitrogen removal in a sequencing batch biofilm reactor and mechanism of toxicity. **Bioresource Technology** 191: 73-78.

Ingram, B. J., Gonzalez, G. B., Kammler, D. R., Bertoni, M. I. and Mason, T. O. (2004). Chemical and Structural Factors Governing Transparent Conductivity in Oxides. **Journal of Electroceramics** 13(1): 167-175.

Joung, D., Singh, V., Park, S., Schulte, A., Seal, S. and Khondaker, S. I. (2011). Anchoring Ceria Nanoparticles on Reduced Graphene Oxide and Their Electronic Transport Properties. **The Journal of Physical Chemistry C** 115(50): 24494-24500.

K Babitha, K., Sreedevi, A., K P, P., Sabu, B. and Varghese, T. (2015). Structural characterization and optical studies of CeO_2 nanoparticles synthesized by chemical precipitation. **Indian Journal of Pure & Applied Physics** 53: 9.

Keely, W. M. and Maynor, H. W. (1963). Thermal Studies of Nickel, Cobalt, Iron and Copper Oxides and Nitrates. **Journal of Chemical & Engineering Data** 8(3): 297-300.

Khan, M. E., Khan, M. M. and Cho, M. H. (2017). Ce^{3+}-ion, Surface Oxygen Vacancy, and Visible Light-induced Photocatalytic Dye Degradation and Photocapacitive Performance of CeO_2-Graphene Nanostructures. **Scientific Reports** 7(1): 5928.

Khan, M. M., Ansari, S. A., Pradhan, D., Han, D. H., Lee, J. and Cho, M. H. (2014). Defect-Induced Band Gap Narrowed CeO_2 Nanostructures for Visible Light Activities. **Industrial & Engineering Chemistry Research** 53(23): 9754-9763.

Kilbourn, B. T. (1992). **Cerium: A Guide to Its Role in Chemical Technology**. CA U.S.A, Inc.: Mountain Pass.

Kim, C., Park, S.-H., Cho, J.-I., Lee, D.-Y., Park, T.-J., Lee, W.-J. and Yang, K.-S. (2004). Raman spectroscopic evaluation of polyacrylonitrile-based carbon nanofibers prepared by electrospinning. **Journal of Raman Spectroscopy** 35(11): 928-933.

Kumar, S., Ahmed, F., Anwar, M. S., Choi, H. K., Chung, H. and Koo, B. H. (2012). Signature of room temperature ferromagnetism in Mn doped CeO_2 nanoparticles. **Materials Research Bulletin** 47(10): 2980-2983.

Kumar, S., Kim, Y. J., Koo, B. H., Choi, H. and Lee, C. G. (2009). Structural and Magnetic Properties of Co Doped CeO_2 Nano-Particles. **IEEE Transactions on Magnetics** 45(6): 2439-2441.

Kung, H. H. (1989). **Preface: Studies in Surface Science and Catalysis.** H. K. Harold, Elsevier. Volume 45**:** vii-viii.

LavrenčičŠtangar, U., Orel, B., Grabec, I., Ogorevc, B. and Kalcher, K. (1993). **Optical and electrochemical properties of CeO_2 and CeO_2TiO_2 coatings**.

Li, D. and Xia, Y. (2004). Direct Fabrication of Composite and Ceramic Hollow Nanofibers by Electrospinning. **Nano Letters** 4(5): 933-938.

Li, X., Song, J., Liu, Y. and Zeng, H. (2014). Controlling oxygen vacancies and properties of ZnO. **Current Applied Physics** 14(3): 521-527.

Li, Z., Niu, X., Lin, Z., Wang, N., Shen, H., Liu, W., Sun, K., Fu, Y. Q. and Wang, Z. (2016). Hydrothermally synthesized CeO_2 nanowires for H_2S sensing at room temperature. **Journal of Alloys and Compounds** 682: 647-653.

Lin, T.-C., Seshadri, G. and Kelber, J. A. (1997). A consistent method for quantitative XPS peak analysis of thin oxide films on clean polycrystalline iron surfaces. **Applied Surface Science** 119(1): 83-92.

Luo, Y., Yang, T., Zhao, Q. and Zhang, M. (2017). CeO_2/CNTs hybrid with high performance as electrode materials for supercapacitor. **Journal of Alloys and Compounds** 729: 64-70.

Malleshappa, J., Nagabhushana, H., Sharma, S. C., Vidya, Y. S., Anantharaju, K. S., Prashantha, S. C., Daruka Prasad, B., Raja Naika, H., Lingaraju, K. and Surendra, B. S. (2015). Leucas aspera mediated multifunctional CeO_2 nanoparticles: Structural, photoluminescent, photocatalytic and antibacterial properties. **Spectrochimica Acta Part A: Molecular and Biomolecular Spectroscopy** 149: 452-462.

Matsumoto, Y., Murakami, M., Shono, T., Hasegawa, T., Fukumura, T., Kawasaki, M., Ahmet, P., Chikyow, T., Koshihara, S.-y. and Koinuma, H. (2001). Room-Temperature Ferromagnetism in Transparent Transition Metal-Doped Titanium Dioxide. **Science** 291(5505): 854.

Meng, F., Zhang, C., Fan, Z., Gong, J., Li, A., Ding, Z., Tang, H., Zhang, M. and Wu, G. (2015). Hydrothermal synthesis of hexagonal CeO_2 nanosheets and their room temperature ferromagnetism. **Journal of Alloys and Compounds** 647: 1013-1021.

MingYan, W., Wei, Z., DongEn, Z., ShuAn, L., WeiXing, M., ZhiWei, T. and Jun, C. (2014). CeO_2 hollow nanospheres decorated reduced graphene oxide composite for efficient photocatalytic dye-degradation. **Materials Letters** 137: 229-232.

Miri, A. and Sarani, M. (2018). Biosynthesis, characterization and cytotoxic activity of CeO_2 nanoparticles. **Ceramics International** 44(11): 12642-12647.

Mogensen, M., Sammes, N. M. and Tompsett, G. A. (2000). Physical, chemical and electrochemical properties of pure and doped ceria. **Solid State Ionics** 129(1–4): 63-94.

Mousavi-Kamazani, M. and Azizi, F. (2019). Facile sonochemical synthesis of Cu doped CeO_2 nanostructures as a novel dual-functional photocatalytic adsorbent. **Ultrasonics Sonochemistry**: 104695.

Mujtaba, A. and Janjua, N. K. (2016). Electrochemical sensing platform based on $CuO@CeO_2$ hybrid oxides. **Journal of Electroanalytical Chemistry** 763: 125-133.

Murugan, R., Vijayaprasath, G., Mahalingam, T. and Ravi, G. (2016). Defect induced magnetic transition in Co doped CeO_2 sputtered thin films. **Ceramics International** 42(10): 11724-11731.

Nakamura, I., Negishi, N., Kutsuna, S., Ihara, T., Sugihara, S. and Takeuchi, K. (2000). Role of oxygen vacancy in the plasma-treated TiO_2 photocatalyst with visible light activity for NO removal. **Journal of Molecular Catalysis A: Chemical** 161(1): 205-212.

Newville, M. (2001). EXAFS analysis using FEFF and FEFFIT. **Journal of Synchrotron Radiation** 8: 96-100.

Nilmoung, S., Sinprachim, T., Kotutha, I., Kidkhunthod, P., Yimnirun, R., Rujirawat, S. and Maensiri, S. (2016). Electrospun carbon/$CuFe_2O_4$ composite nanofibers with improved electrochemical energy storage performance. **Journal of Alloys and Compounds** 688: 1131-1140.

Noguera, C. (1996). **Physics and Chemistry at Oxide Surfaces**, Cambridge University Press.

Novák, N. P. (2016). **Transition Metal Oxides: Magnetism: Reference Module in Materials Science and Materials Engineering**, Elsevier.

Ohno, H. (1998). Making Nonmagnetic Semiconductors Ferromagnetic. **Science** 281(5379): 951.

Pai, R., Singh, D. A., Simotwo, S. and Kalra, V. (2018). **In Situ Grown Iron Oxides on Carbon Nanofibers as Freestanding Anodes in Aqueous Supercapacitors**.

Pearton, S. J., Heo, W. H., Ivill, M., Norton, D. P. and Steiner, T. (2004). Dilute magnetic semiconducting oxides. **Semiconductor Science and Technology** 19(10): R59.

Phokha, S., Hunpratub, S., Chanlek, N., Sonsupap, S. and Maensiri, S. (2018). Synthesis, characterization and electrochemical performance of carbon/Ni-doped CeO_2 composites. **Journal of Alloys and Compounds** 750: 788-797.

Phokha, S., Pinitsoontorn, S. and Maensiri, S. (2013). Structure and Magnetic Properties of Monodisperse Fe^{3+}-doped CeO_2 Nanospheres. **Nano-Micro Letters** 5(4): 223-233.

Phokha, S., Prabhakaran, D., Boothroyd, A., Pinitsoontorn, S. and Maensiri, S. (2014). Ferromagnetic induced in Cr-doped CeO_2 particles. **Microelectronic Engineering** 126: 93-98.

Ponhan, W., Amornkitbamrung, V. and Maensiri, S. (2014). Room temperature ferromagnetism observed in pure $La_{0.5}Sr_{0.5}TiO_3$ nanofibers fabricated by electrospinning. **Journal of Alloys and Compounds** 606: 182-188.

Qi-Ye, W., Huai-Wu, Z., Yuan-Qiang, S., Qing-Hui, Y., Hao, Z. and John, Q. X. (2007). Room-temperature ferromagnetism in pure and Co doped CeO_2 powders. **Journal of Physics: Condensed Matter** 19(24): 246205.

Qu, X.-M., You, L.-X., Tian, X.-C., Zhang, B.-W., Mahadevan, G. D., Jiang, Y.-X. and Sun, S.-G. (2015). CeO_2 nanorods with high energy surfaces as electrocatalytical supports for methanol electrooxidation. **Electrochimica Acta** 182: 1078-1084.

Ramasamy, V. and Vijayalakshmi, G. (2015). Effect of Zn doping on structural, optical and thermal properties of CeO_2 nanoparticles. **Superlattices and Microstructures** 85: 510-521.

Ravel, B. and Newville, M. (2005). ATHENA, ARTEMIS, HEPHAESTUS: data analysis for X-ray absorption spectroscopy using IFEFFIT. **J. Synchrotron Rad.** 12: 537-541.

Rodriguez, J. A., Liu, G., Jirsak, T., Hrbek, J., Chang, Z., Dvorak, J. and Maiti, A. (2002). Activation of gold on titania: adsorption and reaction of SO_2 on Au/TiO_2(110). **J Am Chem Soc** 124(18): 5242-5250.

Saravanan, T., Shanmugam, M., Anandan, P., Azhagurajan, M., Pazhanivel, K., Arivanandhan, M., Hayakawa, Y. and Jayavel, R. (2015). Facile synthesis of graphene-CeO_2 nanocomposites with enhanced electrochemical properties for supercapacitors. **Dalton Transactions** 44(21): 9901-9908.

Sarpoushi, M. R., Nasibi, M., Golozar, M. A., Shishesaz, M. R., Borhani, M. R. and Noroozi, S. (2014). Electrochemical investigation of graphene/cerium oxide nanoparticles as an electrode material for supercapacitors. **Materials Science in Semiconductor Processing** 26(1): 374-378.

Shan, W., Guo, H., Liu, C. and Wang, X. (2012). Controllable preparation of CeO_2 nanostructure materials and their catalytic activity. **Journal of Rare Earths** 30(7): 665-669.

Shanmuga Sundari, S., Sugan, S. and Pabitha, G. (2018). Induced Ferromagnetism in Fe Doped CeO_2 Nanoparticles. **Materials Today: Proceedings** 5(8, Part 3): 16633-16639.

Sharma, S. K., Thakur, P., Kumar, S., Shukla, D. K., Brookes, N. B., Lee, C. G., Pirota, K. R., Koo, B. H. and Knobel, M. (2010). Room temperature ferromagnetism in Fe-doped CeO_2 thin films grown on $LaAlO_3$ (001). **Thin Solid Films** 519(1): 410-413.

Shiyou, H. and Tianxi, L. (2007). Preparation and Characterization of Porous $Ce_{1-x}La_xO_{2-\delta}$. **Journal of Rare Earths** 25: 247-249.

Shuvo, M. A. I., Karim, H., Islam, M. T., Rodriguez, G., Nandasiri, M. I., Schwarz, A. M., Devaraj, A., Noveron, J. C., Vijayakumar, M. and Lin, Y. (2015). High-performance porous carbon/CeO_2 nanoparticles hybrid super-capacitors for energy storage. **SPIE Smart Structures and Materials+Nondestructive Evaluation and Health Monitoring**, SPIE.

Snook, G. A., Kao, P. and Best, A. S. (2011). Conducting-polymer-based supercapacitor devices and electrodes. **Journal of Power Sources** 196(1): 1-12.

Šolcová, O., Balkan, T., Güler, Z., Morozova, M., Dytrych, P. and Sarac, A. (2014). New Preparation Route of TiO_2 Nanofibers by Electrospinning: Spectroscopic and Thermal Characterizations. **Science of Advanced Materials** 6: 2618-2624

Song, Y. Q., Zhang, H. W., Liu, Y. L., Li, Y. X., Shah, L. R. and Xiao, J. Q. (2010). Annealing effects on the ferromagnetism of $Ce_{0.97}Co_{0.03}O_{2-\delta}$ compounds. **Physica B: Condensed Matter** 405(11): 2530-2533.

Sonsupap, S., Kidkhunthod, P., Chanlek, N., Pinitsoontorn, S. and Maensiri, S. (2016). Fabrication, structure, and magnetic properties of electrospun $Ce_{0.96}Fe_{0.04}O_2$ nanofibers. **Applied Surface Science** 380: 16-22.

Spaldin, N. A. (2003). **Magneticmaterials fundamentals and device applications**

Cambridge, The press syndica of the university of Cambridge**:** 100-101.

Stoller, M. D. and Ruoff, R. S. (2010). Best practice methods for determining an electrode material's performance for ultracapacitors. **Energy & Environmental Science** 3(9): 1294-1301.

Suzuki, T., Kosacki, I., Anderson, H. U. and Colomban, P. (2001). Electrical Conductivity and Lattice Defects in Nanocrystalline Cerium Oxide Thin Films. **Journal of the American Ceramic Society** 84(9): 2007-2014.

Takahashi, Y., Shimizu, H., Usui, A., Kagi, H. and Nomura, M. (2000). Direct observation of tetravalent cerium in ferromanganese nodules and crusts by X-ray-absorption near-edge structure (XANES). **Geochimica et Cosmochimica Acta** 64(17): 2929-2935.

Tang, Y., Fu, S., Zhao, K., Xie, G. and Teng, L. (2015). Synthesis of TiO_2 nanofibers with adjustable anatase/rutile ratio from Ti sol and rutile nanoparticles for the degradation of pollutants in wastewater. **Ceramics International** 41(10, Part A): 13285-13293.

Tsunekawa, S., Wang, J. T. and Kawazoe, Y. (2006). Lattice constants and electron gap energies of nano- and subnano-sized cerium oxides from the experiments and first-principles calculations. **Journal of Alloys and Compounds** 408-412: 1145-1148.

Ueda, K., Tabata, H. and Kawai, T. (2001). Magnetic and electric properties of transition-metal-doped ZnO films. **Applied Physics Letters** 79(7): 988-990.

Vanitha, M., Keerthi, Cao, P. and Balasubramanian, N. (2015). Ag nanocrystals anchored CeO_2/graphene nanocomposite for enhanced supercapacitor applications. **Journal of Alloys and Compounds** 644: 534-544.

Vantomme, A., Yuan, Z.-Y., Du, G. and Su, B.-L. (2005). Surfactant-Assisted Large-Scale Preparation of Crystalline CeO_2 Nanorods. **Langmuir** 21(3): 1132-1135.

Venkatesan, M., Stamenov, P., Dorneles, L. S., Gunning, R. D., Bernoux, B. and Coey, J. M. D. (2007). Magnetic, magnetotransport, and optical properties of Al-doped $Zn_{0.95}Co_{0.05}O$ thin films. **Applied Physics Letters** 90(24): 242508.

Wang, A. Q. and Golden, T. D. (2016). Electrochemical Formation of Cerium Oxide/Layered Silicate Nanocomposite Films %. **Journal of Nanotechnology** 2016: 7.

Wang, K., Chang, Y., Lv, L. and Long, Y. (2015). Effect of annealing temperature on oxygen vacancy concentrations of nanocrystalline CeO_2 film. **Applied Surface Science** 351: 164-168.

Wang, T. and Sun, D.-C. (2008). Preparation and characterization of nanometer-scale powders ceria by electrochemical deposition method. **Materials Research Bulletin** 43(7): 1754-1760.

Wang, W., Howe, J. Y., Li, Y., Qiu, X., Joy, D. C., Paranthaman, M. P., Doktycz, M. J. and Gu, B. (2010). A surfactant and template-free route for synthesizing ceria nanocrystals with tunable morphologies. **Journal of Materials Chemistry** 20(36): 7776-7781.

Wang, W., Zhu, Q., Dai, Q. and Wang, X. (2017). Fe doped CeO_2 nanosheets for catalytic oxidation of 1,2-dichloroethane: Effect of preparation method. **Chemical Engineering Journal** 307: 1037-1046.

Wang, X., Jiang, Z., Zheng, B., Xie, Z. and Zheng, L. (2012). Synthesis and shape-dependent catalytic properties of CeO_2 nanocubes and truncated octahedra. **CrystEngComm** 14(22): 7579-7582.

Wang, Y., Guo, C. X., Liu, J., Chen, T., Yang, H. and Li, C. M. (2011). CeO_2 nanoparticles/graphene nanocomposite-based high performance supercapacitor. **Dalton Transactions** 40(24): 6388-6391.

Wang, Y., Song, Y. and Xia, Y. (2016). Electrochemical capacitors: mechanism, materials, systems, characterization and applications. **Chemical Society Reviews** 45(21): 5925-5950.

Wang, Z., Quan, Z. and Lin, J. (2007). Remarkable Changes in the Optical Properties of CeO_2 Nanocrystals Induced by Lanthanide Ions Doping. **Inorganic Chemistry** 46(13): 5237-5242.

Wen, H., Liu, Z., Yang, Q., Li, Y. and Yu, J. (2011). Synthesis and electrochemical properties of CeO_2 nanoparticle modified TiO_2 nanotube arrays. **Electrochimica Acta** 56(7): 2914-2918.

Wongsaprom, K., Sonsupap, S., Maensiri, S. and Kidkhunthod, P. (2015). Room-temperature ferromagnetism in Fe-doped In_2O_3 nanoparticles. **Applied Physics A** 121(1): 239-244.

Yamashita, T. and Hayes, P. (2008). Analysis of XPS spectra of Fe^{2+} and Fe^{3+} ions in oxide materials. **Applied Surface Science** 254(8): 2441-2449.

Yan, S., Ge, S., Zuo, Y., Qiao, W. and Zhang, L. (2009). Effects of carbothermal annealing on structure defects, electrical and magnetic properties in Fe-doped In_2O_3. **Scripta Materialia** 61(4): 387-390.

Yan, S., Ma, S., Xu, X., Lu, Y., Bian, H., Liang, X., Jin, W. and Yang, H. (2016). Synthesis and gas sensing application of porous CeO_2–ZnO hollow fibers using cotton as biotemplates. **Materials Letters** 165: 9-13.

Yan, S. H., Ma, S. Y., Li, W. Q., Xu, X. L., Cheng, L., Song, H. S. and Liang, X. Y. (2015). Synthesis of SnO_2–ZnO heterostructured nanofibers for enhanced ethanol gas-sensing performance. **Sensors and Actuators B: Chemical** 221: 88-95.

Yang, R., Yu, L., Sun, M., Zhao, X., Cheng, G. and Ye, W. (2018). Preparation of 3D micro/nanostructured CeO_2: Influence of organic/inorganic acids. **Particuology** 37: 17-25.

Yang, X., Shao, C., Liu, Y., Mu, R. and Guan, H. (2005). Nanofibers of CeO_2 via an electrospinning technique. **Thin Solid Films** 478(1–2): 228-231.

Yang, Z., Zhao, Z., Yu, J., Li, J., Ren, Z., Ma, S., Ren, S. and Yu, G. (2019). Effect of Co substitution and magnetic field on the morphologies and magnetic properties of CeO_2 nanoparticles. **Ceramics International** 45(9): 11927-11933.

Yin, D., Zhao, F., Zhang, L., Zhang, X., Liu, Y., Zhang, T., Wu, C., Chen, D. and Chen, Z. (2016). Greatly enhanced photocatalytic activity of semiconductor CeO_2 by integrating with upconversion nanocrystals and graphene. **RSC Advances** 6(105): 103795-103802.

Zener, C. (1951). Interaction between the d-Shells in the Transition Metals. III. Calculation of the Weiss Factors in Fe, Co, and Ni. **Physical Review** 83(2): 299-301.

Zhang, F., Wang, P., Koberstein, J., Khalid, S. and Chan, S.-W. (2004). Cerium oxidation state in ceria nanoparticles studied with X-ray photoelectron spectroscopy and absorption near edge spectroscopy. **Surface Science** 563(1): 74-82.

Zheng, X., Huang, S., Yang, D., Zhai, H., You, Y., Fu, X., Yuan, J., Zhou, X., Wen, J. and Liu, Y. (2017). Synthesis of X-architecture CeO_2 for the photodegradation of methylene blue under UV-light irradiation. **Journal of Alloys and Compounds** 705: 131-137.

Zhu, X., Zhu, Y., Murali, S., Stoller, M. D. and Ruoff, R. S. (2011). Nanostructured Reduced Graphene Oxide/Fe_2O_3 Composite As a High-Performance Anode Material for Lithium Ion Batteries. **ACS Nano** 5(4): 3333-3338.

APPENDIX

APPENDIX

PUBLICATIONS AND PRESENTATIONS

B.1 List of publications

Sonsupap, S, Kidkhunthod, P, Chanlek, N, Pinitsoontorn, S, Maensiri, S, (2016). Fabrication, structure, and magnetic properties of electrospun $Ce_{0.96}Fe_{0.04}O_2$ nanofibers. **Applied surface science** 380: 16-22.

B.2 List of oral presentations

Sonsupap, S, Pinitsoontorn, S, Maensiri, S. (October 2014). Fabrication, Structure, and Magnetic Properties of Eelectrospun CeO_2 Nanofibers. **The 9th Asian Meeting on Feroelectric jointly with the 9th Asian Meeting on Electroceramics (AFM-AMEC-2014).** Shanghai, Chaina.

Sonsupap, S, Kidkhunthod, P, Chanlek, N, Pinitsoontorn, S, Maensiri, S, (September 2016). Fabrication, structure, and magnetic properties of electrospun $Ce_{0.96}Fe_{0.04}O_2$ nanofibers. **The 10th International Conference on Surfaces, Coatings and Nanostructured Materials (NANOSMAT-Manchester)**. Manchester, United Kingdom.

Sonsupap, S, Kidkhunthod, P, Chanlek, N, Pinitsoontorn, S, Maensiri, S, (November 2016). Fabrication, structure, and magnetic properties of Fe-doped CeO_2 various shape. **Nanothailand 2016**. Nakhon Ratchasima, Thailand.

Sonsupap, S, Kidkhunthod, P, Chanlek, N, Pinitsoontorn, S, Maensiri, S, (November 2017). **The First Materials Research Society of Thailand International Conference (1st MRS Thailand International Conference).** Chiang Mai, Thailand.

B.3 List of poster presentations

Sonsupap, S, Kidkhunthod, P, Chanlek, N, Pinitsoontorn, S, Maensiri, S, (November 2016). Preparation, structure, and magnetic properties of La-doped CeO_2 nanostructure. **8th International Workshop on Advanced Materials Science and Nanotechnology (IWAMSN 2016).** Ha Long City, Vietnam.

CURRICULUM VITAE

Name Mister Somchai Sonsupap

Date of Birth July 29, 1986

Place of Birth 27/1 Moo 6 Tambol Wangsapung, Wangsapung District, Loei Province, 42130, Thailand.

Education

2005 -2009 Mahasarakham University, Mahasarakham, Thailand.
B.S. in Appiled Physics.

2009 -2013 Mahasarakham University, Mahasarakham, Thailand.
M.Sc. in Physics

2013-2019 Suranaree University of Technology, Nakhon Ratchasima, Thailand,
Ph.D. in Physics